Dynamic Modelling of Ice Rubble and Extrusion Loads on Offshore Wind Turbines in Crushing Interaction

Maarten Steggink

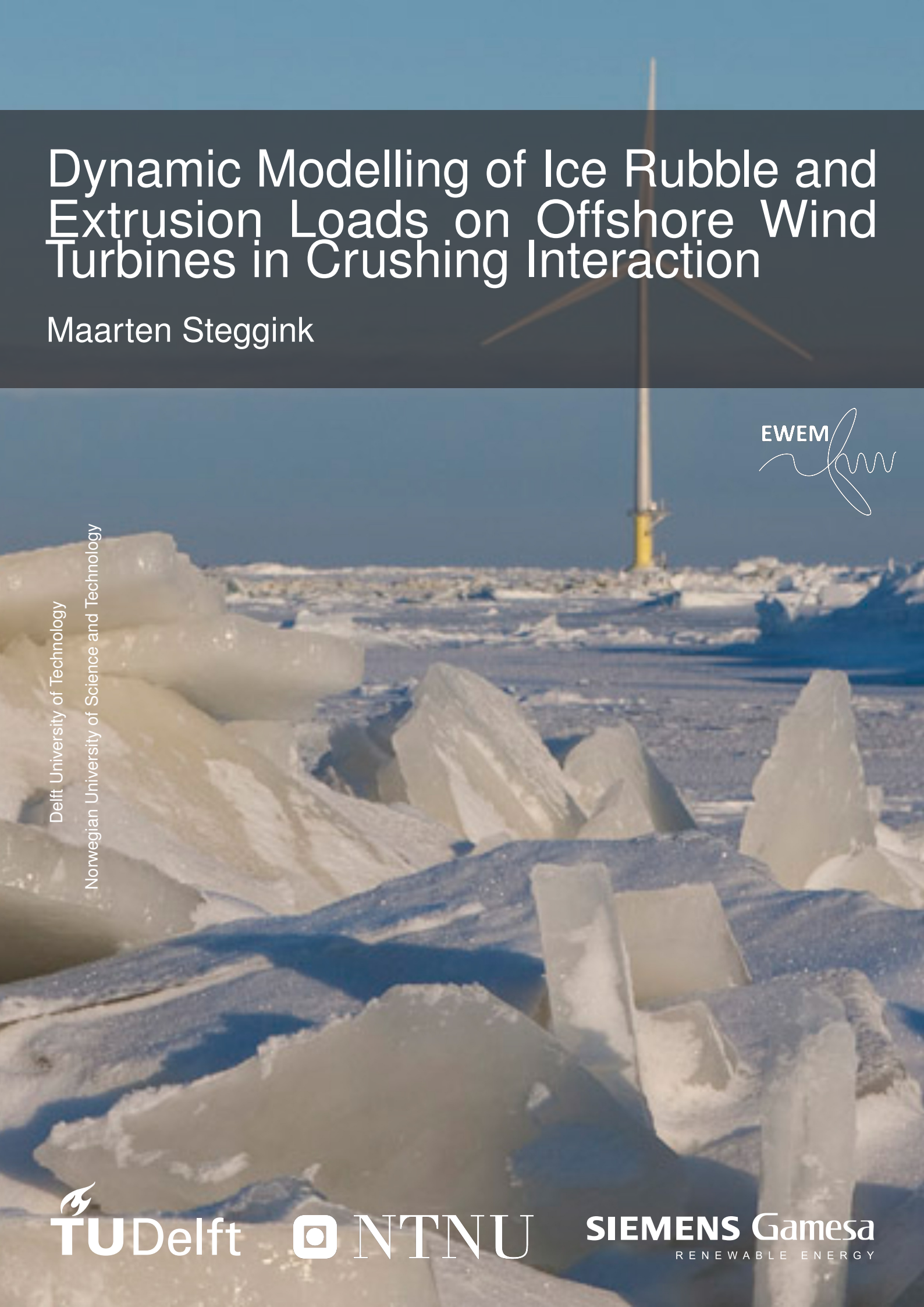

Delft University of Technology
Norwegian University of Science and Technology

TU Delft NTNU SIEMENS Gamesa RENEWABLE ENERGY

Dynamic Modelling of Ice Rubble and Extrusion Loads on Offshore Wind Turbines in Crushing Interaction

To obtain the degree of MSc. in Offshore & Dredging Engineering at the Delft University of Technology and the MSc. in Technology - Wind Energy at the Norwegian University of Science and Technology, as part of the European Wind Energy Master

Maarten Steggink

Student number:	5279909 (TU Delft)	557414 (NTNU)
Project duration:	Feb. - Nov., 2022	
Supervisors:	Dr. Hayo Hendrikse	Delft University of Technology
	Dr. Knut Høyland	Norwegian University of Science and Technology
	MSc. Bart van den Akker	Siemens Gamesa Renewable Energy
	MSc. Tim Hammer	Siemens Gamesa Renewable Energy
Graduation committee:	Dr. Hayo Hendrikse	Delft University of Technology, Chairman
	Dr. Pim van der Male	Delft University of Technology
	Dr. Knut Høyland	Norwegian University of Science and Technology
	MSc. Tim Hammer	Siemens Gamesa Renewable Energy

Cover photo: Tahkoluoto wind farm located offshore Finland in the Baltic Sea
(Eranti, E. (n.d.). Ice forces. Eranti Engineering Oy - Offshore Wind Power. Retrieved June 3, 2022, from https://erantiengineering.fi/ice04-ice-forces.htm)

Abstract

To accommodate the growing demand for renewable energy, installation of new offshore wind energy capacity is increasing in many countries. New projects will be proposed for waters in which floating (sea) ice is a common occurrence in winter. Currently, projects remain limited to regions with mild ice conditions, such as the Southern Baltic Sea, but projects further north are expected. In preparatory work for this thesis, performed at Siemens Gamesa Renewable Energies, it was shown that (edgewise) blade loads increase significantly for Northern Baltic sites when compared to Southern Baltic sites due to ice induced vibrations.

The phenomena of ice extrusion and rubble loads are expected to provide added damping to an ice-structure interaction system. This added damping may lead to less severe structural vibrations, and thus blade loads for an offshore wind turbine, than for a system with only intact ice crushing. VANILLA is the leading ice crushing model in the industry to evaluate the effects of ice induced vibrations for vertical offshore structures such as wind turbines, but the model currently does not (explicitly) consider ice extrusion and rubble loads. Therefore, the aim of this work is to investigate the phenomena of rubble and ice extrusion in crushing and propose a modelling approach.

Following a literature study, a rubble model and an extrusion model are proposed as extensions of the VANILLA ice model. The rubble model shows to be consistent and compute plausible rubble loads for model and full scale, while the extrusion model only predicts reasonable extrusion loads at full scale. Forcing and dynamics found from using the Standard and Adjusted VANILLA model with simplified global bending mode shapes of the SG 14-222 DD offshore wind turbine were compared.

Rubble loads were found to be small in magnitude and of negligible influence on the dynamics. The loads stemming from extrusion introduce additional damping to the system when the relative velocity between the structure and the ice increases, such that (i) the immediate load drop to zero after a failure event observed in Standard VANILLA is omitted, (ii) initiation ice drift velocities for IIV regimes become lower, (iii) dynamic amplitudes reduce, and (iv) a positive force-velocity gradient arises in the CBR regime.

Acknowledgements

This Master thesis is the final work in my journey that has been the European Wind Energy Master (EWEM). EWEM has given me the opportunity to study at three great educational institutaions (DTU, TU Delft and NTNU) and live abroad for two semesters in the amazing cities of Copenhagen and Trondheim. I have made many great friends and experienced and learned about the Scandinavian way of life. The past two years have been a fantastic experience and I would like to thank everyone that has been involved in the organisation of this master programme, before and during my two years as an EWEM student, as well as my fellow students.

The work presented results from a collaboration between Delft University of Technology and the Norwegian University of Science and Technology. Siemens Gamesa Renewable Energy (SGRE) has been involved as an industry partner.

I would like to express my sincerest gratitude to my supervisors. First of all, Bart van den Akker and Tim Hammer for their excellent daily guidance and support during my thesis from SGRE. Also, Dr. Hayo Hendrikse from TU Delft and Dr. Knut Høyland for their extensive contributions. And lastly the people at SGRE who have helped me in my work and with whom I have spent many lunchbreaks playing table football or went out for a walk. Of these people I explicitly want to name Jeffrey Hoek, who has been of great support.

Finally, I would like to thank the people who have not been directly involved in the matter of the studies or the thesis, but who have made a major contribution to arriving at this point. My friends, who have always helped me to get the necessary distractions to keep me mentally and physically healthy along the way, as well as supported me and kept me motivated. Last but not least, my family for always supporting me in my endeavours.

To all of these people, a massive thank you!

Maarten Steggink
The Hague, November 2022

Table of contents

Acknowledgements ii

Nomenclature iv

1 Introduction 1
- 1-1 Problem formulation . . . 1
- 1-2 Research goal . . . 2
- 1-3 Research questions . . . 3
- 1-4 Methodological approach . . . 3
- 1-5 Thesis outline . . . 4

I Theory 5

2 Loads from floating ice 6
- 2-1 Ice characterisation . . . 6
- 2-2 Failure mechanisms . . . 7
- 2-3 Ice induced vibrations . . . 9
- 2-4 VANILLA . . . 10
- 2-5 Measurements from SHIVER campaign . . . 14

3 Extrusion theory 17
- 3-1 Ice extrusion definition . . . 17
- 3-2 Role of extrusion in dynamics of a structure during crushing . . . 17
- 3-3 Crushing process . . . 18
- 3-4 The ice-structure interface . . . 21
- 3-5 Extrusion material characterisation . . . 26
- 3-6 Extrusion modelling in other models . . . 33

4 Rubble theory 35
- 4-1 Rubble definition . . . 35
- 4-2 Rubble pile dimensions . . . 36
- 4-3 Role of ice rubble in loading on vertical structures . . . 37
- 4-4 Loads from rubble for vertical structures . . . 37

Summary of theory 42

II Methods **43**

5 Rubble model **44**
5-1 Model description . . . 44
5-2 Verification . . . 50
5-3 Variation over parameters . . . 50
5-4 Validation . . . 54
5-5 Usage in VANILLA . . . 56

6 Extrusion model **57**
6-1 Model description . . . 57
6-2 Preprocessor . . . 61
6-3 Verification . . . 63
6-4 Usage in VANILLA . . . 66
6-5 Variation over parameters . . . 67
6-6 Validation . . . 71

III Results and discussion **75**

7 Results **76**
7-1 Ice force and displacements plots . . . 76
7-2 Plots of extracted statistics . . . 86

8 Discussion **90**
8-1 Discussion of results . . . 90
8-2 Discussion of other observations/implications . . . 94

9 Model limitations **97**
9-1 Rubble modelling . . . 97
9-2 Extrusion modelling . . . 98

10 Conclusion **101**

Bibliography **105**

A Derivations, descriptions, model parameters and sensitivities **115**

B Code listings **134**

C PSDs of results **139**

D Wind turbine modelling **148**

Nomenclature

Abbreviations

CBR	Continuous brittle crushing
CDF	Cumulative distribution function
FEM	Finite element modelling
FLI	Frequency lock-in
IC	Intermittent crushing
IIV	Ice induced vibrations
OWT	Offshore wind turbine
PDF	Probability density function
PSD	Power spectral density
SDOF	Single degree of freedom
SGRE	Siemens Gamesa Renewable Energy

Symbols

α	Angle between structure and level ice
β	Upper rubble wedge angle
ΔF_{i}	Ice force level in Kärnä model
δ	Friction angle between wall and rubble
δ_{f}	Critical deformation
$\dot{\gamma}$	Shear velocity
η_{kr}	Porosity of rubble in the keel
η_{sr}	Porosity of rubble in the sail
γ_{kr}	Specific weight of rubble on ice in the keel
γ_{span}	Time span for extrusion in Matlock model
γ_{sr}	Specific weight of rubble on ice in the sail
μ	Viscosity
$\mu_{\text{ext,CBR}}$	Extrusion mean ice load in CBR
μ_{f}	Friction coefficient
μ_{ii}	Ice-ice friction coefficient
$\mu_{\text{int,CBR}}$	Intact mean ice load in CBR
μ_{is}	Ice-structure friction coefficient
μ_{kr}	Friction coefficient of rubble on ice in the keel
$\mu_{\text{rub,CBR}}$	Rubble mean ice load in CBR
μ_{sr}	Friction coefficient of rubble on ice in the sail
$\mu_{\text{tot,CBR}}$	Total mean ice load in CBR
ϕ	Internal friction angle
ρ_{w}	Sea water density
ρ_{ice}	Ice density
σ	Normal strength
τ	Shear strength
θ	Angle along structure perimeter

θ_{k}	Keel angle
θ_{s}	Sail angle
A_{c}	Surface of ice crushing
$A_{\mathsf{r,d}}$	Surface of discharged rubble
c	Cohesion
C_1	VANILLA model parameter for linear dashpot
C_2	VANILLA model parameter for non-linear dashpot
C_{R}	Ice strength coefficient
D	Structure width
D_{cone}	Hollow truncated cone inner diameter
f_μ	Scaling factor for determination of $\mu_{\mathsf{CBR,tot}}$
F_{e}	Extrusion force in the Kärnä model
$F_{\mathsf{e}}^{\mathsf{max}}$	Maximum extrusion force in Matlock model
F_{fric}	Friction force
$F_{\mathsf{G}}/F_{\mathsf{ISO}}$	ISO load
F_{ice}	Global ice load
$F_{\mathsf{ice}}^{\mathsf{max}}$	Maximum ice force for the Matlock model
$F_{\mathsf{i}}^{\mathsf{cr}}$	Peak load in Kärnä model
$F_{\mathsf{i}}^{\mathsf{ex}}$	Minimum force level in Kärnä model
$F_{\mathsf{kr,a}}$	Active earth pressure force in the keel
$F_{\mathsf{kr,p}}$	Active earth pressure force in the keel
F_{kr}	Internal failure mode force in keel
F_{N}	Normal force
F_{rub}	Rubble force
$F_{\mathsf{sr,a}}$	Active earth pressure force in the sail
$F_{\mathsf{sr,p}}$	Passive earth pressure force in the sail
F_{sr}	Internal failure mode force in sail
F_{tkr}	Sliding failure mode force in keel
F_{tsr}	Sliding failure mode force in sail
f_{AR}	Empirical term for ISO equation
g	Gravitational acceleration
H	Separation distance for Mohr-Coulomb flow
h	Halve of the crushed zone width/extrusion channel width
h_1	Reference ice thickness
h_{bot}	Height of extrusion channel at bottom
h_{cone}	Hollow truncated cone height
h_{kr}	Height of rubble pile in keel
h_{ridge}	Pressure ridge height
h_{sr}	Height of rubble pile in sail
h_{top}	Height of extrusion channel at top
h_{ice}	Ice thickness
K	Inverse of the shear velocity
K_{a}	Active earth pressure coefficient
k_{c}	Shear velocity
K_{p}	Passive earth pressure coefficient
K_1	VANILLA model parameter for linear spring
K_2	VANILLA model parameter for non-linear spring
L	Halve of the ice thickness/extrusion channel length

l_{cone}	Base length of hollow truncated cone
l_{kr}	Keel length
$l_{\text{sr,side}}$	Length of sail at side of structure ($\theta = 90°$)
l_{sr}	Sail length
m	Empirical coefficient for ISO equation
m_{c}	Mass of ice crushed
m_{d}	Mass of rubble discharged
N	Inverse of the consistency index
n	Consistency index
n	Empirical coefficient for ISO equation
N_θ	Number of segments along perimeter
N_{z}	Vertical segments used
N_{ice}	Number of ice elements
p	Pressure
p_0	Overpressure
p_{G}	Global ice pressure
p_{lim}	Pressure limit for extrusion
p_{m}	Mean platen pressure
$r_{\text{adj,2vt}}$	Adjustment factor at two times transition speed
$r_{\text{adj,3vt}}$	Adjustment factor at three times transition speed
$r_{\text{adj,CBR}}$	Adjustment factor at CBR
$r_{\text{adj,vt}}$	Adjustment factor at transition speed
r_{ks}	Ratio between keel and sail length
t	Time
t_{cont}	Time for establishing contact in Matlock model
t_{frac}	Time when fraction occures in Matlock model
T_{i}^{u}	Time between peak loads in Kärnä model
u_{s}	Structural displacement
u_i	Ice element displacement
v_0	Indenter velocity
v_{d}	Discharge velocity of rubble
v_{N}	Normal velocity
v_{rel}	Relative velocity
v_{struc}	Structure velocity
V_{thc}	Truncated hollow cone volume
v_{ice}	Ice drift velocity
w	Projected width of structure
z	Height

1

Introduction

1-1 Problem formulation

As prominent role in the transition from carbon intensive energy generation towards renewable energies will be held by wind energy, extracting kinetic energy from the wind by using large (mainly horizontal axis) turbines, both on- and offshore. Though the onshore capacity predicted for the year 2050 is five-fold that of offshore wind energy (5044 vs. 1000 GW, IRENA, 2019), the contribution from offshore wind energy generation is set to increase enormously, since current capacity is 35 GW (Council, 2021). This can also be seen in the steep increase in Figure 1-1(a). In this enormous expansion of offshore wind energy, more and more sites around the world will have to be developed for wind power production. Some of these areas are in places where floating (sea) ice occurs.

Sea ice occurs in a large portion of the world's oceans, with up to 10% of the oceanic surface covered by ice. Many northern bodies of fresh water also encounter floating ice. Bohai Bay in China, the Baltic Sea in Europe, as well as the great lakes in the US (see Figure 1-1(b)), are places that encounter floating ice, with favourable wind resources, suitable water depths and proximity to large population centers. This ice poses challenges for the construction of offshore wind turbines (OWTs), since it can exert significant loads on the tower of the structure.

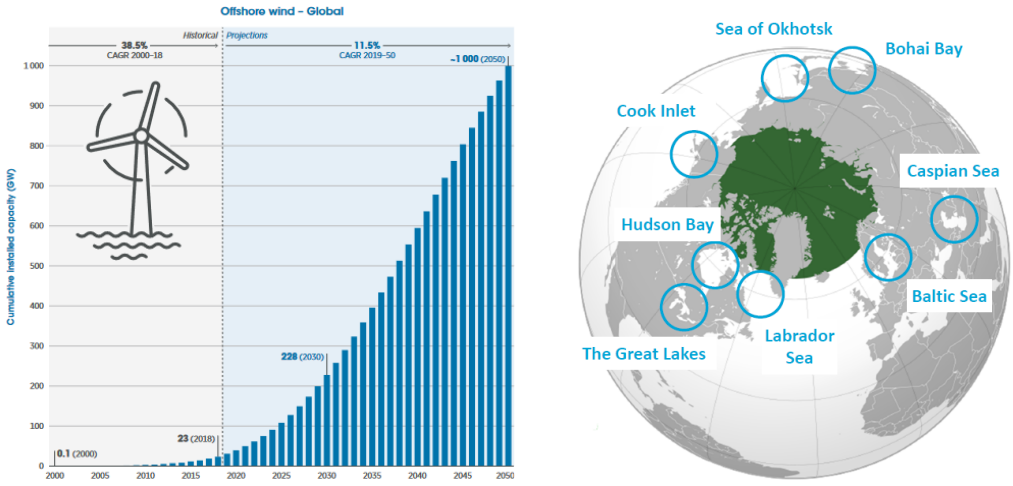

(a) (b)

Figure 1-1: (a) Future outlook of offshore wind capacity installed globally. (b) Overview of the subarctic regions. From (a) IRENA, 2019 and (b) Hoving, 2021.

Moreover, loading from the floating ice can cause excitation at the natural frequencies of OWTs, leading to significant structural motion. This can be hazardous to the structure, due to both fatigue damage and high global peak loads (Hendrikse, 2017). Therefore, it is of great importance for the design of OWTs in (sub)arctic regions, to understand how these *ice induced vibrations* (IIV) originate and to be able to model this effect. The VANILLA model was created at TU Delft for evaluating ice loading and ice induced vibrations on offshore structures. Currently, it is the leading ice-structure simulation software available.

In work leading up to this thesis (performed by the writer) the implications that floating ice acting on the structure has on the turbine blades, was examined. This was done by using VANILLA, coupled to the in-house turbine software BHawC at Siemens Gamesa Renewable Energies (SGRE). This work is presented in Appendix D. This investigation showed that that for future projects in the northern Baltic Sea, the thicker ice leads to significantly higher blade loads. Increased damping in the ice model might thus be beneficial, which could originate from rubble or extrusion loads, which are currently not explicitly modelled in VANILLA.

1-2 Research goal

The goal of this thesis is to investigate what the implications of rubble and extrusion loads are on the dynamics of flexible offshore structures, such as offshore wind turbines, are in an ice crushing event. Moreover, the aim is to find out how to accurately model these loads and to implement these in the VANILLA ice model.

1-3 Research questions

In order to achieve the goal set out in the previous section, the following main research question was identified:

What are the implications of rubble and extrusion ice loads on the dynamics of offshore wind turbines in an ice crushing event?

Subquestions in support to this main research questions are as follows:

1. How can rubble loads be computed for offshore wind turbine structures?
2. How can extrusion loads be computed for offshore wind turbine structures?
3. How can rubble and extrusion loads be implemented in an ice crushing model such as VANILLA?

1-4 Methodological approach

In order to reach the research goals, different steps were identified:

1. A literature study to identify how to describe extrusion and rubble ice loads, as well as general ice crushing and the modelling of ice crushing.
2. Propose a rubble model based on the theory on rubble loads and an extrusion model based on the theory on extrusion loads.
3. Assess sensitivities of the rubble and extrusion model are assessed and compare to measured ice loads (as presented in literature).
4. Verify proper functioning of the combined rubble and extrusion models.
5. Attain coupling of the extrusion and rubble models to a MATLAB version of the VANILLA ice model.
6. Utilise the Adjusted and Standard VANILLA model to compute dynamics for a structure with the global bending mode frequencies of the SG 14-222 DD wind turbine.
7. Evaluate the results of these computations.
8. Advise on implementation of the findings in the VANILLA model and on future research aimed at accurately modelling extrusion and rubble loads.

1-5 Thesis outline

Chapter 2: Loads from floating ice
The concept of floating ice and ice loading is introduced in Chapter 2. Relevant failure mechanisms, as well as ice induced vibrations, are described. The ice model of interest to this thesis, VANILLA, is introduced. Finally, a description of some important findings from the SHIVER campaign on ice crushing at model scale.

Chapter 3: Extrusion theory
A literature study on the phenomenon of ice extrusion is given in this Chapter, with a focus on the importance of and mechanisms in ice extrusion, as well as the ice-structure interface and a material characterisation of pulverised ice for extrusion. The Chapter is finalised by a description of extrusion modelling in other models.

Chapter 4: Rubble theory
This Chapter gives a literature review on the phenomenon of rubble ice loads. Rubble pile dimensions are investigated, followed by a description of the role of rubble loads in dynamics of a vertical structure and the mathematical description of the evaluation of rubble loads.

Chapter 5: Rubble model
Based on the Theory, a rubble model is proposed. The sensitivity on the model parameters is investigated and the found loads are compared to measured ice loads (from literature).

Chapter 6: Extrusion model
In Chapter 6, an extrusion model is proposed, as well as a way for implementation in VANILLA. Sensitivity of the model is assessed and the found loads are validated.

Chapter 7: Results
The Adjusted and Standard VANILLA model are used for calculating dynamics using global bending mode frequencies of the SG 14-222 DD wind turbine, of which the results are shown and described.

Chapter 8: Discussion
The results, as well as implications and other aspects of the model, are discussed here.

Chapter 9: Limitations
In this Chapter, limitations of both the rubble model and the extrusion model are described.

Chapter 10: Conclusion
Finally, conclusions are drawn. This is done by a reflection on the research goals. Furthermore, answers are formulated and supported by the results of the previous Chapters. Lastly, recommendations are given on possible future research.

Part I

Theory

2

Loads from floating ice

The concept of sea ice is introduced in this Chapter. This is followed by a look at the failure mechanisms encountered for level ice, a discussion of ice induced vibrations and finished with relevant load patterns and effects, as obtained from the SHIVER campaign.

2-1 Ice characterisation

Depending on the environmental conditions in an area, the amount of ice can vary. This is described as the *ice concentration*. Based on this, ice bodies have been categorised. Of most interest to this body of work, are *floes*, which are relatively flat pieces of sea ice that can range anywhere between 20 m and larger than 10 km in diameter. For an overview of all ice bodies encountered, reference is made to Løset et al., 2006. The bodies of ice that correspond to one of these various types are not similar either and can boast a number of features. *Level ice* is sea ice that is not broken and is unaffected by deformation. One such deformation could be *ice rafting*, where bodies of ice ride over each other and freeze together. *Ridges* can also occur, which are lines or walls of broken ice within the body of ice, originating from events like collisions. Piles of broken ice (*rubble*) may occur from collisions with structures, called *rubble piles*. Examples of these features are given in Figure 2-1.

Floe ice may move under the influence of driving forces from atmospheric and oceanic skin drag, due to wind and currents, or due to waves or collisions with other bodies of ice, land or structures (Rabatel et al., 2015). In the case of collisions, the forces on the body of ice due to the interaction may lead to breaking of the ice. The ways in which ice breaks are called *failure modes* and are caused by different types of failure. These are introduced in the next Section.

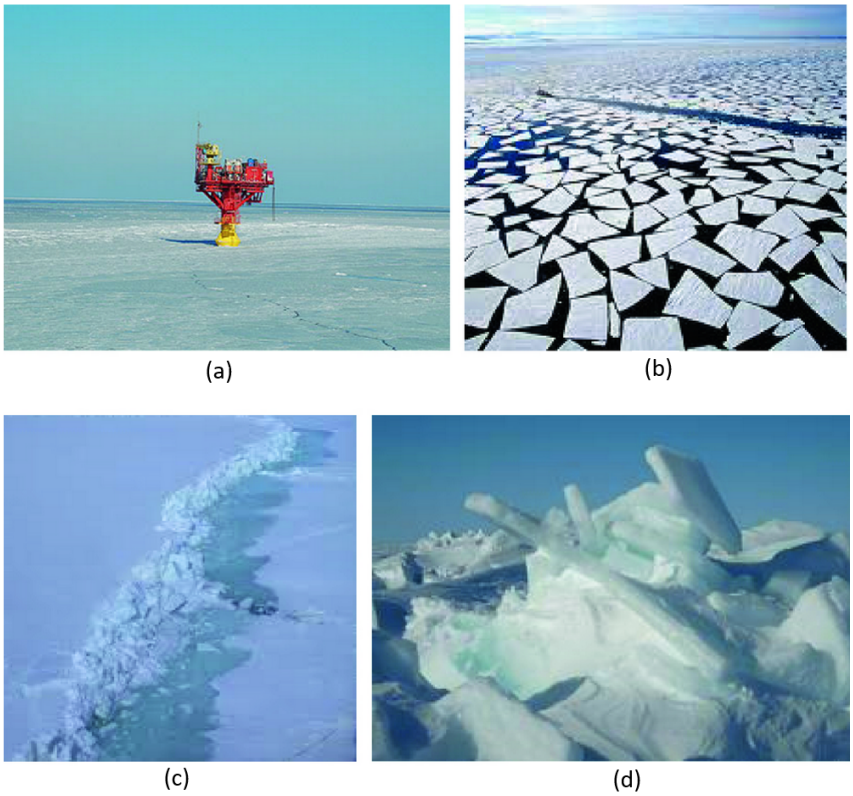

Figure 2-1: Examples of (a) level ice, (b) ice floes, (c) an ice ridge and (d) rubble ice. From Ji and Liu, 2020.

2-2 Failure mechanisms

To be able to correctly model the interaction of structures with floating ice, it is necessary to determine in which way the ice fails upon interacting. Depending on the strength levels, stress distribution of the ice, ice velocity and the structure's shape, the ice may fail in various ways, through yielding, compression, tension or flexural deformation. These failure mechanisms result in different loading on the structure, since the ice can resist to these failure mechanisms up to different maximum loads. The principal failure mechanisms that occur were documented by Sanderson, 1988, who found that ice failed through *creep*, *radial cracking*, *buckling*, *circumferential cracking*, *spalling* and *crushing*, as shown in Figure 2-2. The modes encountered later in this document are now further discussed.

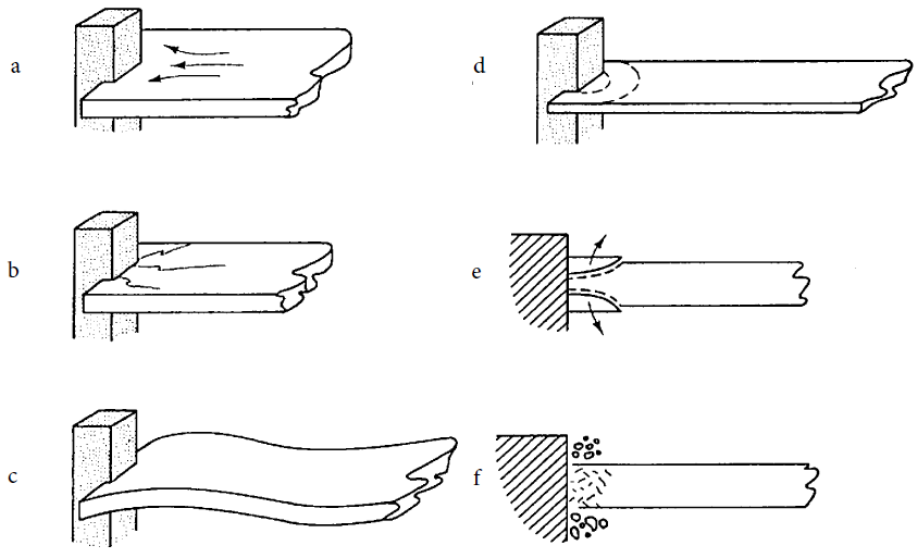

Figure 2-2: Principle failure mechanisms as observed during laboratory indentation tests: (a) creep, (b) radial cracking, (c) buckling, (d) circumferential cracking, (e) spalling, (f) crushing. From Sanderson, 1988.

Creep

Shown in Figure 2-2(a) is creep. This failure mode occurs at low indentation speeds ($v_{\text{ice}} < 3$ mm/s according to Sodhi and Haehnel, 2003), which results in full contact and a uniform pressure at the interface between the ice and the structure. Structural vibrations have not been observed for creep. The deformation of the ice is purely ductile and the ice behaves as a continuum, with low stress rates (Sanderson and Child, 1986).

Spalling

Spalling (Figure 2-2(e)) occurs when horizontal cracks form due to the shear stress being higher than the shear strengths. The cracks run roughly parallel to the ice plane, until they run out on the upper or lower surface. Fragments from spalling are semicircular, with a radius much larger than the ice thickness, while the spall fragment's thickness is less than that of the ice. Some authors consider spalling to be one of the phenomena that takes place in crushing and therefore group them together under this termination.

Crushing

The last relevant failure mode described in literature is crushing, as depicted in Figure 2-2(e). It involves the growth of cracks in random directions, leading to pulverisation and flaking,

as will be discussed in Chapter 3. The fragments are small and their length, width and thickness are of the same order. Crushing occurs at high indentation velocities and is more likely to occur for low aspect ratio ice-structure interactions. A formula that is widely used for calculating the global pressure on a structure in a crushing event is the one in Equation 2.1 (The International Organization for Standardization (ISO), 2019).

$$p_{\mathsf{G}} = C_{\mathsf{R}}\left[(\frac{h_{\mathsf{ice}}}{h_1})^{n_{\mathsf{ISO}}}(\frac{w}{h_{\mathsf{ice}}})^{m_{\mathsf{ISO}}} + f_{\mathsf{AR}}\right], \qquad f_{\mathsf{AR}} = e^{\frac{-w}{3h_{\mathsf{ice}}}}\sqrt{1+5\frac{h_{\mathsf{ice}}}{w}} \tag{2.1}$$

In Equation 2.1, p_{G} is the global average ice pressure (in MPa), w is the projected width of the structure (in m), h_{ice} is the ice thickness (in m), h_1 is a reference ice thickness of 1 m, m_{ISO} is an empirical (dimensionless) coefficient of -0.16. n_{ISO} is also an empirical (dimensionless) coefficient, equal to $-0.50 + \frac{h_{\mathsf{ice}}}{5}$ for $h_{\mathsf{ice}} < 1.0$ m and to -0.30 for $h_{\mathsf{ice}} \leq 1.0$ m. C_{R} is the ice strength coefficient (in MPa). f_{AR} is an empirical term, which can be disregarded when $\frac{w}{h_{\mathsf{ice}}} > 5$.

For an aspect ratio above one, when spalling and flaking occur, ice induced vibrations may be encountered. This potentially hazardous situation is described in more detail in the next Section.

2-3 Ice induced vibrations

Ice induced vibrations is the term used for describing vibrations originating from loads by level ice on structures, due to interaction in crushing (see Figure 2-3). IIV was first observed by Peyton, 1968 on offshore structures in the Cook Inlet in Alaska. In theory, IIV can occur for all bottom-founded offshore structures in areas where floating ice occurs, since no structure is completely rigid, but are more likely to occur for flexible, vertical-sided structures. Three regimes can be identified over the ice velocity v_{ice}, as depicted in Figure 2-3. These regimes are *intermittent crushing* (IC), *frequency lock-in* (FLI) and *continuous brittle crushing* (CBR).

In IC, there is a gradual build-up of a load, until the strength of the ice is reached, after which unloading takes place. The structural displacement and global load show a sawtooth-like pattern. When v_{ice} is increased, FLI may occur. In this situation the structural displacement follows a quasi-harmonic pattern, while the loading follows a periodic pattern, with peaks around the time of the structure displacement reversing. Lastly, CBR occurs at even higher ice velocities. For these velocities, the load signal varies in a seemingly random pattern around a mean value (within distribution boundaries). The structural displacement is almost constant, with small variations around an equilibrium.

According to Ye et al., 2019, there were until recently two theories established for describing the mechanism of IIV, namely the forced vibration theory and the self-excited theory. An

alternative view was recently put forward by researchers from Delft University of Technology (Hendrikse and Metrikine, 2015), who state that plastic deformation of the ice, occurring when the ice velocity with respect to the structure is low, leads to an increase in global loads. This makes for efficient energy transfer from the ice to the structure, resulting in IIV. The VANILLA ice crushing model, which is discussed in the next Section, was developed based on this theory.

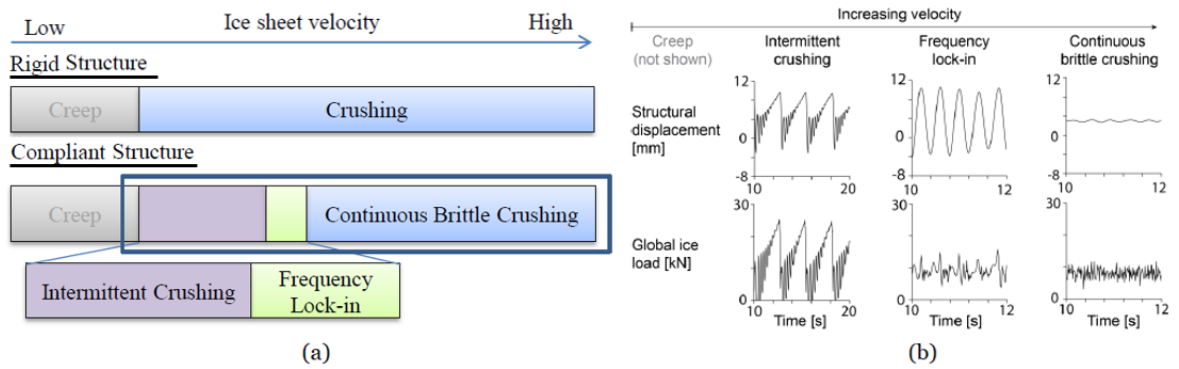

Figure 2-3: (a) Overview of IIV regimes. (b) Typical structural response and global ice load in the three regimes of ice-induced vibrations. Global ice load and structural displacement values were obtained from numerical simulations and do not reflect real measurements. From Hendrikse, 2017.

2-4 VANILLA

The Hendrikse model of TU Delft, more widely known as VANILLA, is a relatively new model for evaluating ice loading in crushing events. It is based on the alternative views of the creators on the theory behind the origin of IIV, as discussed in the previous Section. The model was designed such that the fracture length and the stress-strain-rate dependence for the compressive strength are omitted, two debated factors used in most other models, are omitted. Moreover, it is based on and aims to reproduce a large number of measurements and observations on ice deformation and failure and is thus a phenomenological model. It uses N 1D ice elements to model an advancing ice floe, where each element is modelled with a combination of springs and dashpots so that elastic, visco-elastic and viscous effects are incorporated. The model is illustrated in Figure 2-4.

The initial state of the ice is given by using a uniform distribution U, as given in Equation 2.2.

$$u_{\mathrm{i},1} = u_{\mathrm{i},2} = u_{\mathrm{i},3} = u_{\mathrm{s},0} - U(0, r_{\mathrm{max}} + v_{\mathrm{ice}} t_{\mathrm{f}}) \tag{2.2}$$

Here, $u_{\mathrm{s},0}$ is the initial position of the structure (in m), r_{max} the maximum offset of an element

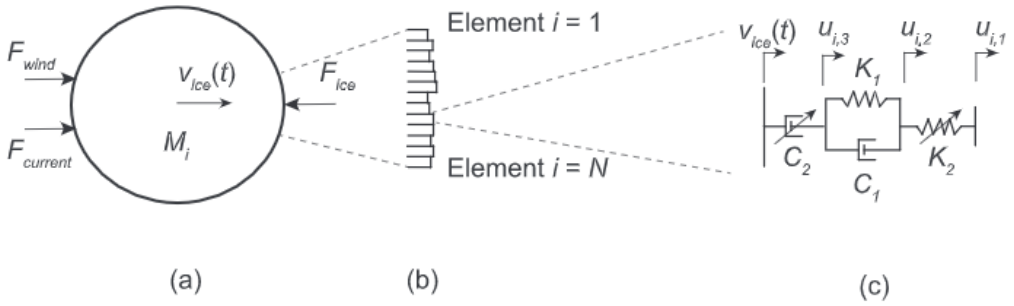

Figure 2-4: VANILLA with (a) A single effective ice floe and wind and current driving forces. (b) The roughness of the ice edge modelled as N independent elements with an individual offset to the structure. (c) A combination of springs and dashpots to model each ice element, to capture elastic, delayed-elastic and viscous deformation. From Hendrikse and Nord, 2019.

from the structure (in m). Further, v_{ice} is the ice drift speed (in m/s), t_{f} is the time between initial contact and failure for an individual ice element for this drift speed (in s). The drift speed was initially a pre-set variable in the model, a later extension allowed for a time varying drift speed. This extension is explained later.

Elastic deformation is modelled with the nonlinear spring in the front of the ice element with spring constant K_2 (in N/m) as defined in Equation 2.3.

$$K_2 = \begin{cases} K_2 & \text{for } 0 < u_{\text{i,2}} - u_{\text{i,1}} \leq \delta_{\text{f}} \\ 0 & \text{else} \end{cases} \tag{2.3}$$

In Equation 2.3, δ_{f} is the (predefined) critical local deformation (in m).

The other components in the ice elements are a spring-dashpot combination, with stiffness coefficient K_1 (in N/m) and damping coefficient C_1, and a dashpot with damping coefficient C_2 (in N^{3}s/m). The spring-dashpot combination captures the visco-elastic characteristics, where the dasphot simulates the power-law creep deformation. This combination of springs and dashpots, result in the EOM as given in Equation 2.4.

$$\begin{gathered} u_{\text{i,1}} = \begin{cases} u_{\text{i,2}} & \text{for } u_{\text{i,1}} < u_{\text{s}} \\ u_{\text{s}} & \text{for } u_{\text{i,1}} \geq u_{\text{s}} \end{cases} \\ \dot{u}_{\text{i,2}} = \frac{K_2}{C_1}(u_{\text{i,1}} - u_{\text{i,2}}) + \frac{K_1}{C_1}(u_{\text{i,3}} - u_{\text{i,2}}) + V_{\text{ice}} - \frac{1}{C_2}(K_2(u_{\text{i,2}} - u_{\text{i,1}}))^3 \\ \dot{u}_{\text{i,3}} = v_{\text{ice}} - \frac{1}{C_2}(K_2(u_{\text{i,2}} - u_{\text{i,1}}))^3 \end{gathered} \tag{2.4}$$

Here, u_s is the displacement of the structure at the location where the ice load acts (in m). The resulting characteristics of the force from one ice element is shown in Figure 2-5.

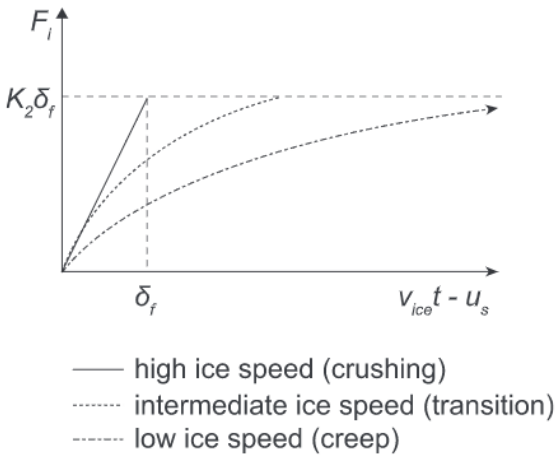

Figure 2-5: Ice load versus total deformation of an ice element, for various (constant) ice speeds. From Hendrikse and Nord, 2019.

From Figure 2.5, it can be seen that the ice elements show different behaviour, depending on both the ice speed and the interaction with the structure. The total ice force of all ice elements combined is then as given in Equation 2.5.

$$F_{\text{ice}}(u_{\text{s}}, t) = \sum_{i=1}^{N} F_{\text{i}} = \sum_{i=1}^{N} K_2(u_{\text{i,2}} - u_{\text{i,1}})\text{H}(u_{\text{i,1}} - u_{\text{s}}) \tag{2.5}$$

The Heaviside step function (H) is used in Equation 2.5 to account for the situation where contact is lost due to movement of the structure away from the ice floe. When δ_{f} is reached, the ice feature breaks and is removed from the model, with a new element taking its place. The initial position of the new element is given by Equation 2.6.

$$u_{\text{i,1}} = u_{\text{i,2}} = u_{\text{i,3}} = u_{\text{s,0}} - U(0, r_{\text{max}}) \tag{2.6}$$

The equations above are sufficient to describe the ice model, but the coefficients need to be known before computation. These are calculated using a preprocessor.

Preprocessor

Five of the seven parameters that are required to run the model, are based on the set of equations given in Equation 2.7.

in Equation 2.7, F_{t} is the maximum global load (in m), μ_{cbr} is continuous brittle crushing mean load (in N, evaluated at 0.15 m/s), σ_{cbr} is the standard deviation of the continuous brittle crushing load (in N, also evaluated at 0.15 m/s). These factors have to be obtained from measurements, for the particular situation that is modelled. These measurements should be performed to obtain the graph of Figure 2-6, from which the factors can be extracted, as well as the ice speed at which the maximum global load, at the transition between creep and crushing, v_{t} (in m/s).

$$\begin{aligned} \delta_{\mathsf{f}} &= \delta_{\mathsf{f}} & K_2 &= \frac{F_{\mathsf{t}}}{\delta_{\mathsf{f}} N} & N &= \frac{(\frac{2F_{\mathsf{t}}}{3\mu_{\mathsf{cbr}}-1})}{(\frac{\sigma_{\mathsf{cbr}}}{\mu_{\mathsf{cbr}}})^2} \\ r_{\mathsf{max}} &= \delta_{\mathsf{f}} \left(\frac{F_{\mathsf{t}}}{\mu_{\mathsf{cbr}}} - 2 \right) & C_2 &= \frac{F_{\mathsf{t}}^3}{N^3 v_{\mathsf{ice}}} \end{aligned} \tag{2.7}$$

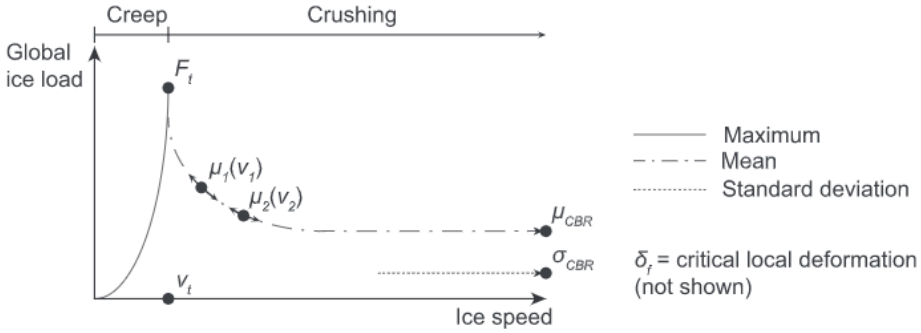

Figure 2-6: Graph for global ice load versus ice speed, obtained from measurements for a rigid structure in a particular setup, used to determine the seven model parameters. From Hendrikse and Nord, 2019.

The two missing parameters, C_1 and K_1 can be obtained by performing an optimisation of two expected values of the mean ice load, μ_1 and μ_2 (both in N), at two ice speeds v_1 and v_2 (in m/s). The equations for μ_1 and μ_2 follow from the equation for $u_{\mathsf{i},1}$ in Equation 2.4, Equation 2.5 and the equation for K_2 in Equation 2.7, with setting $u_s = 0$. The result for μ_1 and μ_2 is then as given in Equation 2.8. Together with the rest of the equations mentioned above, the optimisation can be performed.

$$\mu_1 = \frac{F_{\mathsf{t}}}{\delta_{\mathsf{f}}} \cdot \frac{\int_0^{t_{\mathsf{f}}(v_1)} u_{\mathsf{i},2} \mathrm{d}t}{\frac{0.5 r_{\mathsf{max}}}{v_1} t_{\mathsf{f}}(v_1)} \qquad \mu_2 = \frac{F_{\mathsf{t}}}{\delta_{\mathsf{f}}} \cdot \frac{\int_0^{t_{\mathsf{f}}(v_2)} u_{\mathsf{i},2} \mathrm{d}t}{\frac{0.5 r_{\mathsf{max}}}{v_2} t_{\mathsf{f}}(v_2)} \tag{2.8}$$

Performance and limitations of the model

By comparing simulations with full-scale and experimental observations, Hendrikse et al., 2018 and Hendrikse and Nord, 2019 show that the model is able to capture all regimes of ice-induced vibrations quite accurately, as well as the transitions between the regimes.

Though performing really well and establishing itself as the go-to model for modelling ice loads in the industry, there are a number of improvements that could be made. The current model considers ice crushing, and does not explicitly consider extrusion, and lacks other failure mechanisms, such as spalling, radial cracking, rubble loads, and circumferential cracking. Since the model is based on total load measurements, it could however be argued that some of these phenomena are implicitly modelled.

Moreover, the model does not incorporate much of the inhomogeneity that is present within ice floes, limiting the accuracy for full-scale events. Incorporating these effects (explicitly) in the model will make it useful for more scenarios, as well as make the ice forces found more accurate, closer resembling the ice forcing for physical ice events. In this work, the phenomena of extrusion and rubble piles are aimed to be incorporated.

As a part of ongoing research on ice induced vibrations, the SHIVER campaign was set up, in which ice crushing is examined at the Aalto Ice Tank. In the next Section some of the results of the ice load measurements in this campaign are shown. This is done in order to be able to evaluate the load signals and displacement plots found from simulations with VANILLA with the additions of extrusion and rubble loads, as presented in Chapter 7.

2-5 Measurements from SHIVER campaign

Due to complexity and high costs, past measurements on full scale flexible structures have been limited, with a notable exception being the STRICE campaign at the Norströmsgrund lighthouse of the Northern Swedish coast. Therefore, most research has focused on developing understanding of phenomena in ice-structure interactions at model scale, such as in the recent SHIVER project (Hendrikse et al., 2022), performed at the Aalto ice basin. In this campaign, ice crushing tests were done on both rigid and flexible setups using a vertical cylindrical indenter. In van den Berg et al., 2022, the results of the crushing measurements on a rigid structure and on models representing singe-degree-of-freedom (SDOF) oscillators are discussed in detail. A discussion of their most important findings to this work now follows.

Force-velocity dependencies

A first observation made by the authors on the results is an initial decrease in ice force mean and standard deviation for increasing ice drift speed (up to about 20 mm/s), followed by what is described as an 'indication for a positive force-velocity gradient' at higher indentation

speeds. This is indicated in Figure 2-7.

While the negative dependency at low speeds is an established phenomenon in research, it is noted by the authors that tests at higher velocities (more than 150 mm/s) are required to definitively establish the positive force-velocity gradient. The trend has been observed in a previous similar setup by Hendrikse et al., 2018, and in other model scale tests by Kärnä et al., 1993. In medium scale, the effect has been observed by Fransson, 2008, who measured at considerably higher indentation speeds (up to about 2 m/s). Blenkarn, 1970 observed the effect in full scale, but measurements at the Norströmsgrund lighthouse as presented by Bjerkås et al., 2003 do not show this dependency. The latter could be considered most representative for ice-structure interaction for most full-scale applications, but these measurements are somewhat ambiguous due to varying ice characteristics at the moment of measuring and could be skewed due to failure in other modes than crushing. Other examples of reports confirming the effect are Gravesen et al., 2005 and Jones, 2007. Moreover, the phenomenon has been observed in many other materials such as concrete, steel, soil and composite materials. Considering the above, it is likely that the positive force-velocity gradient is an intrinsic feature of the ice-structure interaction and that the observation in the SHIVER campaign is accurate.

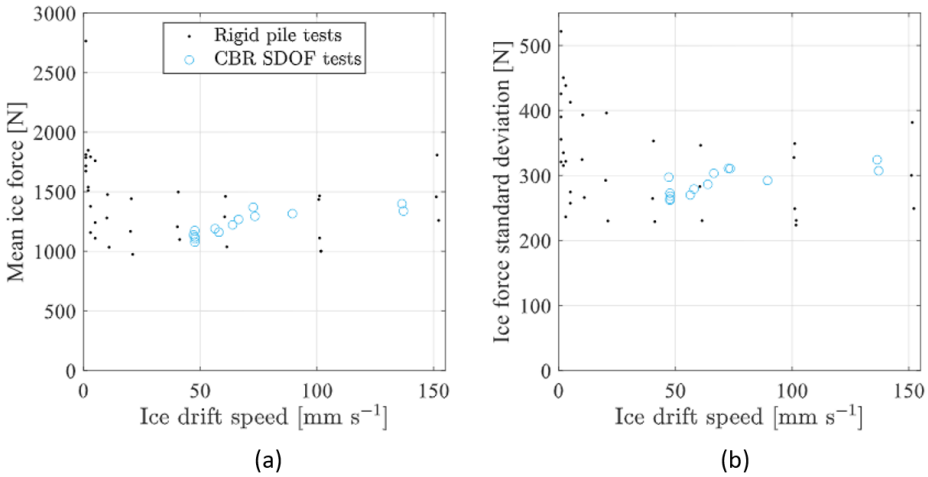

Figure 2-7: (a) Mean ice force as a function of ice drift speed and (b) ice force standard deviation as a function of ice drift speed in measurements on a rigid structure in the SHIVER campaign. From van den Berg et al., 2022.

In the paper by van den Berg et al., 2022, the consequences of the positive force-velocity gradient on the dynamics of the structure are examined, by running numerical simulations. In these simulations the load signal of one of the rigid structures is applied to the SDOF oscillators, first without any velocity dependency and then with the negative and/or positive force-velocity gradients (for details, reference is made to the original paper). These are then compared. From this, the authors conclude that not including the added damping from the

positive force-velocity gradient leads to overestimation of structural oscillation amplitude in the CBR regime. For the FLI regime, it was found that including the positive force-velocity gradient leads to more accurate predictions of FLI initiation drift speeds, which would otherwise be overpredicted. In IC, the analysis was no longer possible with the model they used (which was, in their own words, kept 'as simple as possible').

Measured signals

For later reference, parts of the measured signals (for one of the test ID's) of the structural displacement, ice force and relative velocity from the SHIVER campaign are included here, for FLI and IC. The former is shown in Figure 2-8, while the latter is shown in Figure 2-9. Notable features are the load drops to 0 N upon contact loss for a negative relative velocity, and the load drops after a major crushing event for IC. This load drop is mentioned by van den Berg et al., 2022 to show an immediate decrease in load to an intermediate level, at a magnitude encountered at higher ice drift speeds. They ascribe this to a mix of crushing and extrusion. The concept of extrusion is explained in the next Chapter.

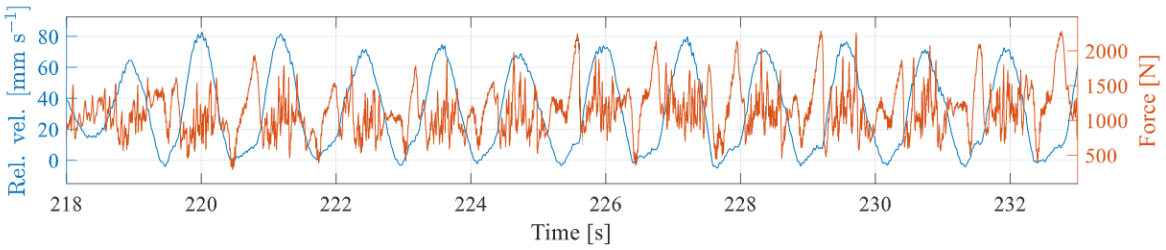

Figure 2-8: Ice force and relative velocity measured at an ice drift speed of ∼33 mm/s (FLI) for a SDOF structure during the SHIVER campaign. From van den Berg et al., 2022.

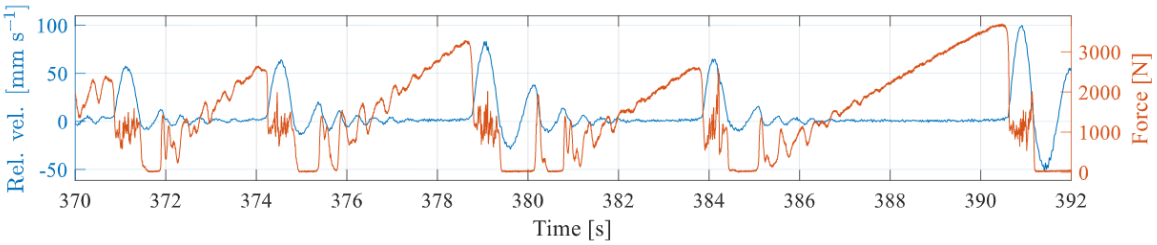

Figure 2-9: Ice force and relative velocity measured at an ice drift speed of ∼8-2 mm/s (IC) during the SHIVER campaign. From van den Berg et al., 2022.

3

Extrusion theory

Asdiscussed in Chapter 2-4, one of the missing phenomena in VANILLA is the extrusion of crushed ice material. This Chapter treats the definition of extrusion, as well as the various processes taking place during extrusion and their respective phases during interaction. This is then followed by a description of the ice-structure interface during crushing and a characterisation of the extruded material. Lastly, mathematical description of the flow is discussed.

3-1 Ice extrusion definition

Ice extrusion can be described as the ejection of crushed, or pulverised ice, from the interface between the intact ice and the structure. After a failure event of the ice, the structural integrity of the (previously intact) ice is lost and it loses (most of) its strength, such that it can be *extruded* to clear the way for new intact ice to come into contact with the structure.

3-2 Role of extrusion in dynamics of a structure during crushing

Crushing is often, and also in VANILLA, modelled by a load increase until a maximum deformation in the ice is attained. The ice then fails and the respective ice feature is removed from the model. This results in a sudden loss of the load experienced by the structure, such that the structure rebounds without damping from the ice until contact with the ice is restored. In reality the ice does not disappear, but is turned into granular, pulverised ice. The extrusion of this material can pose a damping. Thus, ice extrusion has implications on the dynamics of crushing events for flexible structures. A sketch of a zoomed in portion of a pressure pattern

during crushing is shown in Figure 3-1. In this figure, BC is when extrusion takes place and the pressure is gradually reduced.

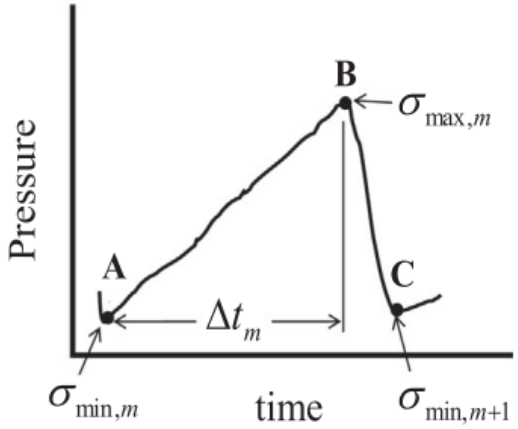

Figure 3-1: Idealised portion of a pressure pattern during crushing, showing extrusion between B and C. From Taylor and Jordaan, 2015.

The damping resulting from the extrusion could lead to a less severe gradient of the load drop after failure, as well as a decrease in the maximum load drop amplitude. This in turn could lead to decreased structural vibration, or alter the ice speeds and thicknesses at which the most detrimental effects from the ice-structure interaction are sustained. This has implications for the possibilities and challenges with regard to the design of offshore structures in ice infested regions.

Moreover, it is well possible that extrusion causes higher ice loads for higher indentation velocities, or that the extrusion influences the interaction and dynamics such that the intact ice leads to higher loads at higher indentation speeds. This could explain the positive force-velocity gradient for high indentation speeds, as shown previously in Section 2-5.

With the potential importance of extrusion established, the crushing and extrusion process is set out in detail in the next Sections.

3-3 Crushing process

According to Daley et al., 1996, there are four possible mechanisms that take place in crushing. These mechanisms have been identified from observations and showed to result in break up of the ice after failure from interaction of ice with a vertical structure. After these mechanisms lead to failure, they are followed by extrusion. The various mechanisms are explained below.

Microcracking

The first mechanism identified as crushing is the build up of so called microcracks. This particular mechanism is governing the interaction at very low indentation velocities, extending into the regime that is normally described as creep. In Sinha, 1989 and Sinha, 1991, observations and corresponding mathematical formulations were presented, showing behaviour that follow reasoning from the field of damage mechanics. In these observations tiny cracks developed throughout the entire ice layer. Due to these cracks, the strength of the ice reduces, until the strength of the ice is reached and a rapid growth of these small cracks takes place. The entire layer is then near to instantly pulverised. This process is displayed in Figure 3-2.

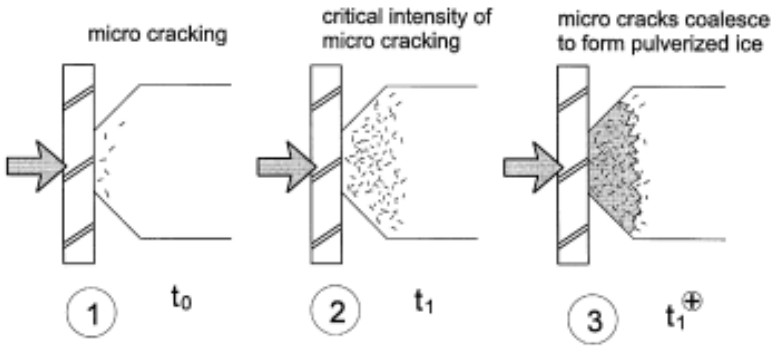

Figure 3-2: Pulverisation due to microcracking. From Daley et al., 1998.

Flake formation and explosion

At higher indentation velocities, larger cracks can form. These cracks can run from the direct contact in the middle of the ice layer (as explained in the next Section), to the edge of the ice. This can be both to a point along the sloping edge of the ice, or even further through to the horizontal edge of the ice. When this happens, a so called flake is formed. Tuhkuri, 1994 analysed results from crushing tests by different researchers, with slightly different setups. From the resulting grain sizes, it was concluded that at least for some tests, the break up of the ice must have been the result of the formation of these flakes. Depending on the confinement of the flake, it would then be broken up in different ways. Confinement could in this case be the result of a very narrow extrusion channel, or an overburden pressure due to previously extruded material (either still in the channel or resting on top as rubble). In the case of (almost) no confinement a flake is suddenly released of the compression that was built up during contact. No confinement could happen for example shortly after initial contact, before a build up of rubble has taken place, or for a very wide channel, Following the release of compressive stresses, the flakes may almost instantly expand, leading to break up of the flake. Due to the very sudden break up, this can be described as *explosion* of the flake. This is depicted in Figure 3-3.

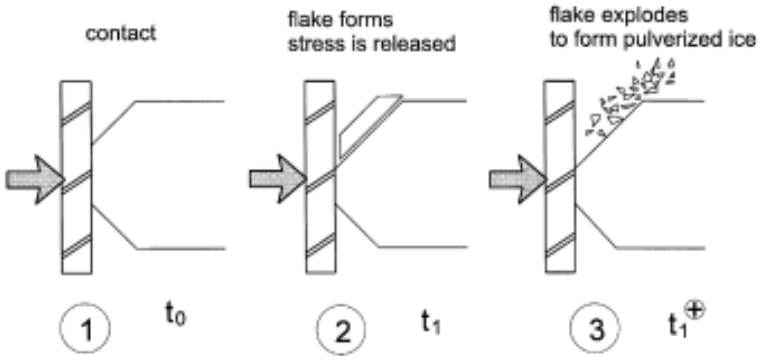

Figure 3-3: Pulverisation due to the formation of a flake and subsequent flake explosion. From Daley et al., 1998.

Comminution

The process of comminution was introduced by Palmer et al., 1983. As described by Tuhkuri, 1994, it is the break up of a flake after a flaking event in the case that the movement of the flake is restricted. The flake can then break due to interaction with the intact ice, the structure or other pieces of ice that have broken off. The resulting pieces of ice then undergo the same, until eventually only pulverised ice remains. The mechanism is shown in Figure 3-4. This mechanism also mainly takes place at higher indentations velocities.

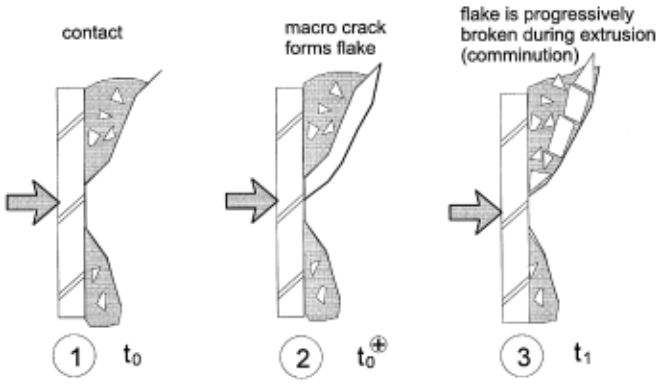

Figure 3-4: Pulverisation due to comminution of flakes resulting from macrocracks. From Daley et al., 1998.

Cascade and coalescence of macrocracks

A last mechanism identified for the break up of intact ice is a cascade of macrocracks. When a macrocrack is formed that does not lead to flaking (the crack does not run until the ice

edge), it does not lead to a significant stress reduction, nor to a temporary balance, such that other macrocracks will quickly form as well. Cracks may form from these cracks towards each other, so called *coalescence*, leading to a cascade of further break up of the ice front until the ice is relaxed. Tuhkuri, 1997 has shown by using computational fracture mechanics, that this cascading of these cracks can happen in ice. Comminution of the created ice pieces then takes place until the ice is pulverised and can be extruded.

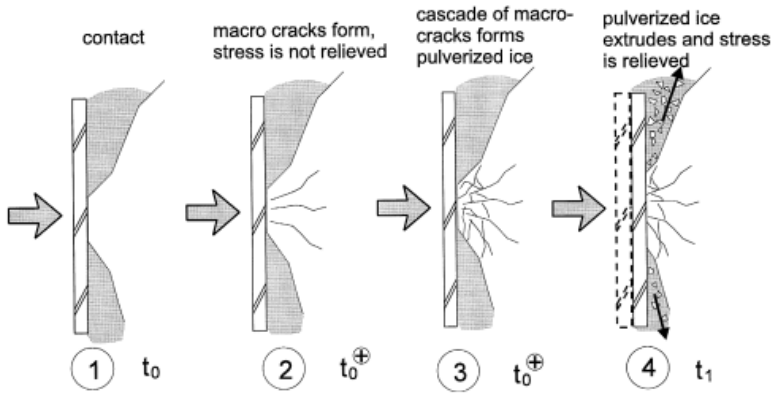

Figure 3-5: Pulverisation due to a rapid cascade and coalescence of macrocracks. From Daley et al., 1998.

Interplay of mechanisms

It is important to note that the mechanisms presented above, likely all happen simultaneously along the ice-structure interface, with different mechanisms governing for changing interface geometries and circumstances. However, in general, the mechanism of microcracking is more likely to happen for lower indentation velocities, while the other mechanisms due to the formation of macrocracks and flakes happen at high indentation velocities. In intermediate regimes, both may happen. The mechanisms as described above can be represented by a discrete flow, in which the steps followed can change during the interaction.

3-4 The ice-structure interface

With the understanding of the mechanisms taking place at the ice-structure interface as set out above, we can now look at what implications those have for the geometry of the interface during crushing.

Crushed layer

First notice of a crushed ice layer was made following observations of drop ball tests(Kheisin and Cherepanov, 1973 and Kurdyumov and Kheisin, 1976). In these tests they observed microcracking and they made notion of a “finely dispersed crushed layer behaving as a layer of viscous liquid”, which they thought was caused by pressure melting and frictional heat. Timco, 1987 performed indentation tests with a vertical indenter and observed a similar crushed layer to be present. They hypothesised that there was a crushed layer along the entire interface, which would transfer the load from the structure to the intact ice behind it. This would lead to damage in the intact ice, so that the crushed layer would be replenished from behind, while simultaneously losing material due to extrusion at the top and bottom of the layer. Their observations are shown in Figure 3-6(a), with a schematic representation of that observation in (b) and a hypothetical interface representation in (c) of that same Figure.

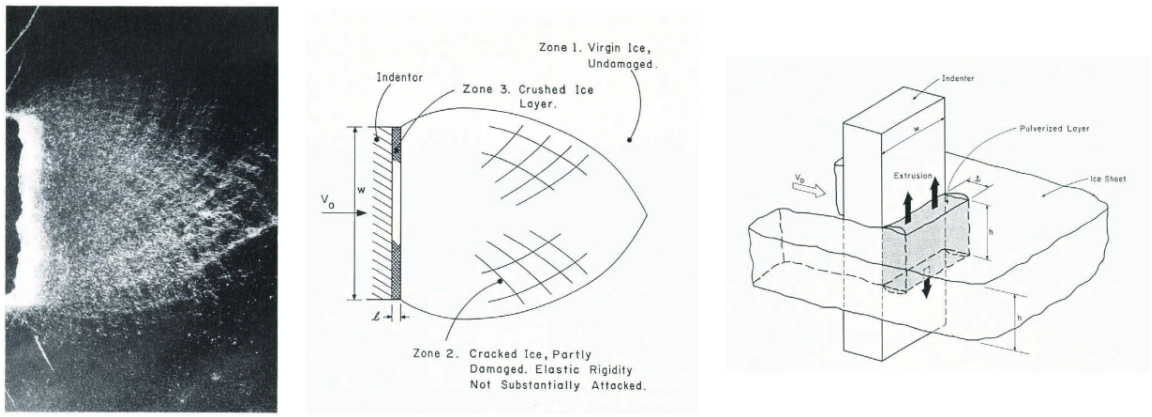

Figure 3-6: (a) observations from indentation tests, (b) schematic overview of observations, (c) hypothesised vertical representation of indentation geometry, with a flat layer of crushed ice. From Jordaan and Timco, 1988.

R. Frederking et al., 1990 performed field crushing tests at medium scale, from which they observed two distinct ’zones’, a white zone consisting of crushed ice, as well as a blue zone made up of intact (though damaged) ice. The white zone was relatively solid near the centre and was soft and could easily be broken further away. Moreover, they reported a clear distinction between the two zones. According to Jordaan, 2001, the blue zones, or high-pressure zones experience a state of stress that is triaxial in the ice and the contact pressure can reach up to 70 MPa (according to other tests), leading to intense shear stress. These shear stresses in turn lead to micro-structural change in the ice, as described by damage mechanics. Near the edges of the high-pressure zone, where pressures are relatively low compared to the centre, microcracking and crystallisation occurs. Towards the centre, pressure softening due to the high pressures leads to the formation of highly

recrystallised material. These regions, as well as the clear distinction, as observed in medium and small-scale tests are shown in Figure 3-7. From these tests, it can be concluded that the representation as hypothesised by Timco, 1987 is inaccurate, as there are hard, high-pressure zones at the interface, in which intact ice is in contact with the structure.

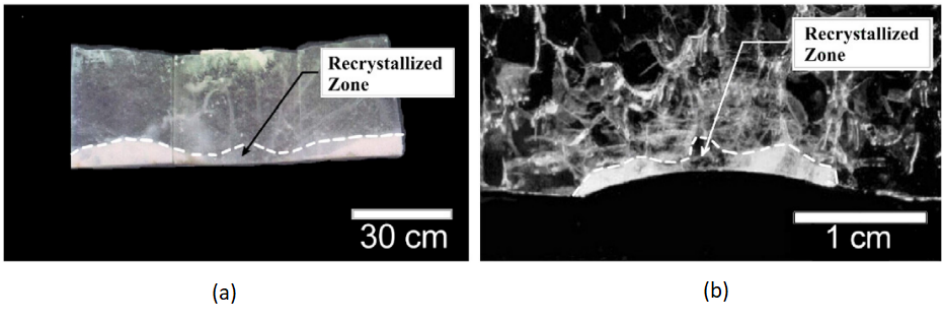

Figure 3-7: Blue zone (dark) of recrystallised ice and white zone of crushed ice as observed in (a) medium-scale and (b) small-scale experiments. From Wells et al., 2011.

Tests by Tuhkuri and Riska, 1990 have shown that the crushed layer is responsible for a considerable portion of the load transfer from the structure to the ice (or vice versa). Gagnon et al., 2020 reports from impacts tests that the load is close to evenly distributed between the high-pressure zone and what he calls the low-pressure zone, with crushed ice. Moreover, he reports that the size of the low-pressure zone is about 2-6 times the size of the high-pressure zone, with the transition between the two at about 15 MPa. It is however important to emphasise that these observations were done on impact tests, which may vary from continuous crushing in indentation. The shape of the high- and low-pressure zones can vary due to spalling/flaking, which is now explained.

Spalling/flaking

As said in the previous section, for sufficiently high velocities (above creep indentation velocities), spalling or flaking can occur from the development of macrocracks. For an in-depth discussion of the mechanisms at grain size level that lead to fracture, reference is made to Frost, 2001. The flaking results in release of energy from the highly stressed regions and significantly changes the ice-structure interface. This causes a shift from a flat layer with high-pressure zones, to a so called *pressure ridge* in the middle of the interface, where there essentially is one high-pressure zone that stretches from one side of the interface to the other. This *line-load* contact was first reported by Joensuu and Riska, 1989 and further investigated by Fransson et al., 1991 and Tuhkuri, 1993. Määttänen et al., 2011 performed medium-scale crushing tests where they registered pressures over the interface, from which the pressure ridge at relatively high velocities can clearly be seen, as shown in Figure 3-8 and 3-9, with resulting interfaces and corresponding pressure distributions respectively. They note that the vertical location of the pressure ridge is constantly moving up and down the interface, but

stays relatively constant in thickness, namely 5-9 mm (with limited accuracy due to a limited resolution of the pressure sensors). Similar observations were done by Riska et al., 1990 in full-scale, from an observation window in a ship's hull during ship-ice impacts (see also Riska, 2018).

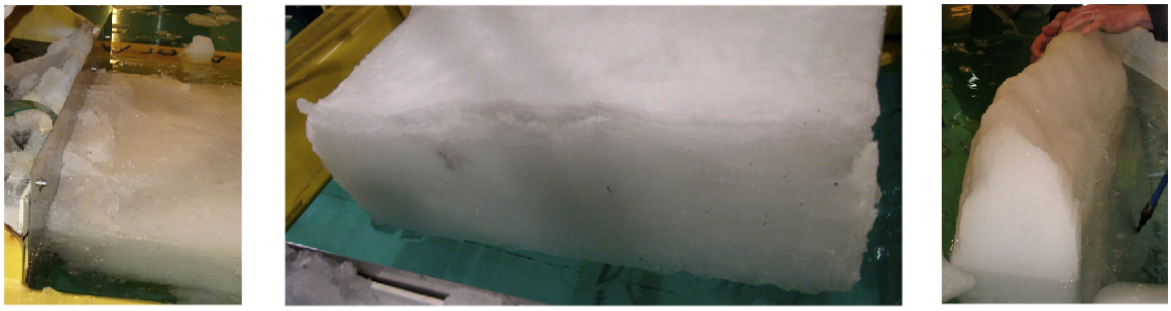

Figure 3-8: Indentation tests as shown in (a) with resulting interfaces after the tests showing (b) a flat interface at creep velocities (here v_{ice} < 1 mm/s) and (c) a pressure ridge at higher velocities. From Määttänen et al., 2011.

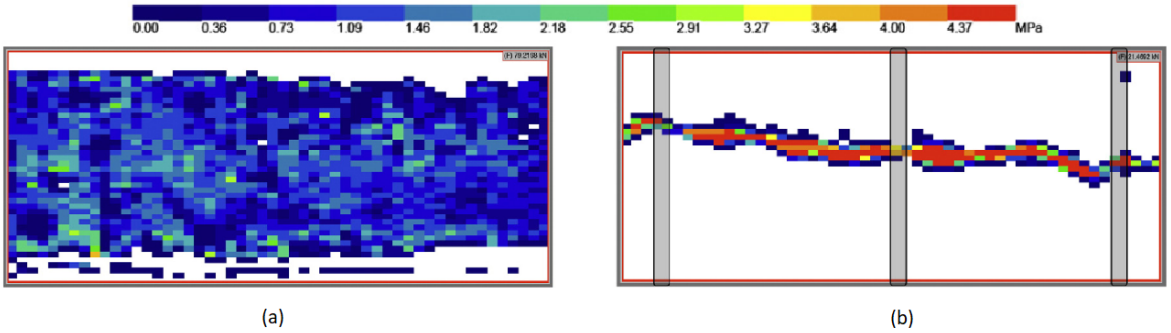

Figure 3-9: Indentation tests showing pressure distributions corresponding to the two resulting interfaces in Figure 3-8 for (a) creep velocities (here v_{ice} < 1 mm/s) and (b) at higher velocities. From Määttänen et al., 2011.

Daley, 1991 developed a model for flaking, which includes a crushing region at the ice-structure contact in which the high pressures initiate shear flakes, of which the angle is determined by applying a Coulomb failure criterion. Daley assumed straight fracture lines for the flakes, resulting in wedge-shaped extrusion channels. He set out why flaking would result to smaller subsequent flakes, running to the edge created by 1st order flakes, which he called 2nd (or higher) order flakes. With a known inclination of the tested ice cone, he simulated flaking (and subsequent extrusion) and obtained good agreement between tests and simulations. However, in later tests, it was observed that fracture paths were

curved, leading to curved flakes, such as mentioned by Kärnä, 1994. This was theoretically underlined by Kujala, 1994, who adapted Daley's approach to include fracture lines that followed a logarithmic spiral, where the shape of the spiral is related to the inner friction angle of ice and to the geometry of the ice edge. He obtained even better results for simulation of the conical indentation tests. Figure 3-10 shows thin sections of interfaces after indentation, showing curved (1st and higher order) spalls, as well as a schematic representation of the logarithmic spiral as used by Kujala, 1994. Daley et al., 1996 discuss the role that crushed ice plays in the development of flakes. Crushed ice in the contact zone leads to confinement of the intact ice, such that formation of local flakes is greatly inhibited. They state that a pressure of 0.5 MPa acting on both sides of the hpzs will close the surface cracks and thus significantly hinders their growth.

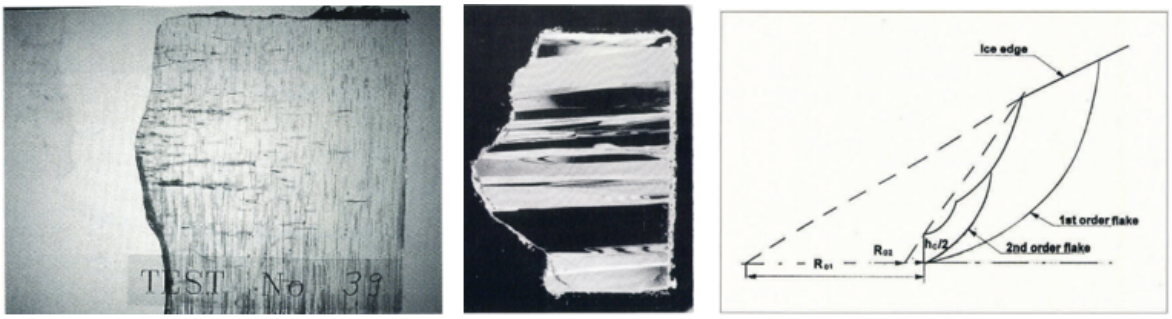

Figure 3-10: (a) interface showing curved flake paths, (b) interface showing curved flake paths, as well as 2nd and higher order flaking and consequently a rough edge, (c) schematic representation of the curved flakes following the logarithmic spiral. From (a) Kärnä, 1994 and (b),(c) Kujala, 1994.

From the above, it can be concluded that defining a distinct geometry for the extrusion channel of the ice-structure interface is complicated. Moreover, the geometry constantly changes during the interaction. This is mentioned by Kärnä et al., 1999, who reports this angle to be dependent on the indentation velocity. However, the internal VTT report in which that dependency is described, is no longer available.

The process of flaking is one of the causes of ice loads to vary in time, since a flaking event reduces the contact area of both high-pressure zones and low-pressure zones. This is described in detail by Hendrikse and Metrikine, 2015 and depicted in Figure 3-11 for intermittent crushing. This is especially significant in ice induced vibrations. Further, Gagnon et al., 2020 have observed that spalling leads to greater reduction in the contact area of high-pressure zones, than low-pressure zones. They stated that 20% reduction in size of a high-pressure zone following a spallation event, results in 3-10% reduction for a low-pressure zone. Thus, loads from extrusion are likely to fluctuate less than the loads from the intact ice.

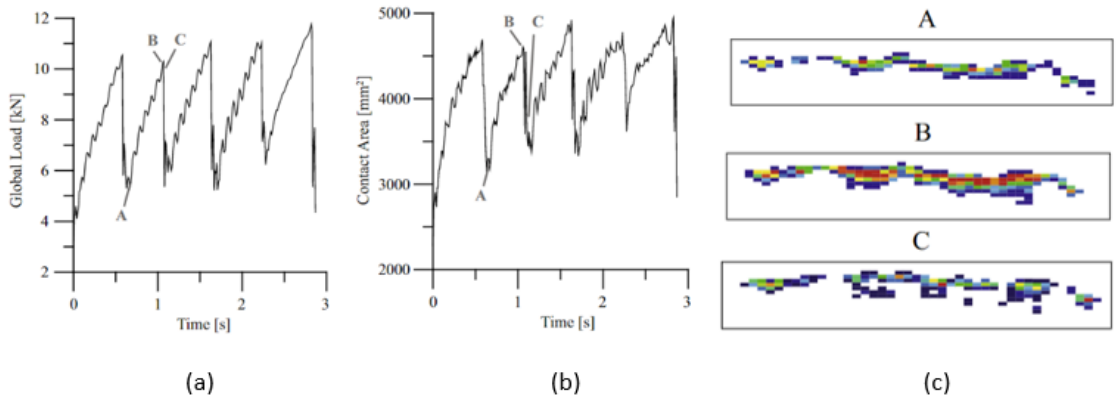

Figure 3-11: Corresponding figures of (a) global load signal during intermittent crushing, (b) contact area and (c) interface pressures. From Hendrikse and Metrikine, 2015.

3-5 Extrusion material characterisation

From the literature described above, it can be concluded that the process of extrusion is rather complicated. Daley et al., 1996 have proposed modelling the process of crushing/spalling and subsequent extrusion as a discrete chaotic model. Apart from a discrete flaking model, this was not followed up by the creation of a model that considers all steps in such a discrete model, likely because of the complexity of the process. Instead, it has been proposed to model extrusion by considering the to be extruded material as a continuum, or by using an FEM approach, such as by Herrnring and Ehlers, 2022. FEM uses more computational time and power, requires a large amount of data to accurately be able to resemble the real-life situation (which is often not available) and its complexity makes reproducibility difficult. Therefore, VANILLA uses a different approach, and FEM is not further considered here.

Extrusion tests

The continuum approach makes use of a number of simplifications and assumptions to come to an equation, or a set of equations, that describe the extrusion process. In order to identify what a suitable description and characterisation of this flow is, extrusion was examined experimentally by various researchers, such as by Sayed and Frederking, 1992 and Spencer et al., 1992, who used similar setups. In this setup, readily crushed ice is placed in between two converging parallel and rigid (steel) plates, in which flow is prevented in one direction, to obtain a plain strain condition with two dimensional flow as a result. One of the plates was fitted with pressure cells to measure the pressure from the extruding material. For a detailed description of the experimental setup, please see the original papers.

The extrusion tests by Spencer et al., 1992 were analysed in detail in Singh et al., 1995. The

velocities ranged from 2.5 to 160 mm/s. Figure 3-12 shows the pressure as a function of the distance from the centre for various stages during the test.

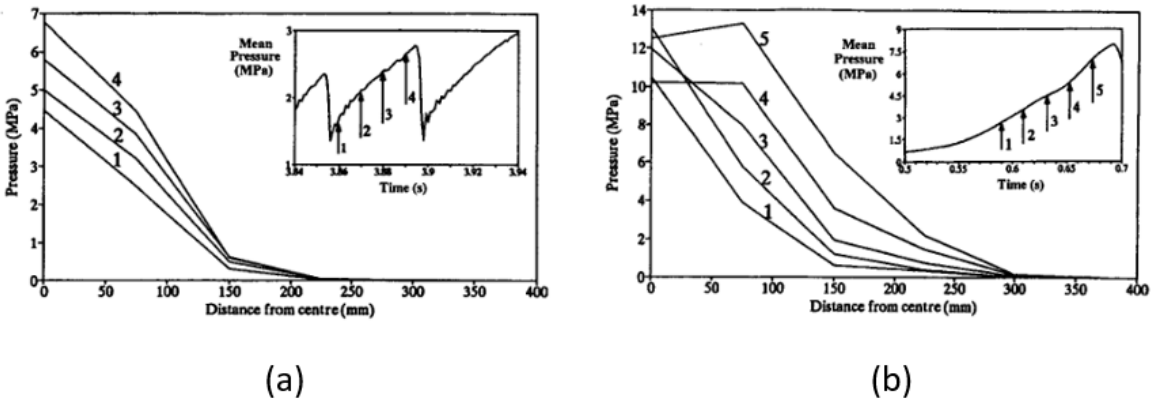

Figure 3-12: Results from extrusion tests of Spencer et al., 1992 for pressure over the distance from the centre for (a) 25 mm/s and (b) 160 mm/s. The smaller graphs show to which point in the mean pressure signal the numbers of the lines correspond. From Singh et al., 1995.

The authors report that the deformation of the crushed ice at early stages of loading is dominated by granular flow and compaction. When pressure is higher, a cycle of solidification and breaking occurs. This solidification happens when groups of particles stick together and form a fused mass, under high pressure. Pressure rises rapidly during this period and slow solid extrusion from the central region takes place.

In more detail, as can be seen from Figure 3-12(b), the load is carried by a narrow central zone of fused ice during the initial phase of the extrusion, when the mean pressure is low. When the pressure rises, the distribution flattens to a parabolic shape and the fused zone that carries the load becomes wider. A similar pattern could be seen in individual dynamic cycles for the intermediate velocity extrusion, as is shown in Figure 3-12(a). Due to this widening of the fused zone, a large pressure gradient forms at its edges, from which high shear stresses result. This leads to failure, that starts at the edge of the fused zone and moves towards the center. When a concave shape of the pressure distribution is attained, the high pressure gradient in the center forces the ice outwards towards the low pressure zones.

Density of the material was found to significantly change during the extrusion (from 0.55 g/cm^3 initially to over 0.80 g/cm^3 in the middle of the fused zone). Starting as a granular material, the increasing pressure compacts the material significantly, further enhanced by pressure melting and diffusion, leading to solidification. After the extrusion test, the authors observed that there was a distinct boundary between the fused zone in the center, and the material towards the boundaries, which was still granular. This is in agreement with the earlier mentioned observations by Tuhkuri and Riska, 1990 that a distinct boundary between crushed

and intact ice will form, and that there is a maximum pressure for crushed ice. This was reflected by the density measurements, which further showed that the compaction was most severe for low velocity extrusion. A schematic of the development of the fused zone is shown in Figure 3-13(a).

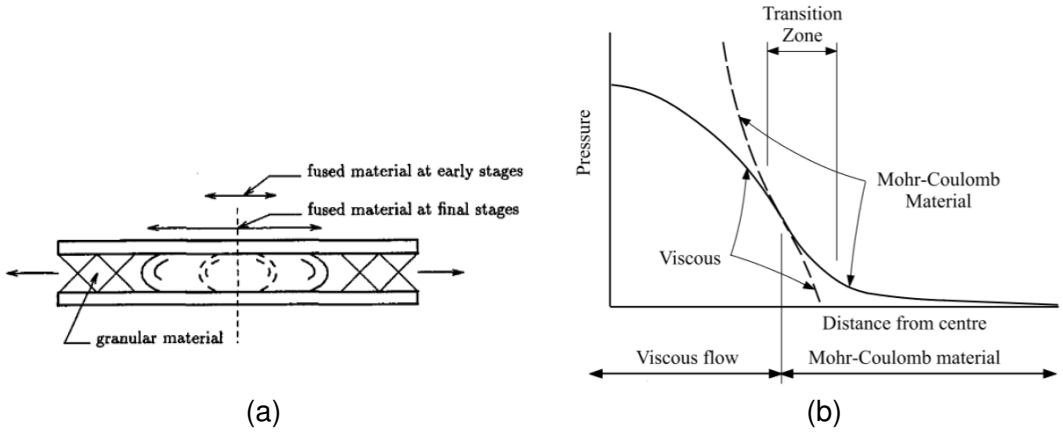

(a) (b)

Figure 3-13: (a) Development of the fused zone throughout the extrusion. (b) Transition from viscous behaviour to Mohr-Coulomb. From (a) Singh et al., 1995 and (b) Jordaan, 2001.

Lastly, based on the shapes of the graphs in Figure 3-12, appropriate flow description changes from Mohr-Coulomb for the early stages of the extrusion (convex shape), to a viscous description at later stages (concave shape), when the pressure is higher. This is sketched in Figure 3-13(b).

Mohr-Coulomb flow

As pointed out in the previous Section, in both the extrusion tests by Sayed and Frederking, 1992 and Spencer et al., 1992, the material showed flow characterised by the Mohr-Coulomb description for the stages and regions in the extrusion where the pressure is (relatively) low.

The Mohr-Coulomb theory is often used to describe materials for which the compressive strength far exceeds the tensile strength. The Mohr-Coulomb failure criterion is expressed as:

$$\tau = \sigma \tan(\phi) + c \tag{3.1}$$

in which τ is the shear strength (in Pa), σ is the normal strength (in Pa) and *c* is the intercept of the failure envelope with the axis of the shear strength and is called the cohesion (in Pa). Then, $\tan(\phi)$ is the slope of the failure envelope and ϕ is called the angle of internal friction (in rad). The widely known Mohr's circles are a geometric representation of the 2-D transformation of stresses. Each point on the circumference of Mohr's circle represents a

certain plane, giving the value of normal stress and shear stress at that plane. When the Mohr's circle crosses the failure envelope, failure will occur and the material starts to move. This theory is subsequently used for the description of rubble loads as well.

The Mohr-Coulomb flow description is one of the earlier attempts of describing granular flow, which is the flow of granular materials, like soil and small rocks, plastic granulates or other particles, either as a high concentration suspended in a fluid, or as dry particles. The theories of soil mechanics were extrapolated to obtain equations for the flow by including global inertial effects into the equations of motion. These theories are only valid for slow granular motion.

Hallam and Pickering, 1988 were the first to use the Mohr-Coulomb description for the flow of crushed ice. Savage et al., 1992 followed up their experimental work with an analysis in which they made use of the Mohr-Coulomb description to match what they found in their experiments, as mentioned earlier. The definition of the Mohr-Coulomb flow they obtained makes use of a separation distance H (in m) between the two converging plates. This form of the description cannot be used in a model that considers contact between structure and the ice, as is described in Appendix A-1, which includes the flow description. Furthermore, as can be seen in Figure 3-13(b), the Mohr-Coulomb description is accurate for the tail of pressure graph, towards the exit of the extrusion channel. This part carries only a small portion of the loads, while the bulk of the load is carried by the material towards the center, which is more accurately described by a viscous flow description. Therefore, the Mohr-Coulomb flow is not further elaborated here.

Viscous flow

A viscous fluid is a fluid in which the stresses present are dependent on the rate of change of the deformation over time. The viscosity is a measure of the resistance in the fluid to deformation at a given rate. This relation is given in Formula 3.2, known as Newton's law of viscosity.

$$\tau = \mu \frac{\partial u}{\partial y} = \mu \dot{\gamma} \tag{3.2}$$

Here, τ is the shear stress (in Pa), $\dot{\gamma}$ is the local shear velocity (in s^{-1}), which are related to each other through the (dynamic) viscosity μ (in Pa·s). The value for μ depends on the state of the fluid, such as the temperature and pressure. For crushed ice, Timco and Jordaan, 1987 and Finn et al., 1989 report values between 0.0009 and 1 MPa·s, while Xiao et al., 1991 used finite element modelling to find an even larger range based on the damage state of the crushed ice. Fluids following the constitutive equation above are called Newtonian fluids, for which μ is independent of the strain rate ($\dot{\gamma}$) and the shear stress varies proportionally with the strain rate. Alternatively there are liquids for which μ may change with strain rate. These have a constitutive relation that is of the form as in Equation 3.3.

$$\tau = k_c \dot{\gamma}^n \tag{3.3}$$

In Equation 3.3, k_c is the so called consistency index with units Pa·s^n and n is the dimensionless consistency index. Relevant for this thesis are shear thinning (or pseudoplastic) fluids. For shear thinning liquids, viscosity reduces with increasing shear rate, with $n < 1$.

In the analysis of the tests with drop balls in the previously mentioned paper from Kurdyumov and Kheisin, 1976, the crushed layer was treated as a Newtonian viscous fluid (Equation 3.2). This was also done by Nevel, 1986 in the analysis of iceberg impact forces. Jordaan and Timco, 1988 then adopted this treatment for their analysis of the crushed layer they assumed to be present between indenter and ice edge, as was shown in Figure 3-6. In their analysis, they made use of the continuity equation given in Equation 3.4 and equilibrium equations as in Equation 3.5.

$$\partial u/\partial x = -\partial v/\partial y \tag{3.4}$$

$$\begin{aligned} \partial p/\partial x &= \mu \nabla^2 u \\ \partial p/\partial y &= \mu \nabla^2 y \end{aligned} \tag{3.5}$$

In the equations above, u and v are the velocities (in m/s) in the x and y directions respectively, while p is the pressure (in Pa), ∇^2 is the Laplacian ($\partial^2/\partial x^2 + \partial^2/\partial y^2$) and μ the viscosity as given before. A sketch of the geometry is given in Figure 3-14(a), which includes the thickness of the crushed zone $2h$ and the ice thickness $2L$.

Using the above equations and assuming that $v(y) = 0$ at the ice surface ($y = 2h$) and equal to the indenter velocity v_0 at the indenter surface ($y = 0$), Jordaan and Timco, 1988 found a mean pressure as in Equation 3.6. They also assumed that $u(x, y)$ was 0 at the solid surfaces ($y = 0$ and $y = 2h$) due to frictional effects.

$$p_x = \int_0^{2h} p(x, y) \mathrm{d}y = \frac{3\mu v_0}{h} [(\frac{L}{h})^2 (\frac{1}{4} - (\frac{x}{2L})^2)] \tag{3.6}$$

In the analysis of the extrusion tests by Singh et al., 1995, the authors conclude that a Newtonian description for the flow behaviour of the crushed ice, as found above, is not appropriate. Instead, they use a power law description as in Equation 3.3, which they adopted in a slightly different form, as in Equation 3.7.

$$\frac{\partial v_x}{\partial r} = \dot{\gamma} = K \tau^N \tag{3.7}$$

In Equation 3.7, K is now the inverse of k_c and N is the inverse of n when compared to Equation 3.3.

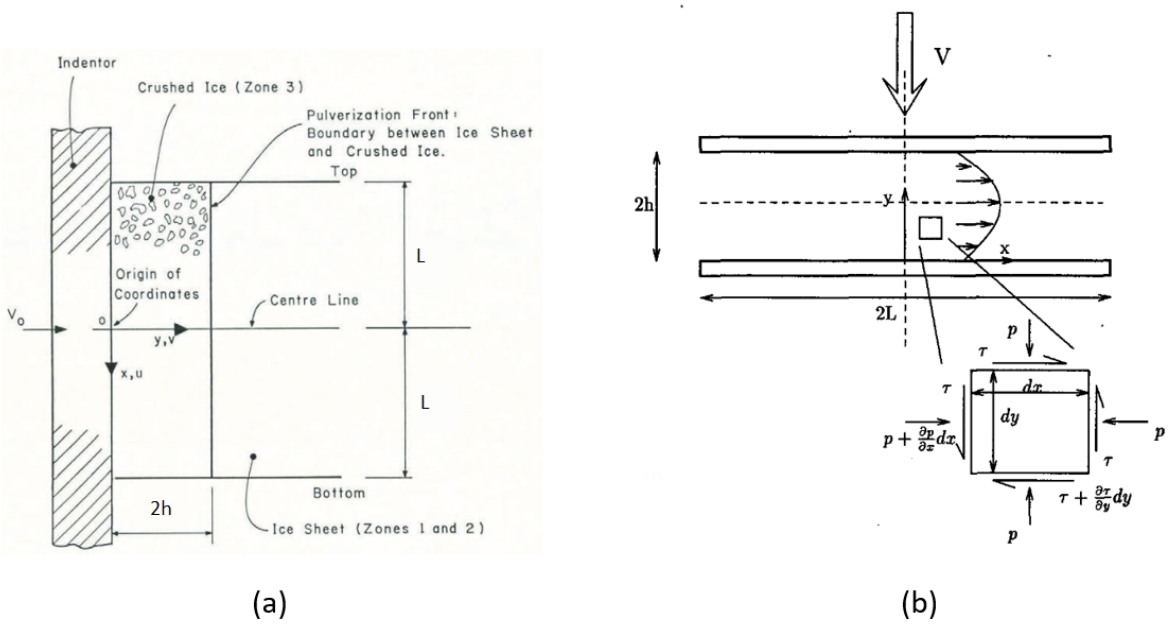

Figure 3-14: Sketch of the geometry used in (a) the analysis of Jordaan and Timco, 1988, from their paper, and (b) the analysis of Singh et al., 1995, from their paper.

They further make use of *lubrication theory*. Lubrication theory is a widely used theory for the description of two solid bodies that move or slide relative to each other, with a thin layer of fluid in between. An example is the case of a hydraulic bearing, where the thin layer of fluid acts to reduce friction. Lubrication theory makes use of the assumption that the layer is thin, such that $L \gg h$. Further, fluid flow is assumed laminar and inertia and body forces are neglected. This can significantly simplify the problem for describing certain flow fields. Often applied additional assumptions are those of using an incompressible, as well as a Newtonian fluid. Though these further simplify the problem, they are not strict requirements. Moreover, lubrication theory allows for the implementation of non-parallel surfaces in the geometry that describe the problem.

Singh et al., 1995 do assume the fluid to be incompressible and isotropic. The geometry is shown in Figure 3-14(b).

The use of lubrication theory results in uniform pressure distribution in the y-direction. With that, a pressure distribution as in Equation 3.8 is found (for the derivation, reference is made to the original paper). In Equation 3.8, p_0 is the pressure at the exit ($x = L$).

$$p_y(x) = \frac{AN}{N+1}[L^{(N+1)/N} - x^{(N+1)/N}] + p_0 \qquad A = [\frac{V(N+2)}{2Kh^{(N+2)}}]^{1/N} \tag{3.8}$$

The mean pressure p_m (in Pa) is then obtained by integrating Equation 3.8 between $x = 0$ and $x = L$, which results in Equation 3.9.

$$p_{\mathrm{m}} = \frac{AN}{2N+1}L^{(N+1)/N} + p_0 \tag{3.9}$$

The mean platen pressures that were measured in the tests are plotted in Figure 3-15(a), as well as the compaction that was found by blocking the outflow of material at a speed of 2.5 mm/s. From Equations 3.8 and 3.9 it follows that

$$p_{\mathrm{m}} - p_0 \propto (\frac{1}{h})^{(N+2)/N} \tag{3.10}$$

With this relation it can be seen that from plotting the mean platen pressure logarithmically against the inverse of the layer thickness, the gradient indicates $(N+2)/N$. The authors found a value of 2.2 for speeds of 60-160 mm/s, which corresponds to $N \approx 1.67$ (such that $n = 1/N < 1$ and indicating shear thinning behaviour). For 2.5 mm/s, they found a gradient of 8, which they attributed to the critical zone forming at an earlier stage in the test due to compaction. At 25 mm/s, there was a lack of data and no gradient could be extracted. The effect of the rate of extrusion was found by the authors to be difficult to analyse, due to the variance in compaction rates (or lack thereof at high speeds).

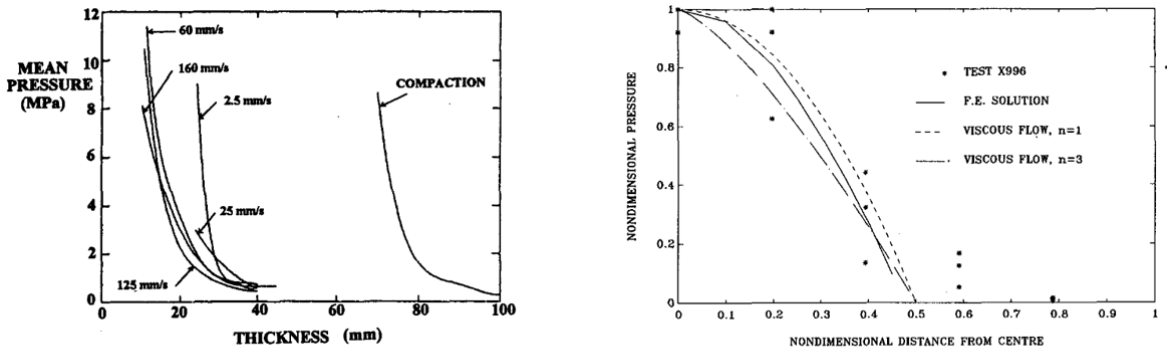

(a) (b)

Figure 3-15: (a) Mean pressure results, from which N can be obtained. (b) Comparison of a linear and nonlinear viscous description with a finite element approach and test results by Xiao et al., 1991. From Singh et al., 1995.

From plotting test results of Xiao et al., 1991, as well as FEM simulations by the same authors and the mathematical evaluation of a linear and nonlinear viscous material (at $N = 1$ and $N = 3$ respectively), the authors conclude that the nonlinear approach yields a good fit, particularly in the fused zone. Since the resulting pressure distribution is convex (for parallel plates), they further state that the theory is inaccurate for describing the pressure distribution at the edges, for which a Mohr-Coulomb description is more appropriate. However, since the majority of the force is concentrated in the critical zone, they conclude that the (nonlinear) viscous theory models the material well during high pressure interactions. Lastly, they recommend the effect of volumetric deformation due to to pore collapse (i.e. compression) to be further investigated and incorporated into a general formulation for extrusion.

3-6 Extrusion modelling in other models

This Chapter is finished with an investigation of how extrusion is modelled in two other well known models, the Matlock model and the Kärnä model.

Matlock model

One of the earlier ice models was proposed by Matlock et al., 1971, based on the forced vibration theory for IIV. In their model, the structure is represented by a single degree of freedom oscillator system, in which the structure is replaced with a linear model. For the details, please see the original paper. Various adjustments have been proposed over the years. One of these is the introduction of the process of extrusion, which is of interest to this work.

In the original Matlock model, the ice force goes to zero immediately after breakage, until contact with the next tooth is established. In reality, a residual ice force remains. Therefore, an adaptation of the model is required. The proposed adaptation considers a residual force after breaking, F_{e} (in N), which originates from the force required to extrude the broken ice (Huang and Liu, 2009). It is applied in the EOM when the ice is in contact with the structure. For the Bohai Sea, Tongkui and Jizu, 1989 suggest that a value of one third of $F_{\mathrm{ice}}^{\mathrm{max}}$ (the maximum ice force, in N) should be used for F_{e} (this might be different for others regions).

A further extension to this modelling of the ice extrusion force, is described by Withalm and Hoffmann, 2010. Based on a paper by Kärnä et al., 1999, which states that the time span between maximum minimum force after a fracture is about 10 to 20% of the time span necessary to reach the maximum force before the fracture, they proposed that a smoothing function can be applied for F_e. This smoothing function takes the form of Equation 3.11. In Equation 3.11, t_{cont} is the time when contact between ice and structure is established (in s), while t_{frac} is the time when fraction occurs (in s). $\gamma_{\mathrm{span}} = 0.15$ is the average of the time span mentioned above. For $F_{\mathrm{e}}^{\mathrm{max}}$, the value of one third of $F_{\mathrm{ice}}^{\mathrm{max}}$ could be applied.

$$F_{\mathsf{e}} = \frac{F_{\mathsf{e}}^{\mathsf{max}}}{2}[\cos(\frac{\pi(t - t_{\mathsf{frac}})}{\gamma_{\mathsf{span}}(t_{\mathsf{frac}} - t_{\mathsf{cont}})}] \qquad \text{for} \quad t_{\mathsf{frac}} \leq t \leq [t_{\mathsf{frac}} + \gamma_{\mathsf{span}}(t_{\mathsf{frac}} - t_{\mathsf{cont}}] \tag{3.11}$$

Kärnä model

A later model was the so called PSSII (Procedure for dynamic Soil-Structure-Ice Interactions) model, by Karna, 1992. The model is constructed by combining a far field spring-damper system, with multiple near-field elements. For these near-field elements, specific constitutive relations were established for each phase (5 in total) in the crushing process. Again, reference is made to the original paper for a more in-depth discussion of the model.

Initially, Kärnä and Järvinen, 1994 considered ice extrusion as a dynamic process that is driven by the lateral force interacting between the ice sheet and the structure, while the extrusion is also retarded by mass forces as well as frictional forces on the crushed ice. This dynamic model of ice extrusion proved very sensitive to model parameters considered. Therefore, combined with difficulties posed by the edge geometry, a simplified version of the extrusion process was later adopted. The simplified extrusion was added to the model in a later extension (Kärnä et al., 1999). *Unloading with ice extrusion* is one of the phases considered in the Kärnä model. In this phase, according to Kärnä et al., 1997, the force can be described with an incremental force function as given in Equation 3.12 (for *major* flaking, in which flaking happens simultaneously at the top and bottom of the ice).

$$\Delta F_{\mathsf{i}}(t) = 6(F_{\mathsf{i}}^{\mathsf{cr}} - F_{\mathsf{i}}^{\mathsf{ex}})\left[(\frac{t}{T_{\mathsf{i}}^{\mathsf{u}}})^2 - (\frac{t}{T_{\mathsf{i}}^{\mathsf{u}}})\right]\frac{\Delta t}{T_{\mathsf{i}}^{\mathsf{u}}} \tag{3.12}$$

In Equation 3.12, ΔF_{i} is the ice force (in N), $F_{\mathsf{i}}^{\mathsf{cr}}$ is the peak load at the preceding ice failure event (in N) and $F_{\mathsf{i}}^{\mathsf{ex}}$ (in N) is the minimum force level at the end of the unloading, which is sustained until the next loading event occurs. $T_{\mathsf{i}}^{\mathsf{u}}$ is time between the peak load and the next minimum (in s), which is again taken as 10-20$\%$. The formula changes slightly in the case of *secondary flaking*, which is alternating flaking at the top and bottom, said by the authors to occur at high indentation speeds.

In addition to extrusion, Kärnä mentions the positive force-velocity gradient encountered in Chapter 2 in descriptions of the model. However, arguing that the effect is not accepted by some experts, the choice was made to not include the effect into the PSSII model.

With the theory of ice extrusion known, an extrusion model is set up, which is explained in Chapter 6. First, the theory behind rubble loads is introduced in the next Chapter, followed by explanation of the rubble model proposed in Chapter 5.

4

Rubble theory

The next phenomenon that is not currently part of VANILLA is the presence of rubble (piles) from ice crushing. In this Chapter, this phenomenon is discussed. Rubble is first defined, after which the loading from rubble piles is investigated. This is followed by a description of the theory on rubble pile dimensions.

4-1 Rubble definition

Rubble is the collection of ice pieces that have a maximum length in the order of magnitude of the ice thickness, while it was shown in Chapter 3 that the size can be much smaller. They result from breaking of an ice floe, for example through one of the failure mechanisms shown in Chapter 2. As explained in Chapter 2, rubble can have a significant impact on the magnitude of ice loads when it forms ice ridges. This happens when the rubble for example accumulates from impact in one location, refreezes and then travels to a different location, where it encounters another structure. In this chapter however, the rubble piles forming from extruded ice from crushing are of interest. For that type of rubble pile, there is not sufficient time for the crushed ice to refreeze, such that the material remains mobile. The loading case is then significantly different, so that it is important to make a distinction between newly formed rubble and 'old' rubble. An example of such a newly formed rubble pile is given in Figure 4-1.

Figure 4-1: Photograph of the Norströmsgrund Lighthouse with a rubble pile after crushing failure of drifting level ice (Photo by Kari Kolari, VTT).

Another important aspect related to the origin of rubble piles is the geometry of the structure. For sloped structures, the ice is bent up or down. Since the flexural strength of ice is lower than the compressive strength, this leads to flexural failure. The individual ice pieces in the rubble pile resulting from this type of failure, are much larger than from crushing on a vertical structure (Mayne and Brown, 2000). In full-scale, a rubble pile may consist of both large and small scale rubble, from mixed crushing and flexural failure. Next to the rubble size, the loading is also significantly different for sloped structures. In this chapter, the loading on vertical structures is of interest.

4-2 Rubble pile dimensions

Since extrusion happens both up and downwards, rubble piles form above and below the intact ice sheet. The pile above the ice sheet is often termed the *sail*, while the rubble pile below the water is termed the *keel*. These are shown in Figure 5-1. In this figure, h_{sr} is the height of the rubble pile in the sail (in m), whereas h_{kr} is the height of the rubble pile in the keel (in m). θ_k is the angle that the keel makes with the intact ice (in °).

There are plenty of sources on the rubble pile dimensions for sloping structures (Mayne and Brown, 2000, Croasdale, 2012 and Sazonov and Simakina, 2021 to only name a few), both from observations and simulations. Similarly, there are sources for ice ridge dimensions, such as Løset et al., 2006. However, to the author's knowledge, there are none for vertical structures. Thus, the dimensions of the rubble piles are later determined based on video material of crushing events in Chapter 5.

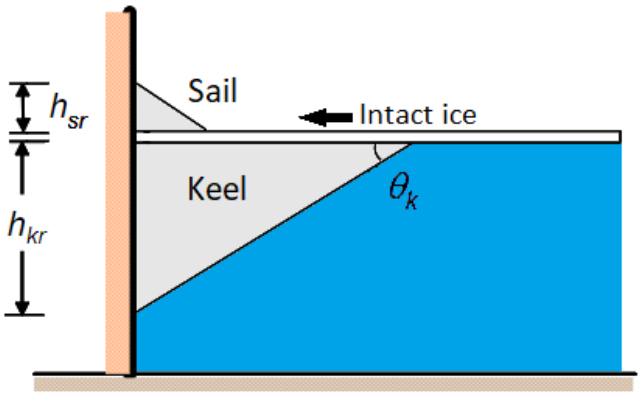

Figure 4-2: Sketch of the two rubble piles, with the sail above the intact ice and the keel below the intact ice. Adapted from Kärnä and Qu, 2005.

4-3 Role of ice rubble in loading on vertical structures

The role of rubble piles in the ice-structure interaction for vertical structures may be similar to that of extrusion, in the way that it constitutes an additional source of forcing that is significantly less intermittent than the crushing of the intact ice. In the occasion of dynamics due to crushing, this forcing is a form of damping.

An additional role that rubble piles may have on ice structure interaction for structures with a vertical wall, is that it may force a crushing event to transition to a state in which the ice fails in buckling. This was observed by Kärnä and Jochmann, 2003, who report a typical amplitude of vertical motion between 3 and 5 cm for 30 cm ice thickness at the Norströmsgrund lighthouse. They attribute the up and down movement of the ice edge to imbalances in the counteracting vertical forces on the ice floe from gravity and buoyancy in the sail and keel respectively. Failure in buckling significantly reduces the magnitude of the force from the intact ice, as compared to failure in crushing. This behaviour is less likely for greater ice thicknesses.

4-4 Loads from rubble for vertical structures

For a structure with a vertical wall, the rubble can interact with the structure through two modes (according to Kärnä and Qu, 2005):

1. Sliding mode: in this mode, the rubble pile slides over the incoming level ice as an intact body. The loads from the pile on the structure stem from the friction between the bottom of the rubble pile and the level ice, with a resulting force acting opposite of the direction

of motion of the rubble pile relative to the ice underneath.

2. Internal failure mode: in this mode, the rubble pile fails internally, such that there is a failure plane starting at the point of contact between the structure and the level ice, extending through the pile towards the sloping edge. The origin of the loads from the pile on the structure is the friction between the wedges rubble in the pile above and below the failure plane.

The two modes are depicted in Figure 4-3. Here, θ_s is the angle of the rubble pile with respect to the level ice (in °), while α and β are the angles (in °) of the structure with the level ice and the angle of the upper wedge with the horizontal (in this case $\beta = -\theta_s$) respectively. F_{tsr} is the sliding mode load from the sail and F_{sr} is the internal failure mode load from the sail (in N).

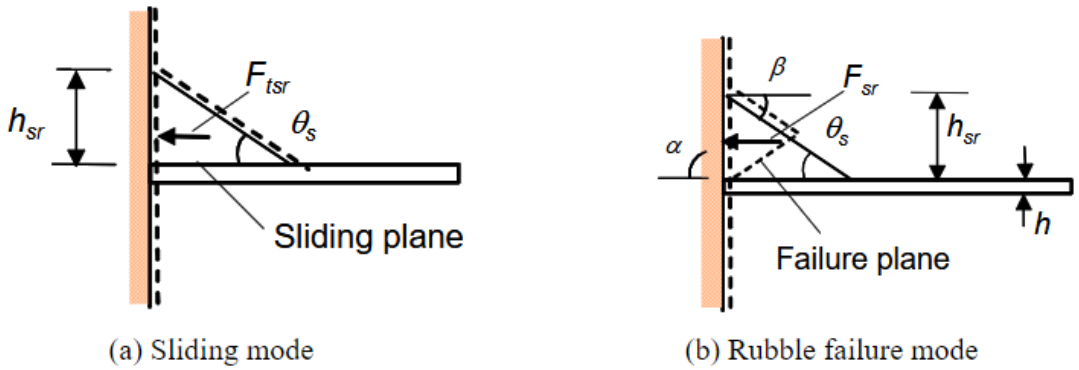

Figure 4-3: Failure modes for rubble piles, with (a) sliding mode and (b) internal failure. From Kärnä and Qu, 2005.

Sliding mode

The sliding mode is more likely to occur when the ice incoming level ice is smooth, without pieces of ice extending from the ice surface and without snow coverage, which increases friction (Fransson et al., 1991). The loads from this sliding motion can be expressed through the simple Coulomb friction law, as given in Equation 4.1.

$$F_{\text{fric}} = \mu_{\text{f}} F_{\text{n}} \tag{4.1}$$

In Equation 4.1, the frictional force F_{fric} (in N) and the normal force F_{n} (in N) are related to each other by the dimensionless friction coefficient μ_{f}. In the case of the rubble pile, this takes the form of Equation 4.2.

$$F_{tsr} = \frac{1}{2}\mu_{sr}\gamma_{sr}h_{sr}^2 \cot\theta_s$$
$$F_{tkr} = \frac{1}{2}\mu_{kr}\gamma_{kr}h_{kr}^2 \cot\theta_k \tag{4.2}$$

Here, the loads are line loads with dimension N/m, μ_{sr} is the dimensionless friction coefficient of the rubble on the level ice, h_{sr} and θ_s are as given above and indicated in Figure 4-3. Where the subscript s, indicating the sail, is replaced by k, it indicates the keel. γ_{sr} and γ_{kr} are the specific weight of the upper rubble pile and the buoyancy of the lower rubble pile respectively (in N/m^3). Their value can be found through Equation 4.3.

$$\gamma_{sr} = (1 - \eta_{sr})\rho_{ice}g$$
$$\gamma_{kr} = (1 - \eta_{kr})(\rho_w - \rho_{ice})g \tag{4.3}$$

In Equation 4.3, η_{sr} and η_{kr} are the dimensionless porosity of the upper and lower rubble pile respectively, ρ_{ice} and ρ_w are the density (in kg/m^3) of ice and water respectively and g is the gravitational constant (in m/s^2).

Internal failure

The internal failure mode can be described by a common approach in soil mechanics, describing the lateral force on retaining walls from the soil they retain. From Figure 4-3, it can be understood that when the structure is moving away from the ice, the upper wedge will slide down. This is called *active earth pressure*. Alternatively, when the structure is moving towards the ice, the upper wedge of rubble will be pushed upwards. The pressure on the structure in this situation is called *passive earth pressure*. Both situations are depicted in Figure 4-4.

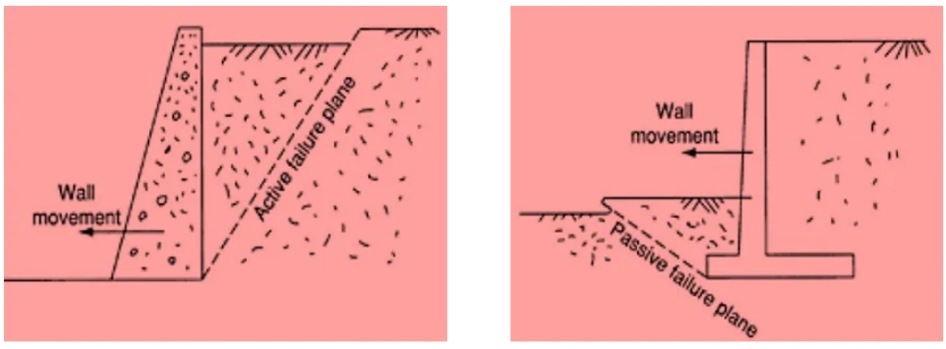

Figure 4-4: (a) Active earth pressure and (b) passive earth pressure. From Suryakanta, 2015.

There are various methods for determining the lateral earth pressure, that adopt different assumptions to obtain formulas for describing the pressure. One of the earlier and most widely used methods is the Coulomb earth pressure theory. The assumptions taken by Coulomb are:

1. Soil is isotropic and homogeneous and has both internal friction and cohesion.
2. The rupture surface is a plane surface and the backfill surface is planar (it may slope but is not irregularly shaped).
3. The friction resistance is distributed uniformly along the rupture surface.
4. The failure wedge is a rigid body undergoing translation.
5. There is wall friction (denoted δ).
6. Failure is a plane strain problem.

For the active earth pressure, the pressure on the structure, given in the terms of the sail as given above, is as given in Equations 4.4 and 4.5 (as a line load, in N/m). A derivation of these Equations can be found in Bowles, 1988.

$$F_{\text{sr,a}} = \frac{1}{2}\gamma_{\text{sr}} h_{\text{sr}}^2 K_{\text{a}} \tag{4.4}$$

where

$$K_{\text{a}} = \frac{\sin^2(\alpha+\phi)}{\sin^2(\alpha)\sin(\alpha-\delta)\left[1+\sqrt{\frac{\sin(\phi+\delta)\sin(\phi-\beta)}{\sin(\alpha-\delta)\sin(\alpha+\beta)}}\right]^2} \tag{4.5}$$

Here, α and β are the angles as shown in Figure 4-3(b). δ is the friction angle between the wall and the rubble (in °). ϕ is the internal friction angle of the rubble pile, which was previously encountered in the discussion of the Mohr-Coulomb criterion in Section 3-5.

Similarly, the line load (in N/m) in the case of passive earth pressure is as given in Equations 4.6 and 4.7.

$$F_{\text{sr,p}} = \frac{1}{2}\gamma_{\text{sr}} h_{\text{sr}}^2 K_{\text{p}} \tag{4.6}$$

where

$$K_{\mathsf{p}} = \frac{\sin^2(\alpha - \phi)}{\sin^2(\alpha)\sin(\alpha + \delta)\left[1 - \sqrt{\frac{\sin(\phi+\delta)\sin(\phi+\beta)}{\sin(\alpha+\delta)\sin(\alpha+\beta)}}\right]^2} \tag{4.7}$$

It should be noted that the passive earth pressure, for a given set of dimensions, is always much larger than the active earth pressure. For the keel, the same Equations for the passive and active earth pressures can be used, when the parameters for the keel are used as input.

When cohesion (see Equation 3.1) is considered, an additional factor should be inserted in Equations 4.4 and 4.6. Then, they become as in Equation 4.8 and 4.9 for the active and passive case respectively.

$$F_{\mathsf{sr,a}} = \frac{1}{2}\gamma_{\mathsf{sr}} h_{\mathsf{sr}}^2 K_{\mathsf{a}} - 2c\sqrt{K_{\mathsf{a}}} \tag{4.8}$$

$$F_{\mathsf{sr,p}} = \frac{1}{2}\gamma_{sr} h_{\mathsf{sr}}^2 K_{\mathsf{p}} + 2c\sqrt{K_{\mathsf{p}}} \tag{4.9}$$

With the two modes defined as above, sliding and internal failure, it can be stated that the mode leading to the lowest load will occur for a given set of geometry and ice conditions. This is true for both the sail and the keel. Then, the rubble load (in N/m) can be defined as in Equation 4.10.

$$F_{\mathsf{rub}} = \min[F_{\mathsf{tsr}} + F_{\mathsf{tkr}}, F_{\mathsf{sr}} + F_{\mathsf{tkr}}, F_{\mathsf{tsr}} + F_{\mathsf{kr}}, F_{\mathsf{sr}} + F_{\mathsf{kr}}] \tag{4.10}$$

For background theory of the values later used for the parameters in the formulas above, see Appendix A-3.

Summary of theory

Chapter 2: Loads from floating ice

- Ice induced vibrations are vibrations originating from loads by level ice on structures, due to interaction in crushing, that can be hazardous to the structure.
- The phenomenological VANILLA ice model uses N 1D ice elements to model an advancing ice floe, where each element is modelled with a combination of springs and dashpots so that elastic, visco-elastic and viscous effects are incorporated.
- The VANILLA model currently does not explicitly include rubble and extrusion loads.
- A positive force-velocity gradient is observed in measurements at high indentation speeds. Not including the added damping from the positive force-velocity gradient leads to overestimation of structural oscillation amplitude in the CBR regime and overprediction of FLI initiation drift speeds.

Chapter 3: Extrusion theory

- The extrusion of pulverised ice can pose a damping, such that ice extrusion has implications on the dynamics of crushing events for flexible structures.
- The processes causing break-up of the intact ice taking place in crushing lead to a wedge shaped ice edge.
- Zones directly adjacent to the high-pressure zones of intact and recrystallised ice, where ice is crushed, carry significant loads.
- A nonlinear viscous flow description is accurate for flow in the region of the extrusion close to the center of the interaction, which carries the majority of the extrusion loads.

Chapter 4: Rubble theory

- Rubble piles on a monopile structure consist of a sail and a keel. The dimensions of these are not described in literature and must be determined separately.
- The role of rubble piles in the ice structure interaction for vertical structures may be similar to that of extrusion, by posing a form of damping in the ice-structure interaction.
- The rubble will exert a load on the structure in either a Sliding mode or an Internal failure mode, whichever is smaller in magnitude.

Part II

Methods

5

Rubble model

As a first extension to the VANILLA code, the theory in Chapter 4 is used to calculate the loads stemming from the rubble piles in a crushing event. These are described in this Chapter. First, the model as used is elaborated, followed by a dependency of the model on the input parameters and some validation. Finally, the way the model is used in VANILLA is discussed.

5-1 Model description

As a first step to calculating the rubble loads, the rubble pile dimensions have to be established. Without extensive measurements of these dimensions, a geometry has to follow from the few observations available, as discussed below, combined with logical reasoning.

Pile dimensions

From video material from crushing events at the Norströmgsrund lighthouse, a flexible structure with a diameter at waterline of 7.52 m, estimates of the pile dimensions can be obtained.

Firstly, the ratio of the keel and the sail are determined. Figure 5-1 shows a frame of a video taken at the Norströmsgrund lighthouse, looking down on the incoming ice, which has a thickness of 0.65 m and a drift speed of 0.02 m/s. It clearly shows the rubble piles, with the sail in bright white and the keel in a grey shade through the clear ice. Their edges are shown by the orange lines. In the figure, the length of the sail l_{sr} (in m) and the keel l_{kr} (in m) are depicted. From the lengths, it is found that in this case the ratio is as in Equation 5.1.

$$r_{\text{ks}} = \frac{l_{\text{kr}}}{l_{\text{sr}}} \approx 2.5 \tag{5.1}$$

Next, the dimensions of the sail are examined, as these are the best observable from photographs. From the same photograph as in Figure 5-1, Figure 5-2 is obtained. The lighthouse and the rubble sail have been extrapolated from the photo. This Figure shows two notable things. The length of the rubble pile seems to stay constant in the first 45° from the point where the ice comes in perpendicular to the tangent of the structure. After that, it gradually decreases. Also, from measuring the size of the rubble pile in front of the structure and at the side of the structure, the ratio in Equation 5.2 can be found.

$$\frac{l_{\text{sr,front}}}{l_{\text{sr,side}}} \approx 1.9 \tag{5.2}$$

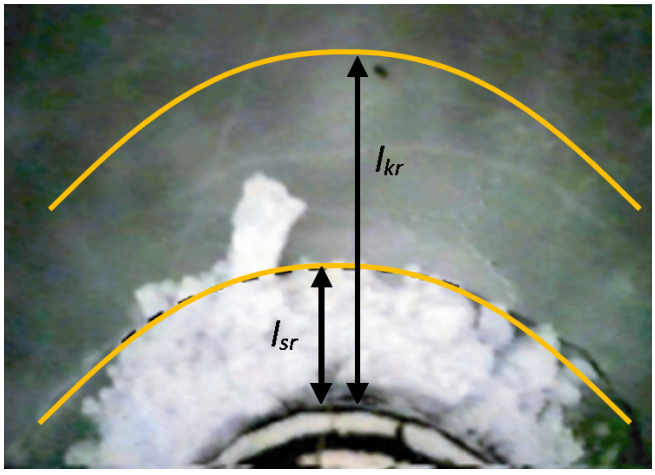

Figure 5-1: Picture of the Norströmsgrund lighthouse showing the sail and the keel. Adapted from Bjerkås and Skiple, 2005.

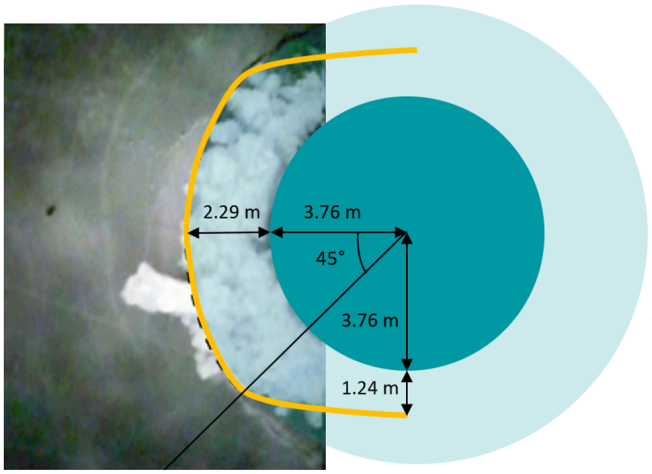

Figure 5-2: Picture of the Norströmsgrund lighthouse showing the dimensions of the sail. Adapted from Bjerkås and Skiple, 2005.

A limited number of other pictures available to the author, showed similar results, though deviations did occur. Since these photographs (or video frames) were taken at a slight angle with respect to the structure, measuring distances was less reliable and therefore these were chosen not to be included in this document.

From these observations, an attempt is now made to calculate the pile dimensions. A first assumption is made that after sufficient time in the crushing event, the amount of ice being crushed has to be equal to the amount of rubble that is discharged from the pile at the sides ($\theta = 0°$ in Figure 5-3). Since the density changes when the intact ice is crushed to rubble ice, this should be represented by an equilibrium of the amount of ice mass crushed (m_c) and discharged (m_d), as given by the mass flow in Equation 5.3.

$$\dot{m}_c = \dot{m}_d \tag{5.3}$$

Here, m_c and m_d have units of kg/s. Equation 5.3 can be written alternatively as in Equation 5.4.

$$\rho_{ice} A_c v_{ice} = \rho_r A_{r,d} v_d \tag{5.4}$$

In Equation 5.4, ρ_i and ρ_r are the ice and rubble density (in kg/m^3) respectively, A_c is the surface of the crushing in front of the structure and $A_{r,d}$ is the surface of the rubble piles next to the structure that are discharged, (both in m^2, see Figure 5). v_{ice} and v_d are the velocities of the incoming ice and at which the rubble is being discharged respectively (in m/s).

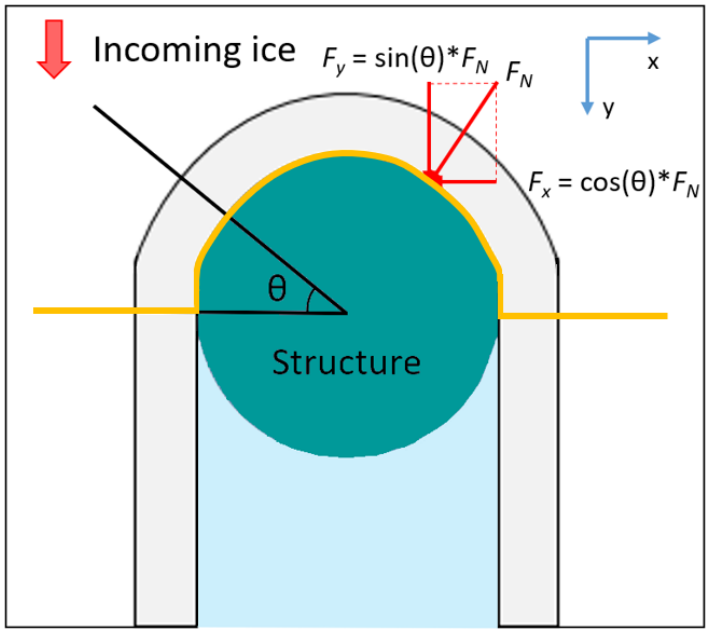

Figure 5-3: Schematic showing the direction of the rubble force.

It is assumed that the rubble piles on the side of the structure, when they are at 90° with the ice drift direction (θ = 0°), do no longer slide and do not experience significant friction with the structure. The piles then move with the drift speed of the incoming ice, that is $v_{\text{ice}} = v_{\text{d}}$. Further, replacing surfaces with the relevant parameters and observing that $\rho_{\text{r}} = \rho_{\text{i}}(1 - \eta_{\text{r}})$ (and assuming equal -dimensionless- porosity η_{r} and thus density for sail and keel), Equation 5.4 then can be rewritten as in Equation 5.5.

$$h_{ice}D = (1 - \eta_{\text{r}})^{*}(l_{\text{sr}}^2 \tan\theta_{\text{s}} + l_{\text{kr}}^2 \tan\theta_{\text{k}}) \tag{5.5}$$

Here, D is the structure diameter (in m), with the other parameters as introduced above. This equilibrium is shown in Figure 5-4, showing the structure with the crushing surface as a red striped area and the rubble piles on the side as they are discharged. This Figure follows the trace of the orange line in Figure 5-3

With the ratio between the sail and keel length known from Equation 5.1, Equation 5.5 can be rewritten to be left with only one unknown, as in Equation 5.6, which can be solved for l_{kr}.

$$h_{\text{ice}}D = (1 - \eta_{\text{r}})^{*}((l_{\text{kr}}/r_{\text{ks}})^2 \tan\theta_{\text{s}} + l_{\text{kr}}^2 \tan\theta_{\text{k}}) \tag{5.6}$$

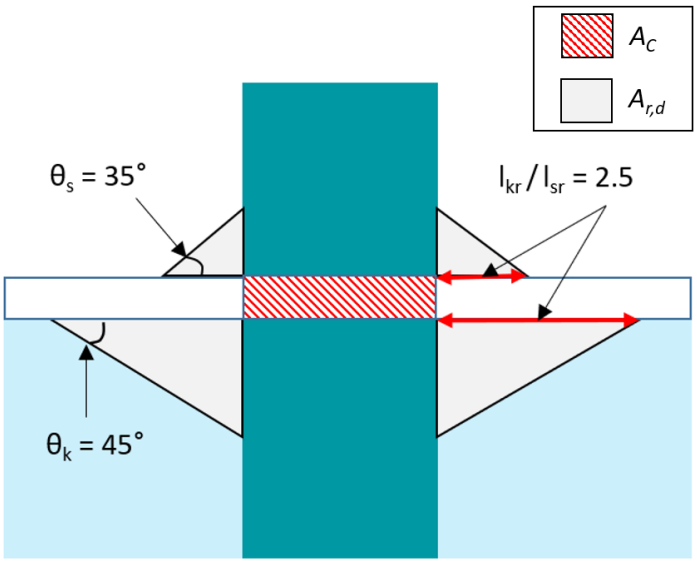

Figure 5-4: Schematic of the equilibrium used in constituting the rubble model.

When l_{kr} is known, it is trivial to find l_{sr}, h_{kr} and h_{sr}, using the ratio in Equation 5.1 and θ_s and θ_k.

Following from the ratio found in Equation 5.2 and the observation that the rubble pile increases to this ratio over 45°, as shown in Figure 5-2, the shape of the rubble piles along the perimeter can be described as in Equation 5.7, with a linear increase over θ up to $\theta = 45° = \frac{\pi}{4}$ rad.

$$\begin{aligned} l_{sr}(\theta) &= l_{sr,side}(1 + 0.9\frac{4\theta}{\pi}), && \text{for } \theta < \frac{\pi}{4} \\ l_{sr}(\theta) &= 1.9^* l_{sr,side}, && \text{for } \theta > \frac{\pi}{4} \end{aligned} \tag{5.7}$$

With the angle of repose staying constant along the perimeter, from Equation 5.7 it follows that the height of the rubble pile also changes along the perimeter. This is indicated in Equation 5.8. Both Equation 5.7 and 5.8 are also used for the keel, with the appropriate parameters.

$$h_{sr} = l_{sr}(\theta)^* \tan(\theta_s) \tag{5.8}$$

Sliding mode

With the dimensions of the rubble piles known, the rubble loads can be computed. For the sliding mode, Equation 4.2 has to be modified, since we are dealing with a circular structure.

The volume of a fully circular truncated hollow cone (V_{thc} in m^3), as we encounter for a rubble pile around a circular structure, is given as in Equation 5.9 In this Equation, D_{cone} is the inner diameter, such as the structure diameter in our case, l_{cone} is then the base length of the cone, which is l_{sr} or l_{kr} in the case of the rubble pile, while h_{cone} is the height of the truncated cone, h_{sr} or h_{kr} in our case (all in m).

$$V_{\text{thc}} = h_{\text{cone}}\pi(\frac{1}{2}D_{\text{cone}}l_{\text{cone}} + \frac{1}{3}l^2_{\text{cone}}) \tag{5.9}$$

Then, from Equation 4.1 and using Equation 5.9 the sliding force in the direction of the ice drift can be calculated through Equations 5.10 ($F_{\text{sl,s,y}}$) and 5.11 ($F_{\text{sl,k,y}}$) for the sail and keel respectively, in N. The integral is evaluated between $\theta = 0$ and $\theta = \frac{1}{2}\pi$ and multiplied by two, such that it is calculated for the semicircle in front of the structure. The parameters used are as described before.

$$F_{\text{sl,s,y}} = 2\int_0^{\frac{1}{2}\pi}(\gamma_{\text{sr}}\mu_{\text{sr}}h_{\text{sr}}(\theta)(\frac{1}{2}Dl_{\text{sr}}(\theta) + \frac{1}{3}l^2_{\text{sr}}(\theta))\frac{\theta}{2}\sin(\theta)\mathrm{d}\theta \tag{5.10}$$

$$F_{\text{sl,k,y}} = 2\int_0^{\frac{1}{2}\pi}(\gamma_{\text{kr}}\mu_{\text{kr}}h_{\text{kr}}(\theta)(\frac{1}{2}Dl_{\text{kr}}(\theta) + \frac{1}{3}l^2_{\text{kr}}(\theta)))\frac{\theta}{2}\sin(\theta)\mathrm{d}\theta \tag{5.11}$$

The notion of the direction of the force, implemented in Equations 5.10 and 5.11 through the addition of $\sin(\theta)$ to the integral, stems from the fact that the sliding force of the pile acts normal to the structure. This normal force can be expressed from a x- and y-component (where y is the direction of the ice drift). This is shown in Figure 5-3. The x-components of the force along the perimeter will balance each other out, such that only the y-component will influence the structure. Note that this is only true when structural motion restricted to the y-direction is considered.

As is discussed in Appendix A-3, it is debated whether or not the friction coefficient of ice on ice is velocity dependent. For this model, it is assumed that the friction coefficient is independent of velocity, so that it is also independent of θ.

It could be argued that in a dynamic crushing model as VANILLA, the static friction should be used when renewed contact between the structure and the rubble pile is formed. However, it is argued that at the time scale and forces involved in the structural motion in a crushing event, the static region is of negligible interest. Therefore, only the kinetic friction is considered here.

Internal failure mode

As will be shown in the next Section, the forces resulting from the rubble are smalle in magnitude. Combined with the knowledge that the active earth pressure is always much

smaller than the passive earth pressure, this renders the ective earth pressure negligible and the forces for this mode will be based on Equation 4.9 only.

Analogously to the sliding force, the forces from internal failure are only evaluated for the y-direction in Figure 5-3. This yields the forces for the sail ($F_{\text{in,s,y}}$) and keel ($F_{\text{in,k,y}}$) in N as given in Equations 5.12 and 5.13, with parameters as described in Chapter 4.

$$F_{\text{in,s,y}} = 2\int_0^{\frac{1}{2}\pi} (\frac{1}{2}\gamma_{\text{sr}} h_{\text{sr}}^2(\theta) K_{\text{p,s}} + 2c\sqrt{K_{\text{p,s}}})\frac{D}{2}\theta\sin(\theta)\mathrm{d}\theta \tag{5.12}$$

$$F_{\text{in,k,y}} = 2\int_0^{\frac{1}{2}\pi} (\frac{1}{2}\gamma_{\text{kr}} h_{\text{kr}}^2(\theta) K_{\text{p,k}} + 2c\sqrt{K_{\text{p,k}}})\frac{D}{2}\theta\sin(\theta)\mathrm{d}\theta \tag{5.13}$$

Note that for a vertical structure (90°), and for equal friction coefficients assumed for sail and keel, it follows from Equation 4.5 that $K_{\text{p,s}} = K_{\text{p,k}}$. This is used in the modelling.

With the above, using Equation 4.10, the rubble loads can be calculated. Because of the variation of h_{sr} and h_{kr}, for the most accurate calculation of the loads, the minimum should be evaluated for every $\Delta\theta$. This means that failure in the sliding and internal failure mode may happen simultaneously in different parts of the pile (for both the sail and the keel). From videos taken at the Norströmsgrund lighthouse, this behaviour can be seen to occur.

5-2 Verification

The verification of the functioning of the rubble model is done simultaneously with the extrusion model, as described in Section 6-3.

5-3 Variation over parameters

The rubble model makes use of a number of model parameters that are given as input. These are listed in Table A-1 in Appendix A, along with a background of these parameters. With the model parameters established, it is worthwhile looking at how sensitive the rubble loads are to a change in these parameters. This is done for the parameters that could be argued to differ from the values in Table A-1, such that the densities of seawater and ice do not have to be examined. The ice thickness and structure width are also assessed, as these vary depending on the case, such that sensitivity to these are of interest as well. The sensitivities are given in absolute terms, and as a portion of the ISO crushing force as given in Equation 2.1, to give a rough estimate of how the changes would impact the additional load due to rubble in a crushing event. In evaluating these sensitivities, the other model parameters are unchanged

from the values in Table A-1. Sensitivities to combinations of changes of these parameters are not considered. The parameters shown and discussed here, are the parameters to which a relatively large sensitivity is shown. The other parameters are shortly discussed at the end of this Section, with their respective graphs shown in Appendix A-4. There, a contour plot of D vs. h_{ice} can also be found.

Length ratios

The sensitivity of the length ratios, as shown in Figure 5-5, show that the rubble force has a negative dependency on ratio r_{ul} (Equation 5.1) and a positive dependency on ratio r_{fs} (Equation 5.2). The latter in particular shows a significant change over the range of input values considered.

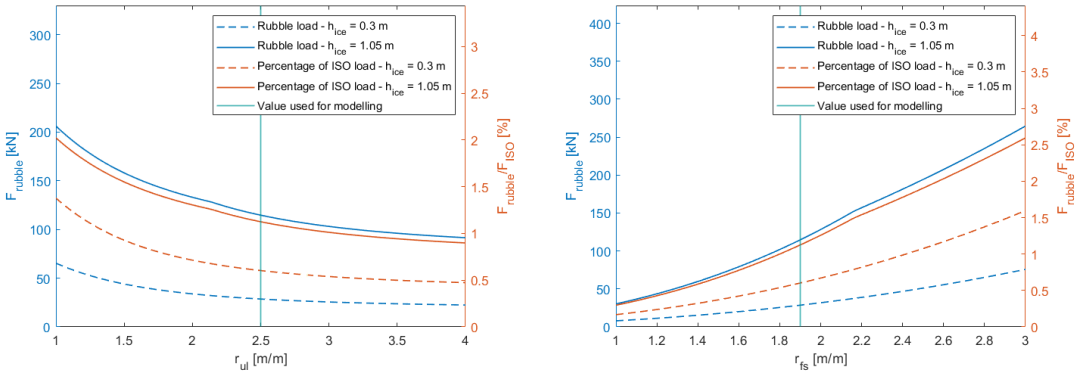

(a) (b)

Figure 5-5: Sensitivity of rubble force on input for length ratios (a) r_{ul} and (b) r_{fs}.

Friction coefficients

From Figure 5-6 it can be seen that for the set of standard parameters considered, the rubble forces are dominated by failure in the sliding mode, such that only the ice-ice friction coefficient μ_{ii} has a significant impact on the rubble force. For the thick ice, the transition to the internal failure mode being governing can be seen for $\mu_{\text{ii}} > 0.5$. As discussed in Appendix A-3, the magnitude of the ice-ice friction coefficient is debated in literature. When a more certain value is settled on, or of the sometimes claimed velocity dependency (see Appendix A-3) is proven, it would be advisable to include it in this model.

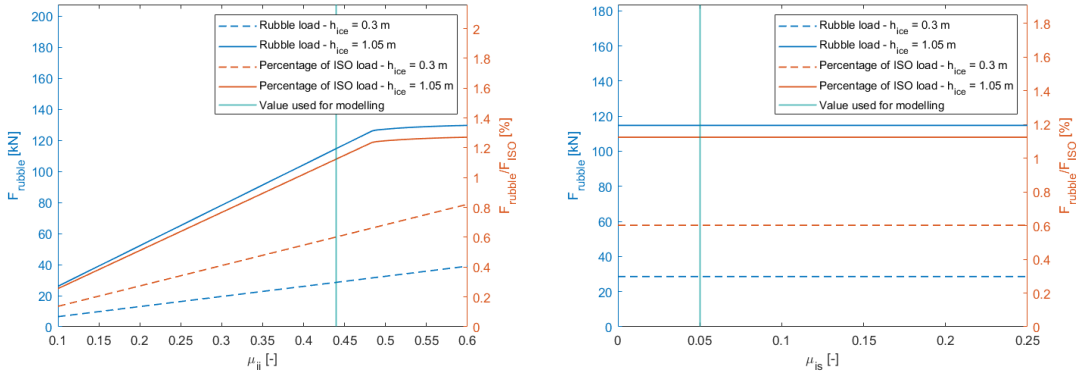

(a) (b)

Figure 5-6: Sensitivity of rubble force on input for friction coefficients for (a) ice-ice (μ_{ii}) and (b) ice-steel (μ_{is}).

Structure width

From Figure 5-7, the dependency of the rubble force on the structure width can be seen.

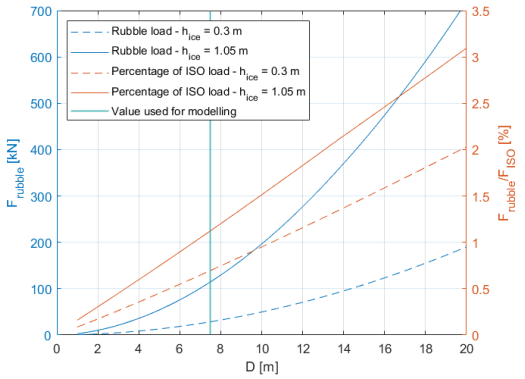

Figure 5-7: Sensitivity of rubble force on input for structure width D.

The graph shows that the rubble force increases rapidly with structure width, as one would expect when the surface area on which the rubble acts, as well as the area over which the ice is crushed (per unit of time, red striped area in Figure 5-4) is increased.

Ice thickness

As for the structure width, the rubble forces increase significantly for increasing ice thickness h_{ice}, as can be seen in Figure 5-8. Just as for the structure width, this is because the area of

ice crushed (per unit of time) increases with ice thickness.

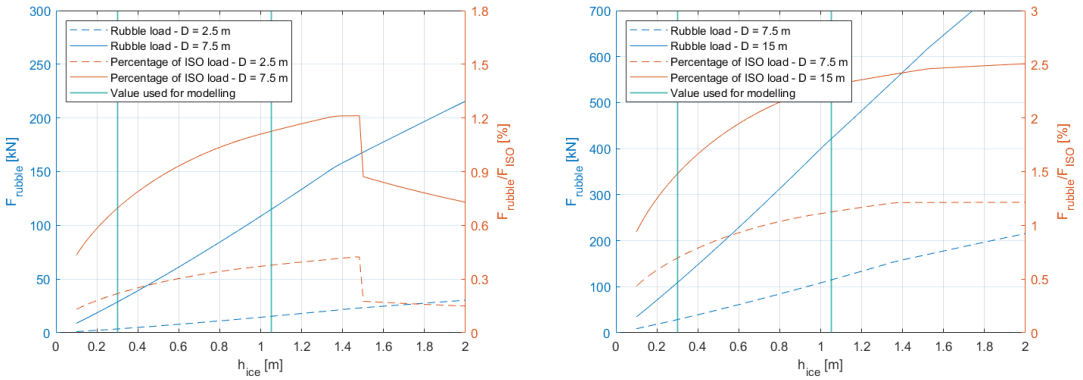

Figure 5-8: Sensitivity of rubble force on input for ice thickness h_{ice} for (a) $D = 2.5$ m and $D = 7.5$ m and (b) $D = 7.5$ m and $D = 15$ m.

Other parameters

For the remaining parameters, as shown in Appendix A-4, the following statements can be made:

- Porosities (η_{sr} and η_{kr}): Sensitivity of the rubble force on the porosities are limited, both for the sail and the keel. For the sail, a slight decrease in rubble force for increasing porosity is shown, while for the keel a slight increase in rubble force results.
- Internal friction angle (Φ): The internal friction angle does not impact the rubble force for the thin ice, while for the thick ice it has no impact up to 45°, after which the rubble loads decrease with internal friction angle.
- Cohesion (c): The rubble loads show little change for a change in cohesion, only slightly for thicker ice for $c < 2$ kPa.
- Pile angles (θ_{sr} and θ_{kr}): The rubble force shows a slight positive dependency on the sail angle and a slight negative dependency on the keel angle. For reasonable values of these angles, the rubble forces do not change significantly compared to the assumed values.
- Horizontal resolution (N_θ): The rubble force found does not change much when more than 10 segments along the perimeter of the structure are considered. Therefore, value of 10 could be used for N_θ in future computations instead of the 50 considered for the results in this report, which had already been partially run.

Overall, the magnitudes of the loads found from evaluating the sensitivities of the rubble loads

on these parameters remain small compared to the force given by the ISO-equation. Also, they show a limited sensitivity around the chosen parameters.

5-4 Validation

Here, the values that the rubble model predicts for certain measured crushing events are compared to the forces measured. This is done for model scale, with very thin ice, as well as full scale, with thick ice.

Thin ice - SHIVER

For the SHIVER campaign, as introduced in Chapter 2, video material analysed showed that the rubble behaves differently than on the scale of the Norströmsgrund lighthouse. Mainly due to a higher liquid content of the crushed material, the movements of the rubble were more intermittent. Nonetheless, it is interesting to compare the value found for the rubble force from the rubble model introduced here, to the mean loads given in Figure 2-7, to assess the magnitude of the force.

For $h_{\text{ice}} = 0.03$ m (mean ice thickness in the SHIVER campaign) and $D = 0.2$ m, the value found is $F_{\text{rub}} = 2.4$ N. This seems plausible for the amount of material that would be in a rubble pile at these dimensions. This would constitute about 0.2-0.5$\%$ of the mean force found in the experiments. As the rubble force was not individually measured, the value cannot be compared directly.

Thick ice - Norströmsgrund lighthouse

For the Norströmsgrund lighthouse, only limited data is available. One force signal available to the writer was the one given in Hilding et al., 2011 and shown in Figure 6-15, which is from the STRICE campaign. For this measurements signal, the ice had a thickness of 69 cm. Moreover, the lighthouse has a diameter of 7.52 m.

When inserting the values for the ice thickness and structure width into the rubble model, a force of $F_{\text{rub}} = 72$ kN is found. For a mean force of 2.5 MN, as follows from the signal in Figure 6-15, this would mean that the rubble forces constitute about 2.9$\%$ of the total load. Like for SHIVER, the rubble force was not separately measured during the STRICE campaign. Therefore, directly comparing the rubble loads is not possible, but 2.9$\%$ of the mean load stemming from the rubble pile seems plausible.

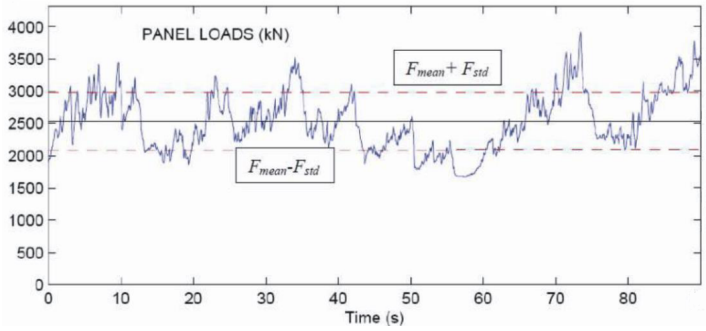

Figure 5-9: Load signal found at the Norströmsgrund lighthouse for a crushing event with $h_{\text{ice}} = 0.69$ m and $v_{\text{ice}} = 0.15$ m/s. From Hilding et al., 2011.

Very thick ice - Molikpaq

For a last comparison, the rubble loads have been calculated for a well known crushing event at the Molikpaq caisson-type offshore drilling platform in the Beaufort Sea, on the 12^{th} of April in 1986. The crushing event, as well as the structure and its ice load measurement setup, is extensively documented in R. Frederking and Sudom, 2006.

Of the different stages in the crushing event, here a look is taken at the situation encountered at 8:00. An overview of this situation is shown in Figure 5-10. Note that the long sides of the structure are 60 m long, with the shorter being 22 m. At 8:00, the rubble piles on top of the ice (the sails) were reported to have a height of up to 5 m at the southeast and eastern side.

It must be noted here that the dimension relation between the sail and the keel is not known for this particular structure and the relation obtained for the lighthouse is used for calculating the rubble loads. Inserting the values given above into the equations used for the rubble model, the rubble force is found to amount to $F_{\text{rub}} = 4.1$ MN. The measured total load on the structure was 118 MN, such that the rubble loads would amount to about 3.5$\%$ of the total loading, close to the 2.9$\%$ encountered at the lighthouse. Again, this value seems plausible.

Overall, it can be concluded that when compared to load measurements at both experimental and full scale, the rubble model as presented here produces rubble force values that could well be (close to) correct. The lower percentage of the mean load found for the thin ice (compared to the full scale cases) can possibly be explained by a lower friction coefficient due to the smoothness of the ice in the ice basin, as well as a higher moisture content. Moreover, the dimension relations found for the full scale situation may not be accurate for model scale setups. More specific rubble load measurements would be required for a better comparison.

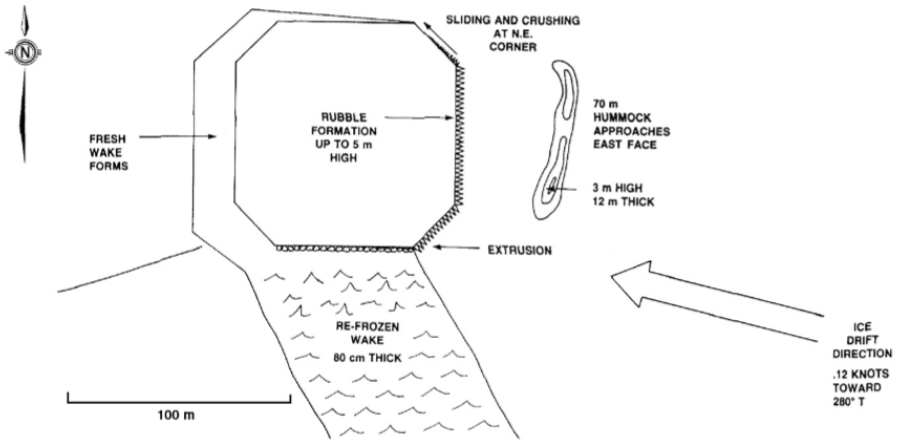

Figure 5-10: Sketch of the situation encountered at the Molikpaq on the 12^{th} of April 1986. From R. Frederking and Sudom, 2006.

5-5 Usage in VANILLA

Following from the values obtained in the previous Sections, the forces from rubble piles can be said to only make a relatively small contribution to the total ice loads on a structure. They also do not change with ice drift speed (based on the assumed friction coefficients). Therefore, the choice is made to not evaluate the rubble loads at every time step, but to pre-calculate the rubble loads based on the to be modelled geometries and ice conditions. The rubble loads are assumed present whenever there is contact between the ice and the structure. This is based on contact with one (or multiple) ice elements of the crushing model. Moreover, the rubble loads are only applied when the relative velocity is positive. That is, the velocity of the structure in the direction of the ice drift is smaller than the ice drift speed.

In the code, the equations of motion are then evaluated by *ssEOMs* including the rubble force, so that the relevant part of *ssEOMs* (regarding the ice loads) then looks as in Listing B.1 in Appendix B-2 (there including the extrusion force as well), in which lines 9, 12 and 15 make for inclusion of the rubble loads.

6

Extrusion model

The next extension made to the VANILLA code is that of extrusion. The addition is based on the theory in Chapter 3. Like in Chapter 5, the extrusion model as used is elaborated, followed by a dependency of the model on the input parameters and validation. A discussion of the way the model is used in VANILLA finishes the Chapter. It is important to note here that the extrusion model used is a physical model, whereas the crushing model that is VANILLA, is phenomenological. The strategy used for the adaptation of the Matlock and Kärnä models, as explained in Chapter 3, was deemed to overgeneralise, since the same values were used in all interaction scenarios. A physical model was preferred over this method.

6-1 Model description

The extrusion model as used, is based on the viscous theory in Chapter 3. The viscous flow solution was found in the extrusion tests of Chapter 3 to represent the high-pressure regions well. Next to that, it can be evaluated relatively efficiently when it comes to computation time. Therefore, the viscous flow solution is deemed a proper starting point for the evaluation of the extrusion force.

Equation 3.7 accurately describes the viscous flow between two parallel plates. However, as was seen in Section 3-5, the ice edge is in reality not parallel, such that the description in Equation 3.7 has to be adapted. Since the viscous solution was based on lubrication theory, the formula can be adapted to non-parallel surfaces. By following the derivation of Equation 3.7, but now using that $h = h(x)$, the formula in Equations 6.1 and 6.2 can be found. The derivation is given in Appendix A. Figure 6-1 shows a schematic of the geometry that the formulas relate to.

$$p_{\text{y,top}}(x) = [\frac{v_{\text{rel}}(N+2)l_{\text{top}}^{N+2}}{2Kh_{\text{top}}^{N+2}}]^{1/N} N(x^{-1/N} - l_{top}^{-1/N}) + p_{\text{0,top}} \tag{6.1}$$

$$p_{\text{y,bot}}(x) = [\frac{v_{\text{rel}}(N+2)l_{\text{bot}}^{N+2}}{2Kh_{\text{bot}}^{N+2}}]^{1/N} N(x^{-1/N} - l_{\text{bot}}^{-1/N}) + p_{\text{0,bot}} \tag{6.2}$$

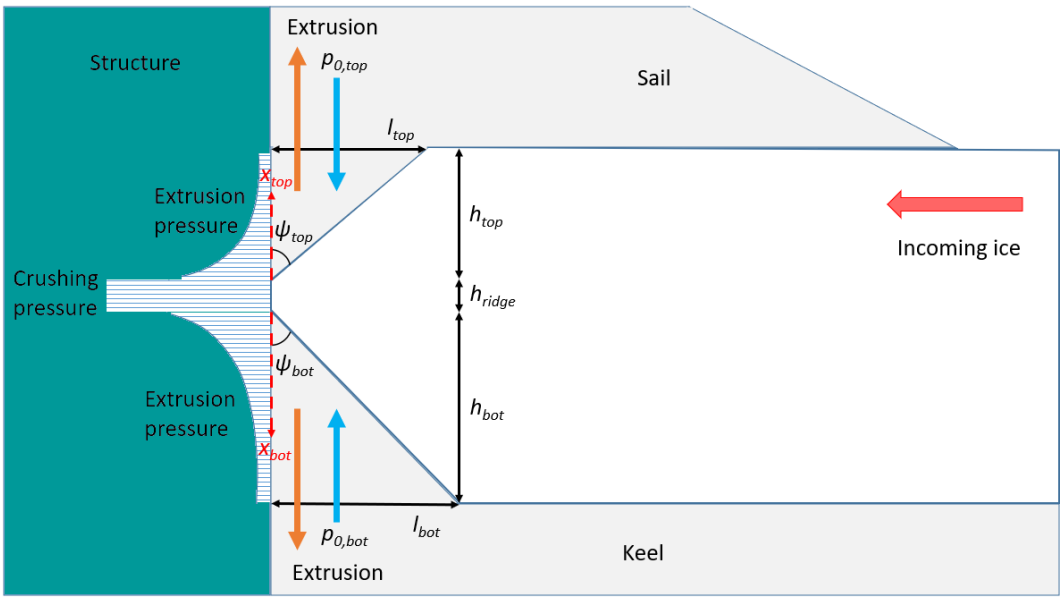

Figure 6-1: Schematic of the geometry used in the extrusion model.

In Formulas 6.1 and 6.2, v_{rel} is the relative velocity between the structure and the ice in m/s, as given in Equation 6.3, where the velocities are defined positive in the ice drift direction.

$$v_{\text{rel}} = v_{\text{ice}} - v_{\text{struc}} \tag{6.3}$$

Channel dimensions

The parameter h_{ridge} is taken as the 9 mm reported in Määttänen et al., 2011. Reduction of increase of this value would reduce or increase the length of the extrusion channel at the exit. Since the main loads from the extrusion originate in the area close the pressure ridge, the value for h_{ridge} is not of great importance. The dimensions of the extrusion channels are assumed to follow from the amount of rubble in the piles, such that the ratio in Equation 5.1 is also used for the ratio of $h_{\text{bot}}/h_{\text{top}}$. Without conclusive literature on the shape and angle of the extrusion channel, the angles of the channels (ψ_{top} and ψ_{bot}) are assumed to be the shear

failure angle of sea ice as reported by Rist and Murrell, 1994, with a value of 40°. With equal angles, the ratio of $l_{\text{bot}}/l_{\text{top}}$ is then also equal to r_{ks}, as given in Equation 5.1. Equations 6.4 through 6.7 then give the dimensions of the extrusion channel.

$$h_{\text{top}} = \frac{h_{\text{ice}} - h_{\text{ridge}}}{1 + r_{\text{ks}}} \tag{6.4}$$

$$h_{\text{bot}} = \frac{h_{\text{ice}} - h_{\text{ridge}}}{1 + r_{\text{ks}}}_{\text{ks}} \tag{6.5}$$

$$l_{\text{top}} = h_{\text{top}} \tan(\psi_{\text{top}}) \tag{6.6}$$

$$l_{\text{bot}} = h_{\text{bot}} \tan(\psi_{\text{bot}}) \tag{6.7}$$

Overpressure

The overpressures $p_{0,\text{top}}$ and $p_{0,\text{bot}}$ are the weight and buoyancy from the rubble in the sail and keel respectively, since the extruded material has to be pushed up/down against these. The added friction from moving the rubble in the sail and keel is at the moment not taken into account. They are defined as in Equations 6.8 and 6.9.

$$p_{0,\text{top}} = \gamma_{\text{sr}} \frac{h_{\text{sr}} + (l_{\text{sr}} - l_{\text{top}}) \tan(\theta_{\text{sr}})}{2} \tag{6.8}$$

$$p_{0,\text{bot}} = \gamma_{\text{kr}} \frac{h_{\text{kr}} + (l_{\text{kr}} - l_{\text{bot}}) \tan(\theta_{\text{kr}})}{2} \tag{6.9}$$

Flow parameters K and N

Nonlinear viscous flow parameter N in Equation 3.7 is taken as 1.67, as explained in Section 3-5. The value for K is not given in the paper. Therefore, it had to be reconstructed from the results of the extrusion tests in Singh et al., 1995. The paper includes a Figure where the mean pressure that is measured, is plotted. It is shown in Figure 6-2. By using Equation 3.9, using the parameters used for the extrusion tests and varying the value for K, the correct value for K can be found.

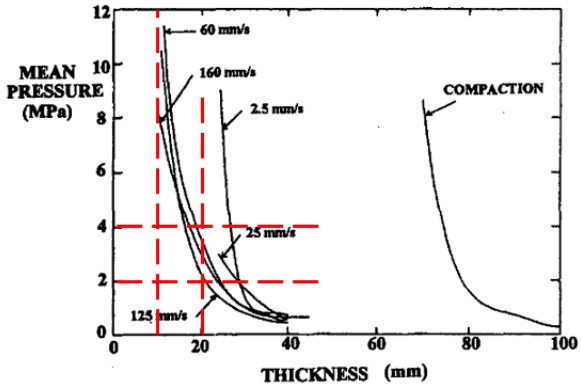

Figure 6-2: Plot of the mean pressures measured by Singh et al., 1995, from their paper.

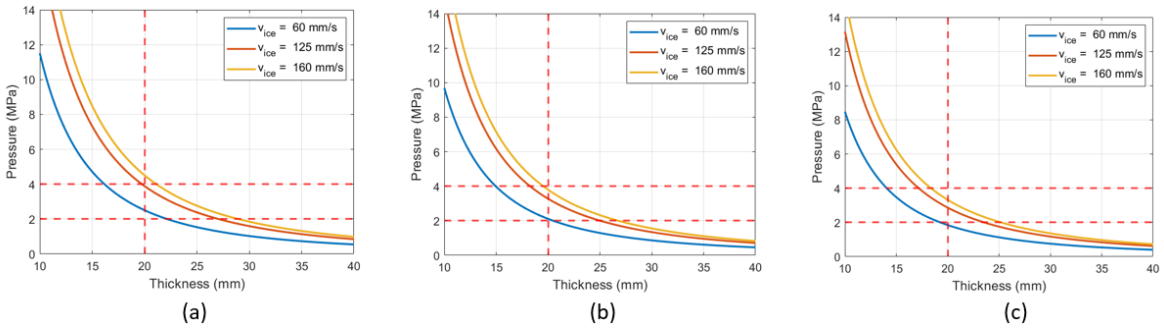

Figure 6-3: Plots used to reconstruct Figure 6-2, with (a) $K = 0.6^{*}10^{-7}$, (b) $K = 0.8^{*}10^{-7}$ and (c) $K = 1.0^{*}10^{-7}$.

Looking at 6-3, it can be seen that $K = 0.8^{*}10^{-7}$ yields good agreement with Figure 6-2. This is the value that is used in subsequent modelling. Note that based on the formulas (used in Figure 6-3), higher indentation velocities yield higher pressures, where Figure 6-2 shows this is not necessarily the case. This was discussed by the authors attributed to secondary effects due to compaction.

Pressure limit

From Equations 6.1 and 6.2, it follows that for $x \to 0$, the pressures go to infinity. Therefore, a limit has to be set for what is considered a credible pressure for the extrusion, and above which pressures are assumed to result from intact ice. For this, the transition pressure found by Gagnon et al., 2020 mentioned earlier, is used, such that in the model $p_{\text{lim}} = 15$ MPa.

Forces along perimeter

Just as for the rubble forces discussed in Chapter 5, the forces from the extrusion act normal on the structure, as illustrated in Figure 5-3. For that reason, an additional factor of $\sin(\theta)$ is added to the calculation of the forces from the extrusion. Then the total force from the extrusion is modelled as given in Equation 6.10 (again, it should be noted that these Equations only apply when structural motion is restricted to the y-direction.).

$$F_{\text{ext,tot}} = 2\int_0^{\frac{1}{2}\pi}\int_0^{h_{\text{top}}} \frac{\pi D}{4}\sin(\theta)p_{\text{y,top}}(\theta,x)\mathrm{d}\theta\mathrm{d}x + 2\int_0^{\frac{1}{2}\pi}\int_0^{h_{\text{bot}}} \frac{\pi D}{4}\sin(\theta)p_{\text{y,bot}}(\theta,x)\mathrm{d}\theta\mathrm{d}x \tag{6.10}$$

The dependency of the pressures on θ stems from the velocity dependency. The velocity of the approaching ice at a given point along the perimeter can be divided in a normal and

tangential velocity, analogously to the forces as discussed above. For the extrusion, the normal velocity is used. Thus, the velocity used in the extrusion calculations is the one given in Equation 6.11.

$$v_{\text{N}} = v_{rel} \sin(\theta) \tag{6.11}$$

To achieve fast evaluation of the integral, as well as being able to cap the pressure at the maximum described above, the perimeter and the height of the ice edge are divided into equally spaced intervals, such that $\Delta h_{\text{top}} = \frac{h_{\text{top}}}{100/(1+r_{\text{ks}})} = \frac{h_{\text{top}}}{29}$, $\Delta h_{\text{bot}} = \frac{h_{\text{bot}}}{71}$ and $\Delta\theta = \frac{90°}{50}$, which were found to give a good balance between computation time and accuracy. Then, the integral above can be approximated through the summation in Equation 6.12.

$$F_{\text{ext,tot}} = \sum_{i=1}^{50}\sum_{j=1}^{29} \Delta h_{top} \frac{\Delta\theta}{360} \pi D \sin(\theta_i) p_{\text{y,top,j}} + \sum_{i=1}^{50}\sum_{j=1}^{71} \Delta h_{\text{bot}} \frac{\Delta\theta}{360} \pi D \sin(\theta_i) p_{\text{y,bot,j}} \tag{6.12}$$

6-2 Preprocessor

Next to using the rubble and extrusion models for inclusion of their respective loads in the ice forcing, the models are also used for a correction in the calculation of the input parameters in the preprocessor for the crushing model in VANILLA, as discussed in Chapter 2-4. To do this, the factors used in the preprocessor, as shown in Figure 2-6 are altered. It must be noted that the exact factors used cannot be stated here, since these are confidential.

Firstly, it is noted that the parameters in the model are based on ratios between μ_{CBR}, which is the mean of the continuous brittle crushing load, and F_t, μ_1 and μ_2, as indicated in Figure 6-4, as well as σ_{CBR}. In the standard model, the total mean of the continuous brittle crushing load can be ascribed to the crushing of intact ice ($\mu_{\text{CBR}} = \mu_{\text{int,CBR}}$). For the altered preprocessor, $\mu_{\text{tot,CBR}}$ is calculated as the result of $\mu_{\text{int,CBR}}$ from pure crushing, $\mu_{\text{ext,CBR}}$ (at $v_{\text{ice}} = 0.15$ m/s) from the extrusion force and $\mu_{\text{rub,CBR}}$ from the rubble force. This is depicted in Figure 6-4 and given in Equation 6.13.

$$\mu_{\text{tot,CBR}} = \mu_{\text{int,CBR}} + \mu_{\text{ext,CBR}} + \mu_{\text{rub,CBR}} \tag{6.13}$$

To correct for the change in magnitude of $\mu_{\text{int,CBR}}$, adjustments have been made to the factors relating F_{t}, σ_{CBR}, μ_1 and μ_2 to $\mu_{\text{int,CBR}}$.

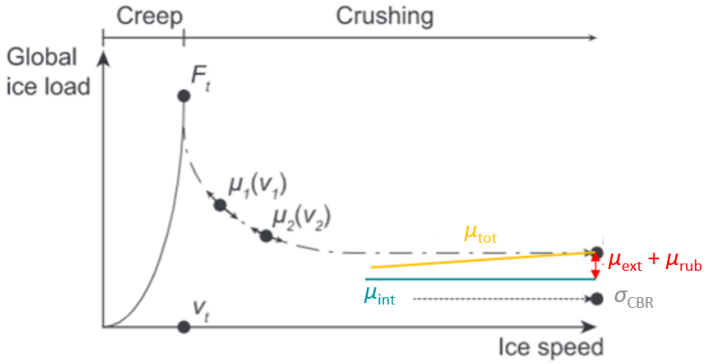

Figure 6-4: Alternative figure for the preprocessing for the crushing model in VANILLA.

The ratio for σ_{CBR} was determined from measurements at the Norströmsgrund lighthouse and must therefore be preserved in the adjusted model. Since the extrusion and rubble loads are (nearly) constant at $v_{\text{ice}} = 0.15$ m/s, the load variation has to come from the crushing of the intact ice. Therefore, the old factor used for relating σ_{CBR} to $\mu_{\text{int,CBR}}$ is multiplied by an adjustment factor, as given in Equation 6.14.

For the other factors (ratios of F_{t}, μ_1 and μ_2 to $\mu_{\text{int,CBR}}$), the choice is made to have them remain equal with respect to the total mean continuous brittle crushing load ($\mu_{\text{tot,CBR}}$). Since these were based on measurements at model scale, for which the portion of the extrusion and rubble loads in the total forcing could be different than for full scale, it could well be that the factors should change when calculating full scale scenarios. However, when adopting different values for the ratios (of F_{t}, μ_1 and μ_2 to $\mu_{\text{int,CBR}}$)) based on the $\mu_{\text{int,CBR}}$, the magnitude of the forcing at low indentation speeds would change dramatically. This would make it difficult to draw conclusions on the effect of adding extrusion and rubble in the structure dynamics in the adjusted model by comparing it with the Standard VANILLA model. Therefore, these ratios are also adjusted by factors as given in Equation 6.14.

$$
\begin{aligned}
r_{\text{adj,CBR}} &= \frac{F_{\text{ISO}}/f_{\mu,\text{old}}}{F_{\text{ISO}}/f_{\mu,\text{old}} - F_{\text{ext,CBR}} - F_{\text{rub,CBR}}} \\
r_{\text{adj,vt}} &= \frac{F_{\text{ISO}}/f_{\mu,\text{old}} - F_{\text{ext,vt}}/C - F_{\text{rub,vt}}/C}{F_{\text{ISO}}/f_{\mu,\text{old}} - F_{\text{ext,CBR}} - F_{\text{rub,CBR}}} \\
r_{\text{adj,2vt}} &= \frac{F_{\text{ISO}}/f_{\mu,\text{old}} - F_{\text{ext,2vt}}/C' - F_{\text{rub,2vt}}/C'}{F_{\text{ISO}}/f_{\mu,\text{old}} - F_{\text{ext,CBR}} - F_{\text{rub,CBR}}} \\
r_{\text{adj,3vt}} &= \frac{F_{\text{ISO}}/f_{\mu,\text{old}} - F_{\text{ext,3vt}}/C'' - F_{\text{rub,3vt}}/C''}{F_{\text{ISO}}/f_{\mu,\text{old}} - F_{\text{ext,CBR}} - F_{\text{rub,CBR}}}
\end{aligned}
\tag{6.14}
$$

In Equation 6.14, F_{ISO} is the ISO load as given in Equation 2.1 (in MN), while $f_{\mu,\text{old}}$ is a (dimensionless) scaling factor that was found earlier (see next paragraph). F_{ext} and F_{rub} are

the extrusion and rubble loads in MN respectively, with vt indicating the transition speed from creep to crushing and $2vt$ and $3vt$ being the twice and three times the transition speed. Lastly, C' and C'' are the (classified, dimensionless) factors found for the ratios of μ_1 and μ_2 with μ_{CBR}.

As for the old preprocessor, a factor f_μ was to be found to define $\mu_{\text{tot,CBR}}$, through the relation $\mu_{\text{tot,CBR}} = F_{\text{G}}/f_\mu$. F_{G} is defined as the ISO load as was previously given in Equation 2.1. f_μ is then defined such that in a crushing event of 90 m at 0.15 m/s (600 seconds), the exceedance probability is 0.5. This corresponds to an exceedance probability of $0.54{\cdot}10^{-5}$ for a single crushing event to have a higher load than F_{G}.

To obtain these conditions, the model has been run for a total of 100.000 events (which previously showed to be sufficient). The load peaks are then extracted from the signal and binned. The data is found to have a beta-distribution. After normalising the data by the mean and subtracting the mean, the data can be transformed to be within the domain [0,1], such that the beta-distribution parameters can be found.

With these parameters, the data can be transformed back to the desired interval, which in this case is between the (normalised) minimum of the data and the maximum load allowed in VANILLA, such that in this case the domain becomes $[\min(\frac{\text{peaks}}{\mu_{\text{peaks}}}),(\text{C}{\cdot}\text{r}_{\text{adj,vt}}\text{-1})]$, where C is the (classified) ratio for F_{t} and μ_{CBR} that was found for the Standard VANILLA model. Integrating the PDF (probability density function) then gives the CDF (cumulative distribution function), where 1 - CDF gives the exceedance probability, which then gives a beta-fit. The intersect with the probability of $0.54{\cdot}10^{-5}$ then gives the new f_μ we were after.

It is important to note that f_μ now is no longer only dependent on the structure diameter, but also on ice thickness, through the dependency of the extrusion force on it. This means that obtaining a simple equation for f_μ is no longer possible and the analysis for f_μ has to be run for every ice thickness (and structure diameter).

6-3 Verification

For the two ice conditions of $h_{\text{ice}} = 30$ cm and $C_{\text{R}} = 0.86$ MPa, and $h_{\text{ice}} = 105$ cm and $C_{\text{R}} = 1.34$ MPa, the process described in Section 6-2 was performed. The VANILLA model was designed such that for 6 runs, 3 have to meet the ISO load from Equation 2.1. For the updated model, these 6 runs are shown in Figures 6-5 and 6-6. As can be seen, there is exceedance for 3/6 runs for both ice conditions, which indicates a good agreement with the requirements set for the model.

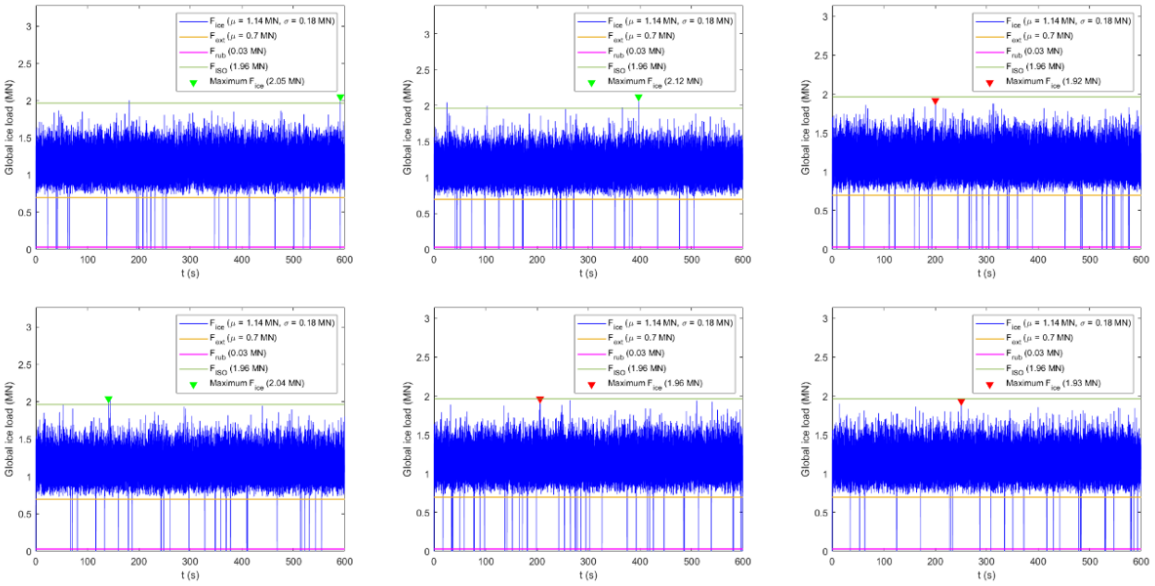

Figure 6-5: Overview of 6 runs to test for exceedance probability of 0.5 of ISO load, for $h_{\text{ice}} = 30$ cm and $C_{\text{R}} = 0.84$ MPa. Green arrows indicate exceedance, red a lower maximum.

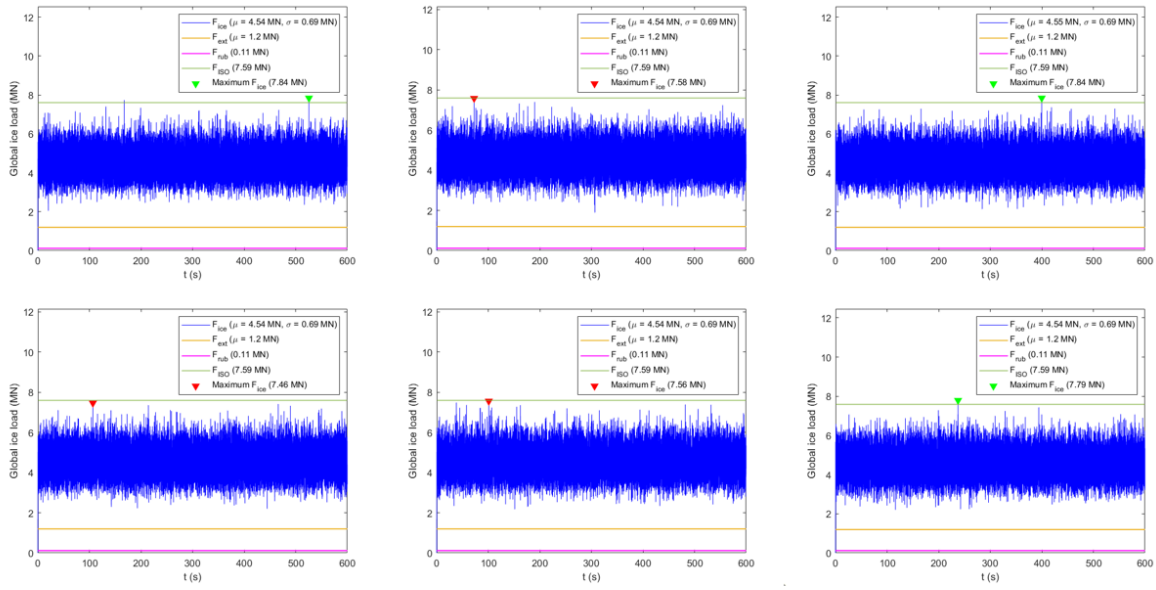

Figure 6-6: Overview of 6 runs to test for exceedance probability of 0.5 of ISO load, for $h_{\text{ice}} = 105$ cm and $C_{\text{R}} = 1.34$ MPa. Green arrows indicate exceedance, red a lower maximum.

One thing that can be seen from Figure 6-5, is that the load drops to zero whenever the total

ice force gets to the level of $F_{\text{ext}} + F_{\text{rub}}$. This happens because for this case the extrusion force is a large portion of the total load. Combined with the fact that we set the standard deviation of the ice force to remain equal, but coming from the intact ice force ($\sigma_{\text{CBR}} = r_{\text{adj,CBR}} \cdot \mu_{\text{int,CBR}}$), this means that sometimes the intact ice force has to drop to 0. The model is set up in such a way that this can only happen when no ice element is in contact. Since the extrusion and rubble force are set to be applied only when the structure is in contact with the ice, means that the total force drops to zero. This is a flaw and should be corrected in later development, but as can be seen in later results this is not of (noticeable) effect to the dynamics, as these drops are only very short-lived. Therefore, this is accepted for now. One solution could be to always apply the rubble and extrusion loads (bypass the *if* statements in the code) above a certain indentation speed, that is well above the start of the CBR regime but below the indentation speed at which this anomalous behaviour starts occurring.

An indication of good functioning of the model is agreement of mean and standard deviation of the ice load at $v_{\text{ice}} = 0.15$ m/s between the Standard and Adjusted VANILLA. To check this, runs were performed with both models for a rigid structure, of which the results can be seen in Figure 6-7. For the thin ice in Figure 6-7(a), the difference in the mean is lower than 1%, with about 5% deviation for the standard deviation, such that the load signals are nearly identical. Although for the thicker ice in Figure 6-7(b), the difference in the mean is larger at about 4% and about 6% deviation for the standard deviation, this can still be regarded as good agreement between the Standard and Adjusted VANILLA. These slight differences could be caused by differences in rounding in the preprocessor, such as for the number of ice features considered. The fact that the difference is slightly larger for the thicker ice, could be because the extrusion and rubble forces contribute less to the total load than for the thin ice. Then, since the model parameters for the intact ice are based on $\mu_{\text{int,CBR}}$, which is now relatively larger, the difference in mean and standard deviation are more pronounced.

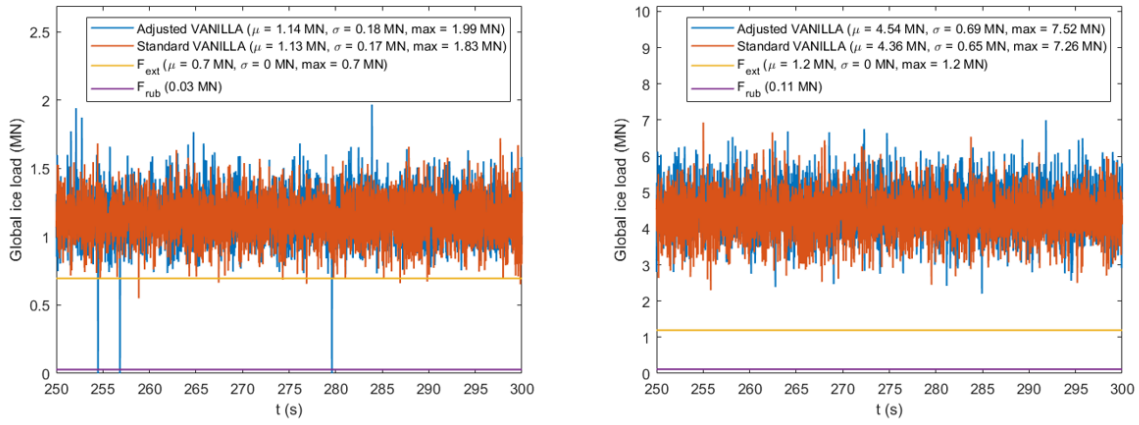

(a) (b)

Figure 6-7: Ice force for (a) $h_{\text{ice}} = 30$ cm and $C_{\text{R}} = 0.84$ MPa and (b) $h_{\text{ice}} = 105$ cm and $C_{\text{R}} = 1.34$ MPa, showing good agreement.

Also, it must be verified that the rubble and extrusion force only are applied when the ice is in contact with the structure, as well as having a positive relative velocity (between ice and structure). To that extent, Figure 6-8 serves as a proof that this requirement is met. It can be seen that the extrusion load peaks for high relative velocity and that the load goes to 0 whenever the relative velocity falls below 0 m/s.

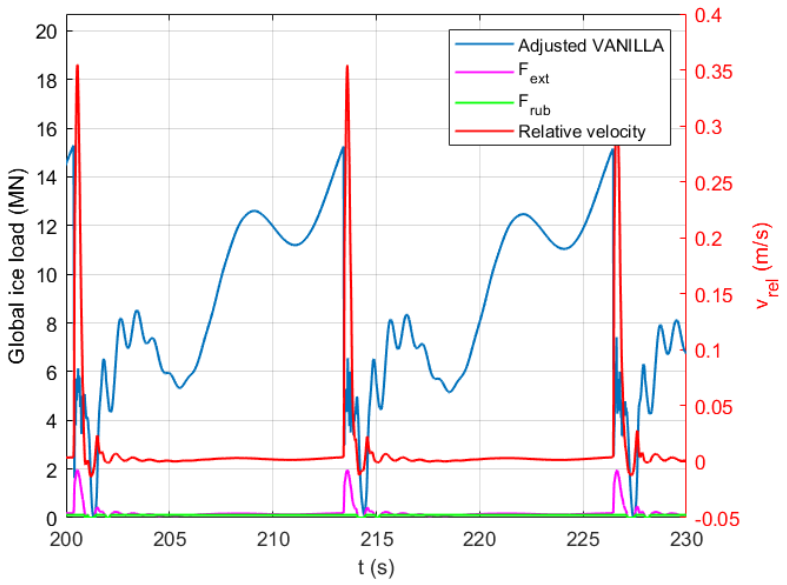

Figure 6-8: Ice force and relative velocity, for $v_{\text{ice}} = 0.15$ m/s, $h_{\text{ice}} = 105$ cm and $C_{\text{R}} = 1.34$ MPa.

With the above tests successfully passed, it is concluded that the model acts as expected and as required, such that the model can now be run for comparison with the Standard VANILLA model.

6-4 Usage in VANILLA

The loads from the extrusion force can reach values that are considerably larger than those of the rubble force. Moreover, they vary significantly for varying relative velocity. This means that unlike the rubble forces, the extrusion loads have to be evaluated at every time step in the interaction. Again, this is only done when the structure is in contact with the ice, that is one of the ice elements of the crushing model, and when the relative velocity between the structure and the ice is positive. This is evaluated in the same manner as for the rubble loads. The code used for evaluating the ice loads in VANILLA is then expanded to include the extrusion loads and looks as in Listing B.1 in Appendix B.

6-5 Variation over parameters

The model parameters used in the extrusion model are listed in Table A-2, given in Appendix A-3. Just like for the rubble parameters, here the sensitivity of the extrusion loads to a change in the parameters given in Table A-2 is assessed. This is done for all parameters except the structure angle, as variation in this value is known to be very limited for offshore wind turbines and VANILLA is designed for evaluation of ice loads on vertical structures. Not listed as fixed parameters in Table A-2, but inputs to the model and definitively of interest when sensitivity is concerned, are the ice thickness and indentation velocity. These are also assessed. As the extrusion force depends heavily on the relative velocity between the ice and the structure, the sensitivities are shown for $v_{\text{rel}} = 0.05$ m/s and $v_{\text{rel}} = 0.5$ m/s. As for the rubble forces, the choice is made to only show here the graphs for the parameters on which the extrusion force shows to have a large dependency. The other parameters are shortly discussed at the end of this Section, their respective graphs can be found in Appendix A-5, along with contour plots of D, h_{ice} and v_{rel}. The latter can be examined for sensitivity in input combinations.

Nonlinear viscous flow coefficient

Figure 6-9 show the dependency of the extrusion force on the nonlinear viscous flow coefficient K. Note that in this figure, a log-log plot is used. This shows that the extrusion forces found are majorly impacted by the value used for K, with a power law dependency showing around the value of $K = 0.8 \cdot 10^{-7}$ used in subsequent modelling. This makes carefully choosing a value for K essential.

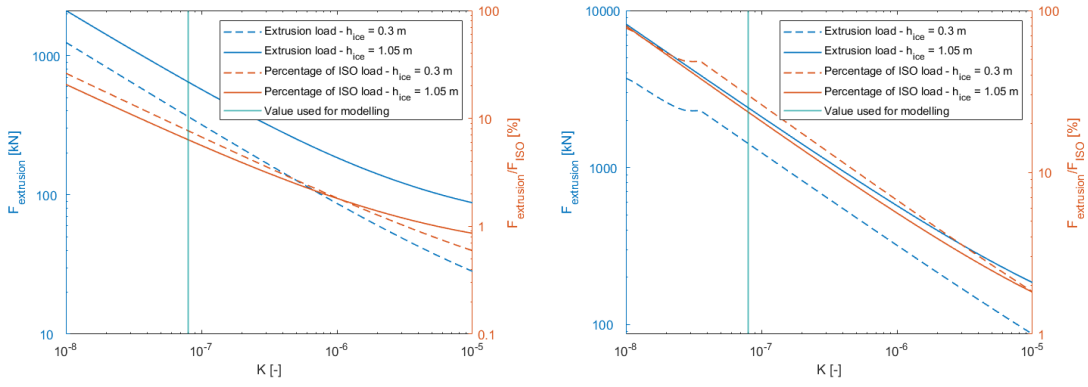

Figure 6-9: Sensitivity of extrusion force on input for the nonlinear viscous flow coefficient K for (a) $v_{\text{rel}} = 0.05$ m/s and (b) $v_{\text{rel}} = 0.5$ m/s.

Nonlinear viscous flow power coefficient

Similarly to K, Figure 6-10 shows that the magnitude of the extrusion force is heavily dependent on the value used for the nonlinear viscous flow power coefficient N, especially around the value of $N = 1.67$ used in the modelling. Note here that a value of $N = 1$ corresponds to a Newtonian fluid, with increasing N indicating increasing shear-thinning behaviour. Careful selection of the nonlinear viscous flow power coefficient parameter is shown by the graphs to be of great importance.

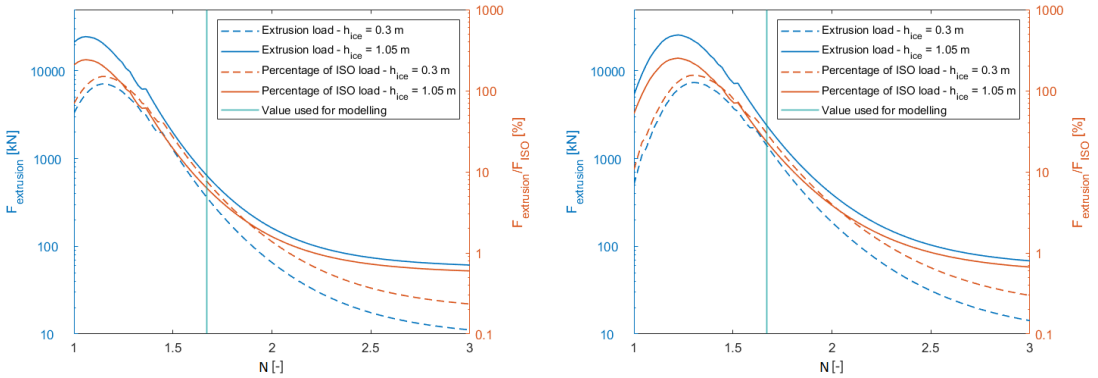

Figure 6-10: Sensitivity of extrusion force on input for the nonlinear viscous flow power coefficient N for (a) $v_{\text{rel}} = 0.05$ m/s and (b) $v_{\text{rel}} = 0.5$ m/s.

Ice edge angle

For a narrowing extrusion channel, it can be expected that it becomes more difficult for the material to be extruded. This also emerges from the equations used, as shown in Figure 6-11. An increasing ice edge angle Ψ shows to decrease the extrusion force significantly. The lack of information available on ice edge angles during crushing therefore may have a significant impact on the accuracy of the model.

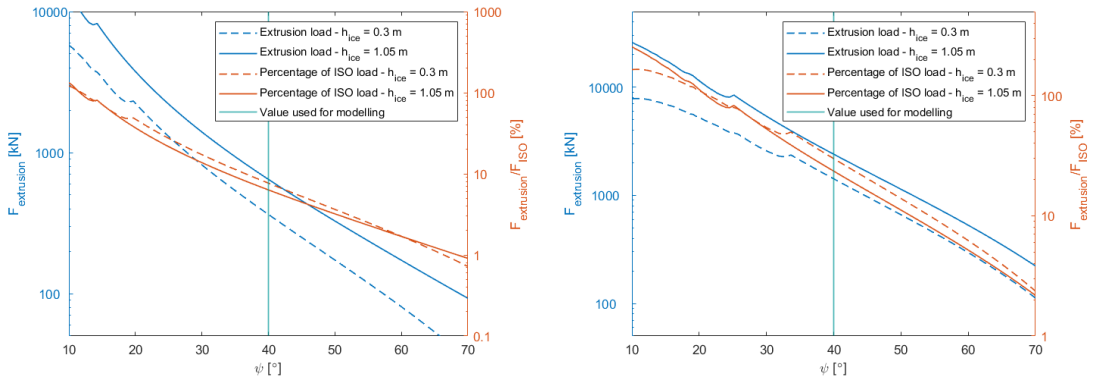

(a) (b)

Figure 6-11: Sensitivity of extrusion force on input for the ice edge angle ψ for (a) $v_{\text{rel}} = 0.05$ m/s and (b) $v_{\text{rel}} = 0.5$ m/s.

Ice thickness

The extrusion force has a positive dependency on the ice thickness, as one would expect. For very thin ice ($h_{\text{ice}} < 0.1$ m) the gradient is larger than for thicker ice. Interestingly, the extrusion force as found here shows to increase less with ice thickness than the ISO force from Equation 2.1.

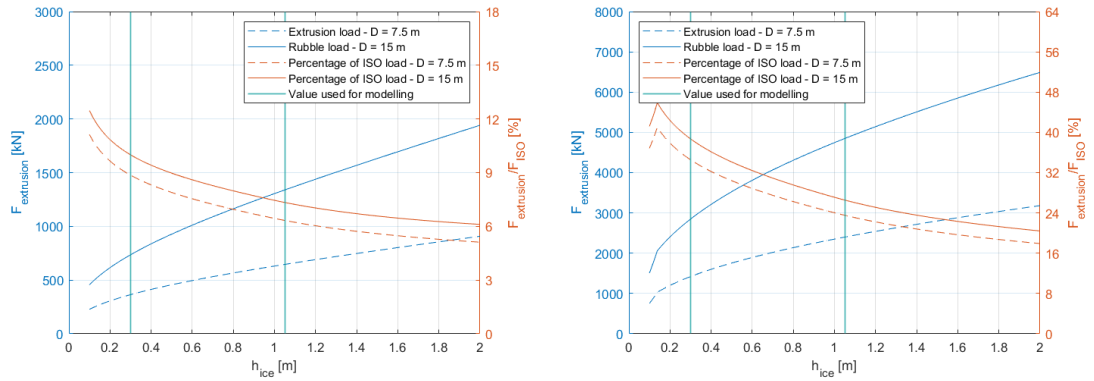

(a) (b)

Figure 6-12: Sensitivity of extrusion force on input for the ice thickness h_{ice} for (a) $v_{\text{rel}} = 0.05$ m/s and (b) $v_{\text{rel}} = 0.5$ m/s.

Indentation velocity

In Figure 6-13 the sensitivity of the extrusion forces on the indentation velocity are shown, both for the standard vertical resolution of $N_z = 100$ in (a) and $N_z = 1000$ in (b). The graphs shows a positive dependency of the extrusion extrusion force on relative velocity, with a decreasing gradient. This follows from Formulas 6.1 and 6.2, which, for the viscous flow power coefficient N of 1.6, show that $p \propto v_{\text{rel}}^{3/5}$.

Figure 6-13(a) shows a force jump in the extrusion force for the thin ice at $v_{rel} = 1.2$ m/s, which is incorrect. This was found to be the resultant of the interplay between the pressure limit and the vertical resolution. When the number of vertical segments considered is increased to $N_z = 1000$ (from the standard $N_z = 100$), the jump disappears. This indicates that for future use, when computational time allows, the value for N_z should be increased to 1000 (or higher). However, the jump is not visible for the thicker ice, limited in magnitude and only appears for very high relative velocities. Therefore, for the results shown in Chapter 7 this is not of much concern.

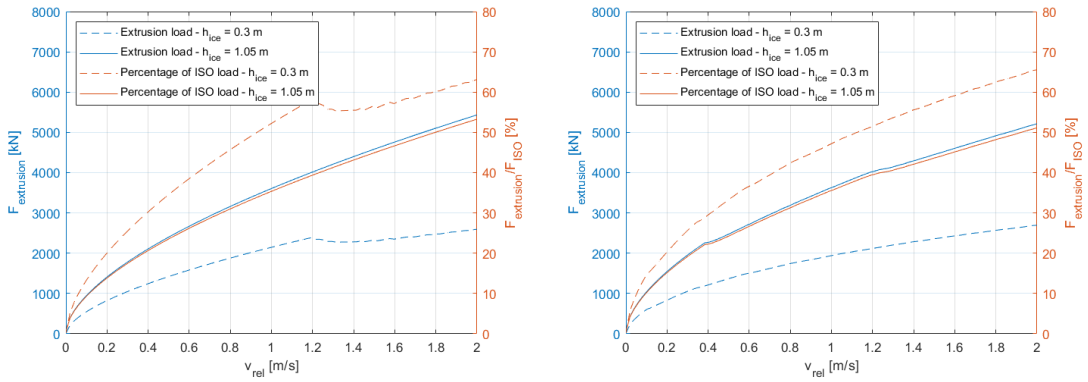

(a) (b)

Figure 6-13: Sensitivity of extrusion force on input for the indentation velocity v_{rel} for (a) $N_z = 100$ and (b) $N_z = 1000$.

Other parameters

For the parameters not yet discussed, of which the graphs are shown in Appendix A-5, the following statements can be made:

- Vertical resolution (N_z): For the number of segments used over the vertical it can be said that the extrusion load has a positive dependency on number of segments used, with a decreasing gradient. Within the broader accuracy of the model, the value of $N_z = 100$ used for evaluating the results is acceptable, but for future use a value of 1000 would be advisable, if computational times allow.

- Horizontal resolution (N_θ): Similarly to to the rubble forces, the extrusion force found does not change noticeably for $N_\theta > 10$, which can be taken for future use instead of the value of $N_\theta = 50$ used for computation of the results in this report.
- Pressure ridge height (t_r): Increasing the pressure ridge height decreases the extrusion channel length at the exit, not close to the pressure ridge itself. Since the majority of the forcing originates in the area close to the pressure ridge, the pressure ridge height shows to be of negligible impact on the values found for the extrusion force (that is, as long as $t_\mathsf{r} \ll h_\mathsf{ice}$), as would be expected. For very thin ice, the value of t_r should be chosen with care.
- Pressure limit (p_lim): Evaluating the sensitivity of the extrusion force on the force limit p_lim shows that for the standard parameters, the force limit has no influence on the forces found. For the relative velocities (v_rel) considered, the pressure of 15 MPa is not attained. Only when a relative velocity of 1 m/s (and $N_\mathsf{z} = 10000$) is considered, p_lim starts to have an influence, with a positive dependency, but with a limited gradient.
- Structure width (D): The extrusion force has a positive linear dependency on the structure width. This is as expected from equations 6.10 and 6.12

6-6 Validation

Like for the rubble forces in Chapter 5, the validity of the extrusion forces as found by the extrusion model is assessed here. This is done for the same cases as for the rubble forces.

Thin ice - SHIVER

For the SHIVER campaign, one of the measurement signals is taken (Case ID: 629, which is for an offshore wind turbine including wind forcing with $h_\mathsf{ice} = 32.5$ mm and $v_\mathsf{ice} = 0.1$ m/s). Based on the measured relative velocities, the corresponding extrusion loads were computed. The result is shown in Figure 6-14(a), with a graph of the extrusion pressure directly in front of the structure ($\theta = 90°$) in Figure 6-14(b).

It can be seen that the extrusion force greatly exceeds the measured total force, which means that there is poor correspondence between the loads found by the extrusion model and the real extrusion loads at model scale.

The shape of the extrusion pressure corresponds to what is expected from the model, although the region of high extrusion pressure seems to run until too close to the upper and lower ice edge. A faster decrease would be expected when comparing with the pressure map shown in Figure 3-9(b).

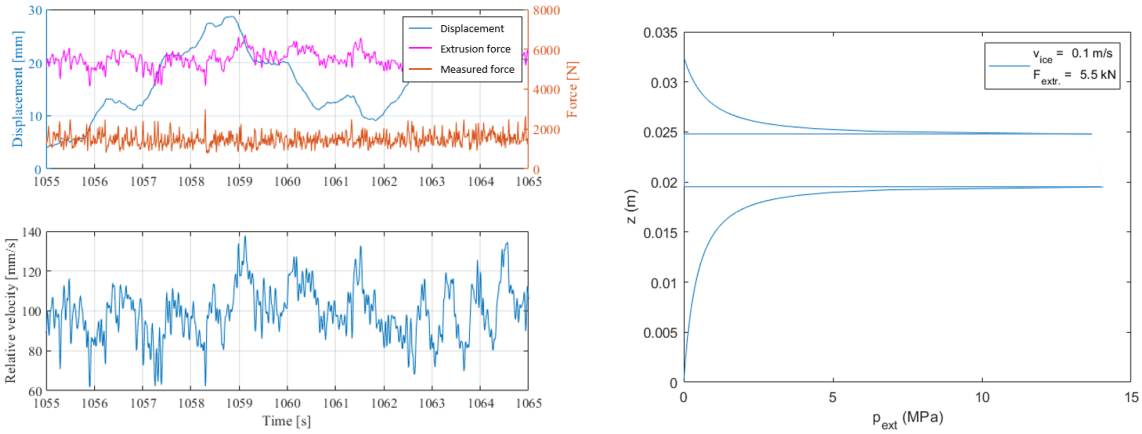

(a) (b)

Figure 6-14: Computation of the extrusion force in one load signal of the SHIVER test campaign, with (a) the load signals and (b) a graph of the extrusion pressure directly in front of the structure ($\theta = 90°$), with the total extrusion force as calculated shown in the legend.

Thick ice - Norströmsgrund lighthouse

The values found for the situation of the load signal shown in Figure 6-15 from the STRICE campaign can be compared to the extrusion loads as found by the extrusion model. To reiterate, for this crushing event $h_{\text{ice}} = 0.69$ m and $v_{\text{ice}} = 0.15$ m/s. The lighthouse has a diameter of 7.52 m.

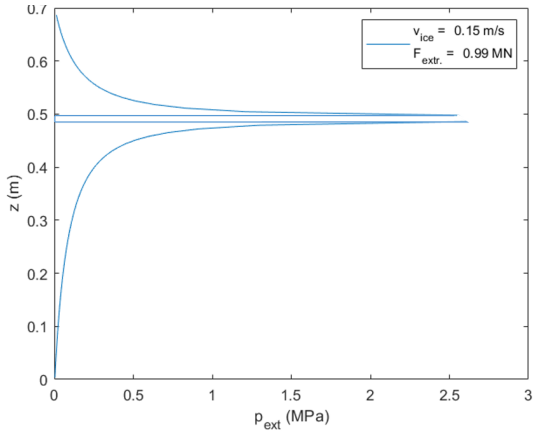

Figure 6-15: Computation of the extrusion force in the load signal at the Norströmsgrund lighthouse (Figure 6-15), with a graph of the extrusion pressure directly in front of the structure ($\theta = 90°$). The total extrusion force as calculated shown in the graph legend.

For these values, an extrusion force of $F_{\text{ext}} = 0.99$ MN is found. This corresponds to 39.6%

of the mean load in the measured load signal. This value seems plausible and could partly explain the absence of a load drop to 0 N in the load signal.

The shape of the pressure graph again shows a decrease in pressure towards the ice edges that is less pronounced than would be expected.

Very thick ice - Molikpaq

Lastly, the extrusion loads have been calculated for the crushing event at the Molikpaq structure as presented earlier, on the 12^{th} of April in 1986, as well as another well known event on the 12^{th} of May of the same year.

12 April
Inserting the values of this crushing event as explained in the previous Chapter, as well as the ice drift speed of $v_{\text{ice}} = 0.06$ m/s as was reported, the extrusion loads are found as $F_{\text{ext}} = 11.8$ MN. Since the loads were measured between 75 and 100 MN, that means that the extrusion force is found to constitute $11.8 - 15.7\%$ of the force found.

12 May
A month after the crushing event above, a second crushing event occurred on the 12^{th} of May. This event is described in full detail in Gagnon, 2012. In this event, the measured load signal was as shown in Figure 6-16. At the start of the interaction, v_{ice} was measured at 0.18 m/s, with the global ice load measured at $F_{\text{ice}} = 25$ MN. 19 minutes after the start of the interaction, v_{ice} was measured at 0.09 m/s. The global ice load was measured at $F_{\text{ice}} = 120$ MN. The ice thickness was reported as $h_{\text{ice}} = 1.8 \pm 0.5$ m for the first year ice, with some $h_{\text{ice}} = 4$ m reported for some multi-year ice that was also observed to be present in the interaction.

For the values given, the extrusion forces were calculated as given in Table 6-1. Comparing this at the start of the crushing event, the extrusion force calculated is as high as the measured load, for the case of the first-year ice thickness. For the multi-year ice thickness, the calculated extrusion force is about 50% higher than the measured load. These results seem unlikely. A possible explanation could be an incorrectly assumed ice edge angle of $40°$ for this indentation speed. As stated in Chapter 3, Kärnä et al., 1997 report a velocity dependent ice edge angle, such that the chosen value may not correspond to the one in the crushing event.

For the situation at 19 minutes after initiation of the load measurements, the results are more plausible, with the calculated extrusion load at about 15.0% of the measured load for the first-year ice thickness and 23.4% for the multi-year ice thickness.

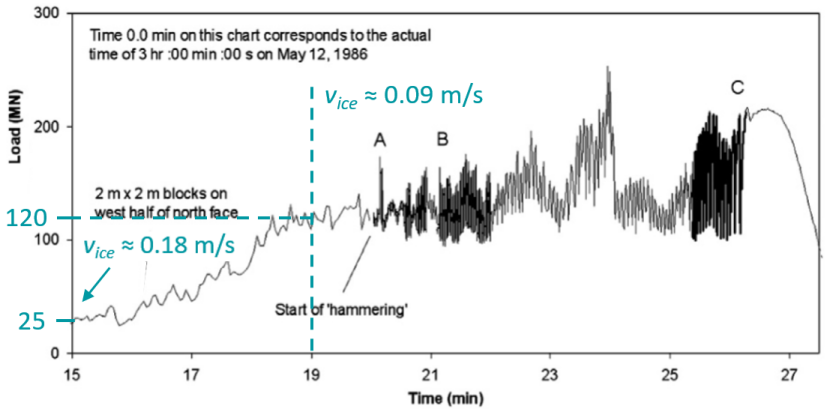

Figure 6-16: Load signal measured for the crushing event at the Molikpaq on the 12$^{\text{th}}$ of May 1986. From Gagnon, 2012.

Table 6-1: Extrusion force found for the various ice thicknesses and indentation speeds reported for the crushing event at the Molikpaq on the 12$^{\text{th}}$ of May 1986.

	F_{ext} (MN)	
h_{ice} (m)	v_{ice} = 0.18 m/s	v_{ice} = 0.09 m/s
1.8	25.2	18.0
4	37.9	28.1

From the comparisons for both model scale and full scale made above, it can be concluded that the extrusion model as is proposed cannot be used for evaluating extrusion loads at model scale, but it predicts plausible values for full scale. Therefore, in the Results Chapter that now follows, only full scale structures are considered.

Part III

Results and discussion

7

Results

With the models as established in the previous Chapters, calculations have been performed. These are shown in this Chapter. First, the results of the calculations using the Standard and the Adjusted versions of VANILLA in Matlab are shown through plots of the ice force and displacements at waterline and tower-top. Then, the statistics from these figures are shown against the ice drift speed.

7-1 Ice force and displacements plots

For this comparison, the minimum ice case of $h_{\text{ice}} = 30$ cm and $C_{\text{R}} = 0.86$ MPa is examined, as well as the maximum ice case of $h_{\text{ice}} = 105$ cm and $C_{\text{R}} = 1.34$ MPa, which are the ice cases used for the wind turbine simulations in Appendix D. For calculation of these results, structural parameters of the SG 14-222 DD platform are used, with the first 10 global bending mode frequencies included.

Simulations have been run for ice speeds of 0.01 m/s to 0.1 m/s in steps of 0.01 m/s, as well as 0.003, 0.15, 0.25, 0.35, 0.5, 0.75, 1, 1.5 and 2 m/s. Additionally, for the thin/weaker ice simulations of 0.005 m/s were done. This was not possible for the more severe ice case, due to some memory issue that was only present for very low ice speeds.

The plots of some of the interesting cases now follow. In the plots of the ice force, μ indicates the mean force, σ the standard deviation and *max* the maximum force encountered. For the plots showing the displacements, *WL* indicates waterline, while *TT* stands for tower-top, with *max* being the maximum displacement and *min* being the minimum displacement. These statistics are based on computations of 600 seconds, of which the first 100 seconds are not taken into account, to eliminate the transient. For the sake of showing clear figures, only 100

seconds (t = 250 to t = 350) are shown. Corresponding power spectral density (PSD) plots are given in Appendix C, in which the frequency content of the signals is more obvious.

IC regime

First, the results for the intermittent crushing regime are shown. These results were obtained for an ice drift speed of $v_{\text{ice}} = 0.005$ m/s for the thin ice case and $v_{\text{ice}} = 0.01$ m/s for the thick ice case. Figure 7-1 shows the results for the thin ice, Figure 7-2 for the thicker ice case.

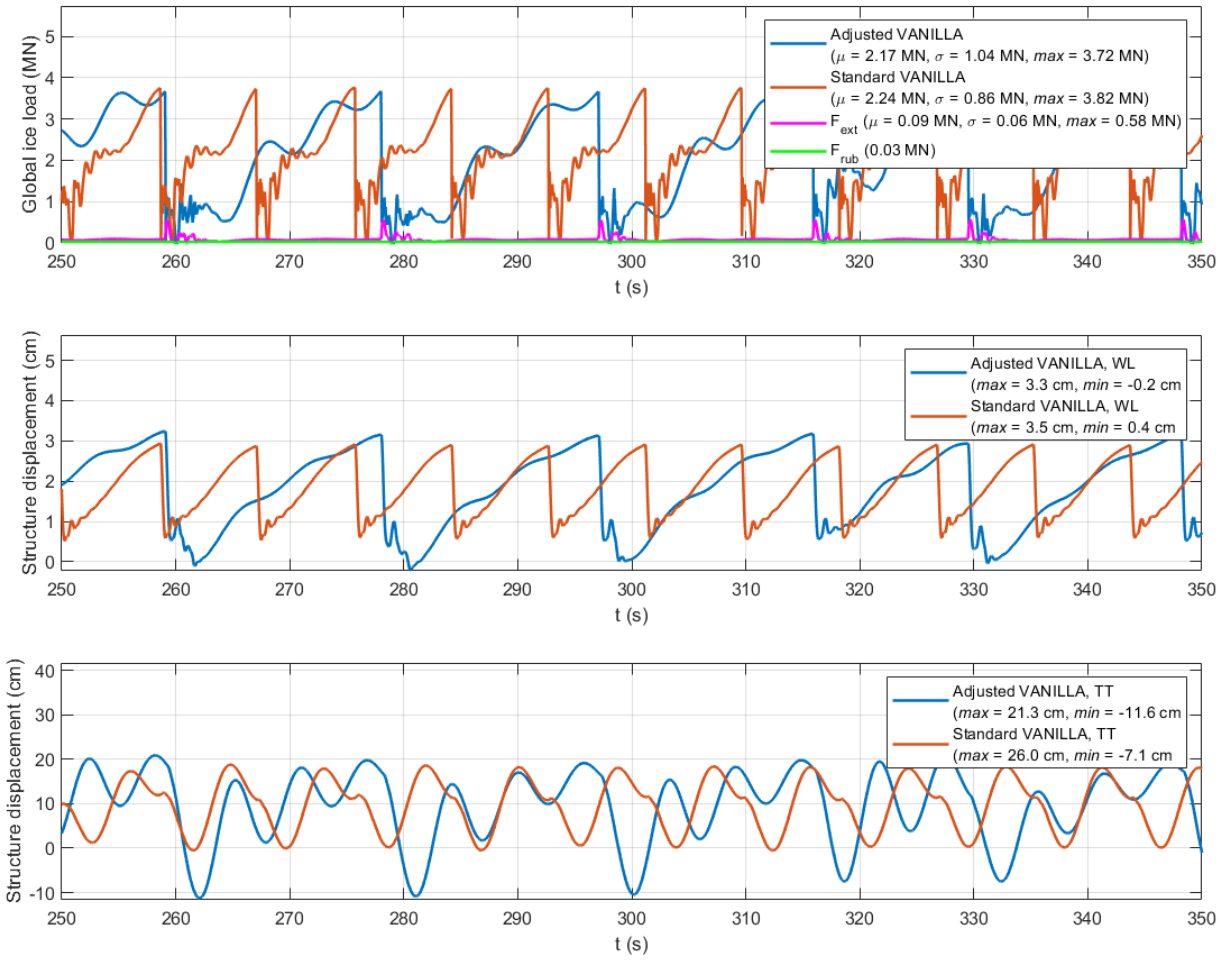

Figure 7-1: Plot of (a) ice force, (b) displacement at waterline and (c) displacement at tower-top for the case of $h_{\text{ice}} = 30$ cm and $C_{\text{R}} = 0.84$ MPa at $v_{\text{ice}} = 0.005$ m/s.

Figure 7-1 shows that for the thin ice, the rubble force only constitutes a small portion of the total load, with about 1.4% of the load stemming from the rubble.

The extrusion force is more pronounced. It stays low in magnitude for most of the interaction, until right after the ice failure. The structure bounces back, the relative velocity is increased and the extrusion force goes up. At the peak of the extrusion load, it is responsible for nearly all the force on the structure. It can be seen that the Standard VANILLA signal drops to zero, while this in not the case for the Adjusted model.

After the initial extrusion load peak directly after failure (at about 15% of the load peak right before failure), a number of smaller peaks can be seen. The relative velocity goes down and the extrusion force remains at a low magnitude, until the next failure is encountered. Also, it seems that the addition of the extrusion and rubble loads smooth the load signal in the build up to the peak right before failure.

As for the displacements at waterline, it can be seen that for the Adjusted VANILLA, the period is more than twice as long than for the standard VANILLA (see also the PSD in Appendix C). The shape of the displacement graph has nearly the same shape for both models, the structure bounces back slightly further for the Adjusted VANILLA model, after initially reversing direction. The displacement signal at tower-top shows larger negative displacements for the Adjusted VANILLA model.

For the thicker ice, Figure 7-2 shows the same changes in the load pattern that were noted above for the thinner ice. A notable exception is that here, the maximum ice force is slightly higher for the Adjusted VANILLA compared to the Standard VANILLA, which is not the case for the thin ice.

The displacements at waterline show similar patterns for the Standard and Adjusted VANILLA for the thicker ice. The same can be said about the displacements at tower-top.

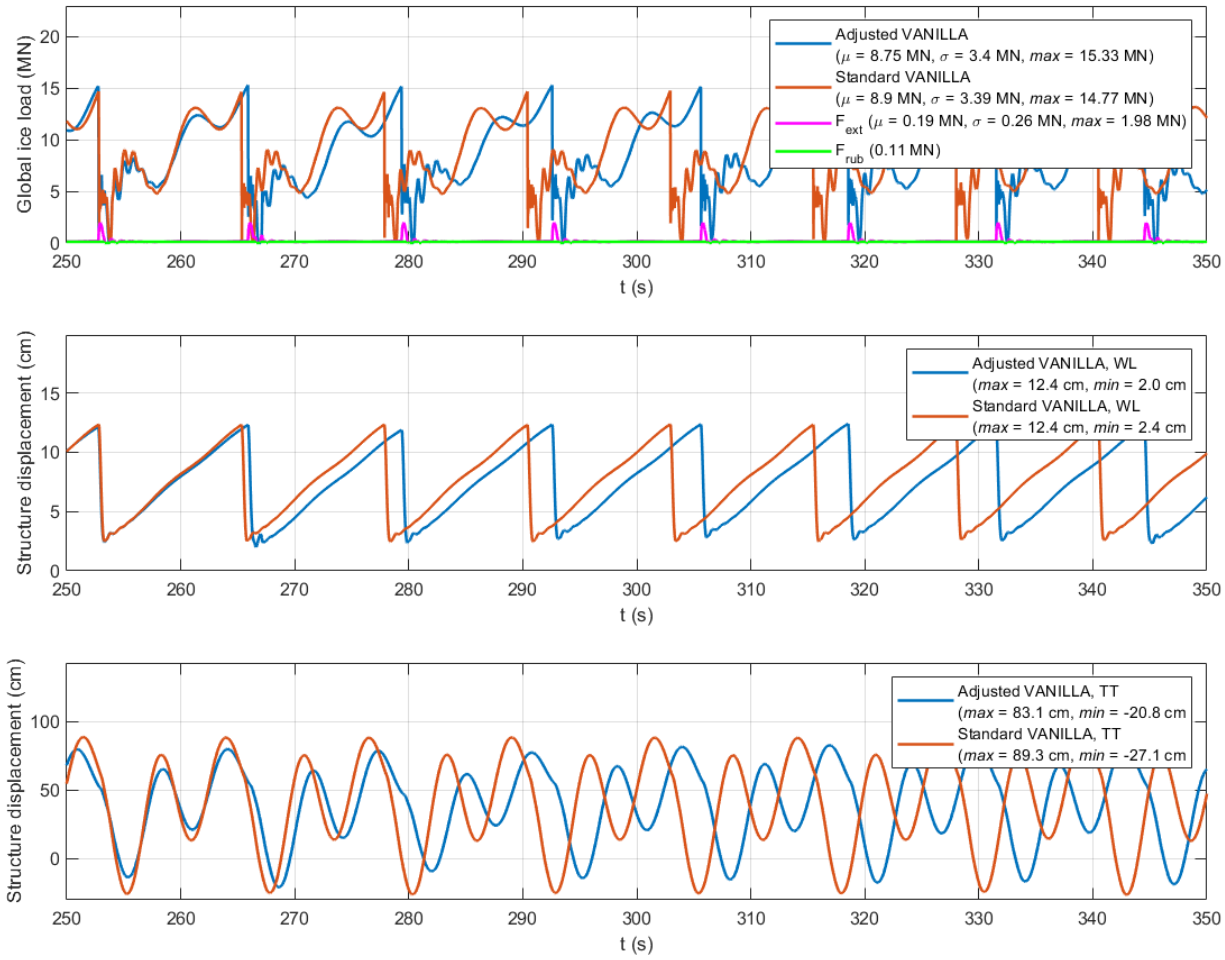

Figure 7-2: Plot of (a) ice force, (b) displacement at waterline and (c) displacement at tower-top for the case of $h_{\text{ice}} = 105$ cm and $C_{\text{R}} = 1.34$ MPa at $v_{\text{ice}} = 0.01$ m/s.

FLI regime

Next are the results for the intermittent crushing regime. These results were obtained for $v_{\text{ice}} = 0.02$ m/s for the thin ice case. For the thick ice, FLI was not observed for the Standard VANILLA model at the indentations speeds considered and only limited FLI was observed for the Adjusted VANILLA model for $v_{\text{ice}} = 0.06$ m/s. Figure 7-3 shows the results for the thin ice, Figure 7-4 shows the results for the thick ice.

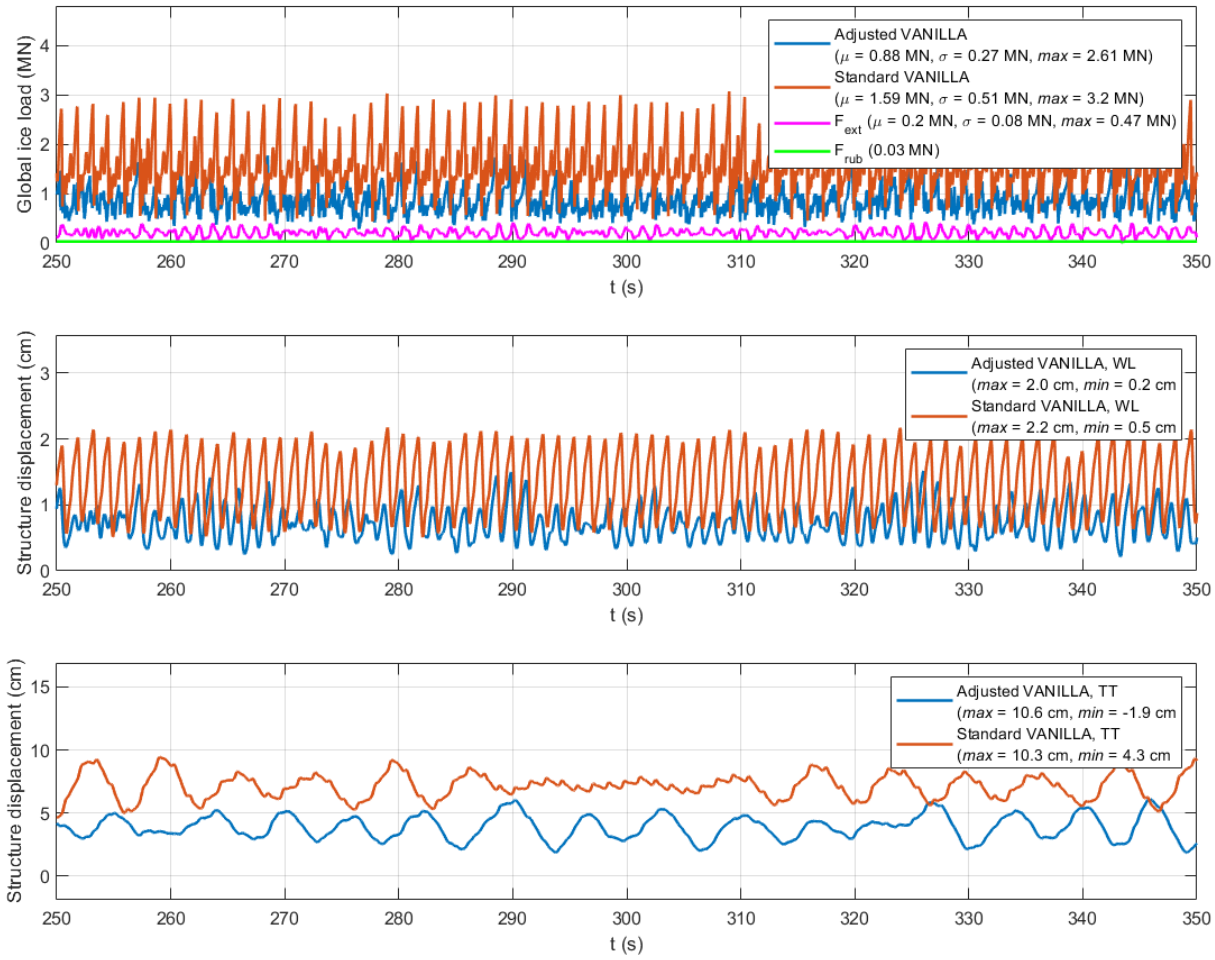

Figure 7-3: Plot of (a) ice force, (b) displacement at waterline and (c) displacement at tower-top for the case of $h_{\text{ice}} = 30$ cm and $C_{\text{R}} = 0.84$ MPa at $v_{\text{ice}} = 0.02$ m/s.

Figure 7-3 shows that the load peaks are significantly lower for the Adjusted VANILLA model, when compared to the Standard VANILLA model. The extrusion force in the Adjusted VANILLA model is more prominent throughout the entire interaction, since the relative velocity rarely goes to zero. The rubble force is again of a very low contribution to the total load (about 3.4$\%$ of the mean load).

The displacement signals are also very different, with the amplitude of the oscillations being much higher for the Standard VANILLA. The oscillations are more constant for the Standard VANILLA.

The signals of the displacements at tower-top do not differ much, except for the mean of the displacements, which is larger for the Adjusted VANILLA.

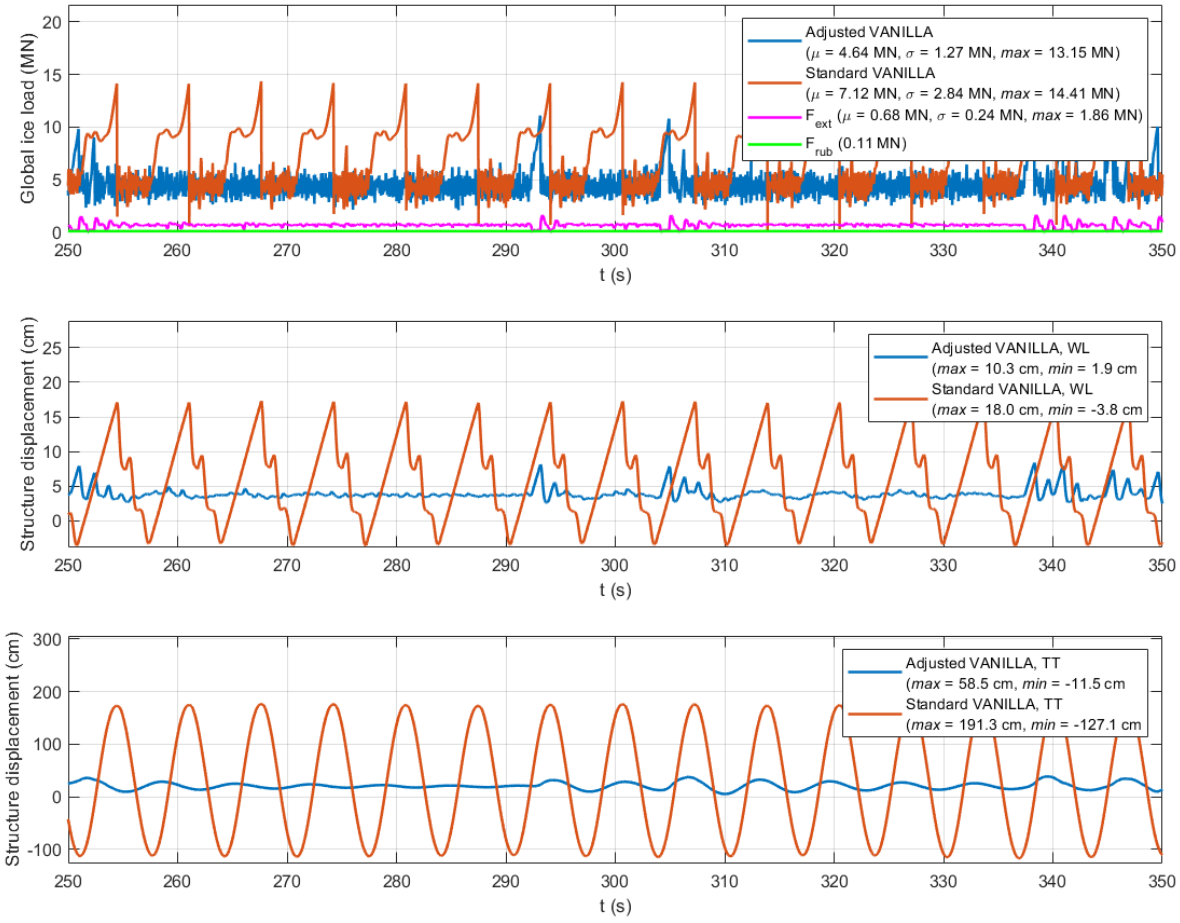

Figure 7-4: Plot of (a) ice force, (b) displacement at waterline and (c) displacement at tower-top for the case of $h_{\text{ice}} = 105$ cm and $C_{\text{R}} = 1.34$ MPa at $v_{\text{ice}} = 0.06$ m/s.

For the thicker ice it can be seen that the interaction found from Standard VANILLA still considers IC at this indentation speed, while the Adjusted VANILLA mainly shows CBR, with some FLI showing in parts of the signal. In the short periods when interaction for the Adjusted VANILLA model shows FLI, it can be seen that the extrusion force shows alternating peaks and troughs, without periods of constant low loads that were previously seen for IC.

The difference in regimes predicted from the Adjusted and Standard VANILLA models are

also clear from the displacement plot, which show very different patterns.

CBR regime - $v_{\text{ice}} < 0.15$ m/s

Here, the first set of results of the continuous brittle crushing regime are shown. These results were obtained below the ice drift speed of $v_{\text{ice}} = 0.15$ m/s used for calibration of the model. These results were obtained for an ice drift speed of $v_{\text{ice}} = 0.05$ m/s for the thin ice case and $v_{\text{ice}} = 0.08$ m/s for the thick ice case. Figure 7-5 shows the results for the thin ice, Figure 7-6 for the thicker ice case.

Figure 7-5: Plot of (a) ice force, (b) displacement at waterline and (c) displacement at tower-top for the case of $h_{\text{ice}} = 30$ cm and $C_{\text{R}} = 0.84$ MPa at $v_{\text{ice}} = 0.05$ m/s.

From Figure 7-5 it can be seen that the mean load found from the Adjusted VANILLA model is significantly lower than for the Standard VANILLA model. The extrusion force is nearly constant at this speed, because the relative velocity is close to constant.

From the dynamics at waterline, it can be seen that the Adjusted VANILLA has a lower mean displacement due to the lower mean ice load. The same can be said about the dynamics at tower-top. Except for the mean displacement, the dynamics are very similar for the Standard and Adjusted VANILLA model.

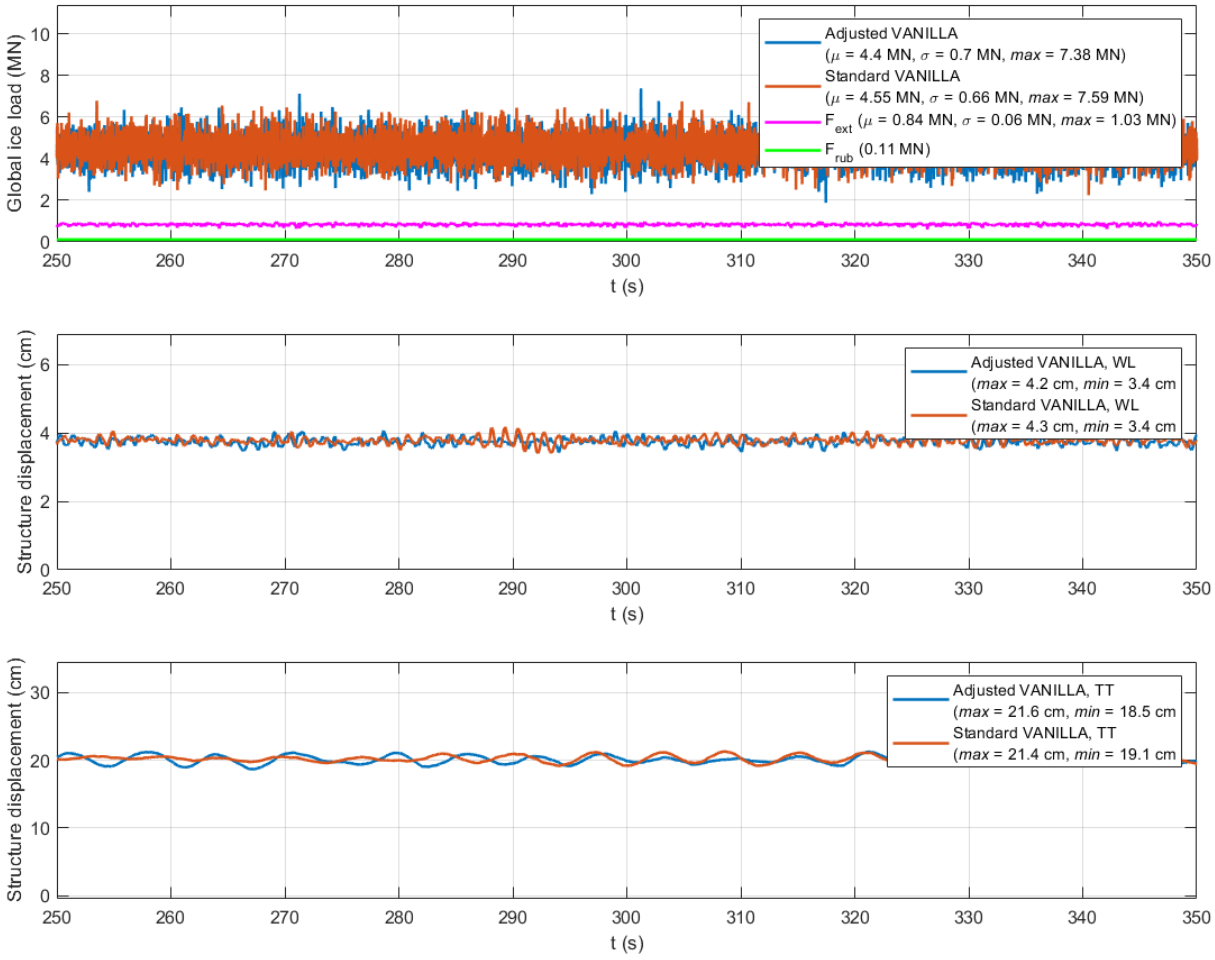

Figure 7-6: Plot of (a) ice force, (b) displacement at waterline and (c) displacement at tower-top for the case of $h_{\text{ice}} = 105$ cm and $C_{\text{R}} = 1.34$ MPa at $v_{\text{ice}} = 0.08$ m/s.

For the thicker ice in Figure 7-6, the extrusion force it notably lower than for the thinner ice. The mean of the total load for the Adjusted VANILLA is closer to the mean load for the Standard VANILLA than for the thinner ice.

The dynamics show a more equal mean displacement, both for waterline and tower-top.

CBR regime - $v_{\text{ice}} > 0.15$ m/s

The second set of results for the continuous brittle crushing regime now follow. These results were obtained above the ice drift speed of $v_{\text{ice}} = 0.15$ m/s used for calibration of the model. These results were obtained for an ice drift speed of $v_{\text{ice}} = 0.5$ m/s for the thin ice case and $v_{\text{ice}} = 0.5$ m/s for the thick ice case. Figure 7-7 shows the results for the thin ice, Figure 7-8 for the thicker ice case.

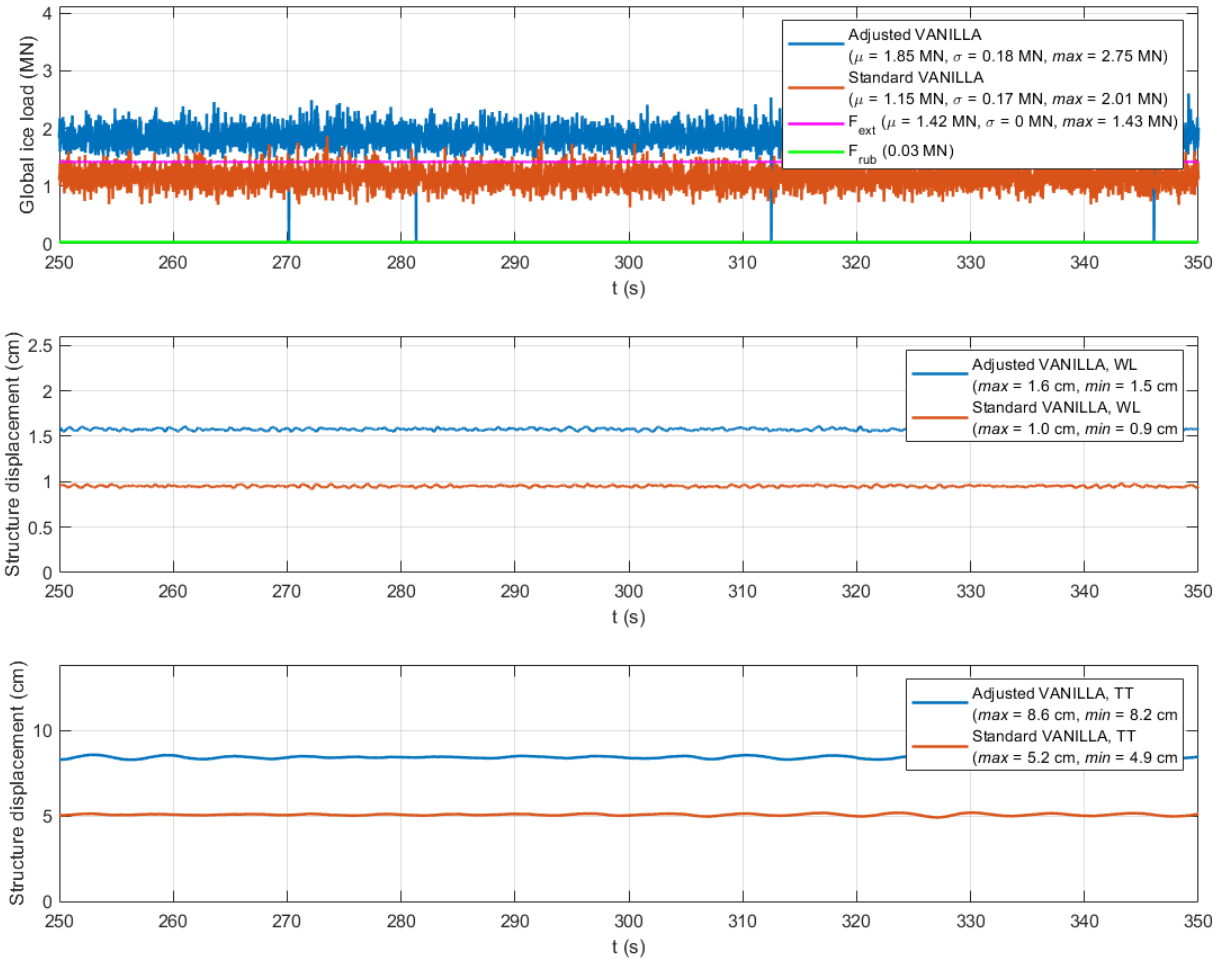

Figure 7-7: Plot of (a) ice force, (b) displacement at waterline and (c) displacement at tower-top for the case of $h_{\text{ice}} = 30$ cm and $C_{\text{R}} = 0.84$ MPa at $v_{\text{ice}} = 0.5$ m/s.

In Figure 7-7 it can be seen that in contrast to below $v_{\text{ice}} = 0.15$ m/s, the Adjusted VANILLA model now shows a higher mean load than the Standard VANILLA model, with the extrusion making for a large portion of the total ice load.

The dynamics show the typical picture for CBR, with little movement. The mean displacements, both at waterline and at tower-top, are now larger for the Adjusted VANILLA model than for the Standard VANILLA model.

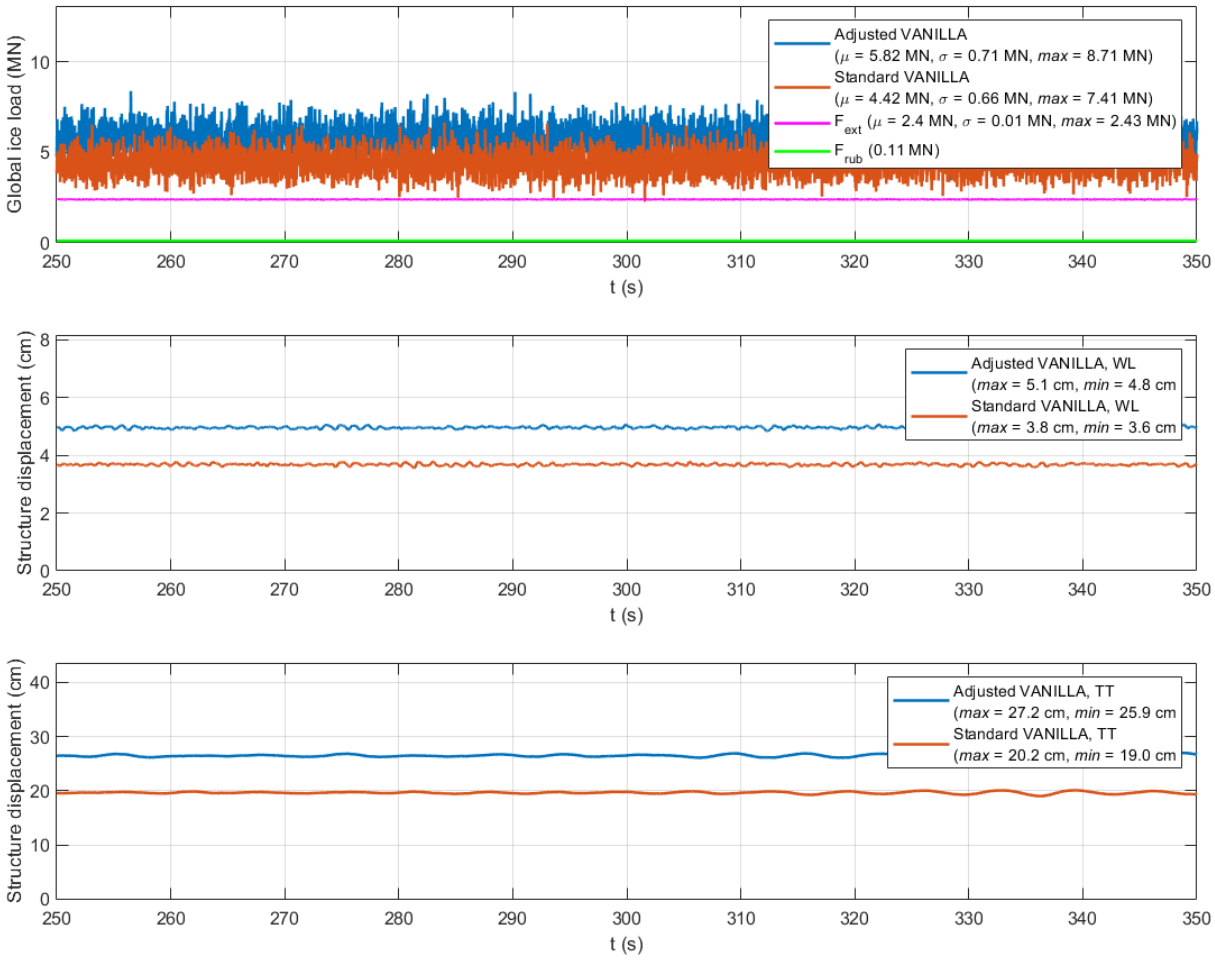

Figure 7-8: Plot of (a) ice force, (b) displacement at waterline and (c) displacement at tower-top for the case of $h_{\text{ice}} = 105$ cm and $C_{\text{R}} = 1.34$ MPa at $v_{\text{ice}} = 0.5$ m/s.

For the thick ice in Figure 7-8, the picture is similar to the thin ice in Figure 7-7. The extrusion force however has a smaller contribution to the total ice load.

7-2 Plots of extracted statistics

The plots given in the last Section included the three ice crushing regimes, but more simulations have been performed at other ice drift speeds. A complete overview of the statistics of

these simulations is given here.

Ice force statistics

First, the statistics of the ice force are given for both thin and thick ice, in Figure 7-9. From the simulations, the maximum, mean and standard deviation of the total ice force were extracted.

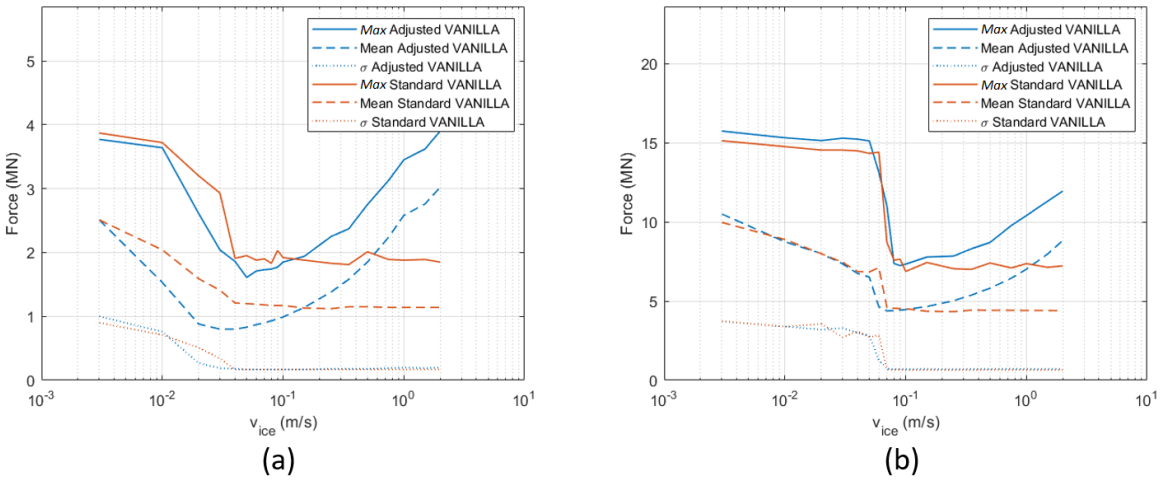

Figure 7-9: Plot of ice force statistics for (a) $h_{\text{ice}} = 30$ cm and $C_{\text{R}} = 0.84$ and (b) $h_{\text{ice}} = 105$ cm and $C_{\text{R}} = 1.34$.

From the plots of the ice force statistics in Figure 7-9 it can be seen that for the lower indentation speeds in the IC and FLI regime, the peak loads are slightly lower for the thin ice (Figure 7-9(a)), while they are slightly higher for the thicker ice (Figure 7-9(b)). Meanwhile, the mean force is not significantly impacted for the thicker ice, while it is drastically lower for the thinner ice for increasing indentation speed.

For the CBR regime, the results of the force statistics are drastically different for Standard and Adjusted VANILLA, except for the standard deviation. For the Standard VANILLA model, the peak and mean forces remain more or less equal, while they increase for the Adjusted VANILLA mode. For the extreme ice drift speed of 2 m/s, the peak force even becomes higher than for IC in the thinner ice.

Displacement statistics

Next, the statistics for the displacements follow here. First, the displacement *min* and *max* values at waterline are given in Figure 7-10. Then, the displacement statistics at tower-top are given in Figure 7-11.

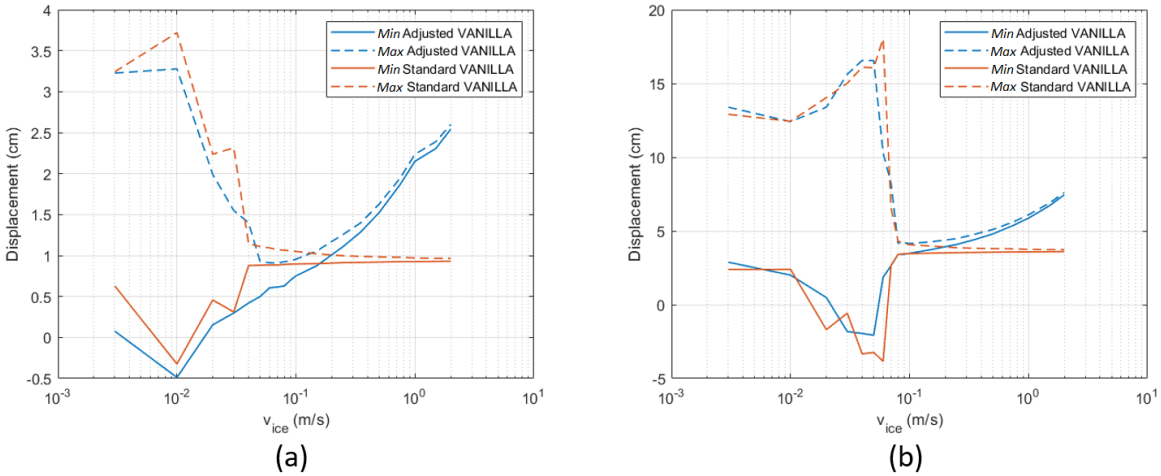

Figure 7-10: Plot of the displacements statistics at waterline for (a) $h_{\text{ice}} = 30$ cm and $C_{\text{R}} = 0.84$ and (b) $h_{\text{ice}} = 105$ cm and $C_{\text{R}} = 1.34$.

From the statistics on the displacement at waterline in Figure 7-10, the observation can be made that for the thin ice, the maximum displacement in IC and FLI is reduced, but the absolute value of the minimum is increased, thus indicating only a shift in mean value. For the thicker ice the effect is different, with the maximum displacements not severely impacted, but the minimum displacement reduced for most indentation speeds. Interestingly, the highest and lowest displacements encountered are both reduced for the thicker ice case (at $v_{\text{ice}} = 0.06$ m/s).

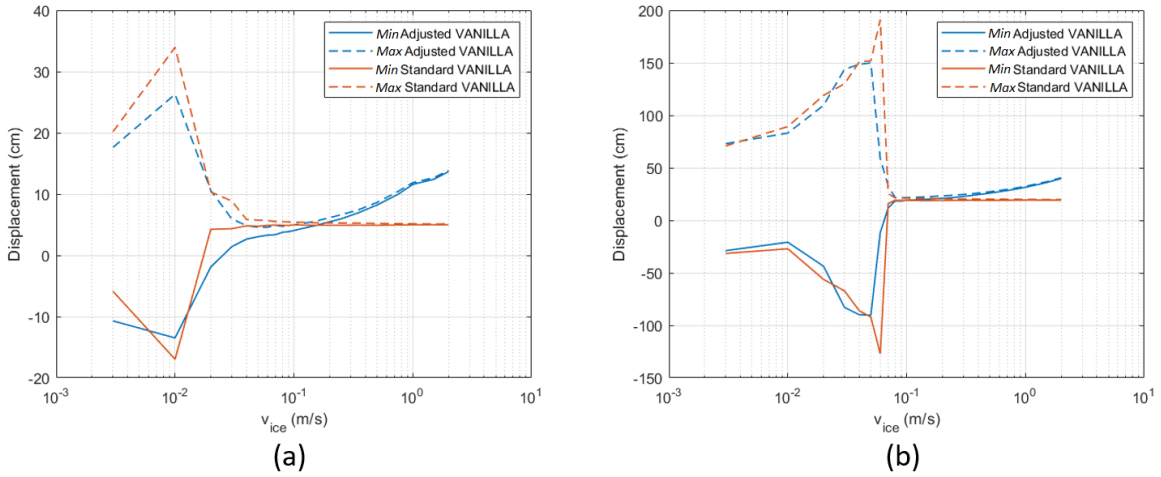

Figure 7-11: Plot of the displacements statistics at tower-top for (a) $h_{\text{ice}} = 30$ cm and $C_{\text{R}} = 0.84$ and (b) $h_{\text{ice}} = 105$ cm and $C_{\text{R}} = 1.34$.

For the displacements at tower-top, a reduction in displacement minimum and maximum can be seen for the IC and FLI regime, in both thin and thick ice, although less dramatic for the thick ice. Especially the peak values are reduced.

For the CBR regimes, the same trend is visible as at waterline, although the relative growth compared to the lower regimes is less noticeable than at waterline.

A discussion of the results given in this Chapter now follows in Chapter 8.

8

Discussion

Here, the results found in the previous Chapter are discussed. This is followed by discussion of further implications of the modelling of the ice extrusion and rubble loads.

8-1 Discussion of results

IC regime

In the results in the IC regime, the force found from the Standard VANILLA model shows drops to zero, while the extrusion force prevents this for the Adjusted VANILLA. The findings from the SHIVER campaign as presented in Chapter 2-5 do not show drops to zero, such that the behaviour of the Adjusted VANILLA model is more accurate in this respect.

The minimum force after the load drop, constituted almost entirely from the extrusion and rubble force, is about 1/4 of the peak force for both ice cases. The ratio between the peak load before the peak load is attained and the load drop immediately after failure used for the extrusion extension of the Matlock model was 1/3, but this might not be true for all ice cases, such that using a fixed value is not preferable.

In Figure 2-9, it can be seen that in the SHIVER measurements the force immediately after failure is between 1/3 and 1/4 of the peak force, such that the result obtained here seems plausible. The time of the load decrease after failure of 10 to 20% of the time for the load build up as given by Kärnä et al., 1997 is not met, with the load still decreasing very rapidly after failure. It must however be noted that the load drop in Figure 2-9 does not indicate a *gradual* load drop as was stated by Kärnä. For the overall load drop to 0 N (upon contact loss), this figure of 10-20% seems more accurate in both Figure 2-9 and the Figures obtained from the

simulations, so that it could well be that Kärnä misinterpreted the stated load decrease period of 10-20$\%$ of the subsequent load buildup.

The observed smoothing of the forcing, with less higher frequency forcing in the build-up to peak load, as well as the period of the force being impacted significantly for the thin ice (see also PSDs in Appendix C), can be explained from the addition of the damping from ice extrusion and rubble, which lower the oscillation frequencies in the system. This is supported by the observation that the smoothing of the force and elongation of the period for IC for the thicker ice is less severely impacted, since the share of the extrusion and rubble loads in the total force are lower for the thick ice case.

The dynamics for the thin ice case are impacted more severely than for the thick ice case as well, with a lower frequency dynamic being present in the signal for the Adjusted VANILLA when compared to Standard VANILLA for the thin ice case. This results in the structure bouncing slightly further back after initially reversing direction. This is supported by the observation that the displacement signal at tower-top shows that indeed different (lower) frequencies are triggered for the Adjusted VANILLA model, while the signal for the Standard VANILLA is nearly sinusoidal, supported also by the PSDs for the signals.

FLI regime

The observed reduction in load peaks for the thin ice in the FLI regime is likely the result of the way the model parameters are obtained from the pre-processor. The parameters are set such that equal loads are produced at $v_{\text{ice}} = 0.15$ m/s for the Adjusted and Standard VANILLA model, as well as at very low speeds v_{t}, $v_{2\text{t}}$ and $v_{3\text{t}}$, but not for intermediate ice drift speeds. At the indentation speed of $v_{\text{ice}} = 0.15$ m/s, the extrusion force is significantly higher than at $v_{\text{ice}} = 0.02$ m/s at which the FLI was observed. The high contribution of the extrusion load to the total load found at $v_{\text{ice}} = 0.15$ m/s, causes the spring constant K_2 (see Chapter 2-4) as found in the pre-processor to be significantly smaller for the Adjusted VANILLA model. At indentation speeds below $v_{\text{ice}} = 0.15$ m/s, but above typical IC indentation speeds, the extrusion force is lower than for $v_{\text{ice}} = 0.15$ m/s, but the interaction is still heavily influenced by spring constant K_2. This is the case for $v_{\text{ice}} = 0.02$ m/s, which explains the lower load peaks found for the Adjusted VANILLA model. This reduction in peak loads does not correspond to the amount of peak load reduction measured in the research that observed the positive force-velocity gradient as mentioned in Chapter 2-5. This indicates that the extrusion force found for the thin ice at $v_{\text{ice}} = 0.15$ m/s is overestimated.

As the load peaks for the Standard VANILLA model are higher than for the Adjusted VANILLA model, the amplitudes of the displacement at waterline are also significantly larger for thin ice. It seems that due to the extrusion load, multiple global bending mode frequencies are triggered for the Adjusted VANILLA model, while the Standard VANILLA model shows dynamics dominated by motion at one global bending mode frequency. This is supported by the corresponding PSDs in Appendix C, where the Adjusted VANILLA model does not show

one specific peak frequency (the energy is also much lower), while Standard VANILLA has one major peak (close to the 2^{nd} global bending mode frequency).

For the thick ice, the observation to discuss is the shift in regimes predicted. This is caused by the added damping from the extrusion force, which elongates the periods of the dynamics, thus causing triggering of different global bending mode frequencies. This can be seen in the PSDs, showing triggering of the 1^{st} global bending mode for the Standard VANILLA and the much lower energy for the Adjusted model spread over the frequency spectrum. Then, the initiation ice drift speed for the FLI and CBR are lowered. A shift in regimes predicted was also stated by van van den Berg et al., 2022 to happen from the added damping due to the positive force-velocity gradient at high indentation velocities. Whether the change in regime prediction from the added extrusion and rubble is accurate cannot be judged from these results.

CBR regime - $v_{\text{ice}} < 0.15$ m/s

For this case, the same discussion as given above for the FLI regime regarding the determination of intact ice model parameters applies. Since here the indentation speed is below $v_{\text{ice}} = 0.15$ m/s as well, the lower mean load found for the Adjusted VANILLA model is thus as expected.

The fact that the extrusion force found with the Adjusted VANILLA model has a lower share in the total force for the thicker ice is likely to be explained from the majority of the forces due to the extrusion coming from the region close to the pressure ridge. With the ice becoming thicker, this region does not grow. It is merely the parts at the exit of the extrusion channels that grows in size. Therefore, the additional pressure due to the extrusion is not very significant and the extrusion load does not increase proportionally to the loads from the intact ice with ice thickness. This was also seen in Figure 6-12, where $F_{\text{ext}}/F_{\text{ISO}}$ decreases for increasing ice thickness.

The fact that for the thin ice, a significant difference in the mean displacements at waterline and tower-top is observed, but not for the thicker ice, can be explained from the pronounced difference in mean ice load for the thin ice, that is much less pronounced for the thick ice.

CBR regime - $v_{\text{ice}} > 0.15$ m/s

The ice force that is now higher for both thin and thick ice for the Adjusted VANILLA when compared to Standard VANILLA, is as expected. Since the intact ice forces remain equal, but the extrusion force grows, the total load is increased for the Adjusted VANILLA model. As the increase in ice extrusion load found from the Adjusted VANILLA model is found to be higher for thin ice than for thick ice, the more dramatic growth in total the thinner ice than for the thicker ice can be understood.

The fact that there is now a transition from the Adjusted VANILLA model finding total loads below the Standard VANILLA forces for $v_{\text{ice}} < 0.15$ m/s and above Standard VANILLA for $v_{\text{ice}} > 0.15$ m/s, indicates that the positive force-velocity gradient as mentioned in Chapter 2 is now part of the model, through the extrusion force that increases with indentation speed. This effect is not found in the Standard VANILLA model. Although the inclusion of the positive force-velocity gradient could be regarded as an improvement, the argument could be made that it should (partly) result of effects in the intact ice, instead of only the extrusion force. Since other materials show similar behaviour, as was described in Chapter 2-5, this is a real possibility. A theoretical explanation for this is said to be given in Shkhinek et al., 2001, but that paper was unavailable to the writer. This paper could shed a light on the credibility of the positive force-velocity gradient stemming from the intact ice, so that also the credibility of the force-velocity gradient originating from the extrusion force can be judged.

The mean displacements being significantly higher for the Adjusted VANILLA, both at waterline and tower-top, can be explained by the increase in mean total ice load.

Extracted statistics - ice force

The observations on the peak and mean loads for the thin ice can be understood following the discussion of the FLI regime on the load peaks (due to a different K_2 found in the preprocessor). The fact that the same observations were not made for the thick ice, likely stems from a lower contribution of the extrusion force in the total load at $v_{\text{ice}} = 0.15$ m/s, such that the effect on parameter K_2 found from the pre-processor is not as severe as for the thin ice.

The cause for the observed slightly higher peak loads in the IC regime for the thick ice can possibly be explained by the same reasoning as the error in the match of mean loads at $v_{\text{ice}} = 0.15$ m/s, as was discussed in the Section on Verification in Chapter 6. There, it was argued that the differences in mean ice loads found for the rigid structure at $v_{\text{ice}} = 0.15$ m/s stemmed from rounding errors in the preprocessor.

The standard deviation is not significantly impacted for both thin and thick ice because of the intermittent nature of the extrusion force at low indentation speeds, with it only being present for significant relative velocities, and the nearly constant value of the rubble and extrusion at high indentation speeds. Then, the standard deviation mainly stems from the intact ice, such that it remains equal to that of the Standard VANILLA model. This also explains why the mean ice forces found, grow in the same fashion as the peak forces, for both the thin and thick ice. Although the mean and peak loads are both found to grow in literature, they do not grow equally. The fact that they do grow equally in the extrusion model might be caused by the assumption made in constructing the model, that the extrusion force is present over the entire ice-structure interface whenever one ice element is in contact with the structure. This causes the variation in the extrusion force that is likely present in reality due to contact area variation, to be lost.

The lack of intermittency in the extrusion force due to contact variation will also have an impact on the standard deviation of the forcing. While that is now found to be constant, adding intermittency to the extrusion force due to incomplete contact will cause the standard deviation to change with indentation velocity. This could be done by altering the prerequisite set in the code for when the extrusion load should be inserted (the *if*-statement in Listing B.3). It could for example be changed to a statement which ensures that the extrusion load is only applied when contact in multiple ice features is established (instead of just 1). By using a varying number of these ice features required to be in contact with the structure, the intermittency can be implemented.

The load increase in the CBR regimes was previously discussed in the discussions on that specific regime.

Extracted statistics - Displacement

The lowering of the mean value of the displacement for thin ice in the regimes of IC and FLI for Adjusted VANILLA is caused by the lower mean value of the total ice force in these regimes, as explained in the discussion of these ice forces.

The fact that this effect is not seen for the thicker ice, can also be understood from the ice load statistics, as the mean ice forces were found to be nearly equal (up to CBR).

What is also visible from the thicker ice case is the earlier transition to CBR for the Adjusted VANILLA when compared to Standard VANILLA, due to the added damping. Again, from these results it cannot be judged if this shift in prediction of the drift speeds at which IC and FLI occur are accurate. For the CBR regimes, it can be seen that the increasing mean force leads to an increase in mean displacement, which is as expected.

The statistics of the displacements for tower-top follow a similar trend as the displacements at waterline. A notable exception is that for the thin ice, the minimum displacements in IC are now smaller in magnitude for Adjusted VANILLA than for the Standard model. The reason for that is not entirely clear to the writer.

8-2 Discussion of other observations/implications

Before obtaining the results, several aspects of the modelling of rubble and extrusion ice loads were encountered that should be discussed to further extend the understanding of the models and the process of ice extrusion.

Memory issue at low ice drift speeds for thick ice

As was briefly mentioned at the start of Chapter 7, a memory issue was encountered when running the Adjusted VANILLA model at slow indentation speeds, especially for the thicker ice case. It was tested what the cause would be, but it could not be directly identified. As it seems, a large constant load (not necessarily from rubble or extrusion) added to the equations of motions in the ice model, causes infinite shortening of the time steps considered, such that convergence cannot be reached. A solution was not yet found.

Model scale

As was shown in Chapter 6, the validation of the extrusion model for model scale ice crushing yielded an ice extrusion force that was impossibly large.

One explanations for this could be that there is a larger ice edge angle for the small scale, which would lead to lower extrusion forces than are found in the model. This could be caused by the formation of curved spalls, for which the region directly above the pressure ridge has a lower gradient than for higher up in the extrusion channel. For thin ice, the spall would run into the ice edge much earlier than for thick ice, such that a lower effective ice edge angle results. This is illustrated in Figure 8-1

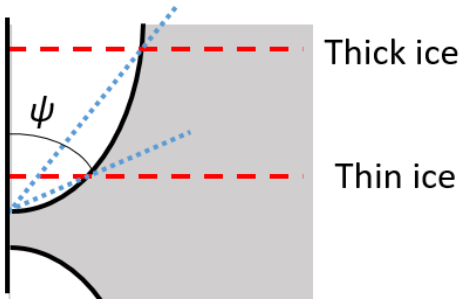

Figure 8-1: Sketch of a larger effective ice edge angle for thin ice.

Another explanation could be the assumption of a 2D flow field that was made for constructing the ice extrusion model. For smaller structures, the curvature of the structure becomes significant, such that flow around the perimeter, instead of solely towards the upper or lower ice edge, may result. This would reduce the magnitude of the extrusion force.

A third explanation could be sought in the crushing mechanism that is at play here. For the model scale, there is very little material in the rubble piles on top of and below the ice, such that the overburden pressure is very low. Moreover, the rubble piles on this scale were observed to be much more mobile than for larger scale, occasionally being propelled forward/outward, such that no overburden pressure is present at all. In these situations, the

likelihood for flake formation and explosion (as described in Chapter 3) is significant, resulting in no extrusion.

Moreover, the material in this situation reaches the upper and lower ice edge earlier in extrusion, so that there is less time for it to compact. The pressure carried by the pulverised ice can be higher when it is compacted, such that in at model scale, the resultant loads are lower.

Crushing strength C_R

In the Results, a distinction was repeatedly made between the thin and thick ice case. However, there was also a difference in ice crushing strength. The ice extrusion model does as proposed does not depend on the ice crushing strength, while it does depend on the ice thickness. It is therefore interesting to discuss what the dependency of the total loads found would be on the crushing strength.

While it is true that the extrusion model does not depend on C_R, the Adjusted VANILLA model does depend on it. Firstly, the model is scaled on the load found by the ISO-equation (Equation 2.1). For higher C_R, the ISO load also increases, while the loads predicted by the extrusion model remain equal. This results in a lower contribution of the extrusion loads in the total ice loads. This would have the same effects as those described for the differences between the thin and thick ice cases in the previous Section.

It would not be unthinkable that the material resulting from crushing ice with a higher C_R-value is different than from crushing of material with a lower C_R-value, as the higher strength is caused by different material characteristics. However is not know whether the resulting crushed ice material is significantly different. If so, this could have implications on the extrusion model (through varying model parameters), such that the extrusion model would partly depend on the ice strength coefficient.

9

Model limitations

When a physical process is modelled numerically, there are factors that will make the results deviate from reality. These are discussed here.

9-1 Rubble modelling

First the rubble model is considered.

Pile dimensions
The accuracy of the rubble model could be lacking for various reasons. Firstly, with a lack of measurements, the rubble pile dimensions were established on only one set of pictures from the Norströmsgrund lighthouse. Though the videos from which these photos were taken showed limited variability of the rubble pile shapes during crushing, the photos only consider one event, such that only one ice thickness and strength is considered. Also, only one surface roughness of the ice is considered, which could potentially influence the angle of repose, significantly impacted the rubble pile shape. This point is valid for the rubble pile on top of the ice sheet, but even more so for the ice underneath the ice sheet. With only being able to measure the length in front of the structure, basing the dimension of the keel on that of the sail makes for possibly even larger errors in the keel dimensions.

Material characteristics
While the dimensions of the piles are up for contention, the material characteristics considered are also very determining for the accuracy of the rubble model. The exclusion of the static friction means that upon renewed contact with the structure after losing contact, the force will (although only very shortly) be higher than when only the dynamic friction is considered. Of even more importance is the dependency of the dynamic friction coefficient

on the various conditions as discussed in Chapter 4. Most notably, a point of discussion is the velocity dependency of the ice friction. As discussed, this dependency is not always present, depending on amongst others the temperature and surface roughness. Therefore, a more detailed description of the friction coefficient could make the rubble model more accurate. This is true for both the ice-ice and the ice-steel friction.

The porosity was based on measurements of field rubble, which has (much) larger ice features than the rubble from crushing events. Moreover, the range of porosity found in these measurements is large. For these reasons, the porosity assumed might be quite different to the reality for crushing events. A larger porosity would mean a larger pile size. This would mostly impact the internal failure mode of the rubble force, since the sliding mode depends on the normal force of the rubble pile, which isn't effected by the porosity.

The angle of internal friction and the cohesion of the rubble are also reported with large ranges in experiments, such that an error might be introduced in the internal failure mode of the rubble force. The angle of repose for the sail and keel might be different for the smaller particle sizes in a crushing event when compared to rubble fields. This would again influence the pile dimensions.

Side-side motion
The model proposed only applies when the motion of the turbine is in the fore-aft direction, such that motion is along the direction of the ice drift. The resulting rubble force then has a x-component that is zero. In reality, the turbine will also have side-side motion. Then, the rubble forces in x-direction do not balance out and there is a restoring force in the x-direction, pushing the turbine back to its starting position. Since the rubble pile does not curve around the monopile for $\theta < 0°$, the rubble force will be smaller in side-side motion than in (positive) fore-aft motion. Moreover, a side-side motion can push away the rubble pile towards the side, such that the total rubble loads decrease momentarily (also in fore-aft direction) until the rubble pile is restored to its initial shape. This is not considered in the model and limits the accuracy.

It must be noted however, that the magnitude of the rubble loads will remain small compared to those of the intact ice forcing and extrusion forces, even for stark deviation of one of the model parameters. Therefore, the limitations of the rubble model are not as significant to those of the extrusion model. These are now discussed.

9-2 Extrusion modelling

The extrusion model has various limitations as well, as set out here.

High force at high speeds
The most obvious inaccuracy of the extrusion model is the unrealistically high extrusion force found for higher ice speeds, especially for the thinner ice cases. This means that the velocity

dependency of the model is not representative. Multiple reasons could be thought of that would skew this dependency.

The first is the point raised earlier when the flow parameters K and N were discussed. In the graph from the paper by Singh et al., 1995, the pressures at higher indentation speeds were not higher, but lower than for low indentation speeds. The authors ascribed this to the effect of compaction of the crushed ice in the extrusion tests. Without taking this compaction into account, the pressures at higher indentation speeds are thus significantly overrated. At the same time, the parameters were based on an indentation speed of 60, 125 and 160 mm/s, but for 2.5 mm/s, the factors were quite different, such that the values found may also not represent low indentation speeds well and forces for these speeds are underestimated.

Another reason one could think of is the shape of the extrusion channel. One value is assumed here, because of a lack of data for the shape of the extrusion channel. With the loads found being heavily impacted by the dimensions of the extrusion channel, this means using proper dimensions for the extrusion channel is important. Kärnä mentioned that the shape of the ice edge, and thus the extrusion channel, is dependent on the indentation speed, such that using one value will lead to inaccuracies. If in reality the angle of the extrusion channel increases with indentation speed, the forces would not increase as much with indentation speed as found by the current model.

No-slip boundary condition

The dependency of the ice extrusion loads on the ice thickness seems to be partly inaccurate as well, especially for thin ice. This seems to be because the pressures are found to increase exponentially when coming closer to the pressure ridge. Then, the boundary condition of no-slip at the solid walls becomes increasingly important. Where this condition is deemed appropriate for large scale flows of purely viscous fluids, we are currently dealing with an in essence granular fluid, at a small scale. The granular fluid happens to be well described by the nonlinear viscous flow description, but the boundary condition of no slip is likely not appropriate, especially where the extrusion channel is very narrow. And since this is the region where the highest pressures are found and the boundary condition is of most importance, it is likely that the assumption of no-slip makes for (potentially significant) overestimation of the loads.

Lubrication theory

Aside from the no-slip boundary condition likely being incorrect, the formulas established for the pressures were also based on lubrication theory. One of the (most important) assumptions in lubrication theory is that $L \gg h$, or that the width is much smaller than the length of the channel. It has been shown in various papers that the lubrication theory works quite well in domains where this assumption is questionable (for example in Cawthorn and Balmforth, 2010), its accuracy reduces with $\frac{h}{L}$ getting bigger. In this case, with an angle of the extrusion channel assumed at 40°, the condition of $L \gg h$ is clearly violated. When in reality the extrusion channel has an even larger angle, lubrication theory might not be the proper theory for establishing the pressure formulas.

2D vs. 3D flow

Continuing on the validity of the lubrication theory used, it can be said that the 2D theory used decreases in accuracy for smaller θ, close to the sides of the structure. There, the ice drift is at an angle with the structure, such that flow will not only happen up (or down) the structure's surface, but also to the side, along the drifting ice. This would make it slightly easier for the crushed ice to be abducted, therefore reducing the pressure and thus the force from the extrusion. Similar to this, the high pressure zones in the middle of the structure ($\theta = 90°$) will create a pressure gradient along the perimeter, such that flow along that direction is enhanced. However, with the gradient being much larger going up or down from the pressure ridge, these effect will likely be relatively small.

Side-side motion

Just like for the rubble model, the extrusion model proposed only applies when the motion of the turbine is in the fore-aft direction, such that the resulting extrusion force has a x-component that is zero. With side-side motion, the extrusion force will have a non-zero x-component, that acts as a restoring force. The other points raised about the side-side motion for the rubble model apply here as well. Omission of these effects limits the accuracy of the extrusion model.

Number of pressure ridges

Lastly, it is unclear if for thick ice, only one pressure ridge occurs, or whether high pressure zones develop at various heights along the ice thickness. With high pressure zone at multiple heights, extrusion will look quite different. Because the extrusion between the high pressure zones is restricted, this could potentially leading to high pressures in these in-between zones and thus a higher extrusion force for thicker ice.

10

Conclusion

The aim of this research was to develop an understanding of the phenomena of ice rubble and extrusion, as well as propose models for the evaluation of the loads stemming from these phenomena. This chapter provides the conclusions that can be drawn from the developed insight, poses recommendations on future work and answers the main research question:

What are the implications of rubble and extrusion ice loads on the dynamics of offshore wind turbines in an ice crushing event?

Leading up to answering the main research question, the subquestions that were formulated are answered.

Subquestion 1: How can rubble loads be computed for offshore wind turbine structures?

From a literature review on the rubble loads, this subquestion could be answered. The rubble loads can be modelled in a sliding mode and in an internal failure mode, both for a rubble pile above the water, the sail, and one below the water, the keel. The failure mode that amounts to the lowest loads on the structure is governing.

A rubble loads model for monopile offshore structures was proposed based on a mass flux balance of crushed ice and discharged rubble. The rubble pile dimensions were established from analysing length ratios in video frames of the Norströmsgrund lighthouse. For the internal failure mode, only the passive earth pressure loads amount to non-negligible loads, such that that was used. Parameters required are the densities of ice and seawater, porosities

of sail and keel, internal friction angle of the rubble, rubble cohesion, sail and keel angles and ice-ice and ice-structure kinetic friction coefficients. From these parameters, the rubble force only has a significant sensitivity for the length ratios and the ice-ice friction coefficient. Based on this, it can be stated that further research should be aimed at collecting more data on the rubble pile dimensions for interaction with monopile structures. Next to that, research should be performed on determining the ice-ice friction coefficient for pulverised ice, as this is currently unavailable. However, the magnitude of rubble forces is found to be low compared to measured ice force signals, both for model and full scale. Therefore, the efficacy of this future research can be debated and efforts should be aimed at establishing more knowledge on other phenomena (such as ice extrusion) first.

Subquestion 2: How can extrusion loads be computed for offshore wind turbine structures?

A literature review on ice extrusion made answering this research question possible. The processes taking place in the ice in crushing interaction are found to be highly complex. They reshape the ice edge, such that a curved wedge shaped ice edge results. Then, the crushed and pulverised ice in the wedge is pushed out in the process of extrusion. Close to the pressure ridge of the intact ice, the pulverised ice can carry very significant loads, with local pressures on the order of meganewtons. Due to the high complexity of the crushing processes, continuum approaches are used for modelling ice extrusion loads. Mohr-Coulomb flow can accurately describe the relatively low pressures at the outer edges of the extrusion channel, while viscous flow descriptions are more accurate for the region closer to the pressure ridge. The crushed ice in the region close to the pressure ridge carries the majority of the loading. Thus, a viscous flow description for modelling extrusion loads is most appropriate.

An extrusion load model was proposed based on adapting the nonlinear viscous flow descriptions encountered in literature to a wedge shaped interface. The model was found to be very sensitive to the nonlinear viscous flow parameters, as well as the ice edge angle. The extrusion model was shown to obtain extrusion load values that are plausible for full scale, but not for model scale, It is expected that a more accurate description of the ice edge angle would partially resolve the poor performance of the model at model scale. It was reported by Kärnä et al., 1997 that the ice wedge angle depends on indentation speed, but this dependency is no longer available. Therefore, this dependency should be investigated in future research, ideally for varying ice thicknesses. For this, a similar setup that was used by Määttänen et al., 2011 could be used. This setup would be even better for this purpose, if it could be examined in real time. A transparent plate could be installed on the side, parallel to the crushing direction, to be able to see (and film) the development of the ice front directly.

When performing these, or similar measurements, it would be beneficial to log the pressure distributions over the height of the ice. While this has been done with a focus on the crushing forces of the intact ice, it would help for validation of an extrusion model to log the lower pressures outside of the pressure ridge with a higher resolution. In previous measurement

campaigns, the high pressures in the pressure ridge made that the pressures (just) outside of that were all measured at the lowest value on the scale available, losing any information on the pressure gradient.

Other measurements could be done on a similar setup as the extrusion tests shown in Chapter 3, to get a better understanding of the influence of compaction on the flow parameters describing the nonlinear viscous flow. Moreover, these measurements should be done for higher indentation velocities than was done previously (above 160 mm/s). Possibly, they could also be performed with a non-parallel plate, to closer resemble the ice edge in a crushing event.

Moreover, it is advised to implement a proper boundary condition of the slip at the intact ice and structure surfaces, instead of the no-slip condition used now, which leads to overestimation of extrusion loads. A first attempt could be made by determining a simple Navier slip condition, though other slip conditions could also be considered. Next to this boundary condition being changed, the model could be extended to incorporate 3D flow, instead of only 2D. Different shapes of the ice edge can also be considered, such as the one found from the curved flakes described in Chapter 3. When after implementation of these changes the model is still found to disagree with measurements (up to the desired accuracy), it would be recommended to reconsider the assumption of lubrication theory (if the measured loads confirm that extrusion loads are significant).

Subquestion 3: How can rubble and extrusion loads be implemented in an ice crushing model such as VANILLA?

The answer to this subquestion was found during attempts to implement the extrusion and rubble models into the VANILLA ice model. An appropriate condition must be set on when to apply ice extrusion and rubble loads, which is currently done by applying the loads when one ice feature is in contact with the structure and the relative velocity is positive. It can be concluded that this is a good first attempt, but from issues regarding sudden load drops in CBR as described in Chapter 6 as well as a lack of intermittency in the extrusion loads it is clear that in future research, a better condition should be investigated. A condition based on previous steps could be tried, as well as one based on (a varying number of) multiple ice elements being in contact with the structure.

For accurate inclusion of the rubble and and extrusion loads into the VANILLA model, altering the pre-processor to determine model parameters is a necessity. Adjustment factors are proposed to accurately scale the ratios used in the pre-processor based on subdiving the mean total ice load in a load consisting of intact ice, extrusion and rubble loads. In future research, it should be determined if the original scaling coefficients used in the pre-processor are accurate for full scale crushing, as they were previously based on mainly model scale measurements. A larger contribution to the total load for extrusion in full scale may lower the peak loads at low indentation speeds.

Moreover, future research should be aimed at investigating the cause of the memory issues encountered when rubble and extrusion loads were considered at low indentation velocities. This issue leads to significant computation time increases, or to a situation on which convergence cannot be reached, which is obviously unwanted.

Also, it is recommended to establish to what extent ice rubble and extrusion loads are implicitly modelled in the Standard VANILLA model. This could be done by performing crushing tests for which the loads are measured locally over the ice-structure interface, such that the share of mainly extrusion loads to the total loads on which Standard VANILLA are based can be determined.

Lastly, for calculation of the side-side motion of the turbine, it is necessary to revise the formulas found for the extrusion and rubble forces, so that motion in the x-direction is a factor in the forces found. Then, a time component should also be included in these equations to account for temporal displacement of the ice edge and rubble pile (until ice drift in y-direction restores the situation to an interface where the structure perimeter is covered once more).

In the situation where ice extrusion is deemed to still be too uncertain for implementation, the rubble model could likely be implemented at an earlier stage, as it is easy to implement and uncertainty is considerably lower than for the extrusion model.

Answering of the main research question

With the rubble and extrusion loads established, as well as the proposed models implemented in VANILLA, the main research question could be answered. The rubble and extrusion loads pose additional damping to the system, although it must be noted that the magnitude of the rubble loads is low, such that influence of rubble loads on the dynamics of the structure is negligible. The added damping mainly results from the extrusion model, which has a number of implications on the dynamics of offshore wind turbines in an ice crushing event. These can be summarised as follows:

- In the IC regime, an immediate load drop to zero does not occur when extrusion and rubble loads are considered. As these drops are not observed in measurements, it can be concluded that this is a good result of the addition of extrusion and rubble loads.
- The added damping causes predicted transition speeds between the IIV regimes to be lower. Whether this is an improvement over the Standard VANILLA model cannot be concluded from these computations. Validation from future research would be required.
- A positive force-velocity gradient emerges from the velocity dependency of the extrusion force for the CBR regime. This is in agreement with observations in measurement campaigns, although the magnitude of the gradient as observed here can be questioned. Moreover, it is not certain that the gradient stems from only the extrusion loads, or also from the intact ice.

- Maximum and minimum displacement amplitudes are reduced, except for the minimum amplitudes for thin/weak ice. As the minimum displacement at waterline was found to be indicative of the magnitude of the blade loads encountered in research leading up to this thesis, it can be concluded that this result shows that blade loads modelled could be lower when ice extrusion and rubble loads are considered. However, it must be noted that the simple MATLAB computations performed here, are not nearly as accurate for modelling of offshore wind turbines as a coupled model such as BHawC with VANILLA at SGRE. Therefore, in future research, the Adjusted VANILLA model could be coupled to advanced turbine models (such as BHawC), to evaluate whether the blade loads calculated are indeed decreased.

Overall, it can be concluded that there is ample improvement possible for modelling the ice rubble and (especially) the extrusion loads, but this research has shown to be a good first attempt and that further research on the matter is worth the effort.

Bibliography

Abanades, J. (2019). Wind energy in the mediterranean spanish arc: The application of gravity based solutions. *Frontiers in Energy Research*, *7*, 83.

Al-Hashemi, H. M. B., & Al-Amoudi, O. S. B. (2018). A review on the angle of repose of granular materials. *Powder technology*, *330*, 397–417.

Bjerkås, M., Moslet, P., Jochmann, P., & Løset, S. (2003). Global ice loads on the lighthouse norströmsgrund in the winter 2001. *Proceedings of the International Conference on Port and Ocean Engineering Under Arctic Conditions*.

Bjerkås, M., & Skiple, A. (2005). Occurrence of continuous and intermittent crushing during ice-structure interaction. *18th International Conference on Port and Ocean Engineering Under Arctic Conditions*, 1131–1140.

Blenkarn, K. (1970). Measurement and analysis of ice forces on cook inlet structures. *Offshore Technology Conference*.

Bowles, J. E. (1988). *Foundation analysis and design*.

Brown, T. G., & Määttänen, M. (2009). Comparison of kemi-i and confederation bridge cone ice load measurement results. *Cold Regions Science and Technology*, *55*(1), 3–13.

Cawthorn, C., & Balmforth, N. (2010). Contact in a viscous fluid. part 1. a falling wedge. *Journal of fluid mechanics*, *646*, 327–338.

Cornett, A., & Timco, G. (1995). Laboratory tests on the mechanical properties of saline ice rubble. *NRC Report HYDCTR-002*.

Council, G. W. E. (2021). Gwec| global wind report 2021.

Croasdale, K. R. (2012). Ice rubbling and ice interaction with offshore facilities. *Cold Regions Science and Technology*, *76*, 37–43.

Daley, C. (1991). Ice edge contact-a brittle failure process model.

Daley, C., Tuhkuri, J., & Riska, K. (1996). Discrete chaotic ice failure model incorporating extrusion effects. *Report submitted to the National Energy Board by Daley R&E and the Helsinki University of Technology*.

Daley, C., Tuhkuri, J., & Riska, K. (1998). The role of discrete failures in local ice loads. *Cold regions science and technology*, *27*(3), 197–211.

Dyrcz, C. (2017). Analysis of ice conditions in the baltic sea and in the puck bay. *Zeszyty Naukowe Akademii Marynarki Wojennej*, *58*.

Ettema, R., & Schaefer, J. (1986). Experiments on freeze-bonding between ice blocks in floating ice rubble. *Journal of Glaciology*, *32*(112), 397–403.

Ettema, R., & Urroz, G. E. (1989). On internal friction and cohesion in unconsolidated ice rubble. *Cold Regions Science and Technology*, *16*(3), 237–247.

Evans, D. C., Nye, J. F., & Cheeseman, K. J. (1976). The kinetic friction of ice. *Proceedings of the Royal Society of London. A. Mathematical and Physical Sciences*, *347*(1651), 493–512.

Filsoof, O. T., Hansen, M. H., Yde, A., Bøttcher, P., & Zhang, X. (2021). A novel methodology for analyzing modal dynamics of multi-rotor wind turbines. *Journal of Sound and Vibration*, *493*, 115810.

Finn, D., Jordaan, I., Singh, S., & Spencer, P. (1989). Flow of crushed ice: Physical and mechanical properties and behaviour, volume 2: Analysis of data. *Ocean Engineering Research Centre, Memorial University of Newfoundland, St. John's, Newfoundland, Canada*.

Fransson, L. (2008). *Ice mechanics and shipping in ice-infested waters*. Division of Structural Engineering, Department of Civil, Mining and . . .

Fransson, L., Olofsson, T., & Sandkvist, J. (1991). Observations of the failure process in ice blocks crushed by a flat indentor. *International Conference on Port and Ocean Engineering under Arctic Conditions: 24/09/1991-28/09/1991*, *1*, 501–514.

Frederking, R., Jordaan, I., McCallum, J., et al. (1990). Field tests of ice indentation at medium scale, hobson's choice ice island, 1989. *Proceedings of 10th International Symposium on Ice, IAHR, Espoo, Finland*, *2*, 931–944.

Frederking, R., & Sudom, D. (2006). Maximum ice force on the molikpaq during the april 12, 1986 event. *Cold regions science and technology*, *46*(3), 147–166.

Frederking, R., & Barker, A. (2002). Friction of sea ice on steel for condition of varying speeds. *The Twelfth International Offshore and Polar Engineering Conference*.

Frost, H. (2001). Mechanisms of crack nucleation in ice. *Engineering Fracture Mechanics*, *68*(17-18), 1823–1837.

Gagnon, R., Andrade, S., Quinton, B., Daley, C., & Colbourne, B. (2020). Pressure distribution data from large double-pendulum ice impact tests. *Cold Regions Science and Technology*, *175*, 103033.

Gagnon, R. (2012). An explanation for the molikpaq may 12, 1986 event. *Cold regions science and technology*, *82*, 75–93.

Gravesen, H., Sørensen, S. L., Vølund, P., Barker, A., & Timco, G. (2005). Ice loading on danish wind turbines: Part 2. analyses of dynamic model test results. *Cold regions science and technology*, *41*(1), 25–47.

Hallam, S., & Pickering, J. (1988). Modelling of dynamic ice loading of offshore arctic structures. *Polar Tech 88, Proceedings from the International Conference on Technology for Polar Areas, Trondheim*, *1*, 235–248.

Hansen, M. (2015). *Aerodynamics of wind turbines*. Routledge.

Hendrikse, H., Hammer, T., Owen, C., van den Berg, M., van Beek, C., Polojärvi, A., Puolakka, O., & Willems, T. (2022). Ice basin tests for ice-induced vibrations of offshore structures in the shiver project. *41st International Conference on Ocean, Offshore and Arctic Engineering*, OMAE2022–78507.

Hendrikse, H., Ziemer, G., & Owen, C. (2018). Experimental validation of a model for prediction of dynamic ice-structure interaction. *Cold Regions Science and Technology*, *151*, 345–358.

Hendrikse, H. (2017). Ice-induced vibrations of vertically sided offshore structures.

Hendrikse, H. (2020). Ice strength coefficient c_R. *Informal paper*.

Hendrikse, H., & Metrikine, A. (2015). Interpretation and prediction of ice induced vibrations based on contact area variation. *International Journal of Solids and Structures*, *75*, 336–348.

Hendrikse, H., & Nord, T. S. (2019). Dynamic response of an offshore structure interacting with an ice floe failing in crushing. *Marine Structures*, *65*, 271–290.

Herrnring, H., & Ehlers, S. (2022). A finite element model for compressive ice loads based on a mohr-coulomb material and the node splitting technique. *Journal of Offshore Mechanics and Arctic Engineering*, *144*(2).

Hilding, D., Forsberg, J., & Gürtner, A. (2011). Simulation of ice action loads on offshore structures. *Proceedings of the 8th European LS-DYNA Users Conference, Strasbourg*.

Hoving, J. (2021). Lecture notes in Arctic Engineering.

Huang, G., & Liu, P. (2009). A dynamic model for ice-induced vibration of structures. *Journal of Offshore Mechanics and Arctic Engineering*, *131*(1).

International Electrotechnical Commission (IEC). (2019). Iec616400-3-1: Wind energy generation systems- part 3.1: Design requirements for fixed offshore wind turbines, 158.

IRENA. (2019). *Future of wind: Deployment, investment, technology, grid integration and socio-economic aspects (a global energy transformation paper)* (tech. rep.). International Renewable Energy Agency. Abu Dabhi.

Jenike, A. W., & Shield, R. (1959). On the plastic flow of coulomb solids beyond original failure.

Jenkins, N., Burton, T. L., Bossanyi, E., Sharpe, D., & Graham, M. (2021). *Wind energy handbook*. John Wiley & Sons.

Ji, S., & Liu, L. (2020). Dem analysis of ice loads on offshore structures and ship hull. *Computational granular mechanics and its engineering applications* (pp. 237–310). Springer Singapore. https://doi.org/10.1007/978-981-15-3304-4_8

Joensuu, A., & Riska, K. (1989). Contact between ice and structure. *Laboratory of Naval Architecture and Marine Engineering, Helsinki University of Technology, Espoo, Finland, Report M-88*.

Jones, S. J. (2007). A review of the strength of iceberg and other freshwater ice and the effect of temperature. *Cold Regions Science and Technology*, *47*(3), 256–262.

Jordaan, I. J. (2001). Mechanics of ice–structure interaction. *Engineering Fracture Mechanics*, *68*(17-18), 1923–1960.

Jordaan, I. J., & Timco, G. W. (1988). Dynamics of the ice-crushing process. *Journal of Glaciology*, *34*(118), 318–326.

Karna, T. (1992). A procedure for dynamic soil-structure-ice Interaction. *The Second International Offshore and Polar Engineering Conference*.

Kärnä, T., & Järvinen, E. (1994). Dynamic unloading across the face of a wide structure. *Proceedings of the 12th International Association of Hydraulic Engineering and Research on Ice Symposium (IAHR'94)*, *3*, 1018–1039.

Kärnä, T., Kamesaki, K., & Tsukuda, H. (1997). A flaking model of dynamic ice-structure interaction. *VTT Building Technology Internal Report RTE38-IR-7/1997*.

Kärnä, T. (1994). Finite ice failure depth in penetration of a vertical indentor into an ice edge. *Annals of Glaciology*, *19*, 114–120.

Kärnä, T., & Jochmann, P. (2003). Field observations on ice failure modes. *Proceedings of the 17th International Conference on Port and Ocean Engineering under Arctic Conditions, Trondheim, Norway, June*, 16–19.

Kärnä, T., Kamesaki, K., & Tsukuda, H. (1999). A numerical model for dynamic ice–structure interaction. *Computers & structures*, *72*(4-5), 645–658.

Kärnä, T., Muhonen, A., & Sippola, M. (1993). Rate effects in brittle ice crushing. *12th International Conference on Port and Ocean Engineering Under Arctic Conditions, POAC 93*, 59–71.

Kärnä, T., & Qu, Y. (2005). Analysis of the size effect in ice crushing–edition 2. *VTT, Internal Report RTE50-IR-6/2005*, 205.

Katsaprakakis, D. A., Papadakis, N., & Ntintakis, I. (2021). A comprehensive analysis of wind turbine blade damage. *Energies*, *14*(18), 5974.

Kheisin, D., & Cherepanov, N. (1973). Ice was investigated during the experimental work on natural freshwater. *Problems of the Arctic and Antarctic*, *33*, 239.

Kietzig, A.-M., Hatzikiriakos, S. G., & Englezos, P. (2010). Physics of ice friction. *Journal of Applied Physics*, *107*(8), 4.

Kujala, P. (1994). Modelling of the ice-edge failure process with curved failure surfaces. *Annals of Glaciology*, *19*, 158–164.

Kurdyumov, V., & Kheisin, D. (1976). Hydrodynamic model of the impact of a solid on ice. *Soviet Applied Mechanics*, *12*(10), 1063–1068.

Liferov, P., & Bonnemaire, B. (2005). Ice rubble behaviour and strength: Part i. review of testing and interpretation of results. *Cold Regions Science and Technology*, *41*(2), 135–151.

Løset, S., Shkhinek, K. N., Gudmestad, O. T., & Høyland, K. V. (2006). *Actions from ice on arctic offshore and coastal structures*. Lan St. Petersburg, Russia.

Määttänen, M., Marjavaara, P., Saarinen, S., & Laakso, M. (2011). Ice crushing tests with variable structural flexibility. *Cold Regions Science and Technology*, *67*(3), 120–128.

Makkonen, L., & Tikanmäki, M. (2014). Modeling the friction of ice. *Cold Regions Science and Technology*, *102*, 84–93.

Mamouri, A. R., Khoshnevis, A. B., & Lakzian, E. (2020). Experimental study of the effective parameters on the offshore wind turbine's airfoil in pitching case. *Ocean Engineering*, *198*, 106955.

Marchenko, A. (2022). Thermo-hydrodynamics of sea ice rubble. *IUTAM Symposium on Physics and Mechanics of Sea Ice*, 203–223.

Mathew, S. (2014). Wind turbine design. https://www.lesics.com/wind-turbine-design.html

Matlock, H. H., Dawkins, W. P., & Panak, J. J. (1971). Analytical model for ice-structure interaction. *Journal of the Waterways and Harbors Division*, *97*.

Mayne, D., & Brown, T. (2000). Rubble pile observations. *The Tenth International Offshore and Polar Engineering Conference*.

Metcalf, J. (1966). Angle of repose and internal friction. *International Journal of Rock Mechanics and Mining Sciences & Geomechanics Abstracts*, *3*(2), 155–161.

Nevel, D. (1986). Iceberg impact forces. *Proc. of the International Association of Hydraulic Research symposium IAHR*, *86*, 345–369.

Oksanen, P., & Keinonen, J. (1982). The mechanism of friction of ice. *Wear*, *78*(3), 315–324.

Palmer, A., Goodman, D., Ashby, M., Evans, A., Hutchinson, J., & Ponter, A. (1983). Fracture and its role in determining ice forces on offshore structures. *Annals of glaciology*, *4*, 216–221.

Patil, A., Sand, B., Cwirzen, A., & Fransson, L. (2021). Numerical prediction of ice rubble field loads on the norströmsgrund lighthouse using cohesive element formulation. *Ocean Engineering*, *223*, 108638.

Peyton, H. (1968). Sea ice forces. *Proc. Conference on Ice Pressures Against Structures. National Research Council of Canada*.

Pritchard, R. S., Knoke, G. S., Douglas, C., et al. (2012). Sliding friction of sea ice blocks. *Cold regions science and technology*, *76*, 8–16.

Rabatel, M., Labbé, S., & Weiss, J. (2015). Dynamics of an assembly of rigid ice floes. *Journal of Geophysical Research: Oceans*, *120*(9), 5887–5909.

Renewables, D. E. (2021). How do wind turbines work?: Blog. https://sustainablesolutions.duke-energy.com/resources/how-do-wind-turbines-work/

Riska, K., Rantala, H., & Joensuu, A. (1990). Full scale observations of ship-ice contact. *Helsinki University of Technology, Laboratory of Naval Architecture and Marine Engineering, Report M-97*.

Riska, K. (2018). Ice edge failure process and modelling ice pressure. *Philosophical Transactions of the Royal Society A: Mathematical, Physical and Engineering Sciences*, *376*(2129), 20170340.

Rissanen, S., & Heinonen, J. (2016). Simulations of drifting sea ice loads on offshore wind turbine. *Winterwind 2016*, *1*(1), p1–19.

Rist, M., & Murrell, S. (1994). Ice triaxial deformation and fracture. *Journal of Glaciology*, *40*(135), 305–318.

Ronkainen, I. et al. (2013). Long-term changes in baltic sea ice conditions.

Saeki, H., Ono, T., Nakazawa, N., Sakai, M., & Tanaka, S. (1986). The coefficient of friction between sea ice and various materials used in offshore structures.

Salimi-Majd, D., Azimzadeh, V., & Mohammadi, B. (2015). Loading analysis of composite wind turbine blade for fatigue life prediction of adhesively bonded root joint. *Applied Composite Materials*, *22*(3), 269–287.

Sanderson, T. J. (1988). Ice mechanics and risks to offshore structures.

Sanderson, T. J., & Child, A. (1986). Ice loads on offshore structures: The transition from creep to fracture. *Cold Regions Science and Technology*, *12*(2), 157–161.

Savage, S., Sayed, M., & Frederking, R. (1992). Two-dimensional extrusion of crushed ice. part 2: Analysis. *Cold regions science and technology*, *21*(1), 37–47.

Sayed, M., & Frederking, R. M. (1992). Two-dimensional extrusion of crushed ice. part 1: Experimental. *Cold regions science and technology*, *21*(1), 25–36.

Sazonov, K., & Simakina, A. (2021). On the main factors in ice rubble pile development against the sloped structure. *The 31st International Ocean and Polar Engineering Conference*.

Schulson, E. M. (2018). Friction of sea ice. *Philosophical Transactions of the Royal Society A: Mathematical, Physical and Engineering Sciences*, *376*(2129), 20170336.

Schulze, D. (2014). Flow properties of powders and bulk solids.

Shkhinek, K., Kärnä, T., Kapustiansky, S., & Jilenkov, A. (2001). Influence of ice speed and thickness on ice pressure and load. *Proceedings of the International Conference on Port and Ocean Engineering Under Arctic Conditions*.

Singh, S., Jordaan, I., Xiao, J., & Spencer, P. (1995). The flow properties of crushed ice.

Sinha, N. K. (1991). Kinetics of microcracking and dilatation in polycrystalline ice. *Ice-structure interaction* (pp. 69–87). Springer.

Sinha, N. K. (1989). Microcrack-enhanced creep in polycrystalline material at elevated temperature. *Acta metallurgica*, *37*(11), 3107–3118.

Skjoldan, P. F. (2011). Aeroelastic modal dynamics of wind turbines including anisotropic effects.

Soares-Ramos, E. P., de Oliveira-Assis, L., Sarrias-Mena, R., & Fernández-Ramırez, L. M. (2020). Current status and future trends of offshore wind power in europe. *Energy*, *202*, 117787.

Sodhi, D. S., & Haehnel, R. B. (2003). Crushing ice forces on structures. *Journal of cold regions engineering*, *17*(4), 153–170.

Spencer, P., Masterson, D., Lucas, J., & Jordaan, I. (1992). The flow properties of crushed ice: Experimental observation and apparatus. *Proceedings of the 1 lth International Association for Hydraulic Research Ice Symposium, Banff, Alta*, 258–268.

Strub-Klein, L., & Sudom, D. (2012). A comprehensive analysis of the morphology of first-year sea ice ridges. *Cold Regions Science and Technology*, *82*, 94–109.

Sukhorukov, S. (2013). Ice-ice and ice-steel friction in field and in laboratory.

Sukhorukov, S., & Løset, S. (2013). Friction of sea ice on sea ice. *Cold Regions Science and Technology*, *94*, 1–12.

Suryakanta. (2015). 3 most common types of lateral earth pressure. https://civilblog.org/2015/06/13/3-most-common-types-of-lateral-earth-pressure/

Taylor, R., & Jordaan, I. (2015). Probabilistic fracture mechanics analysis of spalling during edge indentation in ice. *Engineering Fracture Mechanics*, *134*, 242–266.

The International Organization for Standardization (ISO). (2019). Iso 19906: An international standard for arctic offshore structures. https://doi.org/10.4043/22068-MS

Timco, G. (1987). Indentation and penetration of edge-loaded freshwater ice sheets in the brittle range.

Timco, G., & Cornett, A. (1999). Is φ a constant for broken ice rubble? *Proceedings of the 10th Workshop on River Ice.*, 318–331.

Timco, G., & Jordaan, I. (1987). Time-series variations in ice crushing. *9th Int. Conf. on Port and Ocean Engineering under Arctic Conditions, POAC*, *87*, 13–20.

Tongkui, L., & Jizu, X. (1989). Selection of the probabilistic and mechanical models in the bohai sea ice design criteria. *China Offshore Oil & Gas (Engineering)*, *1*(2), 17–24.

Tuhkuri, J., & Riska, K. (1990). Results from tests on ice extrusion of crushed ice. *Otaniemi: Helsinki University of Technology, Faculty of Mechanical Engineering, Laboratory of Naval Architecture and Marine Engineering, M-98*.

Tuhkuri, J. (1997). Experimental investigations and computational fracture mechanics modelling of brittle ice fragmentation.

Tuhkuri, J. (1993). *Laboratory tests of ship structures under ice loading: Volume 1*. Helsinki University of Technology, Faculty of Mechanical Engineering Ship . . .

Tuhkuri, J. (1994). Analysis of ice fragmentation process from measured particle size distributions of crushed ice. *Cold regions science and technology*, *23*(1), 69–82.

van den Berg, M., Owen, C. C., & Hendrikse, H. (2022). Experimental study on ice-structure interaction phenomena of vertically sided structures. *Cold Regions Science and Technology*, *201*, 103628.

Van der Stap, F. (2022). Ice-structure interaction in the baltic sea: Defining a feasibility map for monopiles. *Masters thesis (unpublished)*.

Wang, Q., Li, Z., Lu, P., Cao, X., & Leppäranta, M. (2018). In situ experimental study of the friction of sea ice and steel on sea ice. *Applied Sciences*, *8*(5), 675.

Wells, J., Jordaan, I., Derradji-Aouat, A., & Taylor, R. (2011). Small-scale laboratory experiments on the indentation failure of polycrystalline ice in compression: Main results and pressure distribution. *Cold Regions Science and Technology*, *65*(3), 314–325.

Withalm, M., & Hoffmann, N. (2010). Simulation of full-scale ice–structure-interaction by an extended matlock-model. *Cold regions science and technology*, *60*(2), 130–136.

Xiao, J., Jordan, I., McKenna, R., & Frederking, R. (1991). Finite element modelling of spherical indentation tests on ice. *11 th International Conference on Port and Ocean*

Engineering under Arctic Conditions- POAC'91, St. John's, Newfoundl, Can, 09/24-28/91, 471–485.

Ye, K., Li, C., Yang, Y., Zhang, W., & Xu, Z. (2019). Research on influence of ice-induced vibration on offshore wind turbines. *Journal of Renewable and Sustainable Energy*, *11*(3), 033301.

Yin, L. L., Lo, K. H., & Wang, S. S. (2017). Effects of blade pitch, rotor yaw, and wind–wave misalignment on a large offshore wind turbine dynamics in western gulf of mexico shallow water in 100-year return hurricane. *Journal of Offshore Mechanics and Arctic Engineering*, *139*(1).

A

Derivations, descriptions, model parameters and sensitivities

A-1 Mohr-Coulomb flow description

For completeness, the Mohr-Coulomb flow description is treated here in more detail, after the general discussion in Chapter 3.

The theories of soil mechanics used for obtaining granular flow descriptions start from a continuity equation and a momentum equation as in Equations A.1 and A.2 respectively.

$$\frac{\mathrm{D}(\rho_{\mathrm{S}}\alpha)}{\mathrm{D}t} + \rho_{\mathrm{S}}\alpha\frac{\partial u_i}{\partial x_i} = 0 \qquad \text{(A.1)} \qquad\qquad \rho_{\mathrm{S}}\alpha\frac{\mathrm{D}u_k}{\mathrm{D}t} = \rho_{\mathrm{S}}\alpha g_{\mathrm{k}} - \frac{\partial \sigma_{ki}}{\partial x_i} \qquad \text{(A.2)}$$

Here, ρ_{S} is the density of the solid grains (in kg/m^3), α is the (dimensionless) solids volume fraction and $\frac{\partial u_i}{\partial x_i}$ and $\frac{\partial \sigma_{ki}}{\partial x_i}$ are the velocity (in m/s) and stress (in Pa) tensors respectively.

The first Mohr-Coulomb flow model was proposed by Jenike and Shield, 1959, who use the above equations and the yield criterion from Mohr's circle, to describe a flow in which once the criterion is met and the material starts to flow, the stresses must continue to obey that yield criterion. The yield criterion is the one encountered earlier in Equation 3.1.

By assuming that the continuum only exists of solids and is incompressible, thus having a constant density, they make use of the simplified continuity and momentum equations as in Equations A.3 and A.4.

$$\nabla \cdot \boldsymbol{u} = 0 \qquad \text{(A.3)} \qquad\qquad \rho\frac{\mathrm{d}\boldsymbol{u}}{\mathrm{d}t} = -\nabla \cdot \boldsymbol{p} + \rho\boldsymbol{g} \qquad \text{(A.4)}$$

The purpose of their description, is to describe the process of two rigid plates moving towards each other, as in the experiments. It therefore makes use of the parameters as shown in A-1(a), with *L* the half length of the top plate and *h(x,t)* is the distance between the stationary bottom plate and the upper plate that is moving with a constant velocity *V*. The distance that separates the plates is a function of both time *t*, and the position over the height of the top plate *x*, in the case the top plate is curved. Then *h(x,t)* is given by Equations A.5 and A.6, in which h_0 is normalised with the gap height *H* at $t = 0$ and $x = 0$ ($h(0, 0)$).

$$h(x,t) = h_0(x) - t \qquad \text{(A.5)} \qquad\qquad h_0(x) = 1 - \beta \mathrm{f}(x) \qquad \text{(A.6)}$$

Using this description for *h(x,t)*, it is possible to describe other setups than one that uses parallel plates through varying β and f(*x*). This is shown in Figure A-1(b).

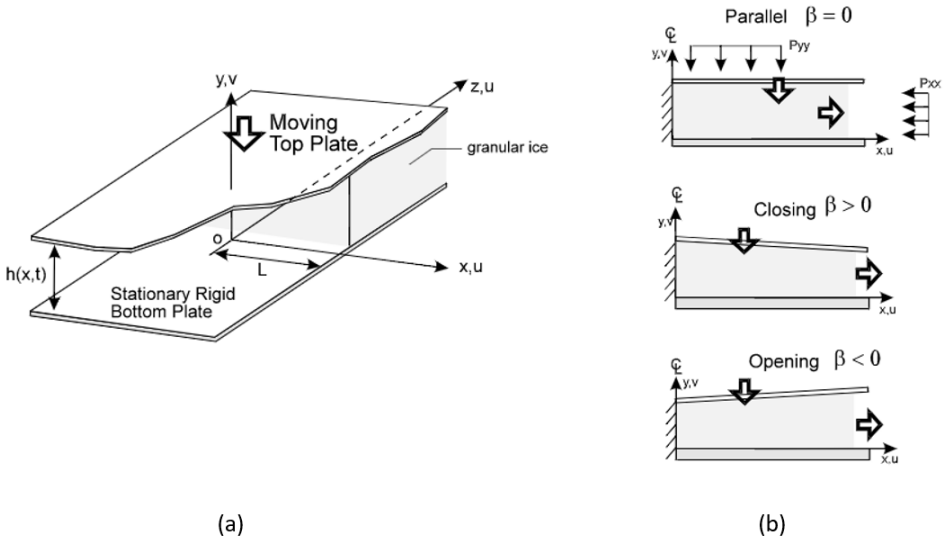

Figure A-1: (a) Definition sketch for extrusion of crushed ice between rigid plates. (b) Sketches showing how varying β defines the geometry. From Daley et al., 1996.

The Mohr-Coulomb criterion, from which this flow description got its name, is implemented through the relation for the pressure at the walls as given in Equation A.7

$$p_{\mathrm{xy}} = \pm(p_{\mathrm{yy}} + \frac{C}{\tan\phi}) \tan\delta \qquad \text{(A.7)}$$

where p_{xy} is the shear stress at the wall, p_{yy} the normal stress, C the cohesion and ϕ the internal friction angle of the granular ice, with δ the friction angle of the wall surface. By assuming that the upper plate is only slightly curved, such that $\beta \ll 1$, and using the above relations, Savage et al., 1992 have found a general solution for the depth averaged normal

stress $\overline{p}_{yy}$. It is as shown in Equation A.8. For the derivation, reference is made to the original paper.

$$\frac{\partial \overline{p}_{yy}}{\partial x} + \frac{\tan\delta_0 + \tan\delta_h}{\varepsilon \overline{k} h}\overline{p}_{yy} = -\frac{C(\tan\delta_0 + \tan\delta_h)}{\varepsilon \overline{k} h \tan\phi} - \frac{G(\tan\delta_0 - \tan\delta_h)}{2\varepsilon\overline{k}} - \frac{2Ex}{h^2\varepsilon\overline{k}} + \frac{Ex^2}{h^3\varepsilon\overline{k}}\frac{\partial h_0}{\partial x} \tag{A.8}$$

Here, the variables are:

δ_0	Wall friction angle at the bottom plate (y = 0) [°]	ϕ	Internal friction angle [°]
δ_h	Wall friction angle at the top plate (y = h) [°]	x	Coordinate (see Figure A-1)
ρ	Density [kg/m^3]	L	Wall length (see Figure A-1) [m]
C	Cohesion [-]	V	Velocity of the top plate [m/s]
		P	Characteristic pressure [Pa]
		H	Initial gap, h(x=0,t=0) [m]

The dimensionless coefficients are as follows:

$$\varepsilon = \frac{H}{L} \qquad \overline{k} = \frac{\tan\delta_h}{2(\tan\delta_0 + \tan\delta_h)}(k_h + k_{zs}) + \frac{\tan\delta_0}{2(\tan\delta_0 + \tan\delta_h)}(k_0 + k_{zs})$$

$$E = \frac{\rho V^2}{\varepsilon P} \qquad k_0 = 2[1 - \sqrt{1 - (1 + \tan^2\delta_0)\cos^2\phi}]/\cos^2\phi - 1$$

$$G = \frac{\rho g H}{P} \qquad k_h = 2[1 - \sqrt{1 - (1 + \tan^2\delta_h)\cos^2\phi}]/\cos^2\phi - 1$$

$$k_{zs} = \frac{1 - \sin\phi}{1 + \sin\phi}$$

The general solution can be simplified for the case of parallel plates, such that it is possible to obtain a closed form solution, as treated in the original paper.

When a non-parallel geometry is to be analysed, the general solution can be solved for using computer aided numerical integration, through for instance the (fourth order) Runge-Kutta method. This would be required for the ice edge geometries seen in crushing, as was shown in Section 3-4.

Daley et al., 1996 put forward a number of approximating methods for simplifying the closed form solution of Equation A.8, to reduce computation time in the simulations they performed. These allow for the addition of an overburden pressure on top and below of the extrusion channel due to rubble, as well as a varying β, though the approximation starts to deviate from the general solution for $\beta < -0.04$.

From the formulas above, it can be seen that when $H \longrightarrow 0$ whenever there is full contact, $\overline{p}_{yy} \longrightarrow \infty$. This prevents usage of this description in a model that considers direct contact. Moreover, approximations for the Mohr-Coulomb flow named above fail for the geometry of

the ice edge in crushing as described in Chapter 3, which shows a larger angle than fit for the approximations. Thus the current forms of the Mohr-Coulomb description cannot be used for extrusion modelling, requiring a new mathematical description for future implementation.

A-2 Derivation of the pressure distribution from extrusion

For the model used, a viscous flow description was adopted. Here, the derivation of the formulas used is shown. The same starting point as in Singh et al., 1995 is used, where the equilibrium in Equation A.9 follows from Figure 3.7.

$$\frac{\partial p}{\partial x} = \frac{\partial \tau}{\partial y} \tag{A.9}$$

With the flow symmetrical about the $y = h(x)$ plane, integrating Equation A.9 in y and with $\tau = 0$ at $y = h$, the shear is found as in Equation A.10, where $G = -\frac{\partial p}{\partial x}$.

$$\tau = G(h(x) - y) \tag{A.10}$$

With flow being positive in the x-direction, the pressure gradient is negative and $G > 0$. Combining Equations 3.5 and A.10 yields Equation A.11.

$$\frac{\partial u_x}{\partial y} = KG^N(h(x) - y)^N \tag{A.11}$$

Integrating between 0 and y, applying boundary condition $u_x = 0$ at $y = 0$, Equation A.12 follows.

$$u_x = \frac{KG^N}{n+1}[(h(x) - y)^{N+1} - h(x)^{N+1}] \tag{A.12}$$

From flow continuity, the relation in Equation A.13 can be found.

$$xV = -2\int_0^{h(x)} u_x dy \tag{A.13}$$

Inserting Equation A.12, yields Equation A.14.

$$\begin{aligned} xV &= -2\int_0^{h(x)} \frac{KG^N}{N+1}[(h(x)-y)^{N+1} - h(x)^{N+1}]dy \\ &= -2\frac{KG^N}{N+1}[-\frac{1}{N+2}(h(x)-y)^{N+2} - h(x)^{N+1}y]\Big|_0^{h(x)} \\ &= -2\frac{KG^N}{n+1}[(\frac{1}{N+2}-1)h(x)^{N+2}] \\ &= -2\frac{KG^N}{N+1}[-\frac{N+1}{N+2}h(x)^{N+2}] \\ &= \frac{2KG^N}{N+2}h(x)^{N+2} \end{aligned} \tag{A.14}$$

Rearranging yields Equation A.15.

$$G = Ax^{1/N} \tag{A.15}$$

where $A = [\frac{V(N+2)}{2Kh(x)^{N+2}}]^{1/N}$.

Letting h vary linearly from 0 (where the intact ice meets the structure) to h_{top} (at the upper ice edge), $h(x) = \frac{x}{L}h_{\text{top}}$. Then from Equation A.15, Equation A.16 follows.

$$\begin{aligned} G &= [\frac{V(N+2)}{2K}(\frac{x}{L}h_{\text{top}})^{-(N+2)}]^{1/N}x^{1/N} \\ &= [\frac{V(N+2)L^{N+2}}{2Kh_{\text{top}}^{N+2}}]^{1/N}x^{-(N+2)/N}x^{1/N} \\ &= [\frac{V(N+2)L^{N+2}}{2Kh_{\text{top}}^{N+2}}]^{1/N}x^{-(N+1)/N} \end{aligned} \tag{A.16}$$

Integrating from x to L, using $G = -\frac{\partial p}{\partial x}$ gives Equation A.17.

$$
\begin{aligned}
\int_x^L -\frac{\partial p}{x} dx &= \int_x^L [\frac{V(N+2)L^{N+2}}{2Kh_{\text{top}}^{N+2}}]^{1/N} x^{-(N+1)/N} dx \\
-p(x)\Big|_x^L &= [\frac{V(N+2)L^{N+2}}{2Kh_{\text{top}}^{N+2}}]^{1/N} \int_x^L x^{-(N+1)/N} dx \\
-p_0 + p_x &= [\frac{V(N+2)L^{N+2}}{2Kh_{\text{top}}^{N+2}}]^{1/N} [-Nx^{-1/N}]\Big|_x^L \\
p_x &= [\frac{V(N+2)L^{N+2}}{2Kh_{\text{top}}^{N+2}}]^{1/N} N(x^{-1/N} - L^{-1/N}) + p_0
\end{aligned}
\tag{A.17}
$$

A-3 Model parameters used in computations

A number of model parameters were used in the computations, both for the extrusion and rubble modelling. For these, decent values had to be assumed from literature. The parameters considered for the rubble computations are listed in Table A-1, those for the extrusion computations are listed in Table A-2.

Table A-1: Model parameters as used for the rubble modelling.

Symbol	Value	Unit	Meaning
ρ_w	1025	kg/m^3	Density of seawater
ρ_{ice}	907	kg/m^3	Density of sea ice
η_{sr}	0.3	-	Porosity of sail
η_{kr}	0.3	-	Porosity of keel
Φ	40	°	Internal friction angle rubble
r_{ul}	2.5	-	Ratio of keel to sail length
r_{fs}	1.9	-	Ratio of rubble pile length at front (θ = 90°) and side (θ = 0°)
c	3	kPa	Rubble cohesion
θ_{sr}	35	°	Sail angle
θ_{kr}	45	°	Keel angle
μ_{ii}	0.44	-	Kinetic ice-ice friction coefficient
μ_{is}	0.05	-	Kinetic painted steel-ice friction coefficient
N_ϑ	50	-	Number of segments around the structure perimeter

Table A-2: Model parameters as used for the extrusion modelling.

Symbol	Value	Unit	Meaning
t_r	5	mm	Pressure ridge height
K	$0.8*10^{-7}$	-	Nonlinear viscous flow coefficient
n	1.67	-	Nonlinear viscous flow power coefficient
p_{lim}	15	MPa	Force limit for viscous extrusion pressure
ψ	40	°	Ice edge angle
α	90	°	Structure angle
D	7.5	m	Structure width at waterline
N_z	100	-	Number of vertical segments
N_ϑ	50	-	Number of segments around the structure perimeter

The theoretical background and explanation for some of the assumed values are given here. These are the friction coefficients, porosity, angle of internal friction, cohesion and the angles of the sail and the keel. They are discussed below.

Friction

At small scale, all surfaces show imperfections (valleys and hills), termed *asperities*, leading to *surface roughness*. Through interlocking and deformation, these asperities oppose motion of one of the surfaces relative to the other, causing friction. Ice-ice friction plays a role for the sliding mode and ice-structure (ice-steel for an OWT) friction as well for the internal failure mode in the rubble model. First, the specifics of ice-ice friction are discussed, followed by ice-steel friction.

Ice-ice friction (μ_{ii})

A very thorough discussion of the mechanisms and characteristics for both static and kinetic ice-ice friction is given in Schulson, 2018, following from an analysis of a great number of tests and campaigns on the topic.

In many reports on the kinetic friction of ice on ice at low temperatures, a velocity dependency is found, where $\mu_k \propto v^{-1/2}$, called *velocity weakening* (such as by Evans et al., 1976). This can be explained from the increase in frictional heating at higher speeds. increasing the lubricating layer thickness. For warmer ice, the increase in layer thickness may increase the friction coefficient when hydrodynamic friction comes into play, so that it was found that $\mu_{k,ii} \propto v^{1/2}$, called *velocity strengthening* (such as by Oksanen and Keinonen, 1982).

However, as found by Pritchard et al., 2012 and Sukhorukov and Løset, 2013, no velocity

dependency can be found for sliding on unsmoothed, previously untouched ice surfaces. This can be explained from the high roughness of these surfaces, such that for all speeds tested the liquid layer never attains a thickness that is significant on the scale of the asperities and the regime is dry friction. By repeated sliding of the same ice block on the same surface, leading to surface polishing, Sukhorukov and Løset, 2013 found the $\mu_{\text{k,ii}} \propto v^{-1/2}$ dependency mentioned earlier. This shows that is important to differentiate between sliding between previously untouched surfaces and surfaces that have seen sliding already.

Further, Pritchard et al., 2012 report decreasing friction coefficient for increased weight of the sliding block, from about 0.6 for a block weighing 0.3 kN, to about 0.4 for a weight of 3 kN. This could be because of increased squeeze out while in the hydrodynamic friction regime, for example for warm ice. It could also be caused by increase in the real contact area, increasing solid-solid adhesion, as was found by Sukhorukov, 2013. As they did not measure the ice temperature, that is hard to evaluate. Sukhorukov and Løset, 2013 reported that there was no dependency of the normal load.

Pritchard et al., 2012 also reports an increase of about 25$\%$ for $\mu_{\text{k,ii}}$ on a snow-covered ice surface. Lastly, they found that the often reported stick-slip motion was caused by compliance of the test setup. This can explain the observation of the same behaviour in other tests, as opposed to it being a fundamental characteristic of ice sliding on ice.

Sukhorukov and Løset, 2013 did not find a difference in kinetic friction coefficient on a wet surface. Likely, the weight of the block squeezes out the initial layer and prevents water seeping in between the asperities. Lastly, they reported that there was no difference between sliding on the top or the bottom of a newly cut out ice block, such that the top and bottom of the ice can be assumed equally rough.

Friction of (small sized) ice rubble on level ice has thus far not been measured. Therefore, the kinetic friction coefficient has to be based on the previously mentioned research. The rubble piles (both above and below the ice surface) slide over an unsmoothed ice surface. Moreover, the rubble in the piles continuously renew from extrusion and discharge. Therefore, it can be assumed that the friction is velocity independent. With the piles having significant weight and buoyancy, no effect from a wet surface below the ice surface is expected. Based on this, the values reported for $\mu_{\text{k,ii}}$ by Sukhorukov and Løset, 2013 can be assumed accurate. These values were obtained for surfaces that were cleared from snow. The average value of $\mu_{\text{k,ii}} = 0.44$ can be assumed representative for the rubble pile sliding mode for both the sail and the keel.

Ice-steel friction (μ_{is})

Ice-steel friction is discussed in detail in Kietzig et al., 2010, with some dependencies deviating when compared to the ice-ice friction. This can be mostly attributed to the (much) higher thermal conductivity of steel. This higher thermal conductivity reduces the effect of frictional heating. Moreover, the fractality of steel is different to that of ice, changing its

dependence on certain parameters, such as temperature and sliding velocity. Saeki et al., 1986 have also shown that there are differences between steel with different treatments (polished/corroded/coated).

However, just like for the ice-ice friction, dependencies found in literature, tend to vary from paper to paper. For coated steel, such as used for OWTs, R. Frederking and Barker, 2002 find a kinetic friction coefficient that decreases with increasing velocity, while Wang et al., 2018 find a clear increases for increasing velocity, where it should be noted that the former was found in the lab, whereas the latter measured in the field. The former however measured the first slide(s) on newly formed ice, whereas the latter measured repeated sliding on the same track, where Sukhorukov, 2013 have shown that repeated sliding leads to different results, as discussed above.

Models for estimating friction coefficients, such as shown in Kietzig et al., 2010 and more recently by Makkonen and Tikanmäki, 2014 try to capture the effects of changing combinations of parameters (sliding velocity/temperature/etc.). These are however overly complicated, include non-physical parameters, or do not distinguish between first-time sliding or repeated sliding. Therefore, the value used for the kinetic friction coefficient for ice-steel interaction of the rubble pile with the coated steel transition piece of the turbine is assumed to be $\mu_{\text{k,is}} = 0.05$ from the results of R. Frederking and Barker, 2002, since they measured first-time sliding.

Porosity

Knowledge of the porosity of the ice rubble is important for evaluating Equation 4.3. For ice rubble, the macro-porosity is defined as in Equation A.18 (from Løset et al., 2006).

$$n = \frac{V_{\text{sea water}} + V_{\text{air}}}{V_{\text{total}}} = \frac{V_{\text{sea water}} + V_{\text{air}}}{V_{\text{sea water}} + V_{\text{air}} + V_{\text{pure ice}} + V_{\text{brine pockets}}} \tag{A.18}$$

Here, V indicates a volume, with the subscript indicating of what (all in m^3) Porosity of ice rubble has been measured on various campaigns in the past. These are based on rubble found in rubble fields, resulting from collisions between ice features, instead of resulting from crushing events with a structure. The difference between the two lies in the size of the ice particles. Rubble fields consist mostly of large ice blocks, resulting from flexural failure, whereas in the rubble from ice-structure interaction may contain (much) smaller particles due to crushing and extrusion. This was reported by Kärnä and Jochmann, 2003, who observed reduced particle sizes in the rubble pile during pure crushing events, when compared to mixed crushing and flexural failure events or pure flexural failure events. Unfortunately, their campaign did not include porosity measurements.

That means that, for now, rubble porosity values remain based on measurements of field rubble. Løset et al., 2006 report typical porosity values of first-year ice ridges of 25-40$\%$. The porosity may vary due to consolidation, which is (re-)freezing of the water between the rubble,

such that the porosity decreases. This takes time (termed hold time), which is longer than the time scales of crushing events. Therefore, values of porosity in rubble stemming from crushing events with structures, should be based on unconsolidated rubble measurements. Strub-Klein and Sudom, 2012 and Marchenko, 2022 contain overviews of the results of various field campaigns. For the Baltic region, values of 20-40$\%$ were reported for unconsolidated rubble porosities.

Angle of internal friction

The angle of internal friction (ϕ) is required for calculation of the passive and/or active earth pressure. It can be described as a measure of the ability of a material to withstand shear stress. It is the angle, measured between the normal force and resultant force attained when failure occurs in response to a shearing stress. It is the slope of the failure envelope in the Mohr's circle diagram. The shear strength, and thus the angle of internal friction results from four components: interlocking, frictional contacts, freeze-bonding and failure of the ice blocks. The interlocking and frictional resistance are macro-level phenomena and affected by the shape and the size of the ice blocks, while the breaking of the freeze bonds and failure of the ice blocks are considered as micro-level phenomena (Patil et al., 2021).

Ettema and Urroz, 1989 report that the shear strength, and thus ϕ, depends on time, normal pressure, porosity, as well as shape and packing of ice fragments. Further, temperatures and water salinity are additional factors which may affect the shear strength. Additionally, Timco and Cornett, 1999 report dependence on confinement and strain ratio. This explains the wide range of reported values for ϕ, found from triaxial and shear box tests. This is further explained by the inconsistency of reporting the peak friction angle, ϕ_{p}, or the continuous shear friction angle, ϕ_{c}. The former is the friction angle at the peak of the stress-strain curve, while the latter is at large strains, for which ϕ is lower. Using ϕ_{p} is appropriate for assessing the internal strength of relatively compact ice rubble at small strains, while ϕ_{c} is appropriate for loose rubble and large strains. Thus, for dynamic processes such as the internal failure mode described above, ϕ_{c} is more appropriate.

Liferov and Bonnemaire, 2005 reported an overview of recently found values for ϕ from various test campaigns, which show a wide spread, with $\phi = 25° - 65°$. Based on their own evaluations, they found that ϕ lies between 36° and 44°, with the lowest being for wet blocks without slush, while the higher value being for dry blocks. This intermediate case of 40° seems appropriate for the case of a dynamic, newly formed rubble pile from ice-structure interaction as of interest here.

Cohesion

Cohesion is attributable to adhesive forces, in ice notably from freeze-bonding happening at the contact points between ice blocks (or smaller bits of ice). In the past, rubble has been considered a cohesionless material, but according to Liferov and Bonnemaire, 2005 this

results in excessively high values for the internal friction angle when evaluating test results. Tests performed to asses the cohesion in ice rubble have been performed for example by Ettema and Schaefer, 1986 and Cornett and Timco, 1995. Values reported vary widely, like for the angle of internal friction above. This is because the cohesion is influenced by normal pressure, contact time and area, and salinity of the water in which freeze-bonding, or fusion, occurs. It increases with normal pressure and contact time and area, while it decreases with salinity (Ettema and Schaefer, 1986).

Since (to the authors knowledge) no tests have been performed on crushed ice at the size observed from crushing events (down to 2 mm), values for the cohesion for now have to be based on tests on larger rubble. Liferov and Bonnemaire, 2005 have analysed data from Cornett and Timco, 1995. They report the cohesion through the attraction a (in kPa). The relation with the cohesion is given in Equation A.19.

$$a = \frac{c}{\tan \phi} \tag{A.19}$$

For the case of $\phi = 40°$, which is reported to correspond to $a = 2.5$ kPa, this equates to $c \approx 3.0$ kPa. This is notably higher than the value assumed by Savage et al., 1992 for calculations on the extrusion tests, who used that $c = 0.5$ kPa (without stating a source). However, Ettema and Schaefer, 1986 have shown that the freeze-bond strength significantly increases due to normal pressure on the ice rubble. With the weight (sail) and buoyancy (keel) of the rubble for the case of rubble piles, the value of $c = 3$ kPa is deemed appropriate.

Angle of sail and keel

The angles that the sail and the keel make with the intact ice, θ_s and θ_k, are the last parameters of interest for the rubble calculations. Extending the analogy of using soil mechanics for the rubble problem, these angles can be seen described as the angle of repose, which is shown in Figure A-2. The angle of repose is the steepest slope of unconfined material, measured from the horizontal plane on which the material can be heaped, without collapsing (Al-Hashemi and Al-Amoudi, 2018). Though close to the same value of the internal friction angle, it is not the same, especially when the material is loosely packed (Metcalf, 1966). According to Al-Hashemi and Al-Amoudi, 2018, the angle of repose depends amongst others on the angle of internal friction itself, grain size and shape, density, moisture content, interface friction angle, stratification, roughness of the base at which the material is heaped, mass of the material, morphology of the material, addition of solvents and the direction a pile is stacked from. Most notable in this list of influential factors for the case of ice rubble piles, are the particle size and the moisture content.

As reported by Kärnä and Jochmann, 2003, particle size decreases for pure crushing events when compared to mixed failure events. According to Al-Hashemi and Al-Amoudi, 2018, the angle of repose increases for decreasing particle size, such that it can be expected that the

angle of repose is larger for pure crushing events, when compared to mixed events. With measurements of the particle sizes at various speeds lacking, it can not be said how the angle of repose is expected to change for varying indentation speeds.

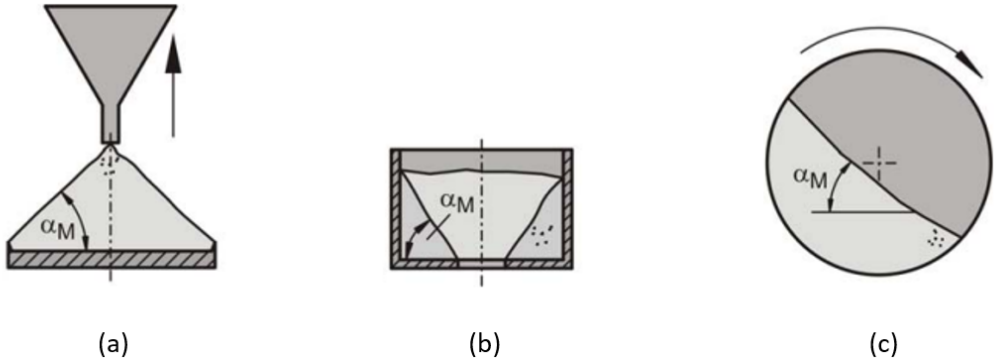

Figure A-2: Angle of repose (denoted α_M here) with some measurement methods, being (a) a conical heap from a funnel, (b) a wedge-shaped heap from a container with a central outlet, and (c) in a rotating drum. From Schulze, 2014.

As for the moisture content, it is stated by Al-Hashemi and Al-Amoudi, 2018 that the angle of repose increases for higher moisture content. In the case of rubble piles, it is therefore expected that the angle of repose of the keel is higher than for the sail (although any of the aforementioned factors of influence may have an additional effect). This is reflected by the assumed values for sail and keel angle of repose by Croasdale, 2012 or ice rubble -25° and 35° respectively- though without supplying a source for these figures.

A possible source for the angle of repose for ice rubble can be found in a paper by Brown and Määttänen, 2009. They analysed measurements from two campaigns, at the Kemi-I test cone in Finland between 1984 and 1987, and at the Confederation Bridge in Canada in 1997. For Kemi-I, they reported angles of repose between 25° and 50°, with an average of 40°. For the Confederation Bridge, they reported values between 15° and 70°, with the majority in the range of 30°-50°. They further noted that the lower values were found when the surface of the incoming ice (supporting the pile) was wet and free of snow, such that the friction coefficient was reduced.

With all of the above, and without any conclusive test campaigns, it is assumed that an angle of repose for the sail (θ_s) in an average crushing event is about 35°, while an angle of 45° is deemed accurate for the keel (θ_k).

A-4 Rubble force sensitivities

Porosity

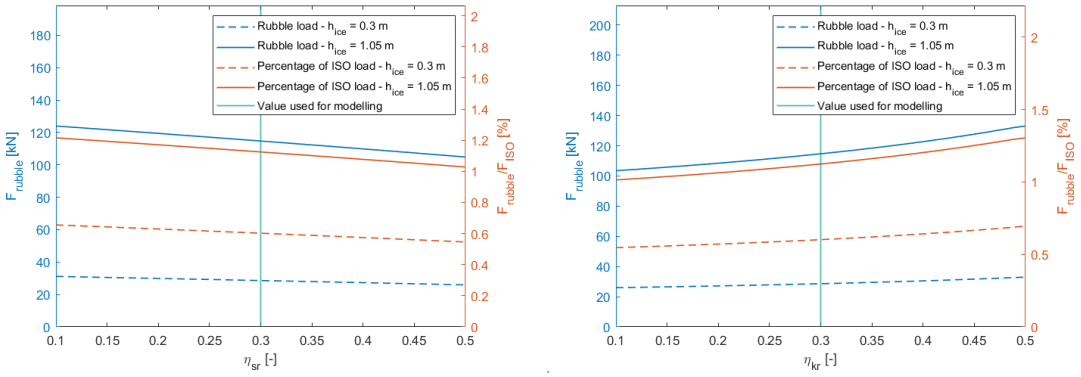

(a) (b)

Figure A-3: Sensitivity of rubble force on input for the porosities in the (a) sail (η_{sr}) and (b) keel (η_{kr}).

Internal friction angle and cohesion

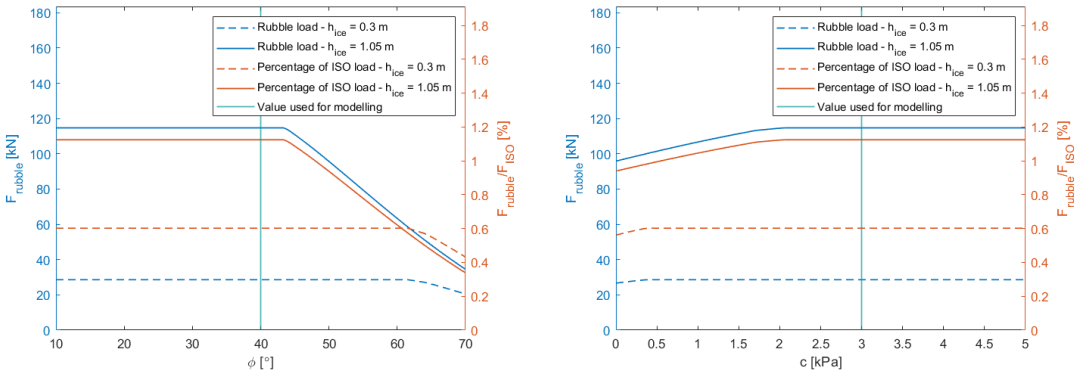

(a) (b)

Figure A-4: Sensitivity of rubble force on input for the (a) internal friction angle (Φ) and (b) cohesion (c).

Pile angles

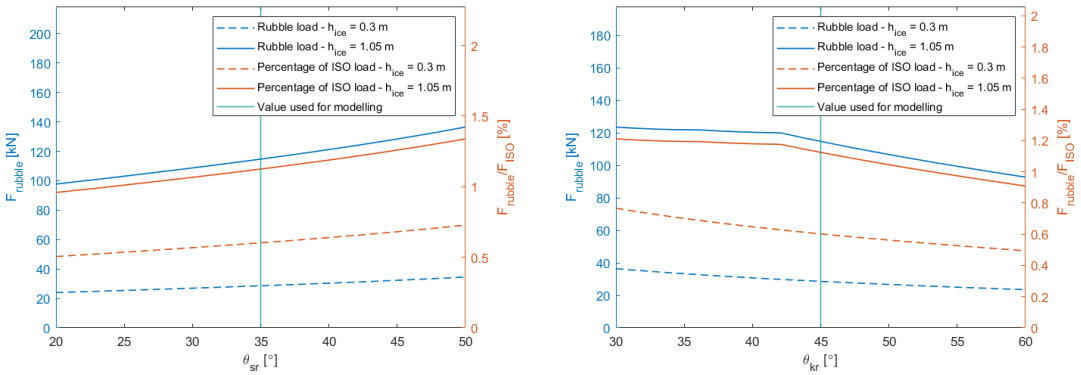

(a) (b)

Figure A-5: Sensitivity of rubble force on input for angles of the (a) sail (θ_{sr}) and (b) keel (θ_{kr}).

Spatial resolution and contour of D vs. h_{ice}

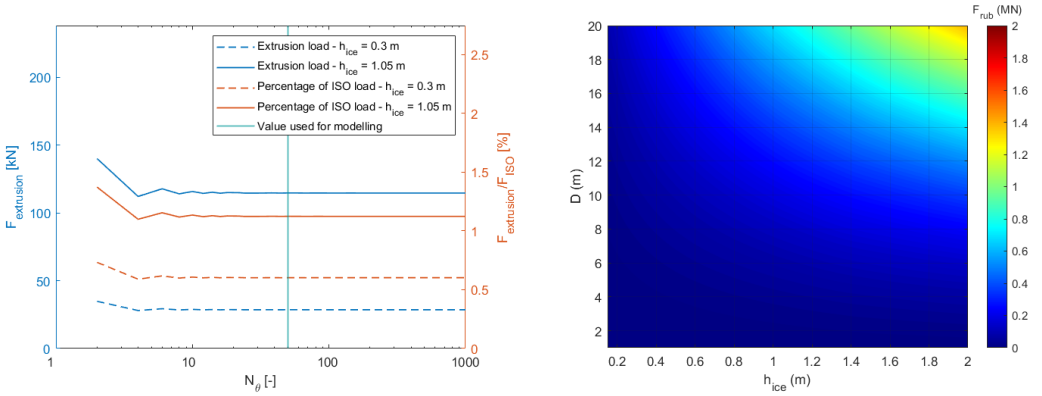

(a) (b)

Figure A-6: Sensitivity of rubble force on input (a) number of segments along perimeter N_θ. and (b) contour plot for D and h_{ice}.

A-5 Extrusion force sensitivities

Vertical resolution

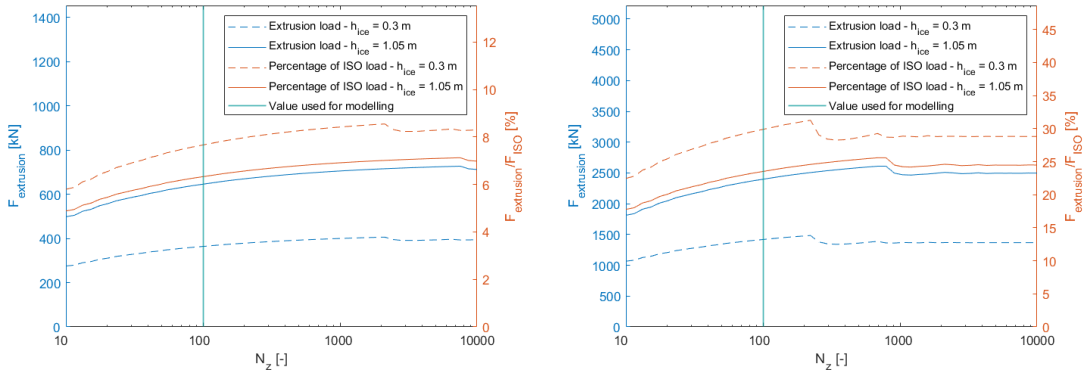

(a) (b)

Figure A-7: Sensitivity of extrusion force on input for the vertical resolution N_z for (a) $v_{rel} = 0.05$ m/s and (b) $v_{rel} = 0.5$ m/s.

Horizontal resolution

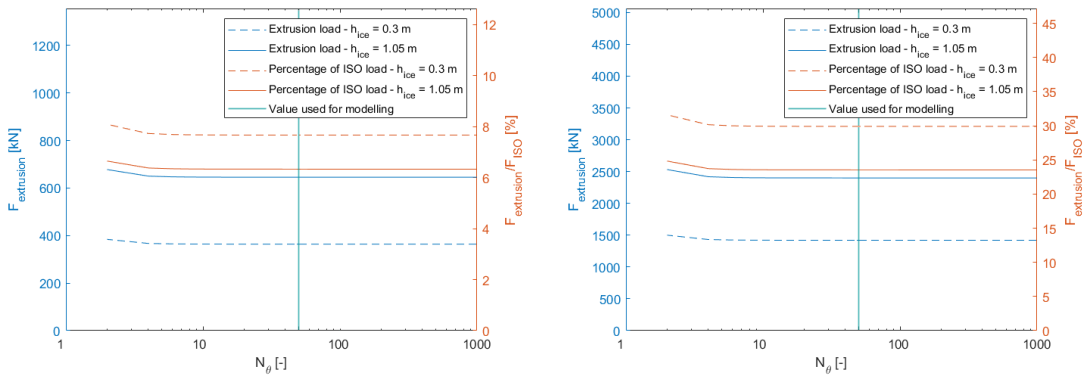

(a) (b)

Figure A-8: Sensitivity of extrusion force on input for the horizontal resolution N

Pressure ridge height

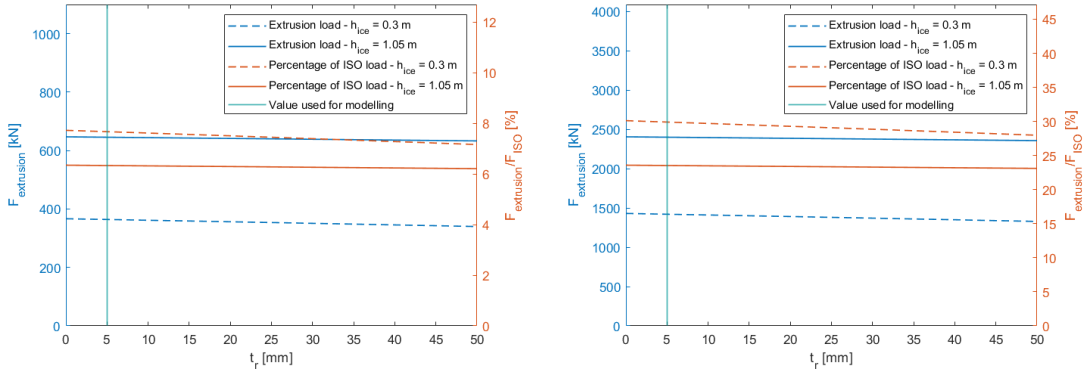

(a) (b)

Figure A-9: Sensitivity of extrusion force on input for the pressure ridge height t_{ridge} for (a) $v_{\text{rel}} = 0.05$ m/s and (b) $v_{\text{rel}} = 0.5$ m/s.

Pressure limit

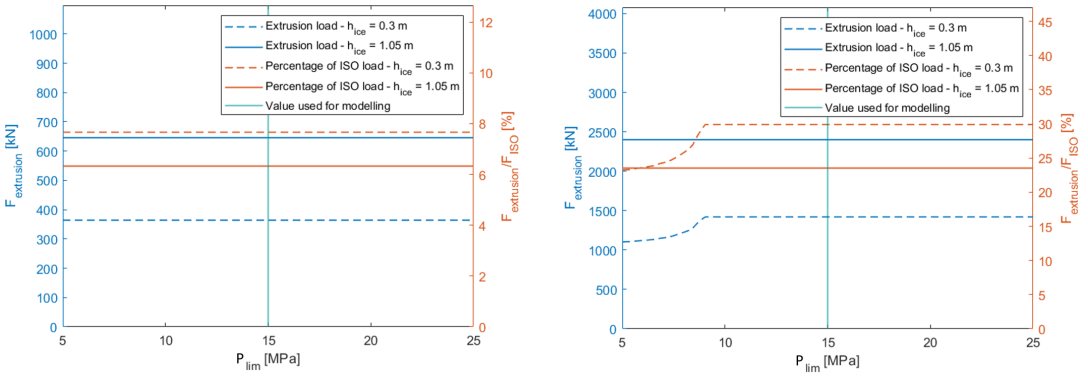

(a) (b)

Figure A-10: Sensitivity of extrusion force on input for the pressure limit p_{lim} for (a) $v_{\text{rel}} = 0.05$ m/s and (b) $v_{\text{rel}} = 0.5$ m/s.

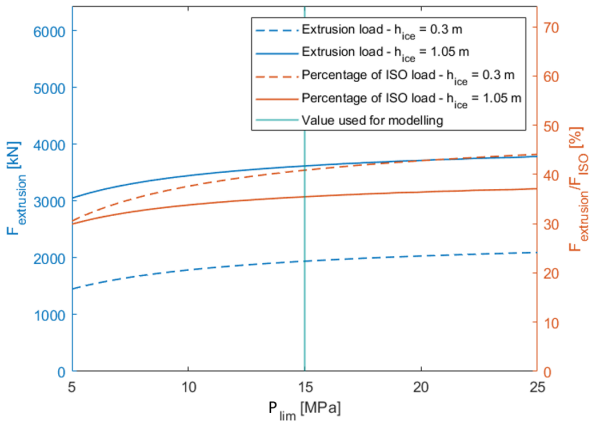

Figure A-11: Sensitivity of extrusion force on input the pressure limit p_{lim} for $v_{\text{rel}} = 1$ m/s and a vertical resolution of $N_z = 10000$.

Structure width

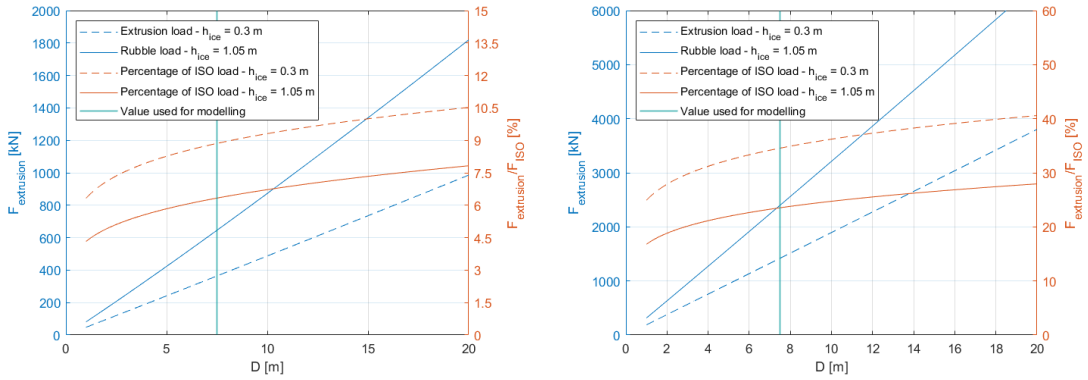

Figure A-12: Sensitivity of extrusion force on input for the structure width D for (a) $v_{\text{rel}} = 0.05$ m/s and (b) $v_{\text{rel}} = 0.5$ m/s.

Contour plots - D vs. h_{ice}

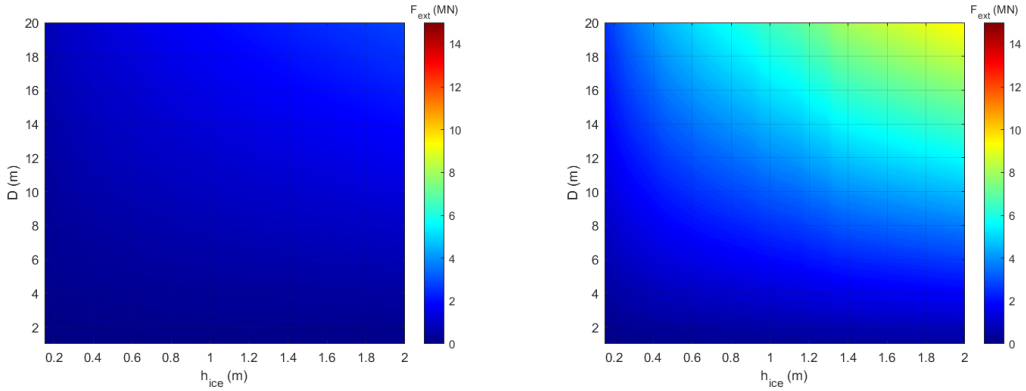

(a) (b)

Figure A-13: Contour plots of extrusion force on input for the structure width D and ice thickness h_{ice} for (a) $v_{\text{rel}} = 0.05$ m/s and (b) $v_{\text{rel}} = 0.5$ m/s.

Contour plots - D vs. v_{rel}

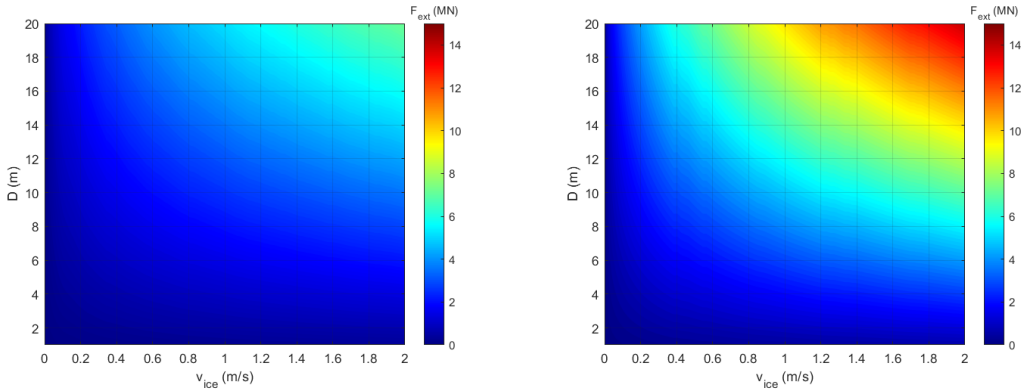

(a) (b)

Figure A-14: Contour plots of extrusion force on input for the structure width D and relative speed v_{rel} for (a) $h_{\text{ice}} = 0.3$ m and (b) $h_{\text{ice}} = 1.05$ m.

Contour plots - h_{ice} vs. v_{rel}

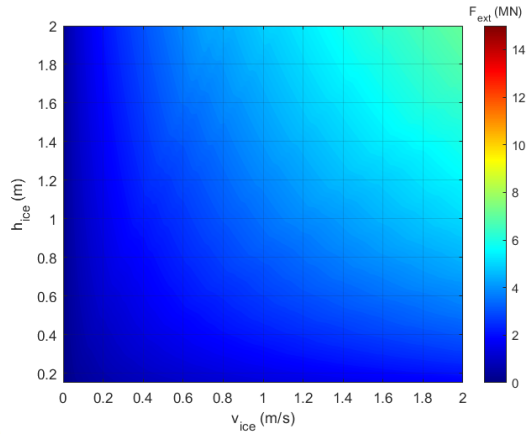

Figure A-15: Contour plot of extrusion force on input for the ice thickness h_{ice} and relative speed v_{rel} for $D = 7.5$ m.

B

Code listings

B-1 Expanded ice force code in VANILLA

```
1  function [fIce] = ssEOMs(obj,yr,yf,strucWLPos,strucWLVel,vIce)
2      a = 10^7; % Sharpness of step function
3      step = 0.5*(1+tanh(a*(yf-strucWLPos))); % 0 if negative, 1 if
           positive, continuous
4
5      relVel = vIce - strucWLVel; % Relative velocity
6
7      if any(step == 1) && relVel > 0
8          fExt = ExtrusionForce(relVel,obj); % Extrusion force
               evaluated each time-step when the ice is in contact and
               the relative velocity is positive
9          fRub = rub.fRub; % Pre-calculated rubble force in case of
               contact and positive relative velocity
10     else
11         fExt = 0; % No extrusion force in case of no contact
12         fRub = 0; % No rubble force in case of no contact
13     end
14
15     fIce = sum((yf-strucWLPos).*step*obj.k2) + fExt + fRub; % Total
           ice force with rubble and extrusion
16 end
```

Listing B.1: Relevant outtake of VANILLA including the extrusion force

B-2 Rubble code

```
function [F_rub] = RubbleForce(rub,str,gen)

    % Ice-steel friction coefficient and angle
    mu_is                   = rub.mu_isk;               % Given
       friction coefficient [-]
    delta_k                 = atand(mu_is);             % Kinetic
       friction angle of ice and structure [deg]

    % Calculate angle variation
    dtheta = 180/gen.ntheta;
    theta_vec = dtheta/2:dtheta:(90-dtheta/2);

    % Initialisation
    F_rub = 0;
    beta = -rub.phi;

    % Compute forces
        for i = 1:length(theta_vec)
            % Determine parameter for pile dimension
            if theta_vec(i) >= 45
                % For larger than 45 degrees along circumference
                C = rub.r_fs;
            else
                % For smaller than 45 degrees along circumference
                C = 1 + (rub.r_fs -1)*theta_vec(i)/45;
            end

            % Calculate slide force for sail
            f_slide_sail = dtheta/360*sind(theta_vec(i))*(rub.
               mu_iik*rub.gamma_sr*C*rub.h_sr*pi*(str.D/2*C*rub.
               l_sr + 1/3*(C*rub.l_sr)^2));
            % Calculate slide force for keel
            f_slide_keel = dtheta/360*sind(theta_vec(i))*(rub.
               mu_iik*rub.gamma_kr*C*rub.h_kr*pi*(str.D/2*C*rub.
               l_kr + 1/3*(C*rub.l_kr)^2));

            % Calculate internal failure force for sail and keel
            K_p = sind(str.alpha - rub.phi)^2/(sind(str.alpha)^2*
               sind(str.alpha + delta_k)*...
                    (1 - sqrt((sind(rub.phi + delta_k)*sind(rub.phi
                        + beta)/...
```

```
34                      (sind(str.alpha + delta_k)*sind(str.alpha +
                            beta)))))^2);
35              f_internal_sail = 1/2*dtheta/180*pi*str.D/2*sind(
                    theta_vec(i))*(rub.gamma_sr*(C*rub.h_sr)^2*K_p + 2*
                    rub.coh*sqrt(K_p));
36              f_internal_keel = 1/2*dtheta/180*pi*str.D/2*sind(
                    theta_vec(i))*(2*rub.coh*sqrt(K_p)+ rub.gamma_kr*(C*
                    rub.h_kr)^2*K_p);
37
38              % Check for lowest loads
39              f_min = min(f_slide_sail,f_internal_sail) + min(
                    f_slide_keel,f_internal_keel);
40
41              % Add to total force
42              F_rub = F_rub + f_min;
43          end
44
45          % Multiply force by two for full 180 degrees (symmetry)
46          F_rub = F_rub*2;
47
48  end
```

Listing B.2: Code used for calculation of the rubble force.

B-3 Extrusion code

```
1   function fExt = ExtrusionForce(vRel,extrusionParam)
2       gen = extrusionParam.gen;
3       rub = extrusionParam.rub;
4       ext = extrusionParam.ext;
5       str = extrusionParam.str;
6
7       % Calculate angle variation
8       dtheta = 180/gen.ntheta;
9       theta_vec = dtheta/2:dtheta:(90-dtheta/2);
10      ntheta_half = gen.ntheta/2;
11
12      % Calculate normalised height variation
13      dz_top = 1/gen.nz_top;
14      dz_bot = 1/gen.nz_bot;
15      z_top_vec = flip(dz_top/2:dz_top:(1 - dz_top/2));
16      z_bot_vec = flip(dz_bot/2:dz_bot:(1 - dz_bot/2));
```

```
17      z_top_mat = z_top_vec' .* ones(gen.nz_top,ntheta_half);
18      z_bot_mat = z_bot_vec' .* ones(gen.nz_bot,ntheta_half);
19
20      % Assign for speedup
21      sin_theta_vec = sind(theta_vec);
22      n = ext.n;
23      over_n_pos = 1/n;
24      over_n_neg = -1/n;
25      h_top = ext.h_top;
26      h_bot = ext.h_bot;
27      K = ext.K;
28      nz_top = gen.nz_top;
29      nz_bot = gen.nz_bot;
30
31      % Compute forces
32      % Calculate top pressure and multiplication factor
33      C = 1 + (rub.r_fs -1)*theta_vec/45;
34      C(C < 1) = 1;
35      p0_top_mat = ((C*rub.h_sr + (C*rub.l_sr - ext.l_top)*tand(rub.
            theta_sr))/2*rub.gamma_sr).*ones(nz_top,ntheta_half);    %
            Pressure from rubble at extrusion channel exit at top [Pa]
36      p0_bot_mat = ((C*rub.h_kr + (C*rub.l_kr - ext.l_bot)*tand(rub.
            theta_kr))/2*rub.gamma_kr).*ones(nz_bot,ntheta_half);    %
            Pressure from rubble at extrusion channel exit at bottom [Pa
            ]
37
38      % Calculate top pressure distribution
39      A_vec = (vRel*sin_theta_vec*(n + 2)*h_top.^(n + 2)/...
40                  (2*K*(ext.l_top/2).^(n +2))).^(over_n_pos);
41      pyy_top_mat = A_vec.*(n*((h_top*(z_top_mat)).^(over_n_neg) -
            h_top.^(over_n_neg))) + p0_top_mat;
42
43      % Correct if pressure becomes to high
44      pyy_top_mat(pyy_top_mat >= ext.Limit_vis) = 0;
45
46      % Calculate forces at the top
47      f_ext_top_mat = (dz_top*h_top*dtheta/360*pi*str.D.*
            sin_theta_vec).*pyy_top_mat;
48
49      % Calculate bottom pressure distribution
50      A_vec = (vRel*sin_theta_vec*(n + 2)*h_bot.^(n + 2)/...
51                  (2*K*(ext.l_bot/2).^(n +2))).^(over_n_pos);
```

```
52      pyy_bot_mat = A_vec.*(n*((h_bot*(z_bot_mat)).^(over_n_neg) -
            h_bot.^(over_n_neg))) + p0_bot_mat;
53
54      % Correct if pressure becomes to high
55      pyy_bot_mat(pyy_bot_mat >= ext.Limit_vis) = 0;
56
57      % Calculate forces at the bottom
58      f_ext_bot_mat = (dz_bot*h_bot*dtheta/360*pi*str.D.*
            sin_theta_vec).*pyy_bot_mat;
59
60      % Calculate forces
61      fExt = sum(sum(f_ext_top_mat)) + sum(sum(f_ext_bot_mat));
62
63      % Multiply force by two for full 180 degrees (symmetry)
64      fExt = fExt*2;
65
66  end
```

Listing B.3: Code used for calculation of the extrusion force.

C

PSDs of results

IC regime

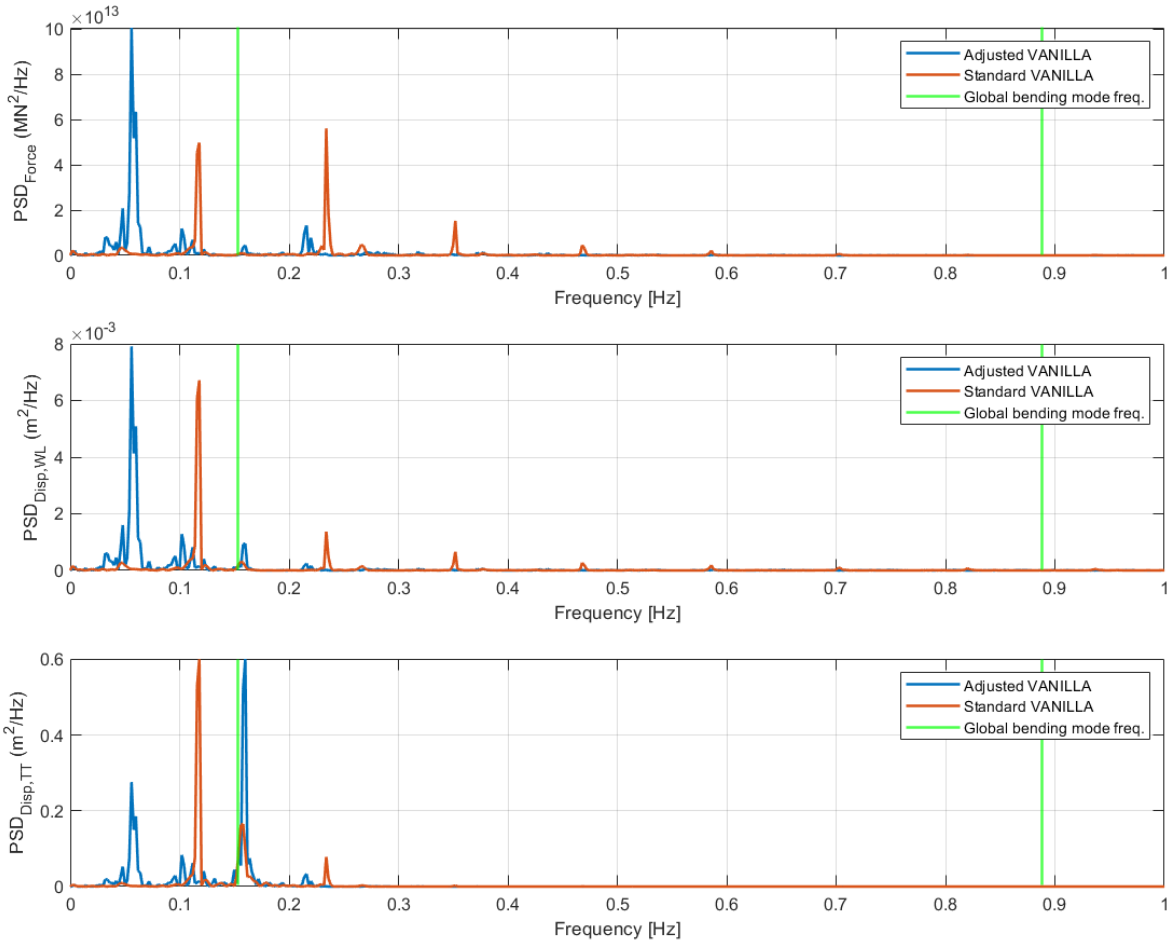

Figure C-1: PSD of ice force and dynamics $h_{\text{ice}} = 30$ cm, $C_{\text{R}} = 0.84$ and $v_{\text{ice}} = 0.005$ m/s.

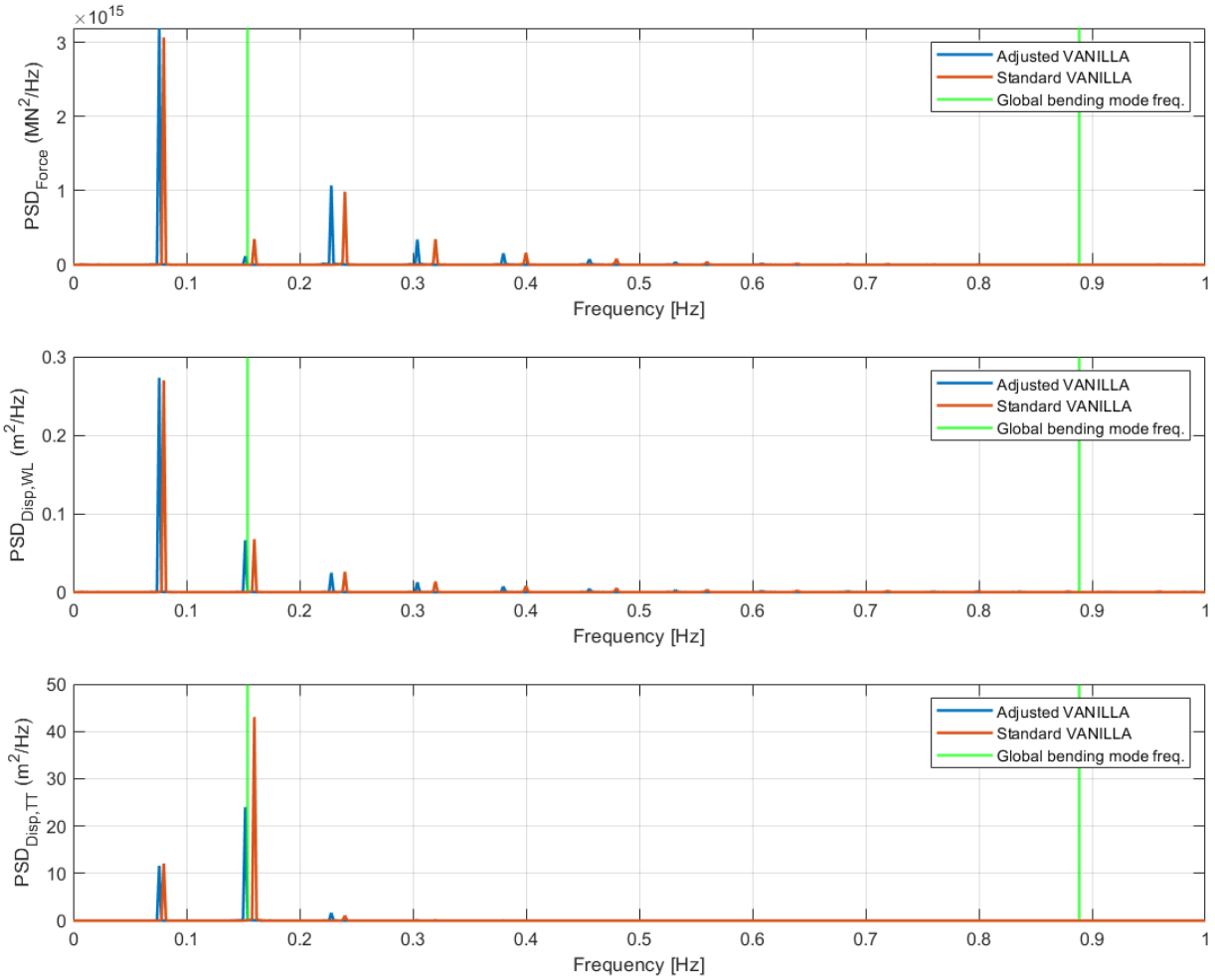

Figure C-2: PSD of ice force and dynamics $h_{\text{ice}} = 105$ cm, $C_{\text{R}} = 1.34$ and $v_{\text{ice}} = 0.01$ m/s.

FLI regime

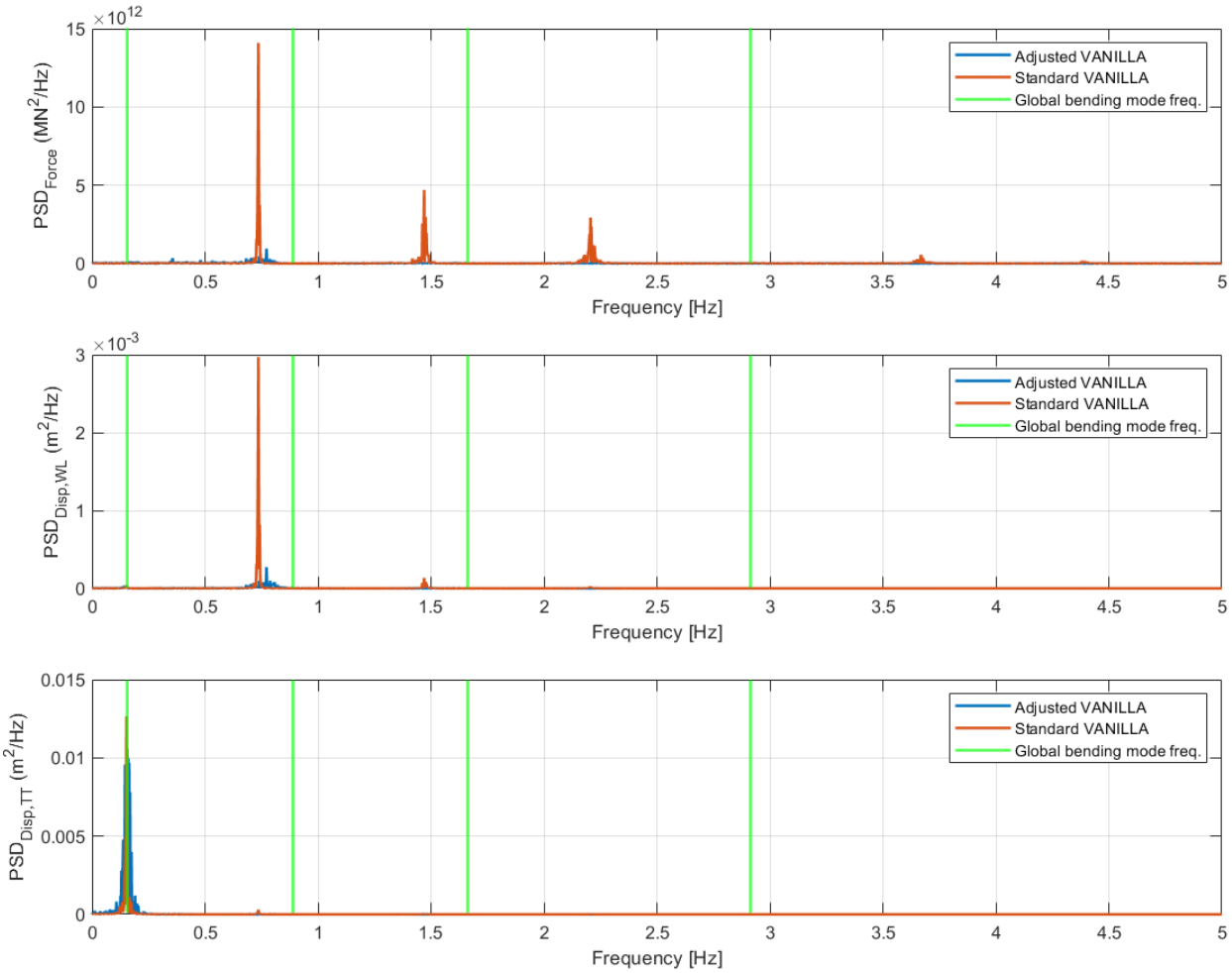

Figure C-3: PSD of ice force and dynamics $h_{\text{ice}} = 30$ cm, $C_{\text{R}} = 0.84$ and $v_{\text{ice}} = 0.02$ m/s.

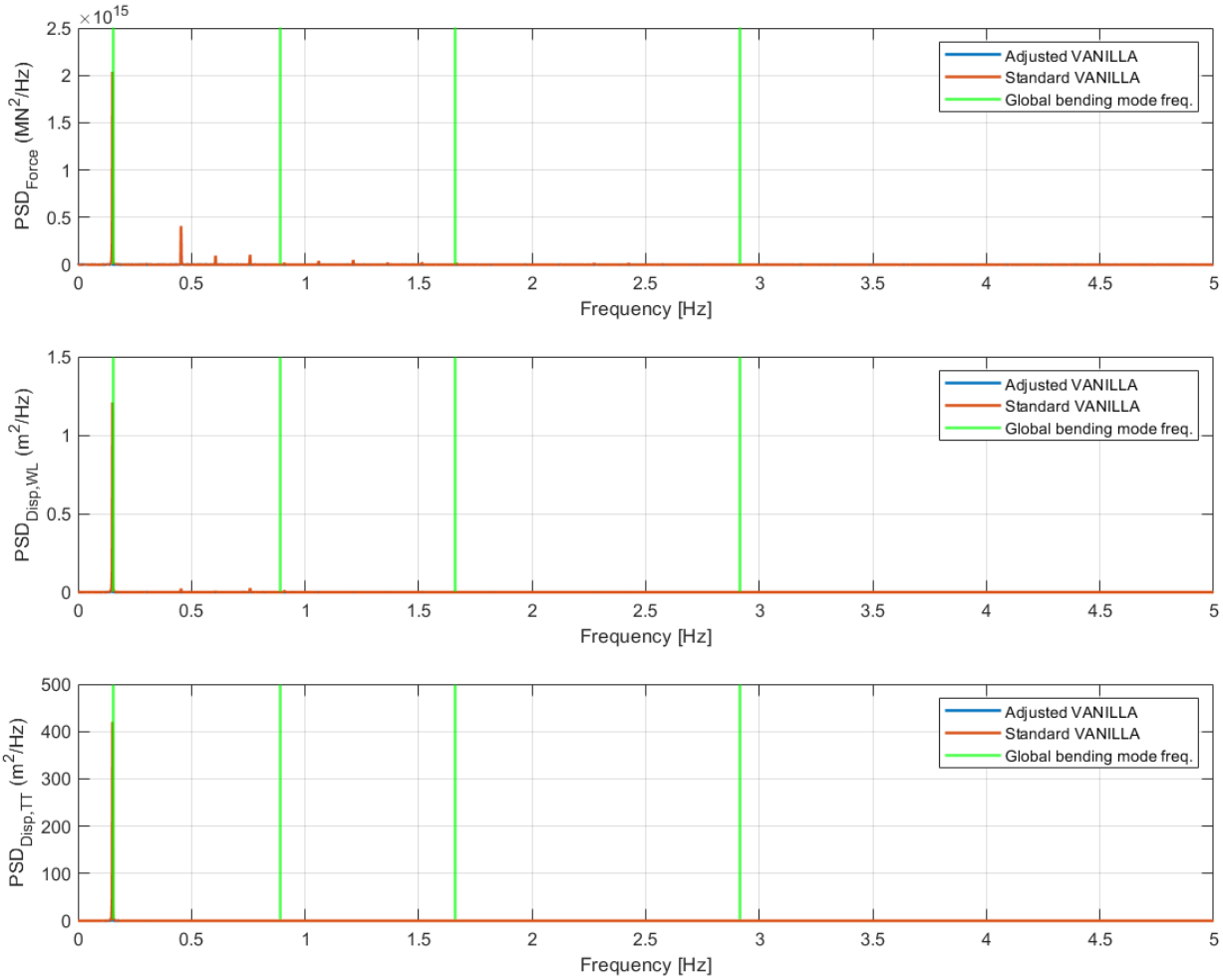

Figure C-4: PSD of ice force and dynamics $h_{\text{ice}} = 105$ cm, $C_{\text{R}} = 1.34$ and $v_{\text{ice}} = 0.06$ m/s.

CBR regime - $v_{\text{ice}} < 0.15$ m/s

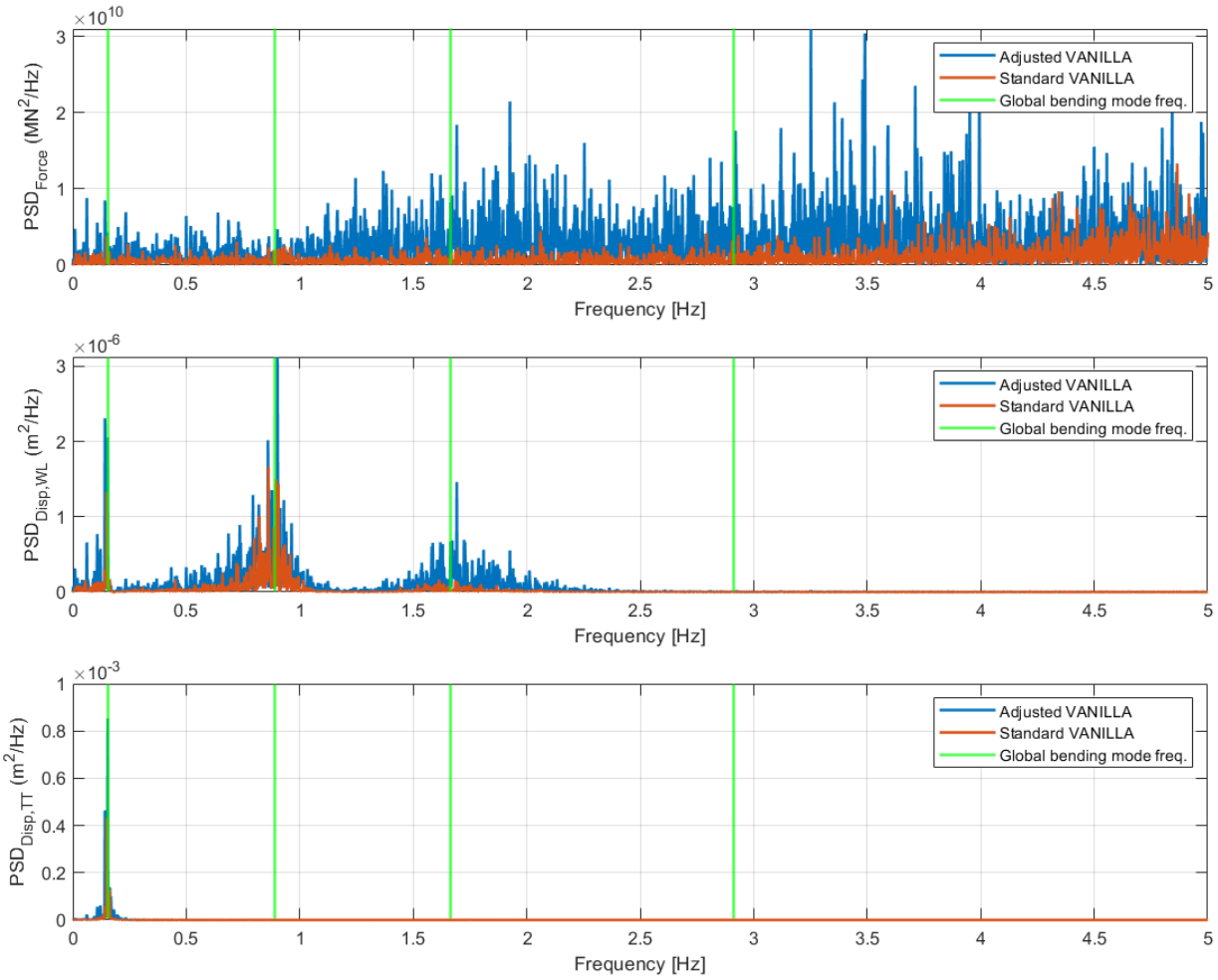

Figure C-5: PSD of ice force and dynamics $h_{\text{ice}} = 30$ cm, $C_{\text{R}} = 0.84$ and $v_{\text{ice}} = 0.05$ m/s.

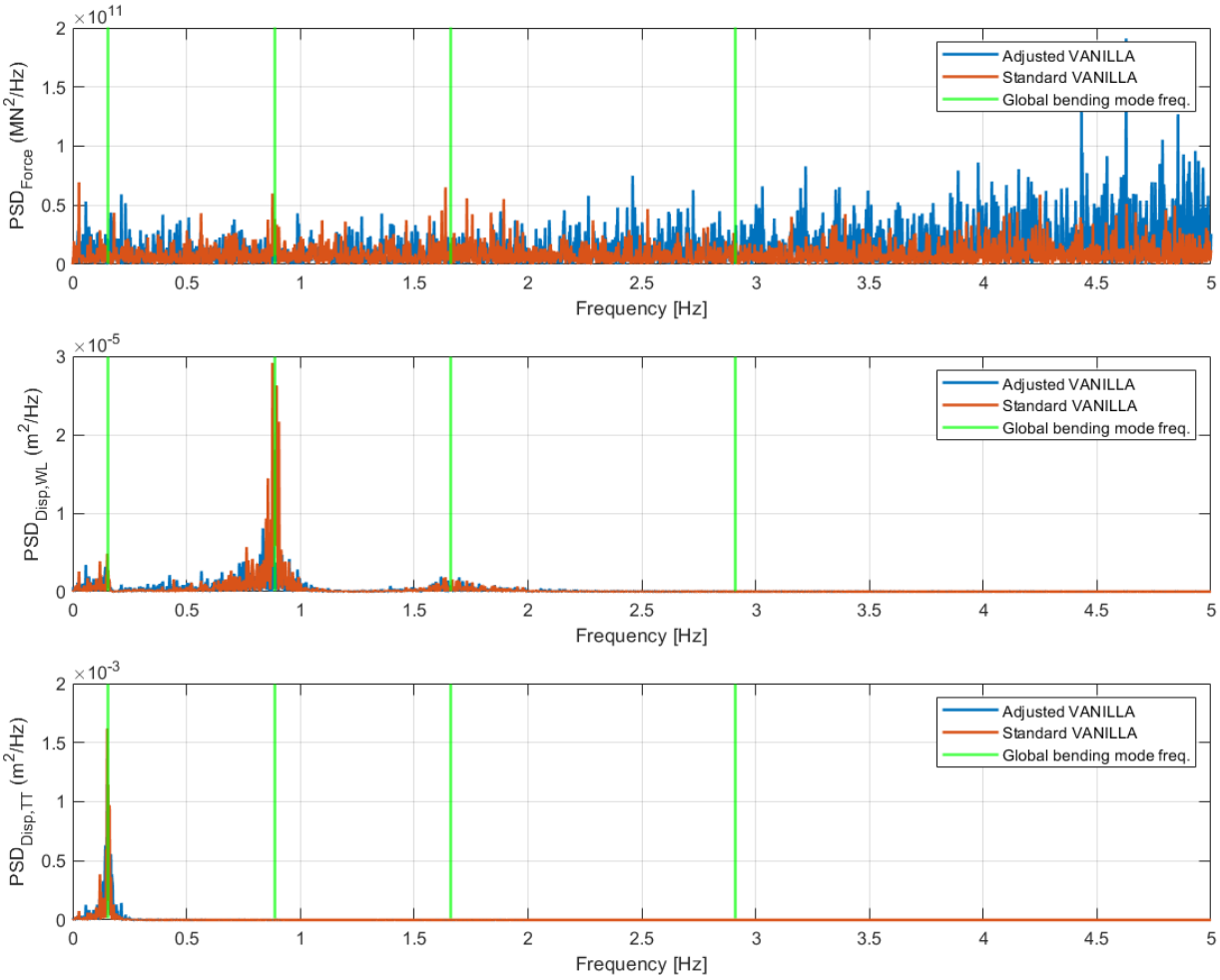

Figure C-6: PSD of ice force and dynamics $h_{\text{ice}} = 105$ cm, $C_{\text{R}} = 1.34$ and $v_{\text{ice}} = 0.08$ m/s.

CBR regime - $v_{\text{ice}} > 0.15$ m/s

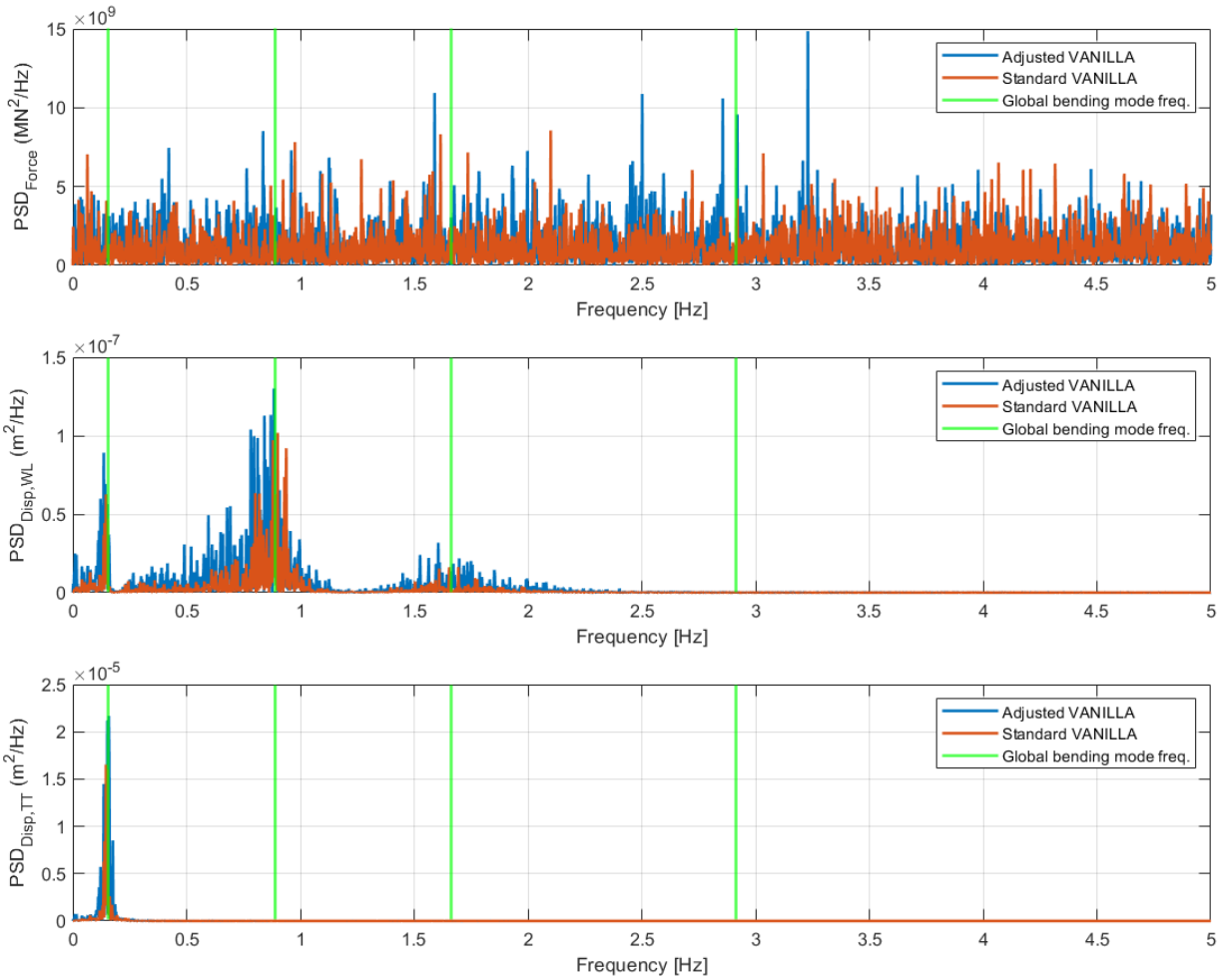

Figure C-7: PSD of ice force and dynamics $h_{\text{ice}} = 30$ cm, $C_{\text{R}} = 0.84$ and $v_{\text{ice}} = 0.5$ m/s.

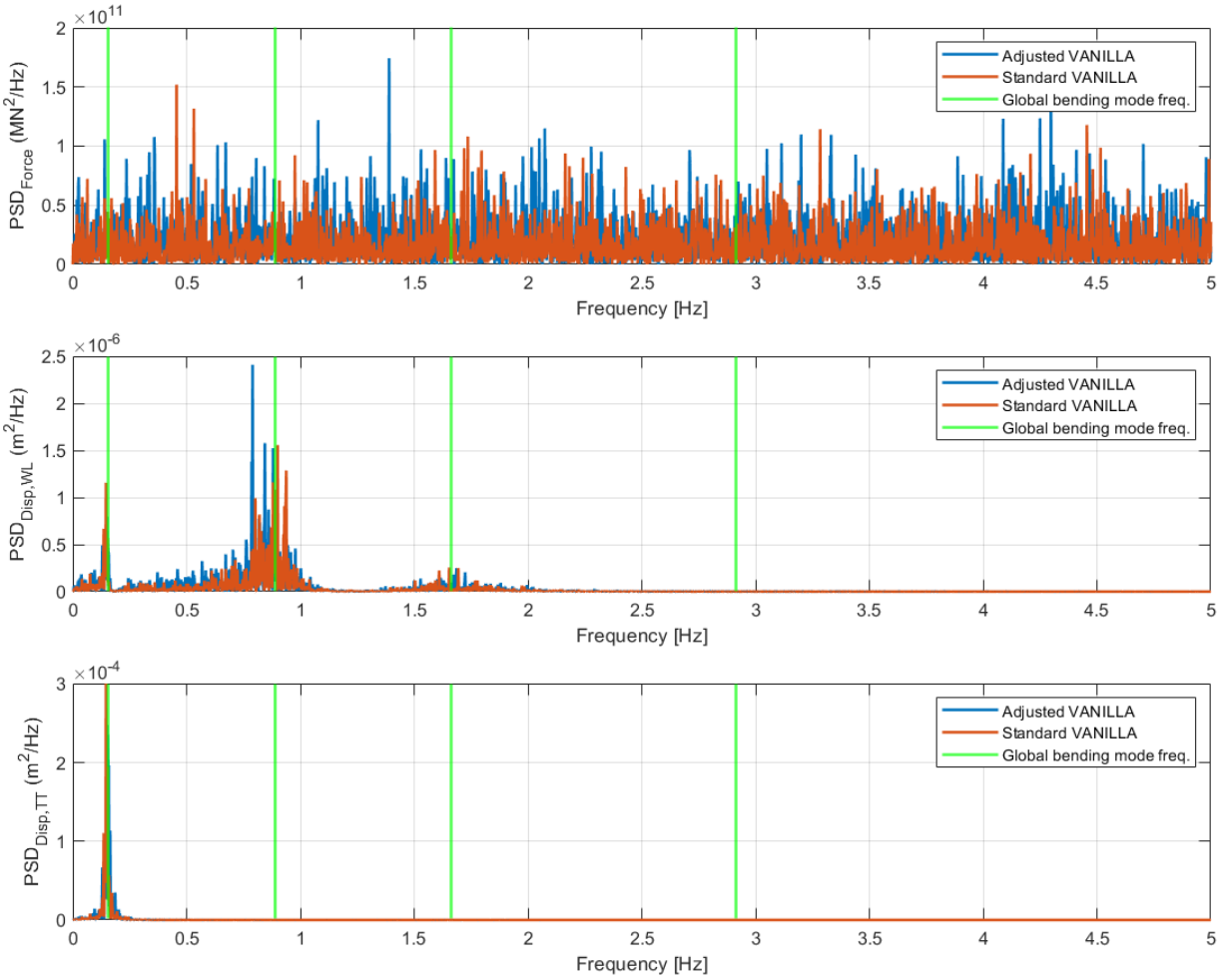

Figure C-8: PSD of ice force and dynamics $h_{\text{ice}} = 105$ cm, $C_{\text{R}} = 1.34$ and $v_{\text{ice}} = 0.5$ m/s.

D

Wind turbine modelling

In this Appendix, the work performed prior to the extrusion and rubble modelling, done on modelling the blade loads due to ice crushing based on the Standard VANILLA model is shown. As set out in the Introduction of this document, the number of offshore wind turbines in the Baltic Sea is expected to increase enormously in the coming decades. Since this body of water has the potential to partially freeze, it is important to know which limitations on structural design and locations for construction are expected due to the presence of sea ice. Previously, this was done in detail for tower and foundation, but research on blade effects is limited. Therefore, for this Appendix, the research question of interest is the following:

How do combined wind and ice forcing affect the blade loads of an offshore wind turbine in the Baltic Sea?

In order to answer this question, this Appendix is structured as follows. First some technicalities of wind turbines and more specifically the blades are introduced, as well as the cases considered for evaluating ice loads on offshore wind turbines, in Section D-1. Then the model used for computing blade loads and dynamics is elaborated in Section D-2, followed by the results in Section D-3, which are also discussed there. Some limitations are discussed in Section D-4 and conclusions from the results in Section D-5 finalise this part.

D-1 Theory

Wind turbine components

Wind turbines are now widely known devices for generating energy from the wind. The individual components are not known to all (engineers) and are thus shortly introduced here. Figure D-1 shows the most important parts. Here, a *horizontal axis wind turbine* is meant when using the term wind turbine.

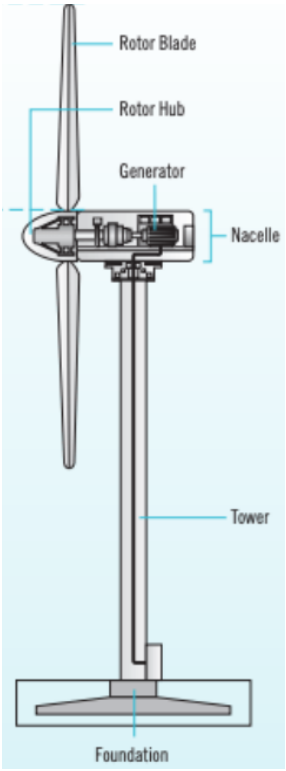

Figure D-1: Schematic of a wind turbine and its components. From Renewables, 2021.

The parts in Figure D-1 are as follows:

- *Blades* are attached to a *hub*, which spins as the blades turn. The blades and hub together form the *rotor*.
- The *nacelle* houses the gearbox, generator and electrical components. The rotor and nacelle together are called the rotor-nacelle assembly (RNA).
- The RNA is placed on top of the *tower*, which holds it in place high above the ground or water. It also houses the wiring going to and from the electrical components in the RNA.
- A *foundation* keeps the turbine in place on/in the ground (or seafloor). For offshore turbines, there are various foundation types that suit different ranges of water depths (see Figure D-2). Over 80% of currently installed offshore wind turbines, as well as most planned turbines, use a monopile foundation (Soares-Ramos et al., 2020).

Each of these components is subject to forces from the wind, water, surrounding soil, gravity or floating ice. These forces influence the dynamics of these components, that each have their respective natural frequencies. For an in-depth discussion of the wind turbine functioning and components, see for example Jenkins et al., 2021. Of particular interest here are the blades of the turbine, which are now further discussed.

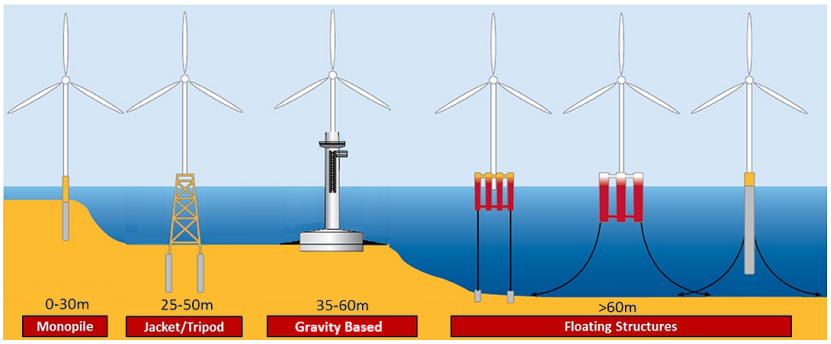

Figure D-2: Offshore wind turbine foundations. Adapted from Abanades, 2019.

Blade specifics

When air is passing through the rotor plane of the turbine, lift is generated by the turbine blades (as shown in Figure D-4(a)). The lift has a component in the direction of the rotor plane, such that the rotor starts to turn, transferring kinetic energy from the wind to the rotor. This kinetic energy is then transferred into electrical energy by the generator. In order to obtain maximum performance, the blades are shaped such that the amount of energy that can be generated for a given location (based on local wind conditions) is optimised, without failure of the blades. This shape and structure varies along the *span* of the blade, from the *root* towards the *tip*, as shown in Figure D-3..

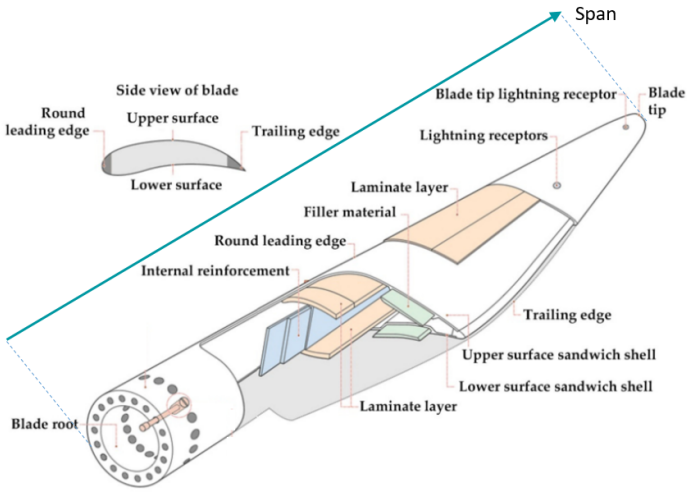

Figure D-3: Wind turbine blade showing its various components, as well as root and tip and the span. Adapted from Katsaprakakis et al., 2021.

Moreover, the turbine uses active control strategies to accomplish this. Two examples in

which the turbine is controlled is by *yawing* the turbine, turning the rotor plane around the vertical axis, as well as *pitching* of the blades, adjusting the *angle of attack* at which the incoming wind hits the blade. Usually, blade pitch is unchanged for lower wind speeds, leading to increasing rotational speeds with wind speed up to the *rated wind speed*, for which the electricity generated equals the capacity of the generator. At rated, the *thrust*, the axial force of the wind on the turbine, is maximum. For higher wind speeds, the blades are pitched, reducing blade efficiency and thrust to keep the generator at its maximum capacity. For a more in-depth discussion of wind turbine aerodynamics and control, see Hansen, 2015.

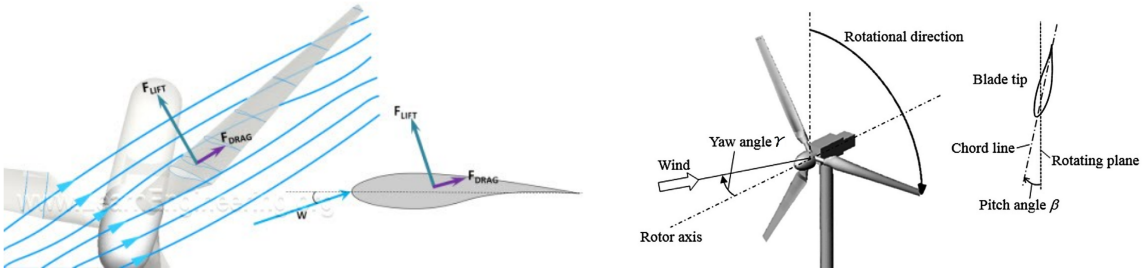

(a) (b)

Figure D-4: Illustrations of (a) lift generated from the incoming apparent wind and (b) pitching and yawing. From (a) Mathew, 2014, (b) Mamouri et al., 2020.

Forcing of the wind, as well as dynamics transferred from the tower to the blades, lead to motion in the blades. This leads to stress on certain parts of the blades, which may eventually end in a loss of integrity. This may happen particularly at the blade natural frequencies. Thus, in modelling blade dynamics, the natural frequencies of the blades are considered. These can be along the *edgewise* or the *flapwise* direction (Figure D-5(a)), and in a symmetrical or (when the rotor is turning) asymmetrical fashion (Figure D-5(b)).

The asymmetrical modes are also called *whirling modes*. Whirling modes are modes that have out-of-phase blade oscillations —for example, the first blade reaches its maximum displacement, then the second, then the third. If a given whirling mode results in maximal blade deflections in blade 1, then 2, then 3, then the oscillation is moving against the direction of rotation, which is called a *backwards whirling* mode. A whirling mode moving with the direction of rotation (maximum blade deflections for blade 1, then 3, then 2) is called a *forwards whirling* mode.

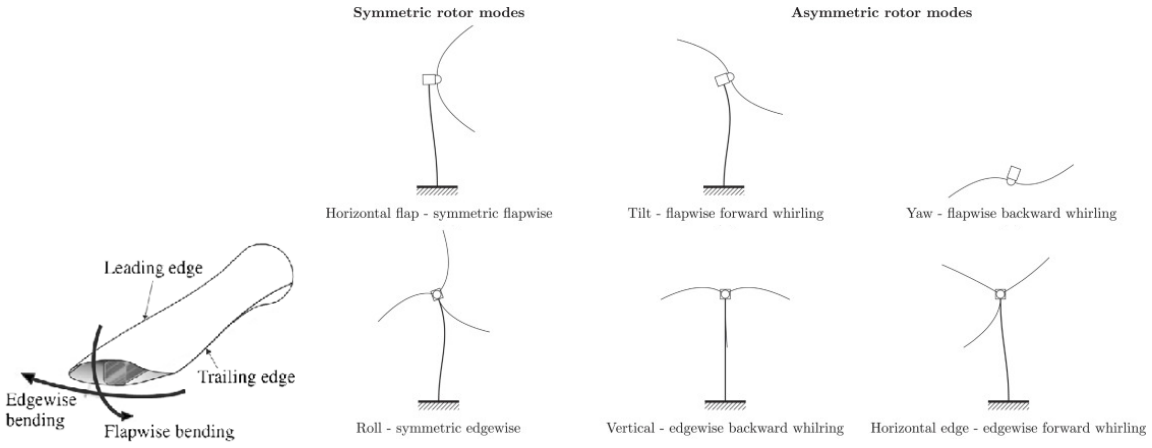

Figure D-5: Illustrations of (a) edgewise and flapwise directions and (b) blade modes. From (a) Salimi-Majd et al., 2015 and (b) Filsoof et al., 2021.

In the observer frame of the blade, both symmetrical and asymmetrical oscillations happen at the blade natural frequency(-ies). However, in the non-rotating observer frame of the structure, there is a shift in frequencies. This results from a transformation in coordinate system, changing the equations of motion of the blade from linear, time-varying (LTV) to linear, time-invariant (LTI), called the Coleman transformation (Skjoldan, 2011). Then, the frequencies are as follows:

$$\begin{aligned} \omega_{\text{NR,SYM}} &= \omega_{\text{n}} \\ \omega_{\text{NR,BW}} &= \omega_{\text{n}} - \Omega \\ \omega_{\text{NR,FW}} &= \omega_{\text{n}} + \Omega \end{aligned}$$

Here, ω represents the frequencies (in Hz), with subscripts n for natural, *NR* indicating non-rotating, *SYM* indicating symmetrical and *BW* and *FW* indicating backward and forward whirling respectively. Lastly, Ω is the rotor speed (in Hz).

Design standards

There are several organizations creating standards for wind turbines, ensuring quality, safety, and efficiency. Examples are the International Organization for Standardization (ISO), the International Electrotechnical Commission (IEC) and the Det Norske Veritas group (DNV).

IEC 61400-3-1, *Design requirements for fixed offshore wind turbines*, outlines the requirements for the assessment of the external conditions at an offshore wind turbine site. It specifies essential design requirements to ensure the engineering integrity of fixed offshore

wind turbines (International Electrotechnical Commission (IEC), 2019). Use is made of the discussions on ice loading set out in the aforementioned ISO standard,coupled to specific wind conditions that are to be considered in modelling of loads for OWTs.

The two *design load cases* (DLC) of most interest here, since they will be used for modelling of the blade loads later, are DLC *D3* and *D8*. Load case D3 considers horizontal loads from moving ice, leading to crushing, and looks at the ULS. Table D-1 shows a summary of the load case, with the full load case focusing on both global pressure (over the entire interaction area) and local pressure (over smaller portions of the interaction area). The wind conditions state that the turbine is considered to be in production, so that the rotor is spinning and electricity is being produced. This is indicated by the statement that the wind speed at hub height (V_{hub}) is in between the cut-in wind speed (V_{in}) and cut-out wind speed (V_{out}).

Table D-1: Design load case D3. From International Electrotechnical Commission (IEC), 2019.

DLC	Ice condition	Wind condition	Water level	Type of analysis	Partial safety factor
D3	Horizontal load from moving ice at relevant velocities $h = h_{50}$ or largest value of moving ice.	NTM $V_{\text{in}} < V_{\text{hub}} < V_{\text{out}}$	NWLR	U	N

Load case D8 is similar to D3, but the difference is that the turbine is now *idling* or *parked*, which means that the blades are *pitched out* (rotated such that they do not generate lift) and the rotor is standing still (or moving minimally). There is no energy produced. Table D-2 shows the conditions considered for this load case.

Table D-2: Design load case D8. From International Electrotechnical Commission (IEC), 2019.

DLC	Ice condition	Wind condition	Water level	Type of analysis	Partial safety factor
D8	Horizontal load from moving ice at relevant velocities $h = h_{50}$ or largest value of moving ice.	EWM Turbulent wind model $V_{\text{hub}} = V_1$	NWLR	U	N

For later modelling, both DLC D3 and D8 are considered.

Ice conditions

As briefly touched upon in the introduction, there are many regions around the globe that encounter floating (sea) ice, as was depicted in Figure **??**. Of special interest to this work is the Baltic Sea, since SGRE is mainly active in that area (out of the areas with sea ice). The ice

conditions in that area vary per year and throughout the season. A thorough discussion of this is given in for example Ronkainen et al., 2013 or Dyrcz, 2017. A rough approximation of the varying extent of the ice is given in Figure D-6. Based on both the temperatures experienced, as well as the time for which these temperatures are experienced, salinity, currents, wind, etc. the ice grows to a different thickness and strength. These ice conditions are indicated by the ice thickness h_{ice} and ice strength coefficient C_{R}.

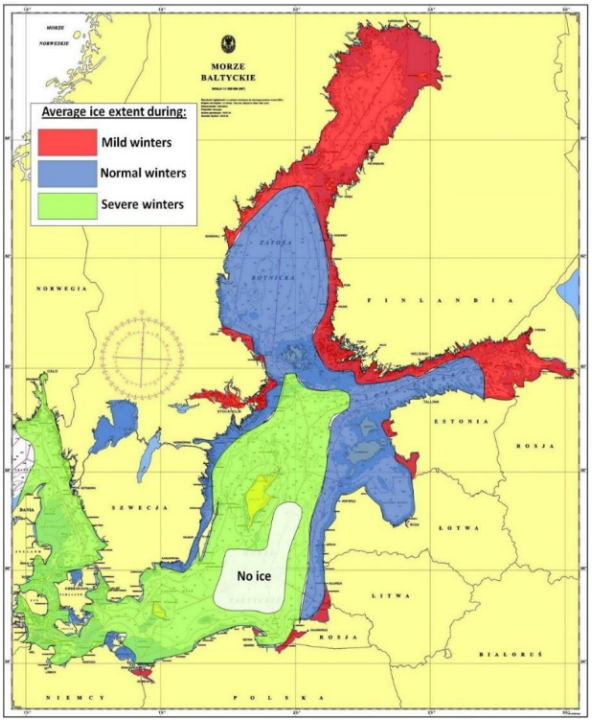

Figure D-6: The average ice extent in the Baltic Sea during typical winters. From Dyrcz, 2017.

The ISO code (The International Organization for Standardization (ISO), 2019) is often used for determination of the ice conditions in a specific location in the Baltic. Recently, a different strategy for calculation of the ice strength was proposed in the unpublished Master thesis 'Ice-structure interaction in the Baltic Sea: defining a feasibility map for monopiles' by Florian van der Stap (available in the TU Delft education repository), based on the informal paper by Hendrikse, 2020. In that thesis, a model is put forward for calculation of the ice strength coefficient C_{R}. Based on that model, a map was generated, as shown in Figure D-7, showing the 1-year maximum value C_1, as well as the 50-year maximum h_{50}. Similar maps were available for C_{50} and h_{50}. In general, these ice conditions are less severe than is predicted using the ISO standard, such that lower ice forces are to be expected from simulations with these conditions. Both the coefficients from the ISO code, as the Hendrikse methods are considered in later modelling.

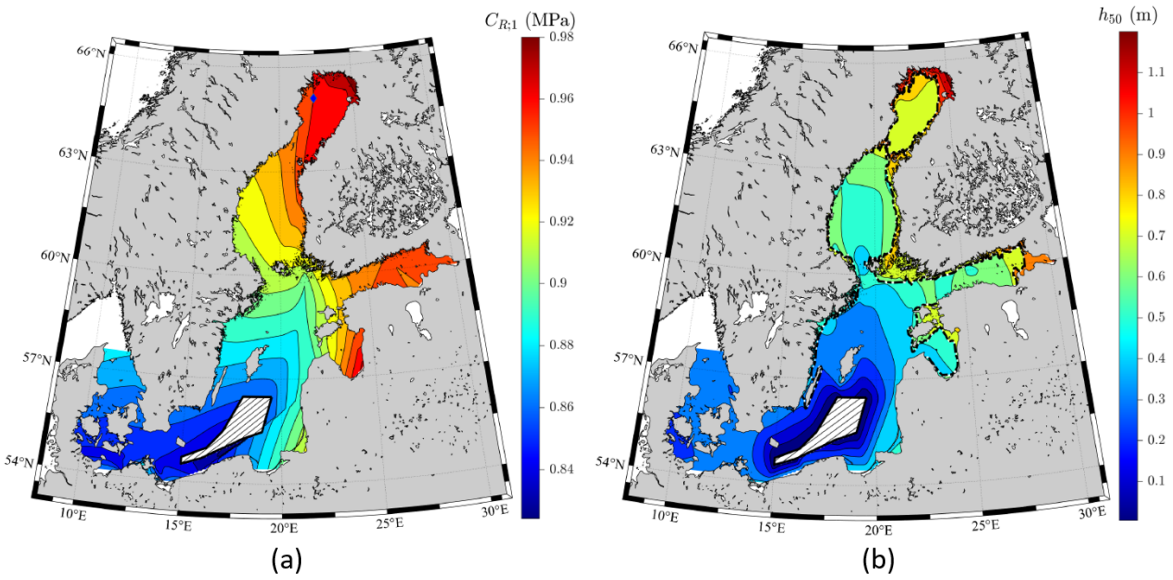

Figure D-7: Maps of the Baltic Sea area showing (a) the 1-year ice strength coefficient C_1 and (b) the 50-year ice thickness. From Van der Stap, 2022.

D-2 Methods

In order to identify the dynamics and the loads on the structure from combined ice and wind, a turbine model is used. The model is explained in this Section, followed by an overview of the site conditions and input parameters used to evaluate the model.

Turbine model

The BHawC software of Siemens Gamesa Renewable Energy (SGRE) is used for calculation of the ice and wind loads. BHawC (Bonus Horizontal Axis Wind turbine Code) is a nonlinear aero-servo-elastic model for dynamic analysis of wind turbines, capable of calculating the dynamics for a wide range of varying structural characteristics and environmental conditions. Coupled to VANILLA, the leading software for evaluating ice crushing loads, it can evaluate the combined influence of wind and ice for an offshore wind turbine.

The model evaluated in BHawC is that of the SG 14-236 DD turbine, which is the newest generation turbine from SGRE. It is designed for offshore wind power generation, with a nominal power of 14 MW, 115 m long blades and a rotor diameter of 236 m. Hub height is case specific, as well as the tower and foundation characteristics. To prevent any connection to existing or planned projects, with the possibility of confidentiality of turbine or site specifics of these projects, representative values are assumed instead of adopting parameters of one of these projects.

In this case hub height is set at 142.46 m above the waterline (LAT). The water depth is 50 m. A monopile of 84 m is used as the foundation, running from 20 m below the mudline up to 14 mLAT. The tower has a length of 125.46 m. For the monopile, a fixity length approach is used for soil modelling. The diameter of the foundation at the waterline is 7.5 m. Lastly, the cut-in wind speed is 4 m/s, cut-out is 28 m/s, with rated wind speed at 12 m/s.

Loads in BHawC

The loads and directions in BHawC conform to conventions set by the developers of the model. These are of importance to understand the results presented later. The conventions are as follows:

- Blades flapwise
  - Positive (+) loads: suction-to-pressure (STP) - from the low pressure zone behind the turbine to the high pressure zone in front of the turbine.
  - Negative (-) loads: pressure-to-suction (PTS) - from the high pressure zone in front of the turbine to the low pressure zone behind the turbine.

- Blades edgewise
  - Positive (+) loads: trailing-to-leading (TTL) - from the trailing edge of the blade, to the leading edge of the blade.
  - Negative (-) loads: leading-to-trailing (LTT), from the leading edge of the blade, to the trailing edge of the blade.
- Tower fore-aft motion (y in Figure D-8)
  - Positive (+) translation: along the direction of the incoming wind.
  - Negative (-) translation: against the direction of the wind.
- Tower side-side motion (x in Figure D-8)
  - Positive (+) translation: at an angle of 270° with the incoming wind.
  - Negative (-) translation: at an angle of 90° with the incoming wind.

These are shown in Figure D-8 for the case of load case D3, production, and D8, idling (when the blades are pitched out).

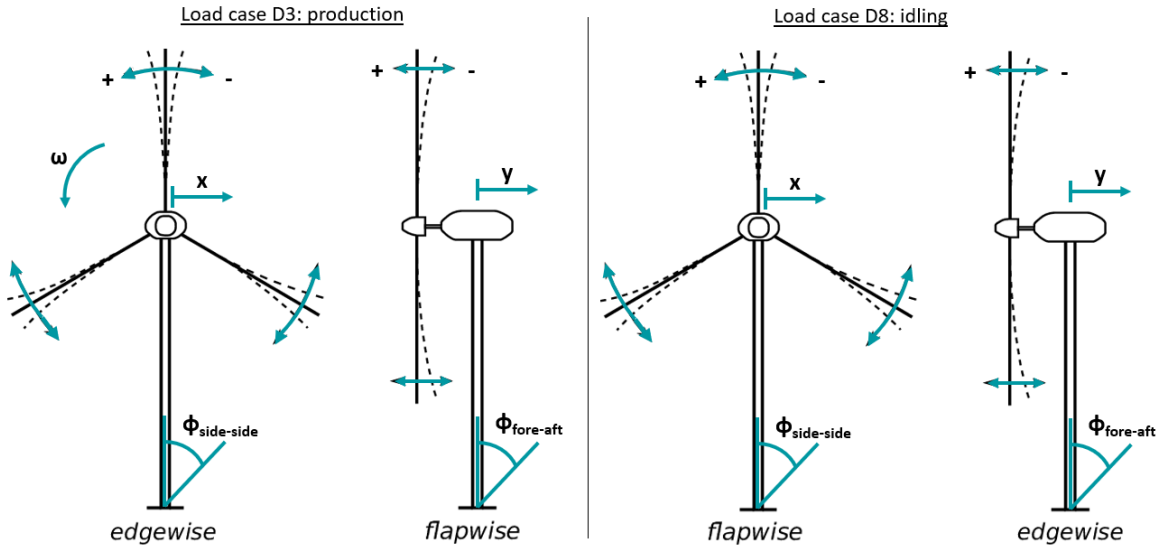

Figure D-8: Direction conventions used in BHawC.

Site conditions

As mentioned in the previous Section, the Baltic Sea area is chosen for evaluation of the (blade) loads from combined wind and ice. Most projects in the Baltic Sea are in the south, in Polish and Danish waters. There, ice conditions are mild, as shown in the Theory, such that evaluation of a turbine in this area can be denoted as a 'minimum' case. On the contrary,

the conditions in the northern Baltic are more severe, with higher occurrence, thicker and stronger ice. Therefore, a turbine in this area can be denoted as a 'maximum' case. For the evaluation of the blade loads, conditions at both the minimum and the maximum case locations are used, such that these can be compared.

For the southern location, a generic set of parameters is used, reflecting a typical Polish project. For the northern location, the site of a project that was investigated for feasibility in 2017, but subsequently cancelled, is used. The location is Suurhiekka, north of the island of Hailuoto in Finnish coastal waters, close to the city of Oulu. The location is shown in Figure D-9. Rissanen and Heinonen, 2016 performed the investigations for the project, including blade load calculations. These can later be compared to the results obtained in this modelling.

Figure D-9: Location of the northern location used for evaluation of the blade loads.

The site conditions in these two locations are based both on values that are from literature, as well as the Hendrikse model for finding ice thickness and strength as explained in the previous Section. They are given in Table D-3.

Two combinations of ice thickness and strengths are considered. Even though direct evaluation of the ISO Equation 2.1 gives one case that has a higher load, due to nonlinear effects in the turbine, it might be the case that a specific combination of ice thickness and strength lead to dynamics that give rise to higher blade loads than a case that gives a higher load according to Equation 2.1. Therefore, both the 50-year maximum ice thickness and 1-year ice strength (h_{50} and C_1) case, as well as the 1-year ice thickness and 50-year ice strength (h_1 and C_{50}) case are considered. For the thin ice location h_1 is 0, thus eliminating that case for the southern location.

Table D-3: Site conditions used for evaluation of the (blade) loads.

Location	Hendrikse model		Literature	
	h_{ice} (cm)	C_R (MPa)	h_{ice} (cm)	C_R (MPa)
South (C_1 & h_{50})	30	0.86	30	1.00
North (C_{50} & h_1)	40	1.37	70	1.71
North (C_1 & h_{50})	105	0.97	105	1.34

Lastly, both the case of aligned wind and ice (both perpendicular to the rotor plane at 0°) and misaligned wind and ice (wind perpendicular at 0°, ice parallel at 90° to the rotor plance) are considered. Both cases are illustrated in Figure D-10. In both cases, a slight yaw misalignment is also considered, with the wind shifted 5.5°.

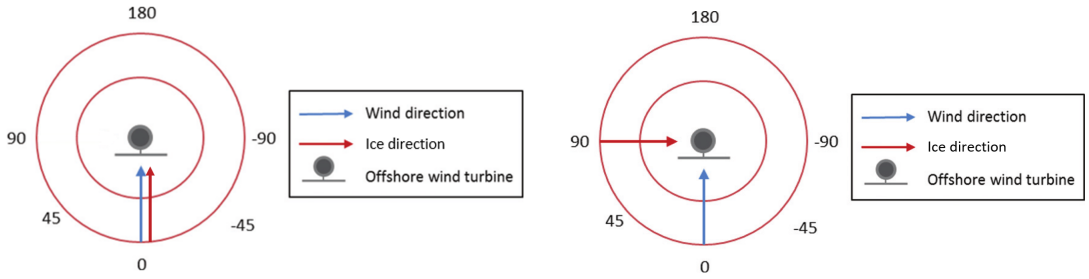

(a) (b)

Figure D-10: Illustrations of (a) aligned wind and ice and (b) misaligned wind and ice. Adapted from Yin et al., 2017.

D-3 Results and discussion

Here, the results of the blade load modelling follow. The results are also discussed.

The results that follow have been normalised to the minimum case of $h_{\text{ice}} = 30$ cm and $C_{\text{R}} = 0.86$ MPa. Tables D-4 and D-5 show the results found for the 6 cases as shown earlier in Table D-3, for the Hendrikse model and literature values respectively. The results are presented for flapwise and edgewise loads, at blade root, 1/3 of the blade span and 2/3 of the blade span. *Max* refers to positive loading, while *min* refers to negative loading, as shown in the previous Section.

Table D-4: Results of the blade load modelling for the new model for the ice conditions. Note that red values indicate more than 5% increase with respect to the minimal case of $h_{\text{ice}} = 30$ cm and $C_{\text{R}} = 0.86$ MPa.

Hendrikse model			South	h_{50} & C_1	North	h_1 & C_{50}	North	h_{50} & C_1
			h_{ice} (cm)	30	h_{ice} (cm)	40	h_{ice} (cm)	105
			C_R (Mpa)	0.86	C_R (Mpa)	1.37	C_R (Mpa)	0.97
Position on blade	Direction	Min/max	Leading DLC	Relative to minimum case (%)	Leading DLC	Relative to minimum case (%)	Leading DLC	Relative to minimum case (%)
root	flap	min	D3	0	D3	0.03	D3	0.41
root	flap	max	D3	0	D3	0.32	D3	1.16
root	edge	min	D3	0	D3	4.43	D3	12.12
root	edge	max	D3	0	D3	0.57	D3	3.03
1/3	flap	min	D3	0	D3	-0.12	D3	0.16
1/3	flap	max	D3	0	D3	0.43	D3	0.36
1/3	edge	min	D3	0	D3	9.42	D8	35.99
1/3	edge	max	D3	0	D3	1.56	D8	7.08
2/3	flap	min	D3	0	D3	0.24	D3	1.06
2/3	flap	max	D3	0	D3	0.96	D3	-0.40
2/3	edge	min	D3	0	D8	38.03	D8	79.55
2/3	edge	max	D3	0	D3	5.13	D8	42.86

Table D-5: Results of the blade load modelling for the literature ice conditions. Note that red values indicate more than 5% increase with respect to the minimal case of $h_{\text{ice}} = 30$ cm and $C_{\text{R}} = 0.86$ MPa.

Literature			South	h_{50} & C_1	North	h_1 & C_{50}	North	h_{50} & C_1
			h_{ice} (cm)	30	h_{ice} (cm)	70	h_{ice} (cm)	105
			C_R (Mpa)	1.00	C_R (Mpa)	1.71	C_R (Mpa)	1.34
Position on blade	Direction	Min/max	Leading DLC	Relative to minimum case (%)	Leading DLC	Relative to minimum case (%)	Leading DLC	Relative to minimum case (%)
root	flap	min	D3	0.35	D3	0.00	D3	1.01
root	flap	max	D3	0.11	D3	3.09	D3	2.09
root	edge	min	D3	1.54	D3	25.21	D3	30.60
root	edge	max	D3	0.45	D3	9.37	D3	9.18
1/3	flap	min	D3	0.60	D3	0.40	D3	0.46
1/3	flap	max	D3	0.34	D3	1.13	D3	2.46
1/3	edge	min	D3	3.67	D8	59.50	D8	88.53
1/3	edge	max	D3	0.90	D8	18.93	D8	37.77
2/3	flap	min	D3	-0.11	D3	0.48	D3	0.71
2/3	flap	max	D3	0.32	D3	0.83	D3	0.16
2/3	edge	min	D3	1.93	D8	132.82	D8	138.83
2/3	edge	max	D3	2.37	D8	70.65	D8	81.63

Discussion of BHawC results

From Tables D-4 and D-5, a number of interesting observations can be made. These are now discussed. It has to be noted that explicit values of (blade) loads, or blade eigenfrequencies, cannot be shown in the plots that follow, since these are confidential.

Power production

A first observation that is mentioned, is not immediately related to blade loads. It is however worthwhile to mention. This observation relates to power production. What is found, is that for thicker/stronger ice, the power production is impacted when the wind and ice are aligned. For thin/weak ice, this effect is not as severe and only present below rated wind speed. This can be seen in Figure D-11.

For the case of $h_{\text{ice}} = 40$ cm and $C_{\text{R}} = 1.37$ MPa, the effect was also found present, as for the remaining more severe ice cases evaluated. The cause seems to be a lower RPM of the rotor for the aligned, more severe ice cases. This is probably related to the controller, curtailing the power produced to ensure structural integrity, but that is still to be confirmed.

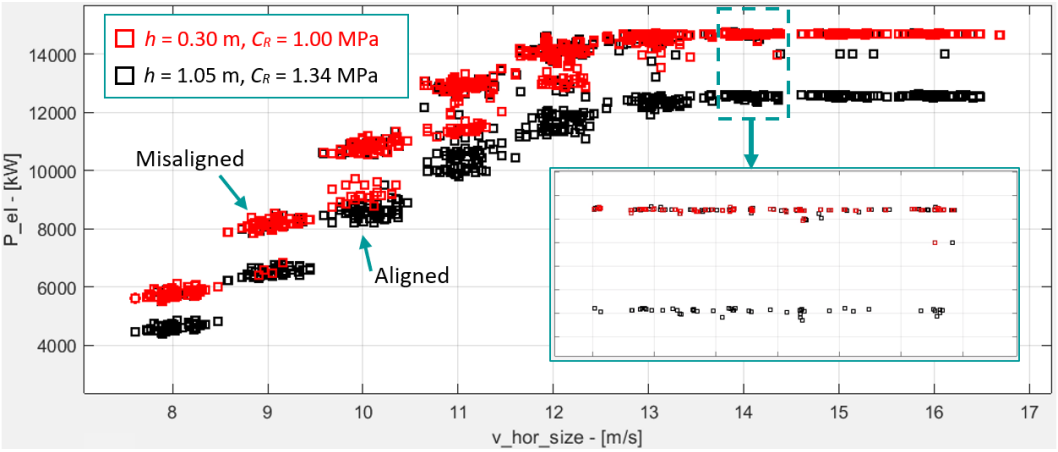

Figure D-11: Plot of the power production against wind speed for the cases of $h_{\text{ice}} = 30$ cm and $C_{\text{R}} = 1.00$ MPa, and $h_{\text{ice}} = 105$ cm and $C_{\text{R}} = 1.34$ MPa.

Flapwise loads

As can be seen from the tables, the flapwise loads are not significantly impacted by an increase in the ice thickness and/or ice strengths. This can be explained from the fact that the flapwise loads are found to be the largest for load case D3, when the turbine is in production. It then experiences a high thrust force acting at hub height, whereas the ice force acts at the waterline. This is reflected in the plot of the minimum flapwise loads, which are largest in absolute value. This plot, given in Figure D-12, follows the thrust curve, with its peak at the rated wind speed of 12 m/s.

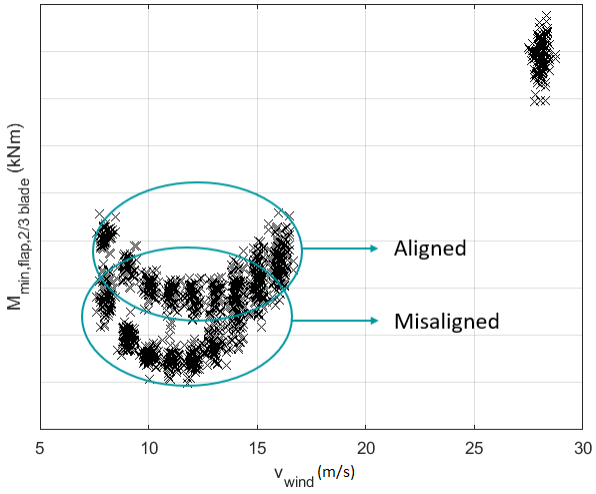

Figure D-12: Plot of the minimum flapwise moment against wind speed in load case D3, for the case of $h_{\text{ice}} = 105$ cm and $C_{\text{R}} = 1.34$ MPa.

In the case of aligned wind and ice, the flapwise loads are lower than for the misaligned case. This is the result of the power curtailment by the controller as shown above, reducing the thrust force on the turbine. This leads to a smaller magnitude of the flapwise blade loads.

Edgewise loads at blade root

Contrary to the flapwise loads, the edgewise loads significantly increase for the more severe ice cases. For the blade root minimum load, the largest increase is about 30% for the $h_{\text{ice}} =$ 105 cm, $C_{\text{R}} = 1.34$ MPa case. This indicates that for the edgewise loads, the ice does have a significant contribution to the loads. Case D3, which is the production case, is governing for the blade root loads.

Interestingly, the case of aligned wind and ice leads to the highest absolute edgewise loads at blade root, as shown in Figure D-13. This is counter-intuitive, since then the ice loads act perpendicular to the edgewise blade direction. Thus, the aligned ice acts in such a way that it invokes a motion in the blades perpendicular to the ice drift. This motion is one of the whirling motions as explained in Section D-1.

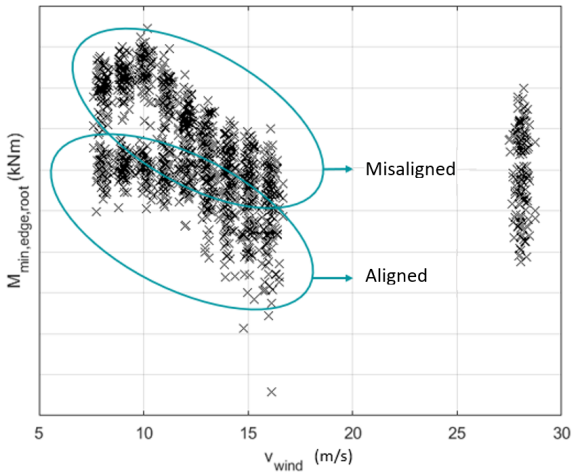

Figure D-13: Plot of the minimum edgewise moment at blade root against wind speed in load case D3, for the case of $h_{\text{ice}} = 105$ cm and $C_{\text{R}} = 1.34$ MPa.

As can be seen in Figure D-14, the misaligned case has a trough in its spectrum at the first backwards whirling mode frequency, whereas the aligned case remains at a significant load at that frequency. This explains the higher edgewise moments at blade root. However, it must be noted that the higher load can also be partly attributed to the higher thrust force at the blade frequencies, as shown in Figure D-15.

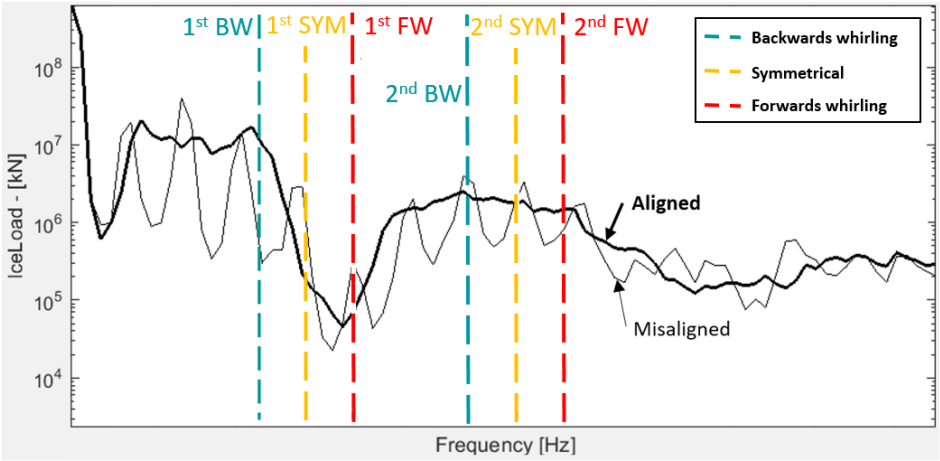

Figure D-14: Spectrum of the ice load for the most severe aligned and misaligned blade root moments for the case of $h_{\text{ice}} = 105$ cm and $C_{\text{R}} = 1.34$ MPa.

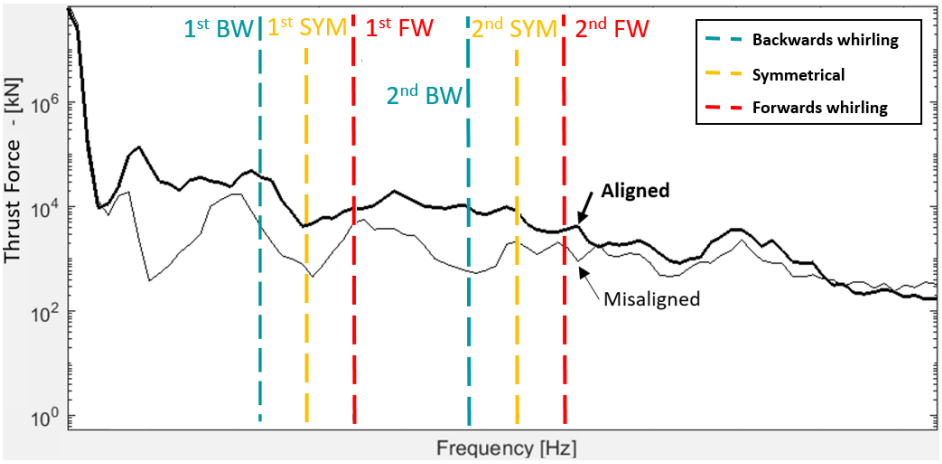

Figure D-15: Spectrum of the thrust force for the most severe aligned and misaligned blade root moments for the case of $h_{\text{ice}} = 105$ cm and $C_{\text{R}} = 1.34$ MPa.

Edgewise loads at 1/3 and 2/3 blade span

Even more so than the edgewise loads at blade root, the edgewise loads at 1/3 and 2/3 blade span are significantly impacted by the more severe ice cases, with a maximum of 138.8% for the minimum edgewise load at 2/3 blade span for the most severe ice case. Also similar to the loads at blade root, the 1/3 and 2/3 span loads are governed by the aligned ice case. However, unlike the loads at blade root, the highest loads for 1/3 and 2/3 blade span occur for the load case D8 (idling), such that the blades are pitched out and they run parallel to the ice in the aligned case, as can be seen in Figure D-16.

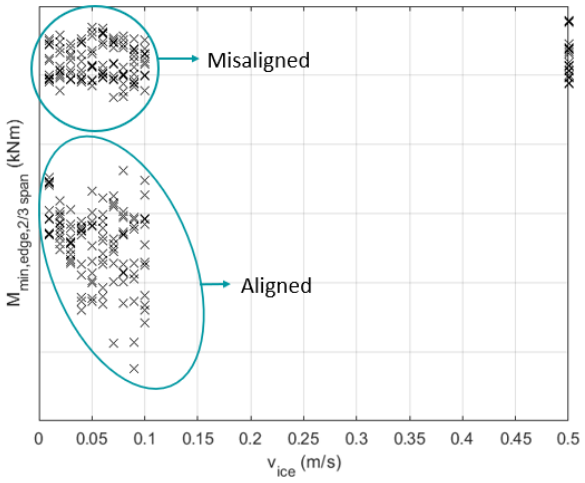

Figure D-16: Plot of the minimum edgewise moment at 2/3 blade span against ice speed in load case D8, for the case of $h_{\text{ice}} = 105$ cm and $C_{\text{R}} = 1.34$ MPa.

This can be understood from the simple fact that in D8 the wind is not a major factor in the forcing when compared to the ice loads for these ice thicknesses, because the blades are pitched out and the rotational speed of the rotor is greatly decreased. Then, the ice force that runs parallel to the edgewise direction for the blades will lead to the highest loads. With the blades pitched out, this is the aligned ice case.

Moreover, it can be seen that the highest loads are obtained for v_{ice} = 0.09 m/s, and that it decreases for lower ice speeds. This is the regime of intermittent crushing, so that this result is as expected. The higher loading can be attributed to the increased excitation at the second backwards whirling frequency, as becomes clear from Figure D-17.

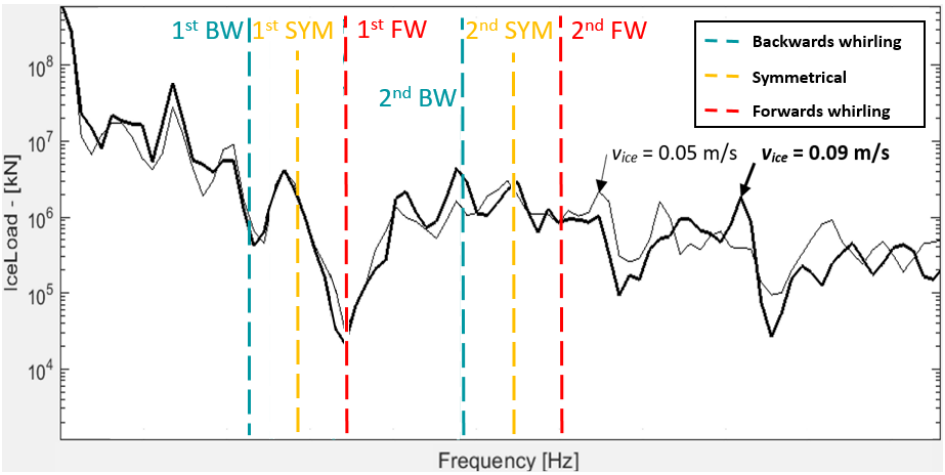

Figure D-17: Spectrum of the minimum edgewise moment at 2/3 blade span for $v_{\text{ice}} = 0.05$ m/s and $v_{\text{ice}} = 0.09$ m/s in load case D8, for the case of $h_{\text{ice}} = 105$ cm and $C_{\text{R}} = 1.34$ MPa.

Literature versus Hendrikse model ice parameters

As expected, the blade loads found are higher for the literature values than for the new model, since for all cases, the ice thickness and strength are equal or higher. However, it can be noted that this difference is especially of importance in the northern part of the Baltic Sea. Since the relative contribution of the ice in the total loading of the turbine increases with the ice thickness and strength, compared to the wind loads, a difference in the ice parameters becomes more noticeable in the loads found for thicker/stronger ice.

h_{50} and C_1 versus h_1 and C_{50}

From comparing the cases of h_{50} and C_1 against h_1 and C_{50}, for both the new model and the literature cases, it can be seen that (apart from some of the flapwise loads), the combination of h_{50} and C_1 always gives the highest loads.

For the Hendrikse model, this is as expected, from the scaling of the ice force. From equation 2.1, it can be seen that $p_{\text{G}} \propto h_{\text{ice}}^{0.86}$ for $h_{\text{ice}} \leq 1$ m (when $\frac{w}{h_{\text{ice}}} > 5$ like for the structure used), or at the lowest $p_{\text{G}} \propto h_{\text{ice}}^{0.66}$ for $h_{\text{ice}} \to 0$ m, where $p_{\text{G}} \propto C_{\text{R}}^{1}$. Evaluating Equation 2.1 for the Hendrikse model, going from h_1 and C_{50} to h_{50} and C_1, means an increase of 175% for h_{ice} and a decrease of 29.2%, such that p_{G} increases from 4.4 MN to 5.5 MN. The higher ice loads lead to the increase in blade moments.

Interestingly, for the literature values, this explanation is not satisfactory, since evaluation of Equation 2.1 gives a slight reduction in ice loads; from 7.7 MN for h_1 and C_{50} to 7.6 MN for h_{50} and C_1. Thus, the explanation must be sought in the dynamics. In Figure D-18, the spectra for the two cases are given, for the maximum blade loads at 2/3 blade span (for which

the moment increases about 11% with respect to the minimum case). It can be seen that the spectrum for h_{50} and C_1 contains a peak exactly at the symmetrical modes, both the first and the second, leading to the higher edgewise blade loads. This could however also be attributed to the velocities considered in the computations, since at intermediate velocities (or outside of the domain considered) this might be different. Nonetheless, this shows that a careful consideration of the parameters opted for, in combination of the velocities evaluated, is necessary.

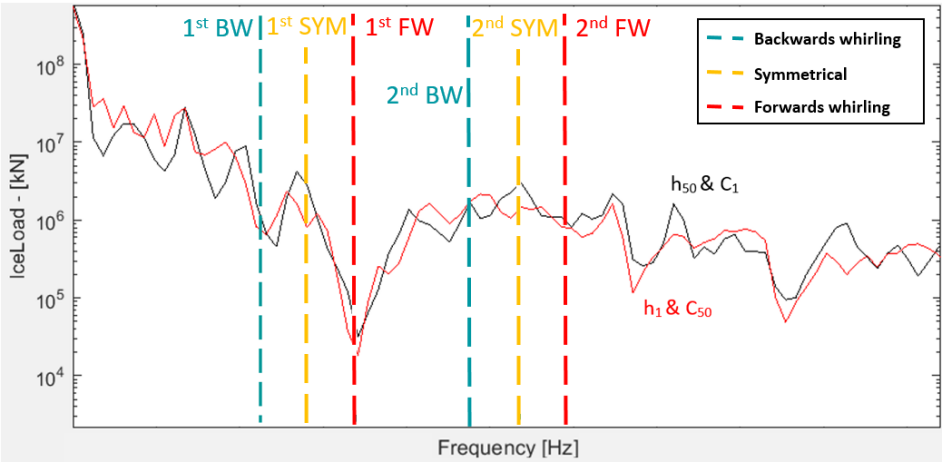

Figure D-18: Spectrum of the ice load for the most severe blade loads for h_1 and C_{50} (in red) and h_{50} and C_1 (in black), with the whirling mode and the symmetrical mode blade eigenfrequencies.

Variation of the value for C_R

The Hendrikse model and literature cases both contain a case with $h_{ice} = 30$ cm and a case with $h = 105$ cm. This allows for a comparison of these, with different values for C_R. It can be seen that the 16.3% increase in the cases with $h_{ice} = 30$ cm does not lead to a significant increase in the loads, with the highest increases being 3.67% for the edgewise minimum load at 1/3 blade span. For the cases with $h_{ice} = 105$ cm, the increase for C_R is higher with 38.1%, but the increase of the edgewise minimum blade load at 1/3 blade span is 52.5% compared to the minimum case.

Thus, the effect of increased C_R has a significantly larger impact for the thicker ice than for the thin ice. This can be explained by the fact that for thicker ice, the ice loads become more significant compared to the wind loads.

Another reason is given by the transition from D3 (leading for thinner ice) to D8 (leading for thicker ice). In idling, the wind loads are less relevant for the loading. Therefore, an increase in one of the ice parameters leads to a larger relative increase in the blade loads.

Tower parameter translating to higher blade loads

In order to evaluate results from simple Matlab calculations with standard VANILLA and a version extended with rubble and extrusion loads (see Chapter 7 of the main document), it is important to (if possible) identify a parameter that can relate the results obtained in Matlab to the blade loads found in the BHawC calculations as discussed above. Since the flapwise loads were found to not be significantly impacted by increased thicker or stronger ice, these are not further investigated or discussed.

It was found that for load case D8, most indicative for increased absolute values of the minimum edge loads is the minimum of the displacement at tower-top, with the absolute value of the minimum edge load increasing for decreasing minimum tower displacement. Figure D-19 shows the minimum blade root moments against the minimum tower-top displacements for load case D8. The spread of the data is the result of varying wind speed and ice cases. Nonetheless, the trend can clearly be observed. Unfortunately, for blade root, with load case D3 governing, this trend could not be observed, as the results were heavily influenced by the variation in wind cases.

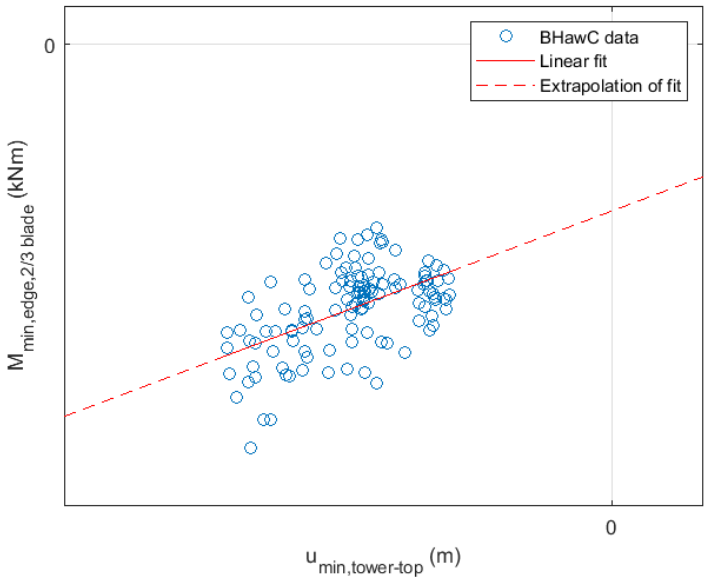

Figure D-19: Plot of the minimum edgewise blade moment at 2/3 blade span against the minimum tower-top displacement for the case of $h_{\text{ice}} = 105$ cm and $C_{\text{R}} = 1.34$ MPa.

D-4 Limitations

For the blade modelling, a turbine model has been used that has been extensively verified and is in use in one of the leading firms in the industry, such that it can be assumed that the results found are not significantly impacted by errors in the turbine model. However, there are still some points that can be made about the inputs to the model, that may negatively impact the trustworthiness of the results found.

Firstly, a fixity depth approach was taken for the foundation of the turbine. This is deemed the simplest method for modelling soil mechanics, with many nonlinear effects in the soil not being taken into account. This may skew the results, although not significantly. Next to that, only one turbine model is examined, such that results may differ for other turbines, with different dimensions and characteristics.

On the topic of ice, more limitations could be brought forward. The accuracy of the turbine model is significantly higher than the ice model. VANILLA has been validated and certified, but is a phenomenological model, based on a limited pool of data sets, of which most not at full scale. With more (full scale) data for verification, the accuracy could likely be improved. However, it is currently the state of the art and arguably the most reliable way of simulating ice loads on offshore structures.

Also, the fact that alignment of the ice was shown to be of great importance for the blade loads raises the question whether only considering 2 angles for the incoming ice (0° and 90°) is sufficient. The dynamics of an offshore wind turbine are highly nonlinear, such that an intermediate angle of misalignment may give rise to higher loads than the once found here.

Next to only 2 values for the alignment angle, only 6 combinations of ice parameters (thickness, strength) were considered. This was done based on the assumption that these would show the minimum and maximum cases encountered in the Baltic Sea. However, due to the many nonlinearities in offshore wind turbines, it might well be that an intermediate value for the ice conditions that was not considered, leads to dynamics that give rise to higher loads than resulted from the cases considered, due to excitation at one of the natural frequencies.

The same could be said about ice drift speeds. Where Figure D-16 seems to show that the peak in absolute value of the edgewise load was encountered, it is only barely. The peak is at 0.09 m/s, while the range in ice speeds considered only goes up to 0.1 m/s. For some of the other ice thicknesses and strengths, the peak might lie at ice drift speeds above 0.1 m/s. This could lead to even higher blade loads. The observed effects and trends will however not differ.

Perhaps the most contentious point found in the blade load modelling, is the trend of the minimum (and maximum) edgewise blade loads. The fit shown in Figures D-16 is for data with a significant spread. Moreover, Figure D-16 is only found for a limited range of minimum displacements, such that outside the data, the trend might be different. Lastly, the trends in the other blades were found to be different, with no trend apparent or showing an opposite

trend, but the magnitude of the loads in those were smaller. Nonetheless, this could mean that the trend is not very reliable and should only be used as a first indication of how the blade loads may depend on tower dynamics.

D-5 Conclusion

From these simulations, the research question introduced at the beginning of this Appendix can be answered. It can be concluded that for this turbine, the blade loads are only significantly impacted by the ice in the edgewise direction, while the impact on the loads in the flapwise direction is negligible. The more severe ice cases show that the edgewise loads increase considerably for a location in the north of the Baltic, compared to a location in the south.

Moreover, the edgewise loads at blade root are governed by the production design load case, with the turbine spinning, while the loads at 1/3 and 2/3 of the blade span are governed by the case of idling.

The edgewise loads are most severe when the ice and wind are aligned. Also, the blade loads depend on the ice force in a non-linear fashion, with certain frequencies in the ice force exciting the blade at one of its natural frequencies, most notably the first backwards and forwards whirling modes, as well as the first symmetrical mode. Lastly, the minimum displacements of the tower-top were found to be reasonably good indicators of the magnitude of the blade loads, which increase for decreasing minimum displacements (increasing absolute value).

Recommendations

Based on the conclusions as given above, a number of recommendations can be made for further research. First, the results of the large increase in modelled blade loads when a turbine is placed in a northern Baltic location, with more extreme ice conditions, suggest that it is worthwhile to further expand the ice model with other phenomena, such as rubble and extrusion. These might lead to increased damping and less severe blade loads.

Additionally, it would be good to check whether these same results would also show for other turbines and/or foundations. Due to the many non-linearities in the turbine modelling, it might be that a different structure shows other results.

Lastly, the difference in blade loads shown for the ice conditions considered from literature and the ISO standard from the Hendrikse model, shows that proper verification of the Hendrikse model (or proof against the values from literature) could benefit future projects.